UTS UNIVERSITY OF TECHNOLOGY SYDNEY

Performance Enhancement of a Switched Reluctance Motor Using Hybrid Excitation Method for Electric Vehicle Applications

by Vijina Abhijith

Thesis submitted in fulfillment of the requirements for the degree of

Doctor of Philosophy

Under the supervision of Prof. Jahangir Hossain and Dr. Gang Lei

University of Technology Sydney

Faculty of Engineering and Information Technology

March 2023

CERTIFICATE OF ORIGINAL AUTHORSHIP

I, Vijina Abhijith , declare that this thesis is submitted in fulfillment of the requirements for the award of Doctor of Philosophy, in the School of Electrical and Data Engineering, Faculty of Engineering and Information Technology, FEIT at the University of Technology Sydney, Australia.

This thesis is entirely my work unless otherwise referenced or acknowledged. In addition, I certify that all information sources and literature used are indicated in the thesis.

This document has not been submitted for qualifications at any other academic institution.

This research is supported by the Australian Government Research Training Program.

Signature: Production Note: Signature removed prior to publication.

[Vijina Abhijith]

Date: 20th March, 2023

Place: Sydney, Australia

DEDICATION

"This thesis is dedicated to my beloved father, who passed away during my Ph.D. course. I am deeply grateful for the time we had together and our shared memories. Although he is no longer with us, his spirit and legacy live on in me and this work. I dedicate this thesis to his memory with love and admiration. "

ACKNOWLEDGMENT

I Would like to express my sincere gratitude to my supervisor, Prof. Jahangir Hossain, for the invaluable support and guidance throughout writing this thesis. His insightful comments, constructive feedback, and commitment to excellence have been instrumental in shaping my ideas and improving the quality of my work. I am grateful for his time and effort in my academic growth and development. The mentorship has inspired me, and I am honored to have worked under his supervision.

I want to express my profound gratitude to Dr. Gang Lei, my co-supervisor, for the excellent advice and assistance that he gave me when I was preparing my thesis. His knowledge, perspective, and helpful criticism helped refine my research and raise the caliber of my writing. His dedication to my success has been evident through his timely responses, attention to detail, and encouragement to keep going. I am grateful for the opportunity to work with Lei and the knowledge and skills I gained from the supervision.

I sincerely like to express my deep appreciation to the University of Technology, Sydney, for providing me with the resources, facilities, and academic support necessary to complete this thesis. The University's commitment to excellence in education and research has enabled me to achieve my academic goals. I am thankful to David McGloin, the research dean who always supported and guided me through all the struggles. I am also grateful to UTS for awarding me the International Research Scholarship to help with my living cost and tuition fees during my candidature.

I appreciate Mr. Tijo Thomas, the chief technology officer of Entuple E-mobility, for his support and contribution to this research project. The company's commitment to innovation and research has facilitated my access to data and resources necessary for completing this thesis. Collaborating with the Entuple team has given me valuable insights into industry practices and real-world applications of theoretical concepts. During difficulties with this job, everyone from the team to classmates, students, and a group of friends offered their assistance. I want to express my deepest gratitude to Premlal for his unwavering support and guidance throughout my academic journey. Without his assistance, this accomplishment would not have been possible. Thank you for being a constant source of inspiration and motivation.

I owe a tremendous deal of gratitude to my family for supporting me in all of my endeavors. They believe in my abilities, and their unwavering support has kept me going during the most challenging times. During the COVID-19 crisis, although I separated from my three-year-old son, my family cared for him. The sacrifices, understanding and dedication have made it possible for me to focus on my studies and have let me concentrate solely on my thesis. I am honored to be a part of this wonderful family. This accomplishment is a testament to their love, and I dedicate this thesis to the family with all my heart.

LIST OF PUBLICATIONS

RELATED TO THE THESIS:

1. Abhijith, V., Hossain, M. J., Lei, G., Sreelekha, P. A., Monichan, T. P., and Rao, S. V. (2022). Hybrid Switched Reluctance Motors for Electric Vehicle Applications with High Torque Capability without Permanent Magnet. Energies, 15(21), 7931.

2. Torque Ripple Minimization of an Innovative Non-Permanent Magnet Hybrid Excited Switched Reluctance Motor for Electric Vehicle Applications, IEEE-Industry Application, **(under review)**.

3. High Torque Capability Non-Segmented Magnet Hybrid Excited Switched Reluctance Motor for electric vehicle application, IEEE Energy Conversion, **(under review).**

CONFERENCES :

4. Abhijith, V., Hossain, M. J., Lei, G., and Premlal, A. S. (2021, October). Performance improvement of switched reluctance motor using hybrid excitation method without permanent magnets. In 2021 24th International Conference on Electrical Machines and Systems (ICEMS) (pp. 74-78). IEEE.

5. V. Abhijith, M. J. Hossain, G. Lei and P. A. Sreelekha, "A Hybrid Excited Switched Reluctance Motor for Torque Enhancement Without Permanent Magnet Behavior in Electric Vehicle Applications," 2022 IEEE 10th Power India International Conference (PIICON), New Delhi, India, 2022, pp. 1-5, doi: 10.1109/PIICON56320.2022.10045190.

6. Abhijith, V., Hossain, M. J., Lei, G., and Premlal, A. S, Sandeep.B.K.High Torque Capability Non-Permanent Magnet Hybrid Excited Switched Reluctance Motor for electric vehicle application (ECCE 2023), IEEE, IAS, PELS.

7. Abhijith, V., Hossain, M. J., Lei, G., and Premlal, A. S, Sandeep.B.K, High Torque Capability Segmented Hydrid Excited Switched Reluctance Motor for

Electric Vehicle Applications.IEEE ETFG 2023, University of Wollongong, Australia.

8. Abhijith, V., Hossain, M. J., Lei, G., and Premlal, A. S, Sandeep. B.K, Hybrid Topologies Of Non-Permanent Magnet-Excited Switched-Reluctance Motors With High Torque Capability For Electric Vehicle Applications.IFEEC2023, University of Technology, Sydney.

PLAN TO SUBMIT :

9. Torque Ripple Minimization of a Non-segmented Hybrid Excited Switched Reluctance Motor for High-performance Electric Vehicle Application (International Journal For Power And Energy).

10. Robust design system-level Parameter Optimization for High-performance Hybrid Excited Switched Reluctance Motor for Electric Vehicle Applications.

ABSTRACT

Switched reluctance motors (SRMs) have been a growing interest in industrial and commercial applications because of their simple construction, reliability, and fault tolerance. Moreover, SRMs are rising in applications in electric vehicles (EVs) because of their unique features and the absence of permanent magnets (PMs). Hence, researchers have been trending over these for years to elevate motor performance by incorporating the behavior of rare earth materials.

The significant contribution of this research is to enhance the performance of the SRMs by using the hybrid excitation method (HESRM) without the utilization of PMs. Consequently, this is achieved by externally injecting direct current (DC) into the separately excited auxiliary windings. The simulation results are verified through the experimental results and are similar for both topologies, which can produce high torque across all the speeds. Subsequently, finding a new shortest flux path by allocating the auxiliary winding to the alternate poles in the second topology contributes more electromagnetic torque than in the first.

The designed motor achieves high torque capability; however, the result shows a high degree of torque ripple. This thesis proposed a method to minimize the ripple through phase advancing to overcome the issue. The turn-on and off-angle would effectively subsidize the delay between the switching on and off currents in the phase excitation. This approach with new topologies aims to enhance the torque performance with a minimal ripple that will lead to acting as a promising candidate for variable speed applications. Furthermore, this research intends to find the maximum torque per ampere for the wide speed ranges. While considering the limitation in motor specifications in EV loads, the analysis of the system models restricted the vehicle parameters. The coupled structure gives the overall idea of the system to analyze the proposed methods that have proven their torque capabilities in EVs. Additionally, this research aims to locate the optimal parameter values for the machines and controllers through a system-level optimization. For this purpose, an integrated multi-objective genetic algorithm (MOGA) approach gains to accomplish the maximum potential design for the desired HESRM. Correspondingly, the research significantly improves the torque profile and efficiency within the machine constraints. Consequently, the novel contribution achieved in the design is to deliver higher torque density with minimum ripple. In conclusion, the research compares and discusses the results of the proposed methods of topologies with conventional motors of the same ratings, and the findings are adaptable for EVs.

TABLE OF CONTENTS

CERTIFICATE OF ORIGINAL AUTHORSHIP i

DEDICATION ii

ACKNOWLEDGMENT iii

LIST OF PUBLICATIONS iv

ABSTRACT vi

List of Figures xii

List of Tables xix

1 Introduction 1

1.1 Background 1
1.2 Research Motivation and Problem Statement 3
1.3 Research Gap and Research Question 3
1.4 Aim and Objectives 4
1.5 Novel Contributions and Outcomes 5
1.6 Thesis Structure 5

2 Literature Review 7

2.1 Introduction 7
2.2 Electric Vehicle Motors 7
2.2.1 Requirement of EV Application 8
2.2.2 Challenges of Electric Traction Motors 9
2.3 Different Types of EV Motors 10
2.3.1 DC Motors 11
2.3.2 Induction Motor 12
2.3.3 Permanent Magnet Synchronous Motors 12
2.3.4 Brushless DC Motors 12
2.3.5 Switched Reluctance Motors 13

2.4 Comparison Between EV Motors 13
2.5 Permanent Magnet Scarcity 14
2.6 Switched Reluctance Motor for EV Application 17
2.7 Fundamentals of Switched Reluctance Motor 18
2.7.1 Inductance Profiles of Four Distinct Regions 19
2.8 Torque Improvement schemes in SRMs 20
2.8.1 Advanced Power Converters 20
2.8.2 Segmented Rotor or Stator Core 22
2.8.3 Hybrid Excitation of Switched Reluctance Motor 24
2.9 Advantages and Disadvantages of the Existing Methods 33

3 Different Topologies of HESRMs 34
3.1 Research Methodology 34
3.2 Objective 1: Different Topologies for HESRM 36
3.2.1 Background 36
3.3 Initial Design: 37
3.3.1 Step 1: Analysis of Conventional SRM 37
3.3.2 Step 2: Analysis of Initial Machine Parameters 38
3.3.3 Step 3: DC Injection to the Auxiliary Poles 47
3.4 Objective 2: Design of Controller for Auxiliary Poles 48
3.4.1 DC Injection in the Auxiliary Winding 48
3.4.2 Controller Design 50
3.5 Machine Topology 1 53
3.6 Mathematical Model of the HESRM 54
3.7 Magnetic Equivalent Circuit Model of the HESRM 56
3.8 Characteristics of the HESRM Using 2D FEA Analysis 57
3.8.1 Magnetic Characteristics of Two SRM 57
3.8.2 Steady-State Characteristics 59
3.8.3 Dynamic Performance of Two SRM Drives in FEM 60
3.9 Experimental Results 62
3.9.1 Rewinding and Remodelling 62
3.9.2 Motor Prototype 63
3.9.3 Dynamic Performance of HESRM without PMs 66
3.10 Comparison of Hardware Solution with FEM Simulation Results . . 69
3.11 Comparison with Conventional SRM 70
3.12 Discussion 70
3.13 Inference: Topology I 72
3.14 Machine Topology II 73
3.14.1 Software Analysis using FEM 73

3.14.2 Experimental Validations 74
3.15 Comparison of the Results of Software and the Hardware 76
3.16 Comparison with Conventional SRM 78
3.17 Discussion 78
3.17.1 Speed- Torque Characteristics 78
3.17.2 Speed -Efficiency Characteristics 79
3.17.3 Speed- Input Power Characteristics 80
3.18 Inference: Topology II 80
3.19 Machine Topology III 81
3.19.1 Case (i): Segmenting the Auxiliary Core (SHESRM) 81
3.19.2 Case (ii) By Changing Stator Outer Diameter 84
3.19.3 Case (iii) Adding Active Poles 86
3.20 Inference: Topology III 87
3.21 Comparison of Different Topologies 88
3.22 Comparison with Existing Methods 89
3.23 Conclusions 90

4 Torque Ripple Reduction in HESRMs 91
4.1 Objective 3: Torque Ripple Reduction in HESRMs 91
4.1.1 Principle of Operation 91
4.2 Torque Ripple Minimization in Conventional SRM 93
4.2.1 Principle of Operation 93
4.2.2 Transient Response 94
4.3 Comparison of Torque Ripple in CSRM 95
4.4 Inference-CSRM 96
4.5 Torque Ripple Minimization in Topology I 96
4.5.1 Structural Analysis 96
4.5.2 Motor Topology 97
4.5.3 Magnetic Flux Line Distribution 98
4.6 MEC Model and Torque Equation 98
4.7 Result and Discussion 99
4.7.1 Software Analysis Using 2D-FEM 99
4.7.2 Dynamic Performance using SRM Drive 102
4.8 Experimental Validation 104
4.8.1 Transient Response of Two SRM's Drive 105
4.8.2 Experimental Validation of Torque Ripple 106
4.9 Comparison of Performance using Hardware and Software Solutions 107
4.9.1 Average Torque Characteristics 107
4.9.2 Speed Torque Characteristics 107

4.10 Comparison with Conventional SRM 108
4.10.1 Torque Ripple 108
4.10.2 Efficiency 109
4.10.3 Input Power 109
4.11 Comparison of Torque Ripple Minimization in Topology I 110
4.12 Inference-Torque Ripple Minimization in Topology I 111
4.13 Torque Ripple Minimization in Topology II 111
4.13.1 Principle of Operation 111
4.14 Dynamic Characteristics -Topology II 113
4.14.1 Moving Torque Characteristics 113
4.14.2 Torque Ripple Characteristics 114
4.15 Comparison of Performance using Hardware and Software Solutions 114
4.15.1 Average torque characteristics 114
4.15.2 Speed Torque Characteristics 115
4.16 Experimental Validation 116
4.16.1 Transient Response of Two SRM's Drive 118
4.16.2 Experimental Validation of Torque Ripple 118
4.17 Comparison of Proposed HESRM with Conventional SRM 119
4.17.1 Torque Ripple 119
4.17.2 Efficiency 120
4.17.3 Input Power 120
4.18 Comparison of Torque Ripple Minimization in Topology II 121
4.19 Inference-Topology II 121
4.20 Conclusions 122

5 System-level Optimization **124**
5.1 Introduction 124
5.2 Objective 4: System-level Optimization in HESRM 124
5.3 Optimization Algorithms 125
5.3.1 Random Surface Methodology 126
5.3.2 Computer-Based Optimal Design 127
5.3.3 Genetic Algorithm Approach 127
5.3.4 Multi-Objective Genetic Algorithm Method 129
5.4 Optimization of Parameters in HESRMs 130
5.5 System Model 132
5.5.1 Torque-Speed Characteristics 133
5.6 Multi-Objective GA Optimization in HESRM 134
5.6.1 Pareto Result 136
5.7 Result and Discussion 138

5.7.1 Analysis of Moving Torque 138
5.7.2 Result of Parameters Optimized 140
5.7.3 Results of Objectives Before and After Optimization 140
5.8 Conclusions 140

6 Conclusions and Recommendation for Future Works 142
6.1 Conclusions 144
6.2 Impacts of the Thesis 145
6.3 Recommendation for Future Works 146

A Appendix 150
A.1 Calculation of Torque Equation in SRM 150
A.1.1 By Electromagnetically Energy Conversion in a Solenoid . . . 150
A.1.2 By Equivalent Circuit 152

Bibliography 155

LIST OF FIGURES

FIGURE **Page**

2.1 Torque-speed characteristics of traction motors. 9
2.2 Power-speed characteristics of traction motors. 9
2.3 Different types of electric motors to drive EV applications. 10
2.4 Parameter comparison of EV motors. 14
2.5 Utilization of permanent magnets. 15
2.6 The chart (a) production rate (b) Demand rate of PM. 16
2.7 Conventional SRM (a) 3-phase, 12/8 poles (b) Magnetic flux distribution lines for 12/8 pole SRM. 18
2.8 Relationship between inductance and rotor position. 19
2.9 Different torque improvement strategies in SRMs. 21
2.10 Structural diagram of (a) Segmented rotor poles (b) Magnetic flux lines in the segmented rotor. 23
2.11 SRM with C-shaped segmented stator poles. 24
2.12 Cross-section of the proposed MSHSRM. 25
2.13 Basic structure of proposed SRM with permanent magnet and auxiliary windings. 26
2.14 Flux path of the proposed SRM of auxiliary windings are wound around the stator yoke. 27
2.15 Cross-sectional view of proposed SRM of double salient permanent magnet machine (DSPM). 27
2.16 Cross-section view and the flux direction of 6-slot-8-pole HEFSSRM. . . 28
2.17 Cross-section view of superimposition stator PM excited HESRM. 29
2.18 The proposed HESRM of collective excitation (a) Flux distribution of hybrid excitation (b) Inductance profile and phase current in hybrid excitation method. 30
2.19 C- dump inverter for hybrid excitation method. 30
2.20 Cross-section view of super multi-polar permanent reluctance generator. 31
2.21 Proposed single-phase hybrid excited SRM for low power applications. . 32
2.22 Cross-sectional view of V-shape concentration flux generated HESRM. . 32

3.1 Four main objectives and the results obtained for the proposed method. 35
3.2 Block diagram for the conventional SRM switching scheme. 36
3.3 Block diagram of hybrid excitation model without using a PM excitation. 37
3.4 Different steps for executing to attain the initial parameter optimization. 37
3.5 Characteristics results of 600 W conventional SRM (a) Torque-speed Characteristics and (b) Air-gap inductance for the designed conventional SRM. 38
3.6 Block diagram of initial motor parameter optimization using Ansys/-Maxwell FEM analysis. 39
3.7 Flow chart for initialization of machine design parameters. 40
3.8 Single-pulse denoting delay time (T_d), rise time(T_r) and fall time (T_f). . 41
3.9 Moving torque characterization for the different delay times. 42
3.10 Moving torque output characteristics for a fixed delay time value, T_d = 46. 43
3.11 Moving torque characteristics for separated auxiliary poles. 45
3.12 Block diagram of initial parameter optimization of selecting the number of turns using MOGA. 46
3.13 The Pareto results for selecting the number of turns in both windings. . 47
3.14 External circuit for an auxiliary winding excitation. 48
3.15 Moving torque with optimized value and modeled with separate excitation concerning time (s) and average torque (N-m). 48
3.16 Moving torque output for various input currents to the auxiliary circuit. 49
3.17 Flux path of HESRM without PMs excitation. 49
3.18 DC injection profile for the proposed HESRM. 50
3.19 Block diagram of the Conventional SRM drive. 50
3.20 Proposed HESRM drive for main and auxiliary winding. 51
3.21 The proposed new switching pattern for proposed HESRM. 52
3.22 PWM excitation scheme for the dc-injected auxiliary windings. 53
3.23 Machine topology of two SRMs with the same rating is shown as (a) a 12/8-pole conventional SRM and (b) a 12/8-pole hybrid excitation of SRM without PMs. 54
3.24 Magnetic flux path for the proposed SRM is shown as (a) Aligned poles and (b) Unaligned poles. 54
3.25 Magnetic equivalent circuit of the proposed HESRM (a) For different phases (b) Single MEC circuit. 56
3.26 Magnetic flux distribution of conventional SRM: (a) Aligned poles (b) Unaligned poles. 58
3.27 Magnetic flux distribution of the proposed HESRM: (a) Aligned poles (b) Unaligned poles. 58

3.28 The characteristics of measured flux density of conventional SRM and the hybrid dc-excited SRM. 59
3.29 Static torque characteristics: (a) Conventional SRM at rated current 15 A and (b) HESRM under various currents concerning the DC field injection. 60
3.30 Comparison of characteristics of moving torque and current of two SRMs. 61
3.31 Comparison of closed-loop current control of conventional SRMs and HESRM. 62
3.32 Closed-loop variable-speed current control strategy: (a) conventional SRM and (b) HESRM; the curves are current (A), torque (N−m), and speed (rpm). 63
3.33 Photograph of rewinding the conventional SRM to HESRM (a) Main winding. (b) Auxiliary winding. 64
3.34 Test bench of SRM coupled with the electric loading 64
3.35 Controller circuit for exciting the main and auxiliary winding. 65
3.36 The real-time implementation of Waveact controller. 65
3.37 Testing platform for the proposed HESRM with hybrid excitation. 66
3.38 Dynamic performance of conventional SRM with variable speed of (a) 1000 rpm and (b) 2500 rpm. 67
3.39 Dynamic performance of proposed HESRM with variable speed of (a) 1000 rpm and (b) 2500 rpm. 67
3.40 Transient response of both SRMs at reference speed (a) Conventional SRM and (b) Proposed HESRM. 68
3.41 Characteristics of the auxiliary dc excitation for the proposed HESRM for different speeds. 69
3.42 Average torque performance for variable speed of proposed HESRM: (a) 1000, (b) 1500, (b) 2000, and (d) 2500 rpm. 70
3.43 Comparison of average torque with variable speed for conventional SRM and proposed HESRM: (a) 1000, (b) 1500, (c) 2000, and (d) 2500 rpm. . . 71
3.44 Comparison of conventional SRM with proposed HESRM: (a) Average torque, (b) Efficiency, and (c) Input power. 72
3.45 Machine topology II of the new proposed HESRM with the same rating with 12/8-pole hybrid excitation of SRM without PMs (a) Conventional SRM (b) Proposed Topology II 73
3.46 Magnetic flux distribution for proposed HESRM: (a) Aligned position and (b) Unaligned position. 74
3.47 Static torque characteristics (a) Conventional SRM at rated current 15 A. (b) HESRM under various current excitation at the auxiliary coils. . . . 75
3.48 Testing platform for the proposed HESRM with separate excitation for auxiliary. 75

3.49 Dynamic performance of conventional SRM variable speed (a) 1000 rpm (b) 2500 rpm. 76
3.50 Dynamic performance of proposed HESRM II variable speed (a) 1000 rpm (b) 2500 rpm. 76
3.51 The auxiliary dc excitation characteristics of topology II HESRM for different speeds. 77
3.52 Average torque performance for topology II HESRM: (a) 1000, (b) 1500, (c) 2000, and (d) 2500 rpm. 77
3.53 Comparison of average torque of conventional SRM and proposed HESRM for different speeds: (a) 1000, (b) 1500, (c) 2000, and (d) 2500 rpm. 78
3.54 The comparison of average torque for conventional and proposed SRMs with variable speed. 79
3.55 The efficiency comparison for conventional and proposed SRMs with variable speed. 79
3.56 The comparison of input power for conventional and proposed SRMs with variable speed. 80
3.57 The isolated poles are changed to high permeable material in SHESRM. 81
3.58 Magnetic flux density of SHESRM when stator poles are (a) Aligned and (b) Unaligned. 82
3.59 The results of segmented hybrid excited SRM (SHESRM) with non-PMs (a) Current versus average torque (b) Static torque versus position of the rotor and (c) Speed- Torque characteristics. 82
3.60 Comparison of average torque for the three topologies (a) Current-Torque characteristics (b) Speed-Torque characteristics 83
3.61 Segmenting the auxiliary core for changing the stator outer diameter (a) Case (i) and (Case (ii)). 84
3.62 Segmenting the auxiliary core for changing the stator outer diameter, case(i): (a) Magnetic flux density and (b) Magnetic field lines. 85
3.63 Segmenting the auxiliary core for changing the stator outer diameter, case(ii): (a) Magnetic flux density and (b) Magnetic field lines. 85
3.64 Average torque characteristics of changing stator OD and the results compared with conventional SRM (a) Torque-current characteristics of both cases (b) Comparison of average torque. 86
3.65 Adding stator and rotor poles for improving active poles to 25% to 75% : (a) 18/12 (b) 24/16 (c) 36/24 (d) 46/32 poles 87
3.66 Comparison of average torque of SRMs added active poles. 88
3.67 Comparison of average torque with existing methods. 90

4.1 Block diagram for the proposed HESRM without PMs excitation. 92

4.2 Block diagram for torque ripple minimization in proposed HESRM without PMs. 92
4.3 The graphical representation of torque ripple minimization. 93
4.4 The block diagram of torque ripple minimization in conventional SRM. . 94
4.5 The switching of phase advance method for torque ripple minimization in conventional SRM. 94
4.6 Performance of torque ripple characteristics in conventional SRM. 95
4.7 Torque ripple comparison of the conventional SRM. 95
4.8 The structural diagram of 12/8, three-phase conventional SRM and proposed HESRM (a) Conventional SRM and (b) Proposed SRM. 97
4.9 The magnetic flux distribution characteristics of both SRMs in aligned and unaligned pole conditions (a) Aligned pole (b) Unaligned pole 98
4.10 Magnetic equivalent circuit model for the cross-sectional view of pole pair of proposed 12/8 HESRM without permanent magnet excitation. 99
4.11 The magnetic flux density characteristics of the proposed HESRM for aligned and unaligned positions (a) Aligned (b) Unaligned. 100
4.12 The magnetic flux linkage characteristics of both SRMs. 100
4.13 The static electromagnetic torque characteristics of both SRMs with phase excitations (a) Conventional SRM and (b) Proposed HESRM. 101
4.14 Experimental results of phase current and the moving torque characteristics of the conventional SRM at variable speed (a) 1500 rpm and (b) 2000 rpm. 102
4.15 Experimental results of phase current and the moving torque characteristics of the proposed HESRM without PM at variable speed (a) 1500 rpm and (b) 2000 rpm. 102
4.16 Experimental results of implementing torque ripple minimization in 12/8 conventional SRM and the proposed HESRM without PM (a) Conventional SRM and (b) Proposed HESRM. 103
4.17 Back-to-back set up for experimentation for the SRMs. 104
4.18 Experimental platform for the proposed HESRM. 105
4.19 Time-varying excitation characteristics of two SRMs (a) Conventional SRM and (b) Proposed HESRM. 105
4.20 Experimental results of Wavect controller outcomes with torque measurement. 106
4.21 Comparison between measured average torque and those predicted using 2-D finite elements of conventional SRM and the proposed hybrid dc excited SRM. 107
4.22 Comparison of speed-torque characteristics of two SRMs between measured quantity and those predicted using 2-D finite elements. 108

4.23 Torque ripple comparison of the conventional and proposed SRMs. 108
4.24 Efficiency comparison of the conventional and proposed SRMs. 109
4.25 Input power comparison of the conventional and proposed SRMs. 110
4.26 Block diagram for torque ripple minimization in proposed HESRM for topology II without PMs. 112
4.27 Experimental results of phase current and the moving torque characteristics of the conventional SRM at variable speed (a) 1500 rpm and (b) 2000 rpm. 113
4.28 Experimental results of phase current and the moving torque characteristics of the proposed HESRM without PM at variable speed (a) 1500 rpm and (b) 2000 rpm. 114
4.29 Experimental results of an implementation of torque ripple minimization in 12/8 conventional SRM and the proposed HESRM without PM (a) Conventional SRM and (b) Proposed HESRM. 114
4.30 Comparison between measured average torque and those predicted using 2-D finite elements of conventional SRM and the proposed hybrid dc excited SRM. 115
4.31 Comparison of speed-torque characteristics of two SRMs between measured quantity and those predicted using 2-D finite elements. 115
4.32 Back-to-back set up for torque ripple minimization experimentation. . . 116
4.33 Assigning the main and auxiliary winding for DC excitation. 117
4.34 Controller circuit for the proposed torque minimization topology. 117
4.35 Time-varying excitation characteristics of two SRMs (a) Main winding excitation (b)Auxiliary winding excitation. 118
4.36 Experimental results of Wavect controller outcomes with torque measurement. 118
4.37 Torque ripple comparison of the conventional and proposed SRMs. 119
4.38 Efficiency comparison of the conventional and proposed SRMs. 120
4.39 Input power comparison of the conventional and proposed SRMs. 120

5.1 Flow chart of the system-level optimization. 125
5.2 Flow chart for the multi-objective genetic algorithm optimization technique.130
5.3 Flow chart of the optimization technique employed in this research. . . . 130
5.4 System modeling, including main and secondary excitation and vehicle level simulation. 132
5.5 Torque-speed characteristics response from the system model analysis. 133
5.6 Results of first-level optimization for machine parameters. 136
5.7 Results of second-level optimization for controller parameters. 137
5.8 Moving torque characteristics before and after optimization. 139

A.1 Solenoid and Flux versus MMF characteristics. 151
A.2 Equivalent circuit of the SRM. 153

List of Tables

Table		Page
2.1	Different EV model and its propulsion system.	11
2.2	Efficiency comparison between EV motors.	14
2.3	Comparison of existing torque enhancement method.	33
3.1	Optimization for initial rotor position.	41
3.2	Optimization for the delay time of the input pulse.	42
3.3	Initial parameter optimization for the (T_r), (T_f) and (P_w) of the conventional SRM.	43
3.4	Different iterations for choosing the optimum number of turns.	44
3.5	The various torque outputs when 2, 4, and 6 poles are removed.	44
3.6	Main dimensions and parameters of two SRMs	57
3.7	Comparison of average torque with conventional SRM and topology I and II of HESRM.	89
4.1	Comparison of torque ripple in CSRM.	96
4.2	Specification of the two SRMs.	97
4.3	Comparison of torque ripple minimization in topology I.	110
4.4	Comparison of torque ripple in topology II	121
4.5	Comparison of torque ripple for different topologies.	122
5.1	Initial parametric value.	131
5.2	Electric vehicle data for system-model simulation.	134
5.3	Iteration results of first-level machine variables	138
5.4	Iteration result of second-level controller variables	139
5.5	Parameter optimized initial and final values.	140
5.6	Evaluation table before and after optimization.	140

Acronyms & Abbreviations

ac	Alternating Current
ANOVA	Analysis of Variance
BEV	Battery Electric Vehicle
BLDC	Brushless DC Motor
CAD	Computer Aided Design
CFD	Computational fluid Dynamics
dc	Direct Current
DCSM	DC Series Motor
DCM	DC Motor
T_d	Delay Time
DSPM	Doubly Salient Permanent Magnet Machine
DSEM	Doubly Salient Electromagnetic Machine
DOE	Experimental Design
EC	Electronic Commutated
EV	Electric Vehicle
EMF	Electro Motive Force
EVSA	Electric Vehicle Supply Apparatus
T_f	Fall Time
FEM	Finite Element Method
GA	Genetic Algorithm
HEV	Hybrid Electric Vehicle

HEFSRM Hybrid Excited Flux Switching Reluctance Motor

HESRM Hybrid Excitation of Switched Reluctance Motor

kW kilowatt

LRT Light Rail Transits

MEC Magnetic Equivalent Circuit

MMF Magneto motive Force

MSHESRM Modular-Stator Hybrid Excitation Switched Reluctance Motor

MOGA Multi-Objective Genetic Algorithm

N-m Newton meter

OD Outer Diameter

PM Permanent Magnet

PMBLAC Permanent Magnet Brushless AC motor

PMSM Permanent Magnet Synchronous Motor

POC Proof of Concept

PI Proportional Integral

P_W Pulse Width

PWM Pulse Width Modulation

REM Rare Earth Material

RSM Response Surface Methodology

rpm Revolution per minute

T_r Rise Time

rms Root-mean-square

SHESRM Segmented Hybrid Excitation of Switched Reluctance Motor

SRM Switched Reluctance Motor

SR Segmented Rotor

SS Segmented Stator

NOTATIONS

μ Permeability of the material

ϕ Magnetic flux in Webber

φ Flux linkage

A Ampere

A' Area of the conductor

B Flux density (Tesla)

F Magneto motive force (MMF) in ampere-turns

H Magnetizing force (ampere per meter)

N Rotor Speed (rpm)

P Output Power (kW)

R Reluctance in ampere-turns per Webber

s Second (time)

T Electromagnetic Torque (N-m)

T Tesla

V' Magnetic Potential (Wb m-1)

V Supply voltage

W Watt

CHAPTER 1

INTRODUCTION

1.1 Background

Global net zero aims to balance between greenhouse gas emissions produced and emissions removed from the atmosphere by human activities, resulting in no net increase in atmospheric greenhouse gas concentrations. This is commonly known as achieving net zero emissions [1].

To reach these emission standards, energy efficiency, renewable energy, and electrification are implemented to reduce greenhouse gas emissions as much as possible [2]. Numerous nations, including the United Kingdom, the European Union, Japan, and Canada, have set net-zero emission targets by 2050 or earlier [3]. The United States and Australia plan to reach net-zero emissions by 2050 [4]. These objectives are essential for combating the escalating threat of climate change, fueled by regulating greenhouse gases in the atmosphere [5].

Transportation is one of the most important sectors that must be addressed to achieve global net-zero greenhouse gas after-emission goals [6]. Several methods, including electric and hydrogen-powered vehicles, can employ the zero-emissions objectives [7]. Electric vehicles (EVs) are essential for reducing transportation-related greenhouse gas emissions. Since EVs run on electricity instead of gasoline or diesel, they produce zero tailpipe emissions [8]. However, the type of energy source used to charge EVs will determine the emissions associated with their production. The resulting emissions will be minimal if the electricity used to power an electric vehicle is derived from renewable sources such as wind or solar energy[9].

EVs are gaining popularity rapidly, and the development of electric motors is a significant factor in this expansion. Electric motors propel EVs, and recent technological advancements have made EVs more efficient, powerful, and accessible

to consumers [10, 11]. An electric vehicle's electric motor converts electrical energy into motion. The earliest electric motors were heavy, cumbersome, and required greater power and efficiency than their gas-powered counterparts [12–14]. However, technological advancements have changed this. Modern electric motors are lighter, smaller, and more efficient, providing consumers with the desired performance and driving experience [15].

Unlike conventional internal combustion engines, EVs use two types of electric motors: permanent magnet (PM) and non-permanent-magnet motors [14]. Permanent magnet motors rely on magnets to generate the magnetic field that drives the motor, whereas alternating current (ac) induction motors and several other motors employ electric currents. Permanent magnet motors are more efficient than non-permanent magnet motors at variable speeds, and their prevalence in electric vehicles is growing [16].

Permanent magnet motor magnets typically comprise neodymium, iron, and boron, which are strong, lightweight, and costly [17, 18]. These magnets are positioned in a circle around the rotor in the portion of the rotating motor [19]. As electric current flows through the motor's stator, the resulting magnetic field interacts with the magnetic field of the rotor's magnets, causing the rotor to rotate and propel the vehicle's wheels [20]. Permanent magnet motors could increase the efficiency and range of electric vehicles while reducing their weight and expense. However, the production and disposal of neodymium magnets may have environmental effects. The search for alternative materials and technologies that reduce or eliminate the need for these magnets is ongoing [21].

The susceptibility of permanent magnets to magnetic deterioration is another disadvantage [22]. A permanent magnet's magnetic field can weaken over time, diminishing its performance and efficiency [23]. This can reduce the performance and efficiency of the electric motor, thereby reducing the vehicle's overall performance. Earth-extracted materials such as rare earth elements are used to manufacture permanent magnets [24]. Significant environmental impacts can result from the extraction process, including air and water pollution, deforestation, and soil erosion [25].

It is essential to continue developing and improving EV technologies, primarily permanent magnet motors. The demand for rare earth metals in permanent magnet motors can be reduced or eliminated by developing alternative materials and technologies, improving the motors' performance and reducing their environmental impact [26]. Recycling and disposing of permanent magnets are also being improved to reduce waste and environmental damage. Using permanent magnet motors is only one way to reduce greenhouse gas emissions from transportation and reach global net zero goals [27].

1.2 Research Motivation and Problem Statement

Switched reluctance motors (SRMs) are a type of electric motor that has garnered significant interest in recent years as an alternative use in electric vehicles (EVs) [28]. SRMs are less complex than conventional permanent magnet motors, which could make them more cost-effective and easier to mass-produce. In an SRM, the rotor is not magnetized; the interaction between the stator and rotor teeth generates motion. When an electric current is passed through the stator, a magnetic field is generated that aligns the rotor with the magnetic pole closest to it. The stator's magnetic field is rapidly reversed, causing the rotor to travel to the next magnetic pole. This switching is controlled by power electronics, which determine the output speed and torque of the motor [29].

SRMs are typically more efficient than other motors, especially at higher speeds. In addition, their structures are more superficial and straightforward than other types of motors, making them more reliable and easier to maintain. Nevertheless, the use of SRMs in EVs presents certain obstacles. For example, they may produce more noise and vibration than other motors and may be unsuitable for applications requiring high torque at low speeds [30]. In addition, SRMs require advanced power electronics to control the switching of the stator's magnetic field, which may increase the complexity and cost of the motor system. SRMs are an excellent option for electric vehicle propulsion; however, additional research and development are necessary to fully comprehend their potential benefits and limitations to optimize their performance for EV's [31, 32].

Correspondingly, the torque-speed characteristics of the SRM machine are the most suitable trait for electric vehicle applications. Induction motors and Permanent Magnet BLDC motors are widely used due to their simplicity and rugged nature. Numerous methods have been used to raise these SRMs to the leading role. Among them, Hybrid Excitation using permanent magnets enhances the torque characteristics. Using these permanent magnets increases the structural difficulty of SRM and creates more complexity in the design. Introducing the dc excitation without permanent magnets can reduce this problem considerably without compromising the torque characteristics. The application of improved control and system optimization can further improve the torque performance by reducing the ripple.

1.3 Research Gap and Research Question

As there is no permanent magnet excitation like a synchronous motor, improving the torque performance of switching reluctance motors for EV applications is necessary. Nowadays, one predominant way to increase torque performance by including PM or

generating the shortest flux component via complexity in the structure design is the newly designed hybrid excitation of the SRM method. Hence, to avoid compromising the unique characteristics of SRM, a new paradigm of hybrid excitation must be developed.

1. How can torque characteristics of SRM be improved without compromising the structural integrity?

2. How to achieve the best design parameters to achieve maximum torque response?

3. How can a new torque control method be developed for SRM to meet the applications in an electric vehicle?

4. How can a prototype be developed for real-time applications corresponding to the results obtained from the simulation?

1.4 Aim and Objectives

This research aims to develop a hybrid excitation method for SRMs (HESRM) without a permanent magnet excitation and provide a torque control method to achieve high torque/power densities for EV applications. The method of hybrid excitation to improve the torque through injecting direct current (dc) is a practical feature that helps the motor work in a high torque with variable speeds. This research focuses mainly on separately excited coil-SRM motors to produce high magnetic flux without a permanent magnet. The proposed topology will achieve high torque production capability in the whole speed range with higher torque/power density and torque per ampere.

To achieve the above aim, the objectives of this dissertation are:

1. Develop a new topology of hybrid excitation SRM using separately excited dc injection to improve the torque characteristics and obtain maximum torque capability from the existing conventional design.

2. Design and develop an independent controller for auxiliary windings to enhance the dynamic performance of SRM in EVs.

3. Implement a technique for torque ripple minimization for the designed new hybrid SRMs to achieve maximum torque output with minimum torque ripple.

4. To optimize the motor and control system to obtain maximum and minimum torque ripple using a multi-objective genetic optimization algorithm.

5. Implement a new prototype for HESRM, experimentally validate the proof of concept (POC), and compare it with the previous simulation results and existing methods.

1.5 Novel Contributions and Outcomes

The main contributions of the works and the outcomes are classified as follows,

- The work's main contribution is introducing a new SRM topology to improve EV application torque performance. To achieve this, different topologies were carried out through software analysis and hardware implementations, showing that the outcomes significantly contributed to the performance of the SRM without using the PM behavior.

- Secondly, contribute a method to reduce the torque ripple in the newly designed motor; hence, it can be used not only for the specified applications. SRMs with high torque and ripple would not be a good resolution for EV applications. Hence, the results of the phase advancing with the proposed topology greatly influenced the performance.

- Third, using a system-level approach to determine the motor's maximum torque capacity so that the best design values can be optimized in the motor controller drive to make the proposed motors for variable speed drive. The optimized design values enhance the topology with better results.

- Finally, redesign the motor and test the proof of concept using conventional SRMs to compare the results with those of the new design topologies. The findings show that the proposed topologies have more flexible control because of two independent windings excitations.

Each chapter provides a complete description of the contribution and results. Different explanations are provided for the discussion and inference of the findings.

1.6 Thesis Structure

The following chapters are organized as follows,

Chapter 2 presents a literature review of the electric vehicle model and its propulsion system with a detailed analysis of electric motors in EVs: the methods and the procedures implemented for the SRMs to heighten the torque performance

through various research outcomes. According to the development of the current technique and results, the challenges and proposals are explained subsequently.

Chapter 3 proposes different topologies for the hybrid excitation method to determine the torque performance in the designed SRMs. The topologies are analyzed using the finite element method (FEM) and verify the results through the hardware implementations. Each topology static and dynamic performance of maximum average torque capabilities is separated and discussed in detail.

Chapter 4 describes the torque ripple minimization technique for reducing the ripple factor of the newly designed hybrid excitation topologies. The prototype of the designed motor test is conducted to verify simulated results and prove the proposed topology. The experimental results of non-permanent magnet-assisted hybrid excited SRMs have improved their performances by adding the ripple minimization technique.

In chapter 5, a multi-objective optimization for both motor and controller parameters is carried out for maximum average torque with minimum torque ripple. The optimization uses a response surface methodology (RSM) and a multi-objective genetic algorithm (MOGA).

In chapter 6, the significant findings from the current research methodologies are highlighted. In addition to the future scope of work, a discussion of those findings is provided. And also conclude the work of the thesis and summarize the research scope.

CHAPTER 2

LITERATURE REVIEW

2.1 Introduction

This chapter aims to provide a literature review of the different propulsion systems and explore the challenges and relevance of electric vehicle motors in section 2.2. In section 2.4, the study compares electric Vehicle (EV) motors in terms of their characteristics and performances. Section 2.5 discusses the challenges and limitations of rare earth element-assisted electric vehicle motors. Section 2.7 clarifies the relevance of switched reluctance motors for EV applications and concisely explains the fundamental structure and operation of SRMs used for this work. Section 2.8 describes the essential torque augmentation and performance strategies for the EV motor in depth. Section 2.9 concludes the review with the advantages and disadvantages of the current torque enhancement schemes.

2.2 Electric Vehicle Motors

An electric motor replaces the internal combustion engine in all-electric vehicles, often called battery electric vehicles (BEVs) [33]. The vehicle's electric motor is powered by a sizable traction battery pack, which must be plugged into a wall outlet or charging apparatus, also known as the electric vehicle supply apparatus (EVSA). The vehicle does not have a tailpipe or standard liquid fuel components like a fuel tank, fuel line, or fuel pump since it is an electric vehicle [34].

Electric motors are essential to electric vehicles and can move reliably and efficiently at a wide range of speeds [35]. As battery technology improves and electric motors get more powerful and efficient, electric vehicles are becoming a more realistic

alternative to vehicles that run on gas [36].

Electric motors drive electric vehicles that turn electrical energy into mechanical energy to move the vehicle. The motors mainly used in EVs can be ac, dc, or special electric machines, depending on the need.

In 1932, William Sturgeon invented the first electric machine, a dc motor (DCM) [37]. Nowadays, it becomes challenging to design and manufacture them due to various constraints such as:

- To achieve high power density to meet the minimum size and weight.
- To achieve high efficiency over a broad torque and speed range.
- To minimize the operational fault.
- To increase the harsh operating conditions.
- To reduce the overall cost.

Electrical machine designers must use them adequately while considering the different applications to meet the overall challenges [38–40]. In research on machines, topologies are examined based on the constraints of their applications. However, similar motors may be effectively used in the same applications.

2.2.1 Requirement of EV Application

With the rapid development of renewable energy and sustainable technologies, hybrid and pure electric vehicles are the most popular electrified transportation options. The critical component of the EV is the electric motor. Therefore, choosing the electric motor with appropriate requirements is crucial [41].

The high-power rating with instantaneous high power can be the primary need for electric propulsion. While accelerating and decelerating, the torque-speed characteristics can be high torque at low speed. The motor reaches a high speed at low torque for cruising. While the machines were operating in the constant torque and power region as they could travel at various speeds [42]. These machines operate well in a broad region of speed and torque. In diverse operating situations, traction machines must have high dependability and resilience [43]. The traction applications' various torque-speed and power-speed characteristics are shown in Figure 2.1 and 2.2, respectively.

Two regions in the torque-speed characteristics of the graphs are the constant torque region and the constant power region [44]. This graph displays the performance of an electric vehicle representing an automobile, a mini car, and the light rail transit system (LRT) [45]. Hence, it is possible for flux weakening to occur in the constant power zone in power-speed characteristics [46].

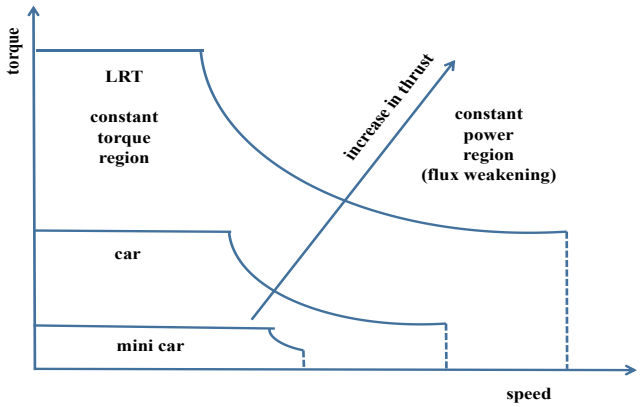

Figure 2.1: Torque-speed characteristics of traction motors.

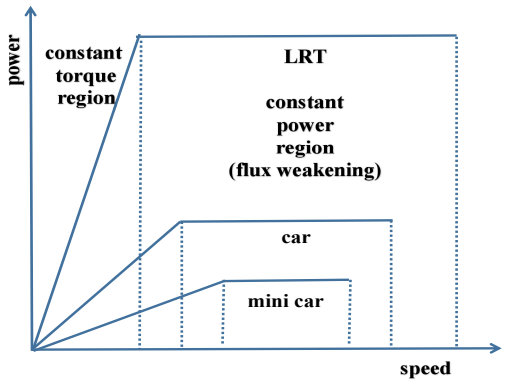

Figure 2.2: Power-speed characteristics of traction motors.

2.2.2 Challenges of Electric Traction Motors

The development of electrically-propelled vehicles required the use of traction motors extensively. A broad and adaptable range of electric motors produces a proper electric traction field solution [47]. Each electric motor is customized to the client's needs and delivers optimum power to meet operational circumstances, resulting in improved efficiency, minimal energy use, and excellent dependability. Several obstacles must be overcome to fulfill the general client limitations and produce a machine with the highest performance and dependability [48].

The following are the primary concerns with electric traction motors:

(i) To function at a standstill, the motor must produce enormous torque, often 3 to 4 times more than the normal. It could only have a modest speed to provide

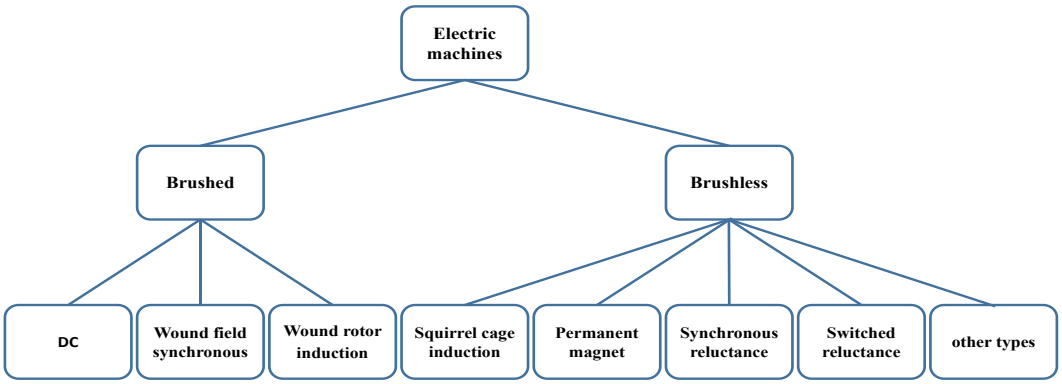

Figure 2.3: Different types of electric motors to drive EV applications.

sufficient acceleration and climbing capacity [49].

(ii) The output power needed should be twice as much as the motor's rated output power while running at medium to high speed.

(iii) The motor's torque and speed working range should be increased [50].

(iv) The machine should have good operational efficiency.

(v) The motor power density would be substantial during regular operation and high.

(vi) The motor seeks to save total energy during the driving cycle.

(vii) The motor achieves high torque density to complete the ascending and accelerating functions [51].

(viii) The machine's overflow capacity delivers the maximum among all working circumstances.

(ix) Electric traction remains cost-effective at the bare minimum levels.

(x) The most critical component of traction motors is reliability.

2.3 Different Types of EV Motors

Figure 2.3 [52] shows the different types of electric motors to drive EV applications. Over the past few decades, control strategies, power electronics, and materials have been used to make different kinds of electrical machines that can be used in EVs [53]. The brushed electrical machines are DCM, synchronous field, and wound rotor induction. However, these machines might need to be fixed often, making them less useful for modern EV applications. Brushless electrical machines have more varieties and are suitable for these applications [52]. They are classified as induction, permanent magnet, and reluctance machines.

Table 2.1: Different EV model and its propulsion system.

EV Model	**Propulsion System**
Holden/ECOmmodore (Australia)	Switched Reluctance Motor
Chloride Lucas (UK)	Switched Reluctance Motor
Nissan/Tino (Japan)	Permanent Magnet Synchronous Motor
Honda/Insight (Japan)	Permanent Magnet Synchronous Motor
Toyota/Prius (Japan)	Permanent Magnet Synchronous Motor
Renault/Kangoo (France)	Induction Motor
Chevrolet/Silverado (USA)	Induction Motor
DaimlerChrysler/Durango (Germany/USA)	Induction Motor
BMW/X5 (Germany)	Induction Motor
PSA Peugeot-Citroen/Berlingo (France)	DC Motor
Tesla (USA)	Model 1- Induction Motor
	Model 2- Permanent Magnet Synchronous Motor
	Model 3- Permanent magnet synchronous reluctance motors

Table 2.1 shows the different EV models and propulsion systems. The traction-purpose motors are mainly dc motors, induction motors (IM), permanent magnet synchronous motors (PMSM), brushless dc motors (BLDC), permanent magnet synchronous reluctance motors (PMSRM), and switched reluctance motors[41].

Renault, Chevrolet, and BMW used induction motors to move their cars, but Peugeot used direct current motors. Nissan, Honda, and Toyota will all use synchronous motors that are based on permanent magnets at the same time. For traction, Holden and Lucas used switched-reluctance motors. One of Tesla's ways to drive vehicles is with a new permanent magnet-inserted reluctance motor for high torque power densities [54].

2.3.1 DC Motors

The primary categories of dc motors are permanent magnet, series, shunt, and separately excited. The field coils are linked to the rotor coils and are used to create a magnetic field for the rotor to spin in the stator. All four kinds are straightforward to manage since they need a dc voltage applied across their terminals to start the motor spinning. All four types use a commutator to control which rotor coils are on at any given time so the motor can keep turning [55].

Series dc motors are now the most common and affordable motors used in hybrid cars. They are great because they are a well-known technology that works up to 90% of the time and only needs to be fixed once every 100,000 kilometers. Even with this, using a commutator is constrained and ineffective. Moreover, it is challenging to do regenerative braking using series dc motors [56].

2.3.2 Induction Motor

AC power can run several motors but is often used for electric vehicles.

In essence, the motor makes a magnetic field spin in the stator, which makes a magnetic field in the rotor and a current flow in the rotor's coils. The rotor coils aren't powered; they merely loop around on themselves [57]. To stay aligned with the field of the rotating stator, the induced field in the rotor turns to follow the field of the rotating stator. The motor's loads compel the rotor's field to revolve more slowly than the stator's field (if kept strictly, there would be no difference in the fields and hence no torque).

Three-phase induction motors are used a lot in the industry because they are reliable and work well [45]. The same benefits apply to electric vehicles, but you need an inverter with a variable speed to control the ac motor from a dc power source (the battery). Even though ac systems are more effective overall and have regenerative braking, they are now about twice as expensive as series dc systems [58].

2.3.3 Permanent Magnet Synchronous Motors

Because of its outstanding efficiency and power density, a permanent magnet synchronous motor is a kind of electric motor that is often used in electric vehicles. The permanent magnets in the PMSM make a magnetic field that interacts with the rotating magnetic field made by the stator windings. The motor could turn the rotor to match the torque made by the interaction of the magnetic fields.

The high power density of PMSMs for EV applications implies that they can provide massive power despite their small size and weight. This is crucial for electric cars, which need compact and powerful motors [59].

A substantial proportion of the electrical energy that PMSMs use can be converted into mechanical energy and is capable of remarkable efficiency. Electric vehicles benefit from this since it increases their range on a single charge and decreases the amount of energy that has to be stored in the battery [60].

The capacity to function at high speeds makes PMSMs ideal for EV applications. In addition, PMSMs can provide significant torque at low speeds, essential for accelerating and climbing hills [61].

PMSMs are the best choice for EVs because they have a high power density, are efficient, and can operate quickly.

2.3.4 Brushless DC Motors

A brushless DC Motor has a stator with a rotating field controlled by electronics and a rotor with permanent magnets. Sensors (rotary encoders or back-EMF (elec-

tromagnetic force)) are used to determine the position of the rotor. Because of this, they don't have a commutator and are often more powerful and effective than motors with commutators. They need a more complex motor controller, but as technology advances and prices drop, they are growing in popularity, especially for smaller motors [62]. The critical drawbacks of EVs are the usage price of the massive permanent magnets needed for the rotor and the additional cost of the speed controller.

2.3.5 Switched Reluctance Motors

Switched Reluctance Motors are electric motor types that use magnetic attraction between the rotor and stator. They lack permanent magnets, making them more cost-effective and their design simpler than other motors.

An SRM can be a suitable option in an electric vehicle for various reasons. First, they might have a high power density, meaning a small motor can produce significant torque. This is essential in a vehicle when capacity is limited. Second, they could be very efficient, improving the vehicle's range. Since they have fewer moving components than other motors, they should be more reliable [63].

SRMs may create more noise and vibration than other motors, which is one of their disadvantages. Nevertheless, this may be minimized by using vibration-damping materials and careful design.

An SRM could work for an electric vehicle, especially when high power density and high efficiency are needed. Nonetheless, as with any motor technology, the applications must be thoroughly examined to select the optimum motor [64].

2.4 Comparison Between EV Motors

Permanent magnet motors offer a higher power density, excitation configuration, efficiency, and cost when compared to alternative EV motors [53]. The induction motor is less costly than permanent magnet motors and offers higher fault torque, dependability, and tolerance. The switched reluctance motors have the same power density and efficiency as the induction motor and a more dependable excitation system. Besides this comparison, recent studies indicate that permanent magnet-inserted drive systems account for more than 85% of roadway EV motors [54]. Figure 2.4 [55]. displays the comparison restrictions of several parameters.

Table 2.2 shows the efficiency of the EV motors in terms of motor and it's controllers component individually compared to other motors. The investigation shows permanent magnet motors are the most efficient (90%). The SRM has a motor efficiency of 94%. However, the complexity of the controller lowers the total efficiency to 85% [65].

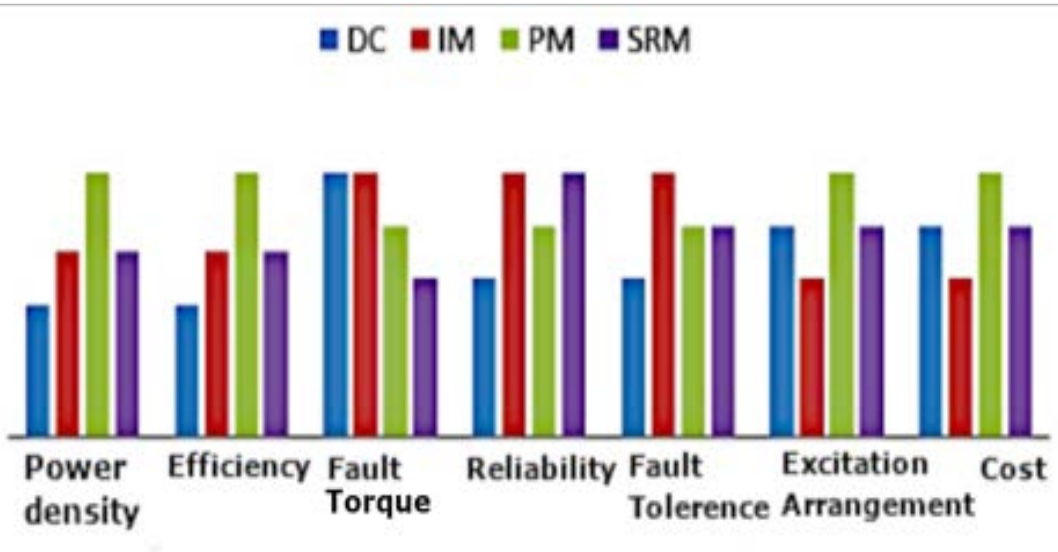

Figure 2.4: Parameter comparison of EV motors.

Moreover, the recent trend of newly designed hairpin EV motors greatly influences high power density with high efficiencies. In contrast to the round wire motor, the hairpin motor also exhibits some drawbacks, such as challenges in design, technological complexity, equipment difficulty, flat wire complexity, and increased losses.

Table 2.2: Efficiency comparison between EV motors.

Efficiency (%) [42]			
	Motor only	**Electronics**	**Motor & Electronics**
PM	97	93	90
SRM	94	90	85
IM	90	93	84
DC	80	98	78

2.5 Permanent Magnet Scarcity

The pie chart in Figure 2.5 shows the use of PMs where 34% of the PMs are utilized to make only motors and generators [66]. According to the PM production and demand rates, electric bicycles, consumer electronics, standard automobiles, and air conditioning account for 96% of the increase, with bonded magnets and high-temperature applications accounting for the remaining 3% and 1%, respectively.

The high-power density and efficiency motor is associated with permanent magnet motors. This is mainly because the permanent magnet does not need any energy

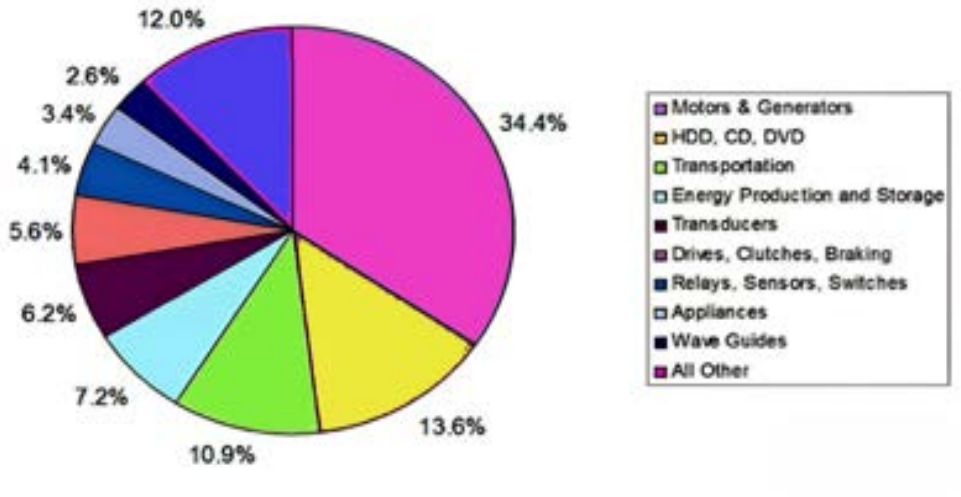

Figure 2.5: Utilization of permanent magnets.

to generate the magnetic field. Most electric motor performance depends upon the permanent magnet behavior. Many permanent magnets are available and depend upon rare-earth material (REM) synthesis to create them [67].

The availability of these permanent magnets depends upon increasing daily due to their wide usage. The graph 2.6 [68] shows the growth rate (%) and the production rate (kilotons) for the 20 years of data [69]. Recently, it has been widely reported that the extraction and refinement of rare earth magnet oxides can cause damage to the potential environmental process. Numerous government projects are available to withstand the unsustained utilization of rare-earth elements. REACT-Rare Earth Alternatives in Critical Technologies by ARPA-E in the U.S. and New Energy and Industrial Technology Development- NEDO developed rare-earth free motor in Japan.

Neodymium (Nd) is the most popular permanent magnet element and is considered the most substantial element. This shows that a small piece of Neodymium can produce a particular magnetic field. Dysprosium (Dy) is another magnetic element that is the mix to increase the coercive force. The name indicates REM is rare, but strictly, it is not infrequent. 38 mg/kg of Neodymium (Nd) and about 5.2 mg/kg of Dysprosium (Dy) are abundant in the earth's crust. The problem is the bulk production of the material extracted from a single country. In China, REMs are relatively abundant, and mineral concentrations mainly provided 95% of output in 2011 [70].

The demand for a permanent magnet is highly fulfilled by applying high-speed drives to electric machines. Even though Cerium (Ce) is the substitute rare-earth element for Neodymium, its price is 90% cheaper than Neodymium. But this can be a temporary solution to the current problem. However, a substantial long-term answer would only be required if the permanent magnet component is eliminated.

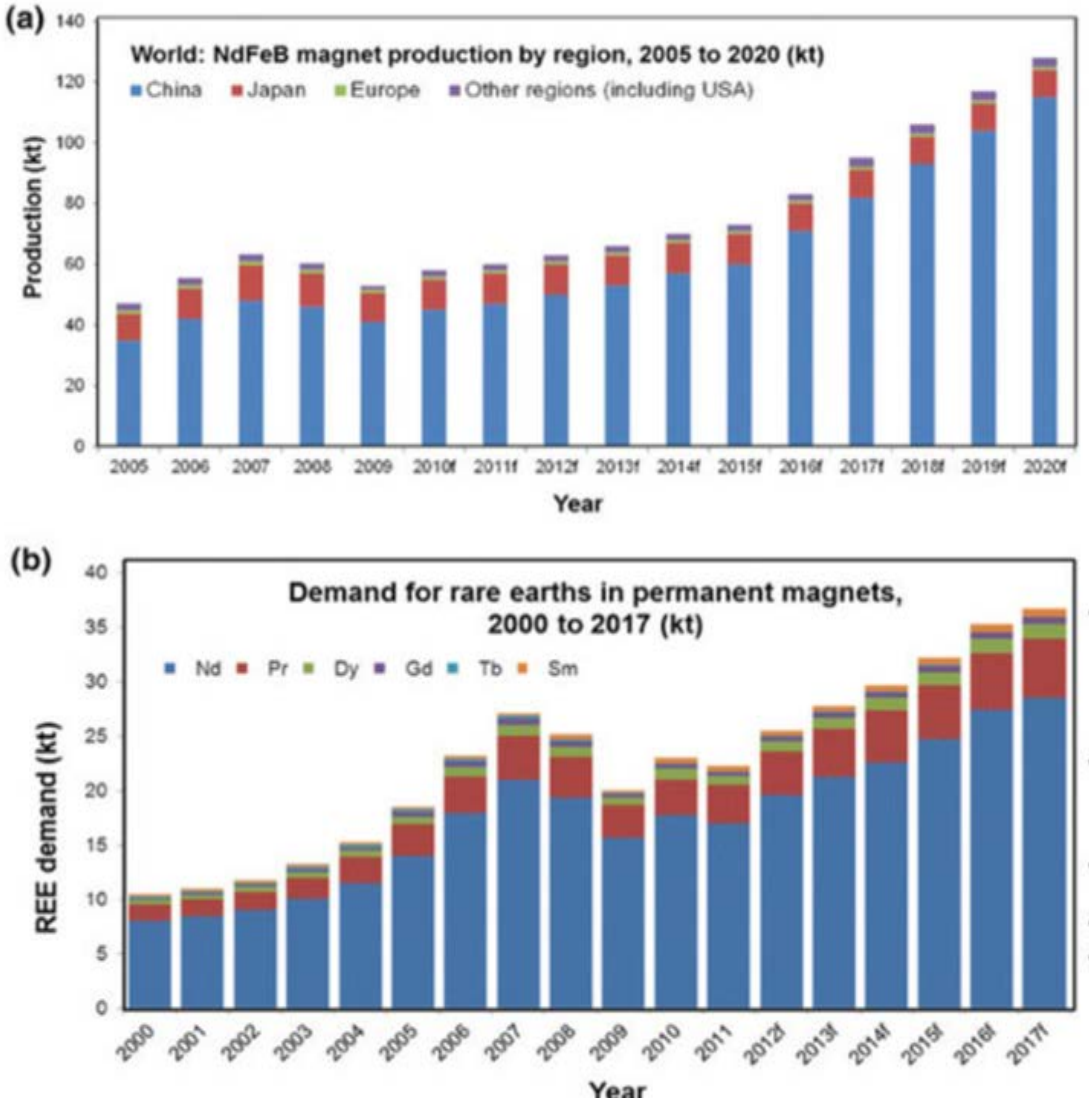

Figure 2.6: The chart (a) production rate (b) Demand rate of PM.

Furthermore, removing the permanent magnet benefits a significant reduction in the cost.

Electric vehicles often employ permanent magnet motors because of their efficiency, dependability, and power density. A permanent magnet motor does not need a separate field winding on the stator since a group of permanent magnets produces the magnetic field on the rotor [67].

Permanent magnet motors in EVs have many benefits, which include the following:

(i) Permanent magnet motors are more efficient than induction motors, particularly at low speeds, which is crucial for electric vehicles that often run in stop-and-go traffic [71].

(ii) Greater power density: Unlike induction motors, permanent magnet motors may produce more torque and power in a smaller space due to their higher power

density.

(iii) Range extension: Permanent magnet motors are more effective, which may extend the number of miles an electric vehicle can go on a single charge [72].

(iv) Reduced maintenance: Unlike other motor types, permanent magnet motors have fewer moving components and need less maintenance [73].

(v) Quick response: For EVs that must swiftly accelerate and decelerate, permanent magnet motors' ability to react fast to changes in load is crucial.

Nevertheless, employing permanent magnet motors in EVs has certain drawbacks as well, such as:

(i) Costlier: Permanent magnet motors are more costly than induction motors.

(ii) Restricted availability: Finding components for these motors might be challenging due to the scarcity of providers of high-quality permanent magnets.

(iii) Temperature sensitivity: At high temperatures, permanent magnets may lose their magnetic characteristics, reducing the motor's performance.

Because of their excellent efficiency, power density, and dependability, permanent magnet motors are suitable for electric vehicles. High-quality permanent magnets are more expensive and harder to come by, which may worry certain manufacturers [74].

2.6 Switched Reluctance Motor for EV Application

In EV traction applications, the 100 hp SRM is to be installed because these machines' initial acceleration and grade ability with minimum power needs the operation entirely in constant power. The capability of any motor in the traction is the base speed, and it is the speed at which the motor's back EMF is equal to the bus voltage. The traction motor reaches the rated power for rated excitation for this specified speed. These peculiarities easily control and withstand the motor at a constant current, which is suitable for traction [75].

(i) SRM has been leading EV propulsion since the 1990s.

(ii) The overall efficiency of SRM motors is similar to induction motors of the same rating since the friction and windage losses are comparable.

(iii) EV application advantages SRM: simple structure, control flexibility, high efficiency, lower cost, and robustness to run under failure conditions. The machine rotor has no windings or permanent magnets,- so it is suitable for high-speed drive applications [69].

(iv) SRM generates torque by varying magnetic reluctance.

(v) No windings and a permanent magnet in the rotor allow operating at the higher temperature.

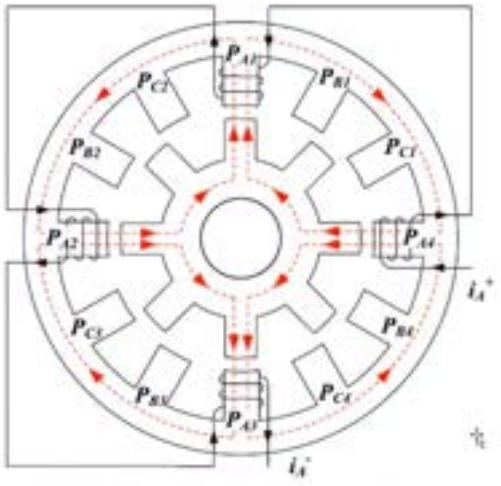

(a)

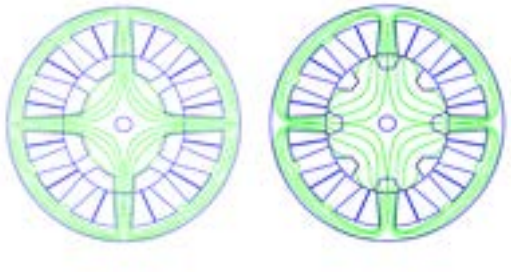

(b)

Figure 2.7: Conventional SRM (a) 3-phase, 12/8 poles (b) Magnetic flux distribution lines for 12/8 pole SRM.

(vi) The machines operate at a reduced load if faults occur in the windings or one phase.

(vii) Due to magnetic saturation, a non-linear characteristic of SRM makes it difficult to control the torque precisely.

(viii) Phases are independent. Any fault happens to one phase, and the SRM motor continues to operate with reduced output power.

2.7 Fundamentals of Switched Reluctance Motor

On 22 September 1839, Robert Davidson created the first electric locomotive on the Edinburgh-Glasgow railway. Later, this simple structural operation evolved into the core idea of contemporary SRM. Eventually, S.A. Nasar created the "dc - Switched Reluctance Motor" in 1969. This model's design is comparable to contemporary SRM. Lawrenson proposed the dimensional characteristics of contemporary SRM and unveiled the design tenet of the renowned SRM structure in 1980 [76].

The design is a doubly salient structure, and the attachment of the opposing stator poles forms a phase. The rotor is made up of silicon steel stamping, whereas

the stator is made up of focused winding. As a result, the rotor's inertia is much lower. This was the SRM motor's distinguishing characteristic compared to other conventional motors. The SRM motors must power on the phase winding in sequence with the pattern of external circuit switching. The rotor moves along a minimal reluctance route to produce a reluctance torque, per the excitation about the switching pattern [77].

Reluctance is the magnet's property that competes with magnetic flux in the circuit. This is similar to that of resistance competing against electricity. The rotation of the rotor depends upon the switching pattern that will be managed through the power electronics converters. Therefore, the consecutive switching pattern energizes the machine windings. Consequently, the rotor starts rotation and continuously varies the inductance's alignment positions of the stator and rotor poles, thus giving an inductance profile [78].

The basic structural diagram of 12/8, which means 12 stator poles with 8 rotor poles having the 3-phase SRM, is shown in Figure 2.7a. Each phase has two pole pairs and is concentrically connected to form a complete flux path in Figure 2.7b. According to the switching scheme provided by the controller, the rotor will start to rotate. The flux carried in the active region depends on the production of electromagnetic torque [79].

2.7.1 Inductance Profiles of Four Distinct Regions

In Figure 2.8, Region 1, 0 to $\theta 1$ and $\theta 4$ to $\theta 5$, the stator and rotor poles are unaligned. The current is almost zero, and flux density will be minimal. Reluctance produced between the rotor and stator will be high or maximum. This region does not contribute to torque production, producing unaligned inductance [80].

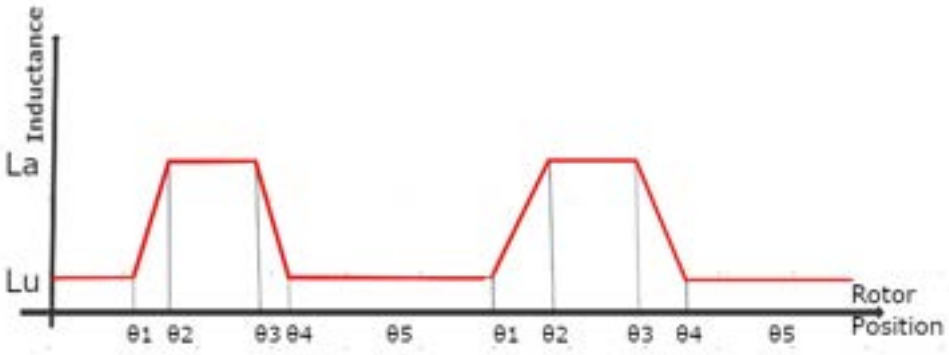

Figure 2.8: Relationship between inductance and rotor position.

In the region, two positions of rotors try to overlap stator poles, and the current increases; hence, flux density increases with reluctance reduction. During the positive slope of the inductance, positive torque is generated.

The rotor and stator poles align in region three, producing the respective inductance concerning the reluctance profile. The inductance will remain constant since the poles are aligned, and no torque will be produced, even though the current is present in the region. The stator current falls to zero or lower levels and is commutated during this time. As a result, they are preventing negative torque generation [81].

In Region 4, $\theta 3$ to $\theta 4$, the rotor pole moves away from the overlapping stator pole, and the inductance will decrease during the negative slope of the inductance region. In this negative torque region, mechanical input generates electrical energy.

Note: The ideal inductance profile is not achieved due to the saturation (increase in H value does not affect B). Current is always provided in the form of the pulsed rectangular waveform for a concise duration; hence, SRM has a large torque ripple, high audible noise, increased shaft fatigue, and possible oscillations at high speeds [82].

The switched reluctance motor has gained popularity in applied electric vehicles due to the development of power electronics. Also, the SRMs have proven to compete with traditional motors and replace the permanent magnet synchronous machine for hybrid and pure electric vehicles. The interior permanent magnet motors have high efficiency and excellent power density; hence, the machine is famous in electric vehicle technology. The SRM machine is beautiful compared to special electrical and conventional machines like BLDC and synchronous machines. These categorized machines have a permanent magnet and have a chance of long-term running and demagnetized issues. However, SRM does not have any winding or permanent magnets in the rotating part, and it is energized only in the stationary part of the machine. This feature leads the SRM motor in future EV applications [83].

2.8 Torque Improvement schemes in SRMs

The torque characteristics must be enhanced to increase the performance of the SRM and make it suitable for EV applications. The torque ripple and noises are the significant drawbacks; several strategies have been employed to minimize these issues. The excellent possibility for enhanced performance in electric vehicle applications is possible with heightened torque and power output in SRMs. These strategies are used for torque improvement in SRMs, as shown in Figure 2.9.

2.8.1 Advanced Power Converters

Power converters are used to drive and regulate motors in various applications. Typically, they control the current flowing through a circuit, other variables, or

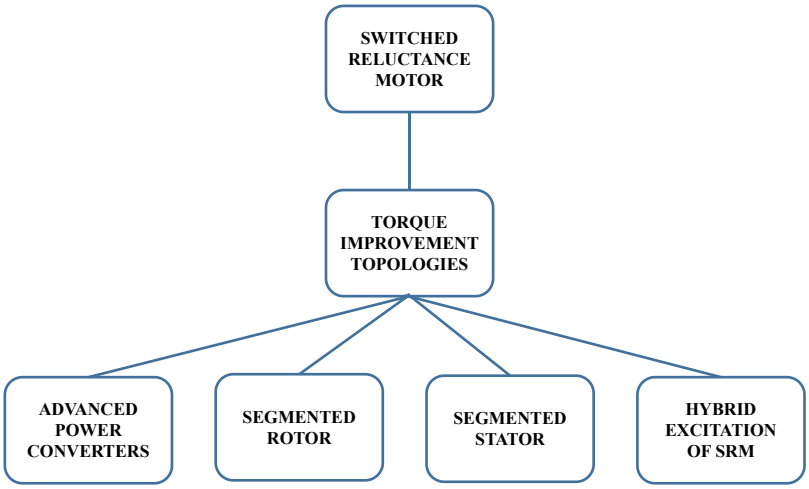

Figure 2.9: Different torque improvement strategies in SRMs.

particular circuit components. Typically, an integrated chip is created to manage all of these attributes. Similarly, electrical circuits may regulate the SRM's current. The torque ripple may be considerably minimized by removing the top and bottom curves from the result [84].

2.8.1.1 Advantages

(i) Using the fast-demagnetizing technique, electronic circuits can effectively control the outputs of the motor. (ii) The excitation of phase current in the machine is given sequentially to improve torque production. (iii) Power electronic converters can be configured according to the new winding topology. (iv) The phase windings used can be similar to the transformer.

2.8.1.2 Disadvantages

(i) Converters slightly caused lower torque per ampere and reflected heavily in the output. (ii) Not suitable for low-speed applications because it takes significant time to demagnetize. (iii) Three-phase standard inverters can improve the torque density, mutually coupled switched reluctance motors similar to conventional SRMs. (iv) The drive circuit's double stator segment facilitates the motor's easy current control. (v) A standard six-switch voltage source inverter was used to supply power to the special type of SRM. (vi) This method is applied only for low-speed applications. [85].

2.8.2 Segmented Rotor or Stator Core

In conventional SRM, the flux passes through the long path along with the stator black iron's full circumstances. The aforementioned phenomenon leads to the occurrence of flux conflicts between the various phases during the execution of phases, which is often referred to as flux reversal phenomena in Switched Reluctance Motors[86]. The flux reversal increases the magneto-motive forces (MMF) and the core loss, making a very low electric utilization of the motor. Therefore, structures with a short flux path impact the improvement in the motor performance [87].

In the conventional SRM, the flux travels long distances to complete the path. The flux flow occurs inside the stator, whereas the rotor exhibits variations in orientation between aligned and unaligned states. In the unaligned position, the reluctance torque experienced will be minimal, and during the aligned condition, the flux position will concentrate and travel through the rotor poles [88].

2.8.2.0 Advantages

(i) Electric utilization is minimal since the motor is segmented and working on the reluctance principle. (ii) The rise in magneto motive force causes the rotor to slip easily through the air gap. (iii) The core loss will be very high due to the long path of the flux.

There are two categorized segmented structures of SRM. Stator Segmented (SS) and Rotor Segmented (RS) mean the core is divided into discontinued segments with the respective stator and rotor parts. According to the pole numbers, the stator core can be shaped as the C- or E-core. The segmented structure achieved the short flux path by redirecting the flux path. The radial force is considered while designing the segmented stator structure; otherwise, the rotor becomes unbalanced and hits the stator during regular operation [89].

2.8.2.1 Segmented Rotor

The segmented rotor core encourages the flux to flow along the shortest path, generating a new magnetic field direction. This approach provides higher electromagnetic torque by carrying more flux in the air gap core. The segmented structure influences the flux to direct the way in a different direction of the core-shaped [90]. The modular-shaped core coordinated the flux to increase the active region's intensity. The motor in which the segmented rotor and its magnetic flux paths for aligned and unaligned positions are shown in Figure 2.10.

2.8.2.1.1 Advantages

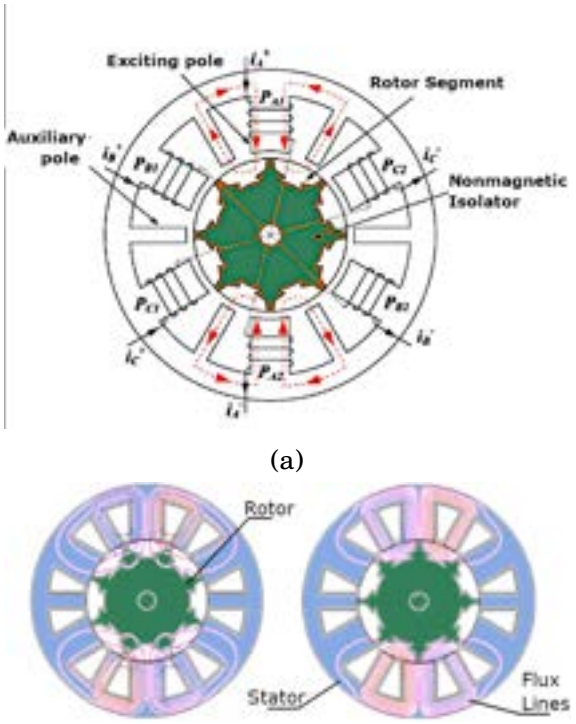

Figure 2.10: Structural diagram of (a) Segmented rotor poles (b) Magnetic flux lines in the segmented rotor.

(i) The rotor is segmented to obtain the shortest flux path. The segmented structure achieves this short path by redirecting the flux path. (ii) Flux path induced and magnetically isolated between the phases according to the shape of the segmented rotor [91]. (iii) Since the air gap flux is improved, output torque density also rises. (iv) The magnetic flux paths can effectively be redirected, improving electric utilization. As a result, core losses can be reduced significantly [92]. (v) The alternate stator poles are excited and wound, except for the auxiliary windings. (vi) The rotor may either be non-magnetic. (vii) Series of these discrete rotor segments are separated and are magnetically isolated from each other. (viii) A 10% increment can be experienced in torque production [93].

2.8.2.1.2 Disadvantages

(i) Rotors are made up of discrete series segments, which provide greater diversity in the electrical design of SRM. Full-pitched windings are used to improve the utilization of machine characteristics to the optimum [94]. (ii) The overall core loss will be very high. (iii) An increase in 41% of torque per unit copper significantly decreased copper loss at the thermal limit [88]. (iv) This type of motor is difficult to design and maintain.

2.8.2.2 Segmented Stator

The stator back iron acts as a path for the flux to flow and is redirected to the rotor poles; hence, it is circulated through the rotor to complete the flux path. Since there are no restrictions, the flux can flow through the least reluctance path without any particular order. The stator is split into segments of various shapes to eradicate this problem and increase the air-gap flux [95]. There are C core and E core. In Figure 2.11, the C core segmented stator core is shown where the flux travels only through each C; hence, the flux can be concentrated and redirected efficiently to the rotor poles. The segmented structure of the stator core is illustrated in Figure 2.11.

When the air-gap flux increases, the electromagnetic force increases significantly, reflected in the output torque characteristics [96].

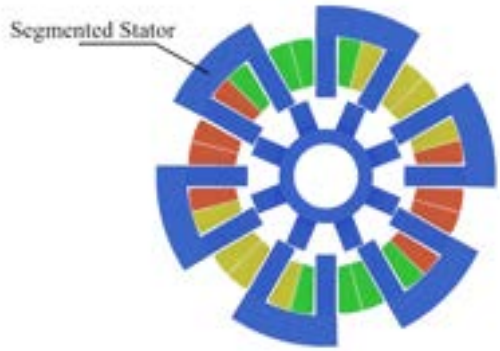

Figure 2.11: SRM with C-shaped segmented stator poles.

2.8.2.2.1 Advantages

(i) Electric utilization is minimal since segmented motors work on the reluctance principle [97]. (ii) The rise in magneto motive force causes the rotor to slip easily through the air gap.

2.8.2.2.2 Disadvantages

(i) The manufacturing of the stators will become highly complex, increasing the cost. (ii) Mutual flux coupling happens between the rotor slots, reducing overall efficiency. (iii) An increase in the windings' total length saves the motor's size. (iv) The additional commutative windings and commutation between phases happen by storing magnetic energy from within the machine. (v) The core loss will be very high due to the long path of the flux.

2.8.3 Hybrid Excitation of Switched Reluctance Motor

The hybrid excitation of switched reluctance motors enhances the torque performance by cooperating with the permanent magnet behavior of the existing machine [98].

The hybrid structure is complicated to manufacture, possibly increasing the overall cost. Like synchronous motors, SRM operation is based on reluctance rather than continuous torque. Due to the reluctance, torque production may make high torque ripple and high non-linear magnetization characteristics. When operated at a low-speed region, the current has enough time to reach the maximum value. In this region, the SRM is controlled to adjust the desired performance. On the other hand, there is not enough time to raise the current in high-speed regions. This section's ON/OFF angle allows more current flow [91].

Wen Ding: 2017 [99] presented a hybrid excited segmented stator for EV application in which the modular stator improvised the motor's performance as shown in Figure 2.12. The modular-stator hybrid excitation with permanent magnet (MSH-ESRM) technique is used for high torque capability in SRMs. In this method, torque increases with the enlargement of the stator tooth deflection angle by increasing the reversed flux [100]. The thickness of the PM determines the reversed flux quantity and thicker PM produces higher torque. The novel motor also has strong load capabilities, higher power densities, and higher torque per ampere. The main advantage of this motor is that the cogging torque is zero [101].

Figure 2.12: Cross-section of the proposed MSHSRM.

This construction features 12/8 modular with six- U-shaped electromagnet modules in the stator. Each stator module has a PM installed between two poles. The configuration of the rotor is similar to the conventional rotor SRM. The rotor has no winding or a permanent magnet [102]. The modular SRM comprises three-phase winding, each consisting of four coils, forming a stator modular with every opposite coil. The magnetizing direction of the permanent magnet should be adequately arranged with the field winding flux path and polarity. In which the mutual inductance and the leakage reactance are disregarded. Stator tooth deflection angle, rotor pole arc coefficient, and PM thickness determine the proposed SRM's optimization parameters. Hence, it can be shown that the torque increases with the enlargement of the deflection angle [99].

The results have shown the average magnetic flux density in the conventional SRM is 1.6-1.9 T and 2.1 T, and the segmented SRM is 1.6-1.9 T, and 2.1 T and 1.3-1.6

T and 2.1 T. MSHESRM obtained higher static torque, especially in the extensive current range. Moreover, the current requirement of MSHESRM is less with the same torque production compared to the other two SRMs [102]. The average torque range is 34.7% higher than the segmented SRM without PM and 71.4% higher than the conventional SRM. The copper loss, iron loss and torque ripple are comparatively smaller than other segmented SRM without PM. However, mechanical strength, difficulty in manufacturing and additional costs are the drawbacks of this proposed machine [103].

Yu Hasegawa: 2012, suggested a novel switched reluctance motor for applications with permanent magnet and auxiliary windings, as shown in Figure 2.13. In this improvised SRM, the stator core has ferrite magnets, and the auxiliary windings are excited with a constant current source of IAUX [104]. This structure is like the flux reversal and doubly salient PM machines [87]. All the magnetic flux passes through the stator circuit with a high utilization factor of an iron core with substantial iron and magnetic losses in the core. This motor's paramount consideration is the very low cogging torque [105].

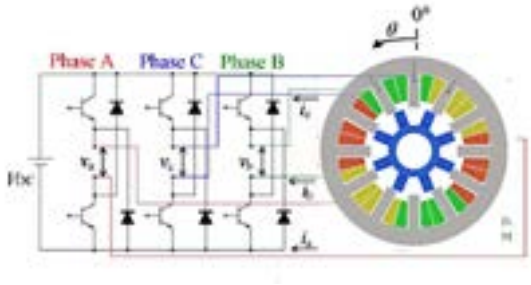

Figure 2.13: Basic structure of proposed SRM with permanent magnet and auxiliary windings.

The new SRM of the 12/8 pole consists of three-phase concentrating winding in each stator pole, and the auxiliary windings are wound around the stator yoke, which is excited by the dc. The stator core is non-oriented silicon steel with magnets-ferrite material of thickness 0.35 mm and the auxiliary winding excited within a maximum saturated value of 4 A [106].

The flux path has changed periodically since the stator and rotor phases aligned. With an auxiliary winding current of 4A and a rotational speed of 3000 rpm (high-speed range), the maximum efficiency was 89.8%, with an output power of 330 W. The exciting auxiliary windings depend on the torque production in the proposed machine, and its advance also allows it to work as a generator in the future [104].

Hybrid excitation is the solution to realize efficiency and controllable excitation. The hybrid excitation machines mainly comprise a permanent magnet. The primary

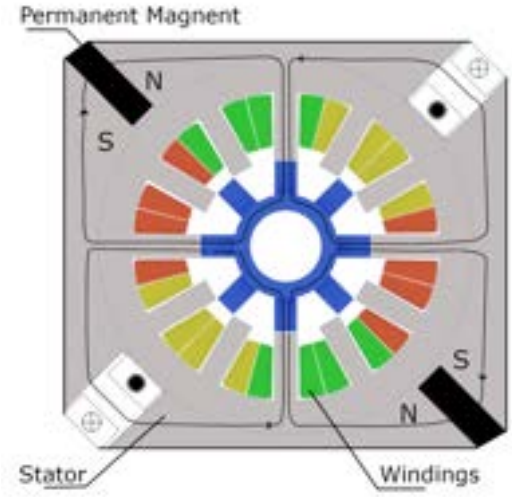

Figure 2.14: Flux path of the proposed SRM of auxiliary windings are wound around the stator yoke.

difficulty during the PM excitation is controlling the flux, and the flux path is shown in Figure 2.14.

Chen Zhuhai presented a new topology with flux control by double salient electromagnet machines. The HESRM techniques combine the merit of the double salient permanent magnet machine (DSPM) and the double electromagnet machine (DSEM), as shown in Figure 2.15. The specified machine comprises two parts - a DSPM on the left and a DSEM on the right. The two rotor parts are installed in the same shaft. The two stator parts in one machine frame share one armature. These features prevent flux production by the PM field winding passes through. The magnetic path of the two parts is independent of each other. The primary benefit is controlling the magnetic flux with a wide operating range by adjusting the field ampere-turns [107].

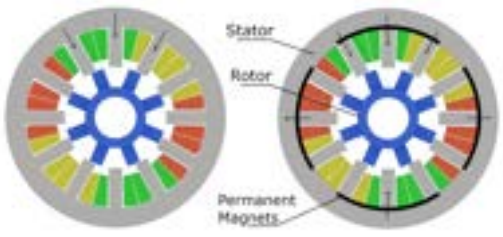

Figure 2.15: Cross-sectional view of proposed SRM of double salient permanent magnet machine (DSPM).

The author proposed that the SRM structure is simple and rugged, with high flexibility in machine design. This machine is accomplished with high torque density and high-speed capability, acquiring fast response. The prominent feature is the low torque ripple and low noise. The copper loss of field winding becomes larger in these machines operated at rated loads [107].

E. Suleiman mentioned a hybrid excitation flux switching machine for hybrid electric vehicles in 2011, as shown in Figure 2.16. In some torque improvement machines, the rare earth permanent magnet is embedded in the rotor core, especially in high-speed applications. These machines are complicated, and PM is installed in the rotor, always keeping enough mechanical strength and performing substantial electromagnetic results. A permanent magnet in the rotor demands more mechanical strength. It depends on the increase in rib thickness and the number of bridges around the PM. It would indirectly affect the torque performance and reduce the machine's maximum torque because of augmented leakage flux [108].

The author invented six slots- 8 poles hybrid excitation flux switching the machine to avoid an odd number of the rotor for unbalanced pulling force. The rotor pole number is reduced by considering the reduction of the inverter supply frequency. The stator and rotor pole widths provide the right balance to withstand inescapable torque pulsations. In this case, the permanent magnet and the wound field excitations are supplied with magneto-motive force sources.

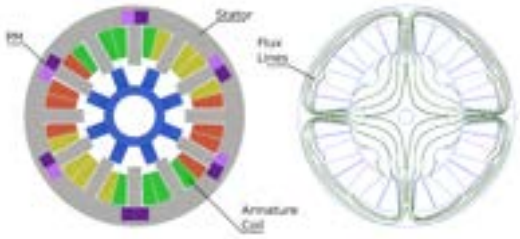

Figure 2.16: Cross-section view and the flux direction of 6-slot-8-pole HEFSSRM.

In this structure, all the active parts comprise the stator body and a rugged rotor construction similar to the conventional SRM suitable for high-speed operation. According to the rotor rotation, the permanent magnet's generated flux flows through the stator as per the MMF of the field coils and is switched and linked with the alternative armature coil. The armature coil's flux linkage has one periodic cycle as the rotor rotates through 1/8 of a revolution. Thus, the induced back electromagnetic force frequency becomes eight times the rotor's mechanical rotation frequency. This embraced construction's principal advantage would be the high torque operation region with 97.4% efficiency and 92.4% in the high-speed operating area, respectively. Hence, the proposed machine efficiency ranges from 92%- 97%. Due to the permanent magnet assembly, the significant iron loss is the drawback of the proposed one [108].

2017 Shaofeng Jia introduced a new topology stator-PM consequent-pole vernier machine in Figure 2.17. A hybrid excitation permanent magnet commonly necessitates a field winding fed with dc, creating conflicts between armature winding and the stator PM. This increases the machine cost as well as construction difficulties. To achieve a hybrid excitation without filed winding, termed current superimposition

stator PM machines or dc-based sinusoidal current. The key feature of the proposed machine exhibits flexible adjustment field capability [109].

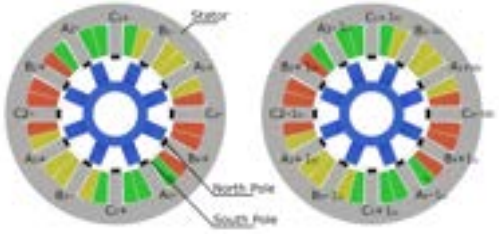

Figure 2.17: Cross-section view of superimposition stator PM excited HESRM.

The arrangement of the offered machine where the PM is embedded in the stator teeth would help dissipate heat. The rotor is a salient structure similar to the flux switching machine, which has no windings and PM and ensures the reliability of high-speed operation in a wide range. The end connections shortened by the non-overlapping concentrated winding help to improve torque density [110]. For cost-saving, one-half of the stator core is inserted by PM, and the dc is injected into the armature coils to produce field excitement that can be adjusted flexibly. The dc produces the flux passing through the iron core near the permanent magnet and then through the air gap. The stator tooth iron parts saturate quickly due to the nearby PM, reducing the machine's torque density and the consequent pole reducing the air-gap length. Due to the low back-EMF under an open circuit, a slight short-circuit fault current will be expected because of the inherent structure [111].

Jin-Woo Ahn introduced a novel hybrid excitation SRM for reducing vibration and acoustic noise shown in Figure 2.18. This scheme reduces the abrupt changes in excitation level by balanced and continuous excitation methods to reduce the machine's vibration acoustic noise. It combines one-phase excitation with two-phase excitation. The C-dump inverter excites the phase winding to reduce the torque ripple, and the acoustics noise is shown in Figure 2.19[112].

In the region in which the torque generation phase, the next phase is turned on before the exciting phase turns off. This may create an exciting overlap region and the demagnetization region of phase during phase commutation. The overlap excited phase scenario smooths the commutation and speeds up the phase commutation due to the magnetic energy absorption. In the overlap excitation region, the magneto motive force changes rapidly from the previous phase-off sequence and is circulated through other phases. The long dwell angle of the phase current prevents the negative torque region. The hybrid excitation method prevents rapid flux changes in such a matter to reduce the vibration and acoustic noise [112].

Nakamura proposed a hybrid excitation to improve the output power and the switched reluctance generator efficiency, as shown in Figure 2.20. Commonly, it

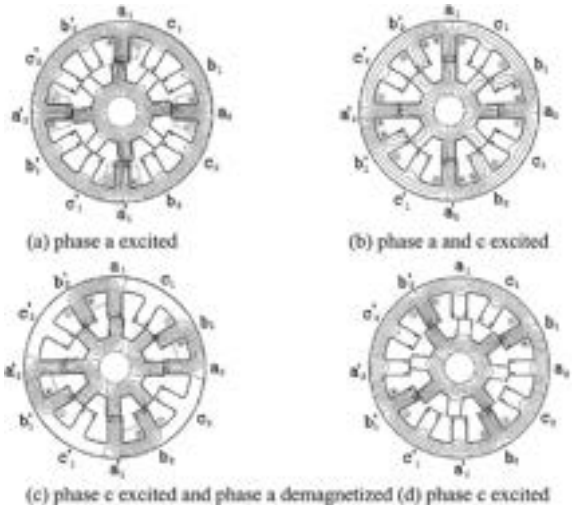

(a)

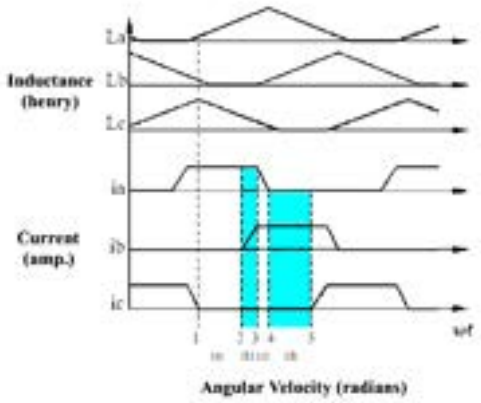

(b)

Figure 2.18: The proposed HESRM of collective excitation (a) Flux distribution of hybrid excitation (b) Inductance profile and phase current in hybrid excitation method.

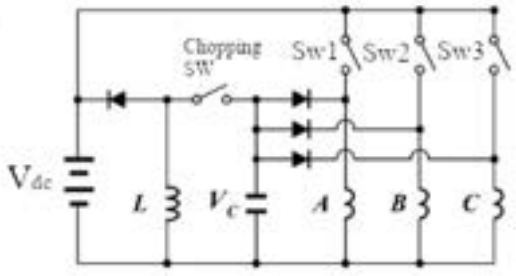

Figure 2.19: C- dump inverter for hybrid excitation method.

enhances the output power and efficiency by effectively increasing the pole number. The small-scale generation wind turbine permanent magnet reluctance generator has two stacked structures, and the rotor is shifted 180 degrees from another rotor. The (Nd-Fe B) rare-earth magnet is arranged in the stator yoke. The proposed motor's efficiency is 90% at 1.0 kW at a load current of 6.0 A [98].

Figure 2.20: Cross-section view of super multi-polar permanent reluctance generator.

Kaiyuan Lu set forth a single-phase hybrid switched reluctance motor in low-power-low-cost applications like the fan and pump drive systems, as shown in Figure 2.21. The permanent magnets would rectify the single-phase SRM low starting torque problem. To increase the torque density and the machine's efficiency, ferrite magnets are added to the stator structure and arranged in a specialized manner to obtain a unique flux concentration. The cogging torque due to the permanent magnet effects is constructively used to minimize the torque ripple. Also, the structure provides positive cogging torque to enable the self-starting of the machine [102].

The assembly of parking makings pole in the stator part is arranged in a V-shaped manner. This construction helped to reduce the leakage flux and provide positive cogging torque in a dead zone. The permanent magnet is inserted between two adjacent sides of the reluctance poles to reduce the torque ripple. The interaction between the armature field and the permanent magnet field will be introduced as an additional torque that improves the machine's overall torque density.

The constructed V-shape concentration flux offers the flexibility to control the flux, shape the field magnet, and protect the magnets against the radial force. The average output torque increased by 1%, in which the starting torque significantly increased up to 150%, and the inverter efficiency was 94%, with machine efficiency 77%, including mechanical and machine iron losses. This enhanced structure would effectively replace the induction motor [102].

Rasmussen and Lu presented a new low-cost hybrid switched reluctance motor to apply an adjustable speed pump, as shown in Figure 2.22. This structure also produces an interaction torque of both reluctance and a permanent magnet to increase the torque density. The bipolar excitation consists of four reluctance poles and two PM poles. The rotor pole has a small slot close to its surface, providing sufficient torque to the motor [113].

The motor will self-start if the positive torque appears when the current increases in the exciting winding. The PM is placed in the middle of the reluctance pole, which

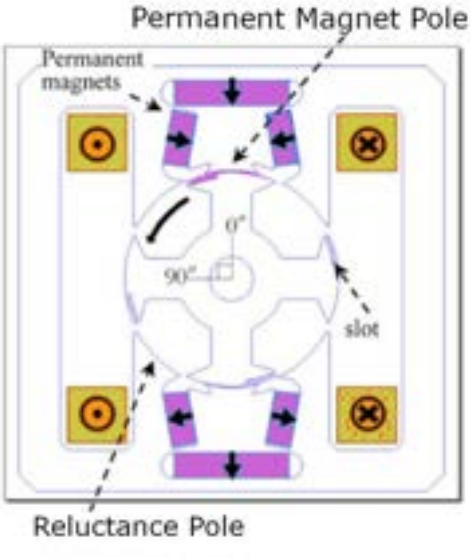

Figure 2.21: Proposed single-phase hybrid excited SRM for low power applications.

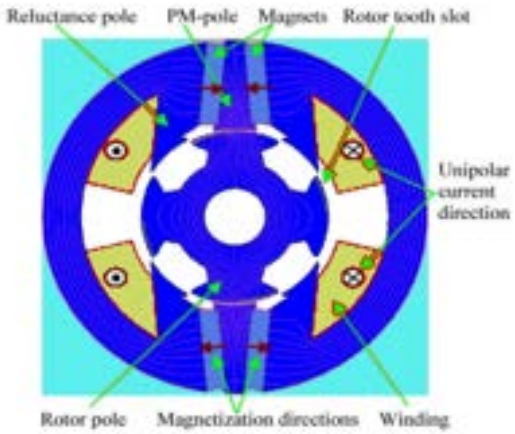

Figure 2.22: Cross-sectional view of V-shape concentration flux generated HESRM.

generates adequate flux that moves the flux linkage cure in such a way as to increase the machine's torque density. This developed structure increased the peak value of cogging torque by about 35%, and the motor is required to operate at a low speed that should be lower than the rated speed. For the variable speed application of the pump, the motor worked in the low torque region. Due to the iron loss, the system operated efficiently with a rated speed of 70%. The major drawback of the hybrid structure is noise because of the complicated magnet pole arrangement.

2.9 Advantages and Disadvantages of the Existing Methods

The advantages and disadvantages of the existing torque advancement methods are explained in Table 2.3.

Table 2.3: Comparison of existing torque enhancement method.

Torque Improvement methods	Advantages	Disadvantages
Advanced power converters	Power electronic converters can be configured according to any new winding topology.	Heavy electronics bring complexity to the circuit.
	No structure difficulty will be experienced.	Power electronics switching complexity is higher in SRM when compared to conventional ac and dc machines.
	High torque and power density can be obtained.	
Segmented Stator	The air-gap flux will be increased.	Mechanical strength will be reduced.
	Stators can be segmented in E and C core patterns.	Manufacturing will become very complex, with high costs.
	Flux only passes through the segmented areas.	
Segmented Rotor	The magnetic flux paths can effectively rotor redirected, and thereby improve electric utilization	The complexity of manufacturing the rotors will become extremely complex, increasing the cost.
	Reduce MMF.	Mutual flux coupling happens between the rotor slots, reducing the overall efficiency.
		High core loss.
HESRM	PM for hybrid excitation	Usage of PM.
		Uncontrollable flux.
		Overall cost.
		Cogging torque production.

Complex control circuits may be costly to design, develop, and install, particularly for small-scale applications. Using sophisticated control algorithms and sensors may further raise the price. The control circuit's design, development, and maintenance might be complex due to its complexity in external switching circuit excitations for SRMs. Despite the numerous benefits, it may also make identifying and resolving issues difficult when they develop.

The stator and rotor of SRMs may be segmented to increase torque production. Nonetheless, it has drawbacks, such as greater complexity, higher losses, increased vibration and noise, a restricted speed range, and higher maintenance needs.

Field windings and permanent magnets are both used in the hybrid excitation of SRMs, which has several benefits over traditional SRMs. Nevertheless, their drawbacks include no longer lowering the conversion efficiency, uncontrolled flux, cogging torque, more expense, more accessible complexity, demagnetization and more sophisticated control procedures.

CHAPTER 3

DIFFERENT TOPOLOGIES OF HESRMS

The machine topologies and the findings for improving torque in switched reluctance motors employing non-PMs hybrid excitation methods are covered in this chapter. Machine designs and software performance analysis are carried out for this aim, and the outcomes are confirmed through hardware implementations. The machine's performance is influenced by the selection and assignment of auxiliary poles for the independent dc injection. To speculate about the flux path identically to the conventional SRM, the first assigned auxiliary poles are identified as the first topology, 3.5. The second topology 3.14 creates a new shortest route for the suggested approach by designating a different pole selection as an auxiliary winding. Furthermore, it explains the different torque enhancement possibilities in conventional SRMs and their simulation results in topology III, 3.19.

The topologies above can transport more flux than traditional SRMs, while topology II has greater electromagnetic torque than topology I. Moreover, these two topologies are constrained regarding maximal torque generation and current injection by design considerations. Topology III determines the intended motor's maximum torque capacity by modifying the material by employing high permeability material in the auxiliary pole core. Increasing the ratio of the number of poles in the stator and rotor core are the different possibilities of torque improvements; all topologies would be using 50% of the active pole as an auxiliary pole, raising the active pole from 50% to 75%.

3.1 Research Methodology

To execute the research methodologies in four distinct objectives that help to analyze the new proposed HESRM without PM excitations. The objectives and outcomes are

detailed in Figure 3.1.

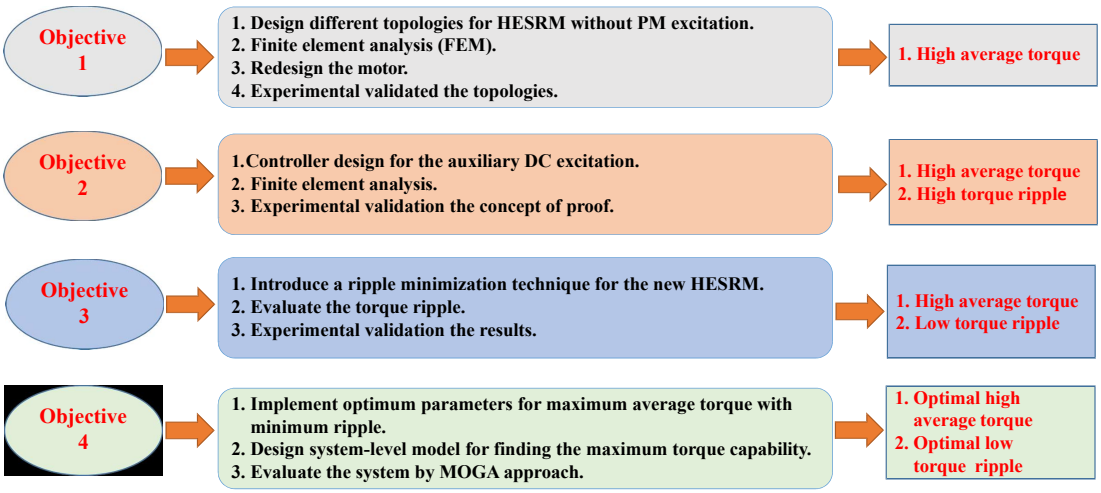

Figure 3.1: Four main objectives and the results obtained for the proposed method.

1. The first goals concern various topologies for new HESRM designs without permanent magnet excitation systems to enhance torque performance. The software analysis was completed using the Ansys/ Maxwell finite element method. Finally, develop the prototype using the new excitation system and verify the findings through experimental analysis. The findings show that the suggested topologies have achieved high average torque with ripple.

2. The second goal is to build the controller for the auxiliary dc excitation system of the proposed machine. The controller's software is analyzed using Matlab/model-based Simulink's program development platform. The hardware implementation authenticates the proof of concept. The second objective is accomplished when the maximum average torque is combined with the high amount of ripple.

3. The third research aim is to minimize the torque ripple identified in the suggested findings while keeping a high torque capacity. Nonetheless, this torque ripple minimization approach using the phase advance method helps to improve the torque performance, resulting in the least amount of torque ripple. This methodology can be considered for different variable-speed drive applications in the industrial and commercial sectors, for example, by reducing the ripple characteristics of the high output torque.

4. System-level optimization, to find the optimum parameter values of machines and controllers, is separately analyzed and performed to obtain an optimal average torque with minimum torque ripple. An integrated response surface methodology approach and a multi-objective genetic algorithm are used as the parameters of multi-objective optimization. The performance study for variable speed drive systems considers the machine and controller variables with the EV load.

3.2 Objective 1: Different Topologies for HESRM

3.2.1 Background

Figure 3.2 shows the traditional SRMs and their switching architecture. The system consists of a controller, switching mechanism, and drive circuit, continuously switching the rotor among various positions. The converter receives the dc source supply for the proper pulse with modulation (PWM) creation of the switching sequence for the motor's spinning in either the clockwise or anticlockwise directions [114]. The rotor needs this input to produce the reluctance force that makes it spin. When a stator phase is magnetized, a closed magnetic field is created between the stator, air gap, and rotor. The flux is forced to flow through the rotor's less reluctance path by the spinning field created by the switching [115]. Following the flux's direction, the rotor poles will rotate to associate. The use of electrical circuits with several switches enables this.

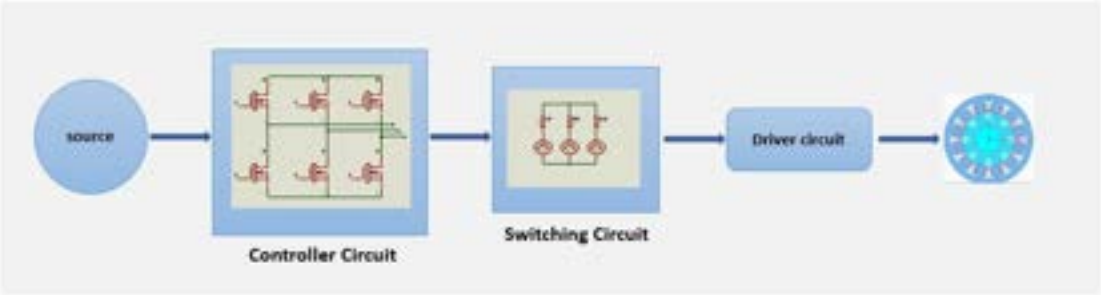

Figure 3.2: Block diagram for the conventional SRM switching scheme.

Two of the four poles from each phase, A, B, and C, are separated and evacuated individually using this methodology shown in Figure 3.3. The number of turns, diameter, material, and other attributes change correspondingly to achieve the required outcomes. These poles' input is supplied independently utilizing a different circuit from the ones used for the other poles. This aids in gaining complete control of the split poles and the motor. As a result, it is possible to effectively manage the input voltage, current, and switching pattern to the auxiliary poles.

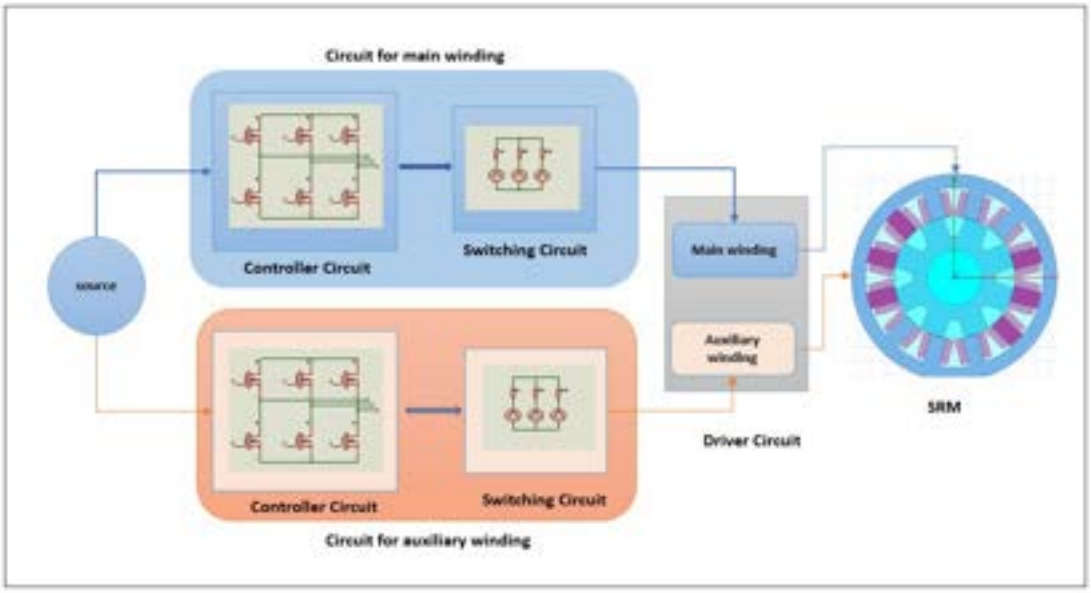

Figure 3.3: Block diagram of hybrid excitation model without using a PM excitation.

3.3 Initial Design:

The initial design is to develop a new topology for the SRM through these steps shown in Figure 3.4. Beginning with this, it is vital to scrutinize and evaluate the outcomes of a motor operating at a low power level. Then, the initial parameters of the motors are assigned to produce better torque results. The stator poles are isolated and provided with a separated dc, and the results are analyzed.

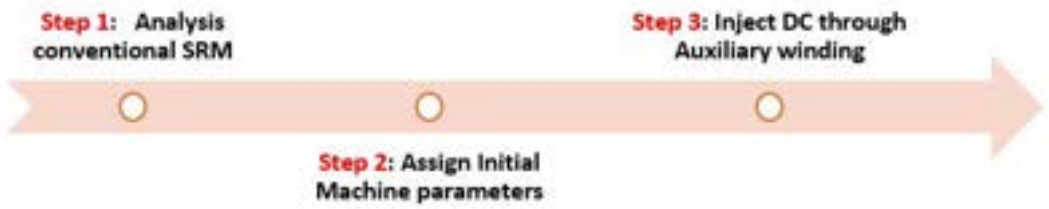

Figure 3.4: Different steps for executing to attain the initial parameter optimization.

3.3.1 Step 1: Analysis of Conventional SRM

The performance of SRM is analyzed for the following cases:
(i) Case I - Standard basic low-power motor.
(ii) Case II - SRM for medium power application.

In case I, the output characteristics of a basic low-power SRM and its variations in input parameters are examined. In case II, similar tests are conducted with a medium-power-rated machine. The results will be analyzed and optimized using Ansys/Maxwell.

(i) Case I - Standard Basic low-power motor.

Tests are conducted to understand the characteristics of SRM with low power specifications (rated voltage of 250 V at the rated speed of 750 rpm, an output power of 600 W, an efficiency of 75%, with an average output torque of 8.17 N−m, tests are conducted. The machine has a configuration of 12 stator poles and eight rotor poles with stator material as steel, $M15_26G$. In the analysis of current, power, torque and efficiency curves, it is evident that current drops exponentially as torque progresses; thus, injecting external dc to the stator windings can improve the torque characteristics of the SRM. The basic simulation graph of torque speed and the air-gap inductance is shown in Figure 3.5.

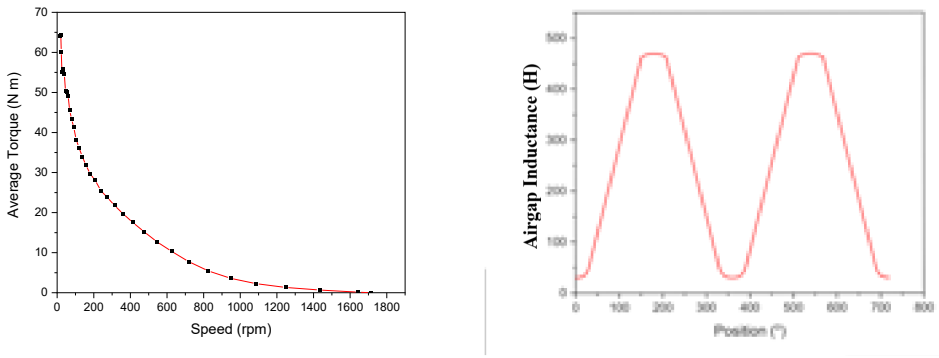

(a) (b)

Figure 3.5: Characteristics results of 600 W conventional SRM (a) Torque-speed Characteristics and (b) Air-gap inductance for the designed conventional SRM.

(ii) Case II - SRM for medium power application.

Electric motors with higher power ratings are required for applications such as electric vehicles. Hence, a conventional 12/8 SRM (12 stator poles and eight rotor poles) is designed in Ansys/Maxwell. This motor has a rated output power of 20 kW, a voltage of 560 volts, and a speed of 2400 rpm. The simulation shows that the torque ripple is very high, almost 78 N-m on average torque. The flux pattern is also plotted to obtain a maximum of 1.7 T. The flux path through the steel also shows how reluctance is formed in the rotor poles.

3.3.2 Step 2: Analysis of Initial Machine Parameters

The main objective of this case study is to compare the torque performance of SRM with and without the optimized parameters. Ansys/Maxwell provides a great

platform to simulate and analyze the various properties and project the optimized output parameters.

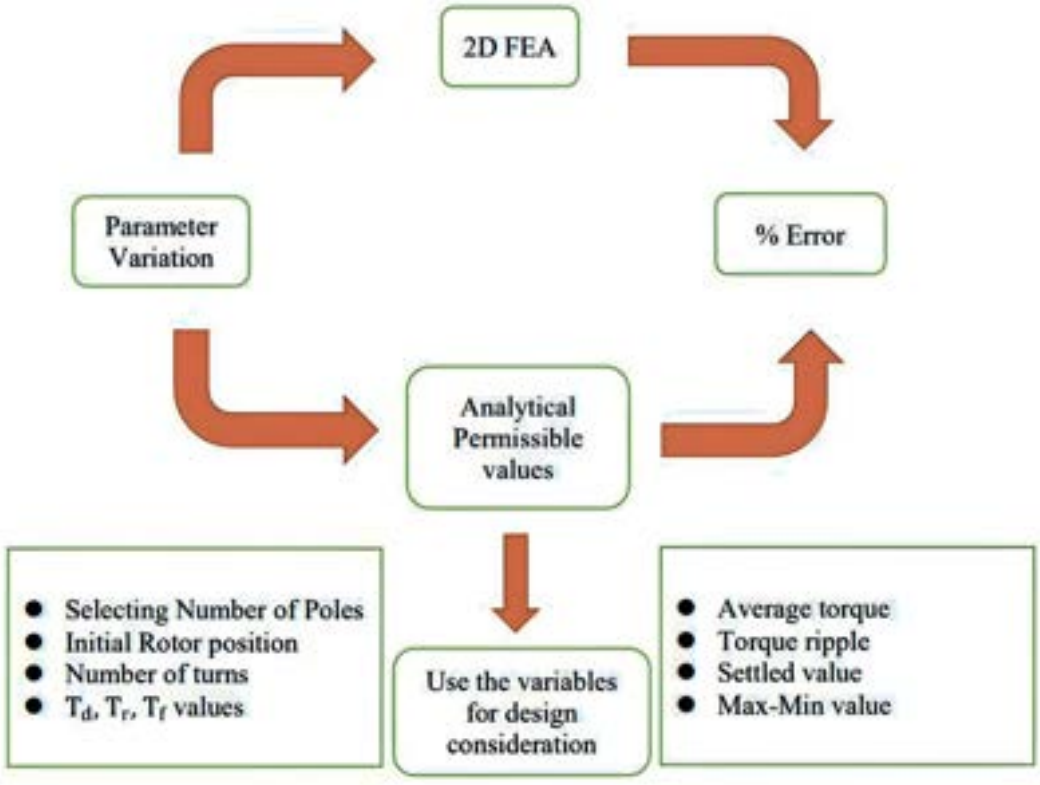

Figure 3.6: Block diagram of initial motor parameter optimization using Ansys/-Maxwell FEM analysis.

A significant amount of torque ripple was observed in the shaft torque measured from the motor output. Ansys/Maxwell is used to perform the finite element analysis to make the asymmetrical waveform more symmetrical and application-appropriate. The switching pulses are used to excite the MOSFETs control, and these parameters are adjustable to obtain a suitable switching sequence. Through a series of iterations, it is possible to determine the initial position of the rotor, the number of turns, the delay time, the rise time, the fall time, and the pulse width analysis are shown in the block diagram Figure 3.6.

This optimization of different parameters techniques aims to obtain a torque output with the most significant average torque and the least amount of ripple. Randomly selecting the values for the initial position of the rotor, the number of turns, the delay time, the rise time, the fall time, and the pulse width are used to initialize these machine parameters responsible for the optimal torque output values. The minimum and maximum values are calculated using proper analytical methods

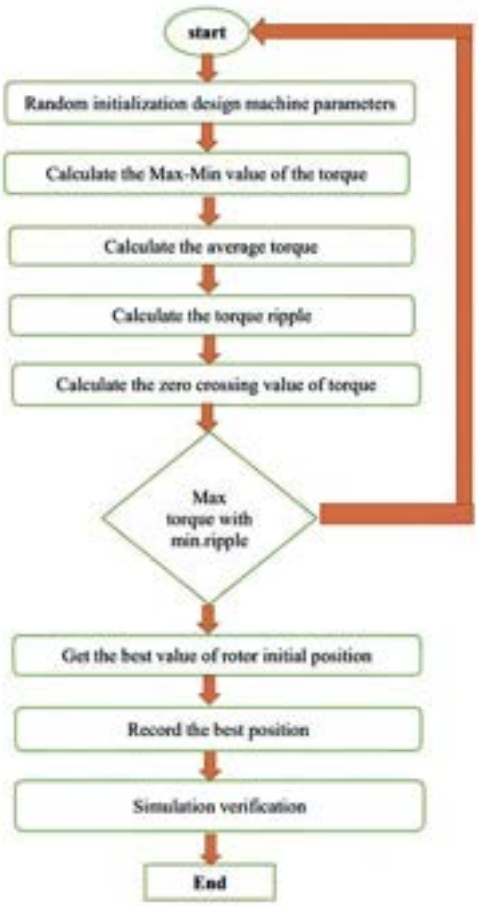

Figure 3.7: Flow chart for initialization of machine design parameters.

from the measured output. The zero crossing values are identified, simulated, and compared to previous outputs based on these results. This procedure is simulated in a loop with various iterations until a satisfactory outcome is achieved. The flowchart illustrated in Figure 3.7 shows the path involving multiple steps.

1. **Design 1**- Initialising the initial rotor position of the 12/ 8 SRM.

SRM generates a magnetic flux path between the stator and rotor poles to enable the windings, resulting in magnetic reluctance. The flux path's reluctance is at its lowest in the aligned position and highest in the unaligned position. Nonetheless, the rotor can be moved to either the aligned or unaligned. Consequently, the initial position of the rotor is vitally essential for the effective starting of the motor. The iteration begins at zero degrees and progresses to one complete electrical degree. The iteration corresponding to angle 16, as shown in Table 3.1, yields the best values, with the optimal average torque and the least amount of ripple. The optimal values for these parameters are categorized, and graphs are generated accordingly. To obtain an average output torque of 54 N−m with a torque ripple of 128%, the initial rotor position must be set to 16.

Table 3.1: Optimization for initial rotor position.

Sl. No	Initial position (degree)	Average Torque (Nm)	Max Peak value	Min peak value	(Max-Min)Value	Below zero (Nm)
1	0	-68.0043	250	-375	625	-375
2	2	-13.9873	360	-280	640	-280
3	4	42.3653	440	-180	620	-180
4	6	88.8346	580	-100	680	-100
5	8	115.146	460	-20	480	-20
6	10	118.6551	360	0	360	10
7	11	113.7739	305	10	295	5
8	12	105.3	260	20	240	9.23
9	13	94.3752	212	22	190	14.87
10	14	81.7139	170	25	145	18.85
11	15	68.2602	129	26	103	19.63
12	16	54.7758	96	26	70	19.41
13	17	42.3226	66	27	39	20.09
14	18	31.7929	40	24	16	19.08
15	19	23.6731	32	18	14	15.83
16	20	17.4095	28	7	21	7.88
17	21	12.4854	21	1	20	1.57
18	22	8.4094	19	0	19	-0.2
19	22.5	6.5873	17	-0.05	17	-0.17

2. **Design 2** -Initializing the time delay function.

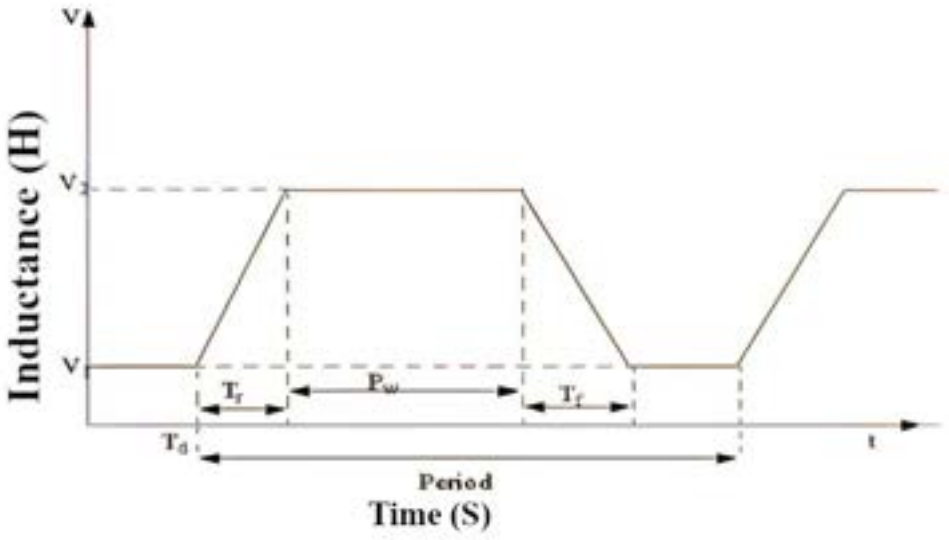

Figure 3.8: Single-pulse denoting delay time (T_d), rise time(T_r) and fall time (T_f).

The delay time plays a crucial role in the correct and efficient switching for the SRM. Several iterations are simulated with varying pulse delay time values, as shown in Figure 3.8. This delay is required to determine which phase must be switched first. As displayed in Table 3.2, phases A, B, and C are optimized to switch at 46, 16, and 31; the B phase must be switched before the C and A phases. In addition to the average, minimum, and maximum torque values, Table 3.2 also

includes the corresponding ripple values. The optimum value selected for average torque is 41 N-m. As the delay time increases, it is obvious to see that the torque ripple experiences a significant flattening. The ripple content was close to 24 for a delay time of 46. This gradually falls to 15 at a delay time of 39; at that time, the average torque is above the rated value and, hence, is considered to have reached its optimal value. Figure 3.9 and Figure 3.10 portray the different moving torque values for various delay time values.

Table 3.2: Optimization for the delay time of the input pulse.

SL.No	Phase A	Phase B	Phase C	Stator Tooth	Rotor Tooth	Average Torque (N-m)	Min Torque (N-m)	Max Torque (N-m)	Torque Ripple	Zero cross-ing	Settled value	Small peak value	Advance angle	Calculations		% of rip-ple con-trol
1	43.25	13.25	28.25	12	81	68.2602	19.6092	129.705	-110.096	26.1525	94.2744	82.6874	15	-110.096	35.4306	-32.1816
2	40	10	25	12	8	130.99	-3.3986	307.4605	-310.859	15.5724	225.8398	184.1166	15	-310.859	81.6207	-26.2565
3	41	11	26	12	8	117.8343	23.9518	254.3234	-230.372	8.5118	186.6236	148.9306	15	-230.372	67.6998	-29.3872
4	42	12	27	12	8	102.8794	26.9845	207.753	-180.769	16.0733	142.934	122.5254	15	-180.769	64.819	-35.8575
5	43	13	28	12	8	87.1429	21.6761	162.96	-141.284	28.1212	125.2191	93.0173	15	-141.284	37.7409	-26.7128
6	44	14	29	12	8	71.3428	24.495	121.2156	-96.7206	29.7388	91.6706	73.7188	15	-96.7206	29.545	-30.5468
7	45	15	30	12	8	56.3138	29.3909	83.9349	-54.544	29.5525	64.0332	55.9218	15	-54.544	19.9017	-36.4874
8	46	16	31	12	8	41.3301	28.2187	52.6747	-24.456	28.0018	45.7712	43.322	15	-24.456	6.9035	-28.2282
9	47	17	32	12	8	29.5733	22.3379	35.3549	-13.017	23.1614	34.2696	28.21	15	-13.017	1.0853	-8.33756
10	48	18	33	12	8	21.0261	12.0165	27.9755	-15.959	12.7108	24.5287	21.433	15	-15.959	3.4468	-21.5978
11	39	9	24	12	8	141.1377	-15.6278	366.8386	-382.466	-15.6278	243.0602	84.2791	15	-382.466	123.7784	-32.3632
12	38	8	23	12	8	147.5239	-36.5952	421.401	-457.996	-7.8722	-36.5952	84.2791	15	-457.996	457.9962	-100
13	37	7	22	12	8	149.2238	-66.5965	485.1923	-551.789	-66.5965	357.242	84.2791	15	-551.789	127.9503	-23.1883
14	36	6	21	12	8	145.3884	-107.167	534.1456	-641.312	-85.9492	409.1869	84.2791	15	-641.312	124.9587	-19.4848
15	35	5	20	12	8	135.3755	-135.881	617.3335	-753.215	-140.796	502.6842	82.2977	15	-753.215	114.6493	-15.2213
16	34	4	19	12	8	117.5203	-190.04	646.9128	-836.952	-156.592	513.6399	66.8381	15	-836.952	133.2729	-15.9236
17	33	3	18	12	8	91.3681	-251.058	605.5065	-856.564	-216.573	402.3723	545.7324	15	-856.564	203.1342	-23.715
18	32	2	17	12	8	59.0687	-296.803	507.2752	-804.079	-328.477	396.0085	465.5323	15	-804.079	111.2667	-13.8378

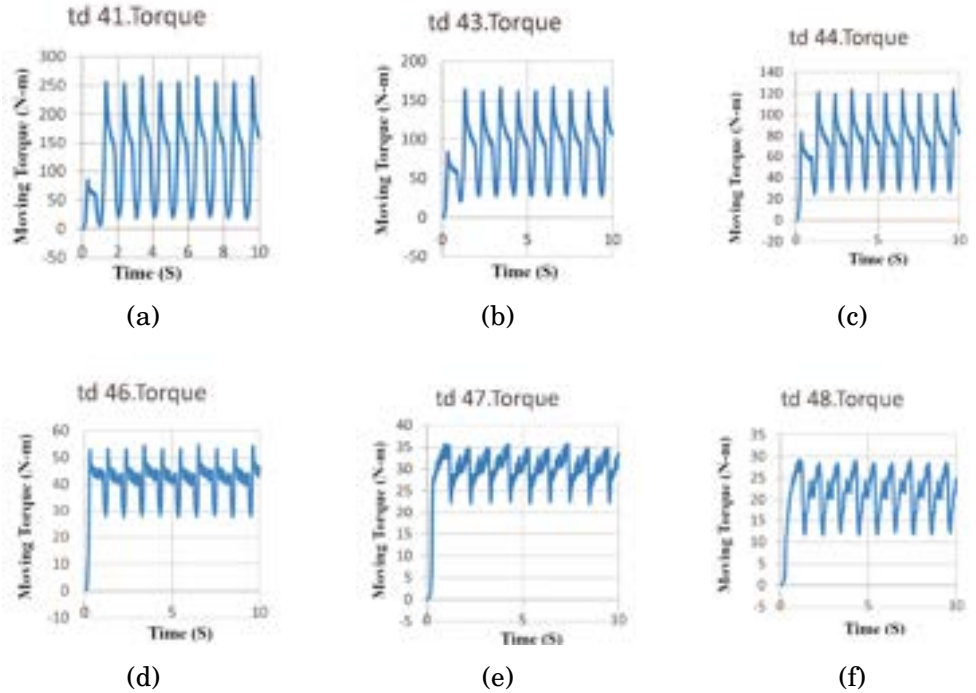

(a) (b) (c)

(d) (e) (f)

Figure 3.9: Moving torque characterization for the different delay times.

a) **Design 3**- Initialising rise time (T_r), fall time (T_f) and pulse width (P_w) of the input pulse provided.

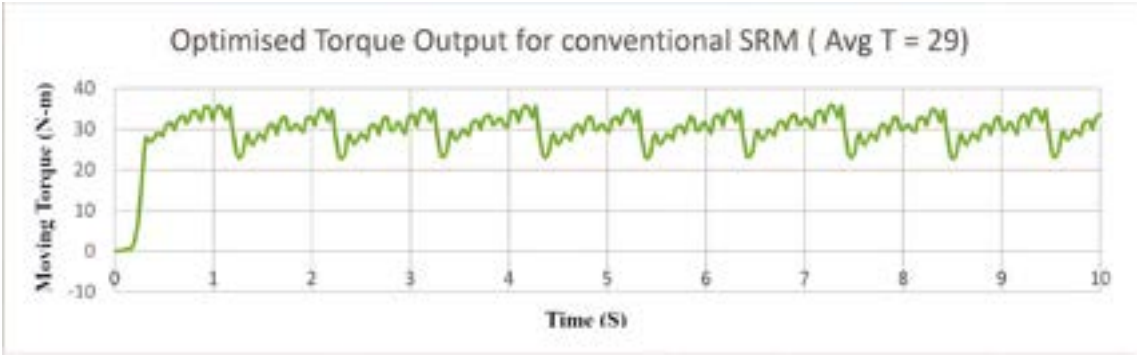

Figure 3.10: Moving torque output characteristics for a fixed delay time value, T_d = 46.

Table 3.3: Initial parameter optimization for the (T_r), (T_f) and (P_w) of the conventional SRM.

SL.No	tr	tf	pw	Stator Tooth	Rotor Tooth	Average Torque (N-m)	Min Torque (N-m)	Max Torque (N-m)	Torque Ripple	Zero cross-ing	Settled value	Small peak value	Calculation	% of ripple control
1	0	0	0	12	8	70.0037	19.6092	129.705	-110.096	26.1525	101.5631	68.9703	60.7347	-0.55165
2	2	2	0	12	8	72.795	49.7237	113.6418	-63.9181	56.4896	86.9089	83.163	30.4788	-0.47684
3	2	1	0	12	8	71.8187	42.4266	112.5558	-70.1292	47.2641	90.2959	84.4878	28.068	-0.40023
4	3	2	0	12	8	64.1861	59.8563	95.9991	-36.1428	52.5201	77.3901	83.9575	12.0416	-0.33317
5	3	1	0	12	8	54.4778	45.4082	81.7999	-36.3917	45.6615	66.7311	67.6963	14.1036	-0.38755
6	4	2	0	12	8	46.5423	44.3062	66.4274	-22.1212	33.5913	55.7367	63.4436	2.9838	-0.13488
7	4	1	0	12	8	47.0586	47.6408	66.8682	-19.2274	36.6094	55.6773	61.8271	5.0411	-0.26218
8	5	1	0	12	8	45.0619	44.7713	65.8275	-21.0562	33.0714	51.5669	59.5379	6.2896	-0.29871
9	6	1	0	12	8	30.3528	21.6783	42.0005	-20.3222	17.8874	38.1774	38.1774	3.8231	-0.18812
1	2	2	15	12	8	72.795	49.7237	113.6418	-63.9181	56.4896	86.9089	83.163	30.4788	-0.47684
2	5	5	15	12	8	17.6394	6.505	25.6177	-19.1127	6.5072	24.1137	20.7467	4.871	-0.25486
3	4	4	15	12	8	8.7057	0.1708	28.8244	-28.6536	-4.0969	13.248	22.6591	6.1653	-0.21517
4	2	4	13	12	8	29.192	27.2303	34.6887	-7.4584	25.9731	33.9818	32.2773	2.4114	-0.32331
5	5	7	13	12	8	2.9804	-4.3362	20.4716	-24.8078	-13.6974	15.846	4.2556	16.216	-0.65367
6	5	5	10	12	8	17.6332	7.3144	26.0409	-18.7265	7.2632	24.6414	20.7585	5.2824	-0.28208
7	5	5	11	12	8	16.4133	6.9051	23.1781	-16.273	7.0395	21.8654	20.3961	2.782	-0.17096
8	2	13	4	12	8	24.5206	7.504	35.6974	-28.1934	7.7015	33.239	27.407	8.2904	-0.29405
9	2	11	6	12	8	26.4915	11.163	34.9118	-23.7488	11.2377	33.72221	27.0508	7.861	-0.33101
1	2	6	11	12	8	29.6244	35.1744	23.1486	12.0258	23.1486	34.6341	22.9622	0.1864	0.0155
2	2	6	13	12	8	25.6878	22.8201	33.2729	-10.4528	18.4549	29.848	30.5887	2.6842	-0.25679
3	2	6	15	12	8	17.7787	10.1419	33.12	-22.9781	7.1679	25.326	28.5543	4.5657	-0.1987
4	2	6	18	12	8	-37.9679	-73.239	30.06	-103.299	-74.664	-33.1258	-33.1258	63.1858	-0.61168
5	2	6	20	12	8	-120.44	-228.411	23.9	-252.311	-309.868	-54.8632	-75.4401	99.3401	-0.39372
6	2	8	11	12	8	29.5923	27.4576	35.8236	-8.366	25.5309	32.9802	32.9802	2.8434	-0.33988
7	2	10	11	12	8	28.442	22.7502	35.8244	-13.0742	21.7128	35.5945	31.7802	4.0442	-0.30933
8	2	12	11	12	8	25.8934	17.1438	35.8249	-18.6811	16.6047	32.721	33.2204	2.6045	-0.13942
9	2	14	11	12	8	21.4404	11.4545	35.8257	-24.3712	10.7129	32.2717	32.6744	3.1513	-0.1293

It is essential to tune the rise time, fall time, and pulse width of the switching pulse depicted in Figure 3.8 of the SRM. To ensure the smooth rotation of the rotor, the magnetization and demagnetization of the stator poles must occur at regular intervals. Incorrect switching will decrease the average torque and increase the motor torque ripple. The values should be optimized based on whether the motor poles are aligned or misaligned at any given time. Numerous iterations are done with various rise and fall times to obtain a sequence of 2, 6 and 11 for T_r, T_f and P_W, respectively, creates an average torque of 29.6 N−m with reasonable torque ripple

12.02 as shown in Table 3.3.

b) **Design 4**- Initialising the windings needed per stator pole.

Table 3.4: Different iterations for choosing the optimum number of turns.

Sl.No	Stator Tooth	Rotor Tooth	Stator Turns	Average Torque (N-m)	Min Torque (N-m)	Max Torque (N-m)	Settled Max	small peak	Torque Ripple	Zero cross-ing	Advance angle	Power
1	12	8	22	51.9172	22.4894	96.3026	72.7019	43.8677	142.1748	22.4506	16	5652.203
2	12	8	20	66.295	28.9469	114.0999	89.4268	52.6684	128.4456	28.9469	16	7275.149
3	12	8	18	86.8054	38.2998	136.3353	110.354	64.119	112.9371	38.2998	16	9625.79
4	12	8	16	116.2065	50.1985	166.1768	138.9033	79.5279	99.80363	79.5279	16	12616.26
5	12	8	14	158.1263	71.894	209.2585	199.0413	100.58	68.72892	71.894	16	18068.93
6	12	8	12	217.5169	108.7066	299.3424	260.6472	217.6063	87.64183	105.5504	16	27320.95
7	12	8	10	298.3422	160.0148	420.0451	399.6491	382.6228	87.1584	149.5316	16	40216.11
8	12	8	8	403.1737	218.9458	555.8667	486.5332	442.08	83.56718	187.1425	16	55027.08

The windings in the poles of the SRM are responsible for developing the flux required for the motor to rotate. The flux will travel through the stator iron and the rotor to form a closed path. This flux path is responsible for the electromagnetic torque produced in the air gap. The intensity of the flux produced determines the strength of the torque produced. However, the magnetic field should not exceed a threshold value that saturates the flux through the core. As a result, the windings per pole must be chosen carefully to produce the maximum flux. Twenty poles were selected for each pole pair to achieve an average torque of 66 N−m while minimizing torque ripple. These results are shown in the accompanying Table 3.4.

After providing turns ranging from 8 to 22, the output average torque and ripple are evaluated to determine the number of stator turns. To produce an average torque of 66.29 N−m, 20 turns are selected.

c) **Design 5**- Assigning Auxiliary Poles.

Table 3.5: The various torque outputs when 2, 4, and 6 poles are removed.

Sl.No	Stator Tooth	Rotor Tooth	Removing poles	Main stator turns per pole	Average Torque (N-m)	Min Torque	Max Torque (N-m)	Settled Max	small peak	Torque Ripple	Zero cross-ing	Advance angle	Power (kW)
1	12	8	2	20	98.3915	31.4822	219.6052	171.1481	103.4622	191.1984	27.7061	16	24728.48
2	12	8	4	20	135.6109	71.5372	231.497	216.7977	167.3738	117.955	30.2583	16	34082.74
3	12	8	6	20	167.0854	74.8846	245.4031	212.1348	195.063	102.0547	75.7835	16	41993.14

The poles' placement must consider the electrical, mechanical, and electromechanical degrees. The adjutant poles of a 12-pole stator must be spaced 30 degrees mechanically and 180 degrees electrically apart. Each of the 12 poles has three phases (A, B, and C), and the three sets of poles corresponding to each phase are separated to form individual windings. As more poles are eliminated from the simulation, the results are shown in the Table. 3.5. It can be observed that the torque value withstands, and the maximum torque is obtained by avoiding windings with

six poles (two from each phase). These poles provide external dc to the stator poles and are assigned as auxiliary poles.

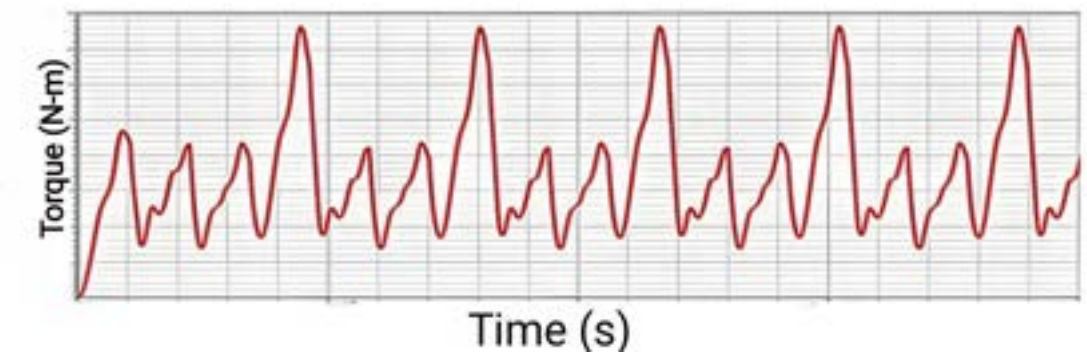

Figure 3.11: Moving torque characteristics for separated auxiliary poles.

After removing the six auxiliary poles and two pole pairs from each phase, the moving torque characteristics are shown in Figure 3.11.

d) **Design 6**- Selection of the turns per poles in both windings.

The multi-level optimization helps to improve the motor's overall performance by maximizing the motor's power density, torque output, and efficiency. It can also help minimize the motor's vibration and noise levels. Optimization can lead to a reduction in the manufacturing costs of the motor by reducing the number of materials and components required. This can make the motor more competitive and increase its demand. It can also improve the motor's durability and reliability, enabling it to be adapted for different applications and environments.

The number of turns has to be optimized for the initial optimization level as part of designing the motor. Optimizing the number of turns on the proposed hybrid excited motor is an essential aspect of initial design-level optimization, as it directly affects the motor's performance and efficiency.

The number of turns in the stator winding determines the amount of magnetic flux the motor generates. By optimizing the number of turns, it is possible to increase the magnetic flux and thereby increase the motor's torque output. The turns also affect the resistance of the winding, which in turn affects the motor's efficiency. By optimizing the number of turns, it is possible to reduce the resistance and improve the motor's efficiency. It is possible to reduce the voltage and current requirements, reducing the size and cost of the motor's power electronics.

The stator winding's number of turns is one of the design elements to be considered to improve the newly designed motor. Optimizing the number of turns is important because it affects the motor's torque output, efficiency, and voltage and current requirements. One approach to optimizing the number of turns is using a genetic algorithm (GA), a robust optimization technique based on natural selection

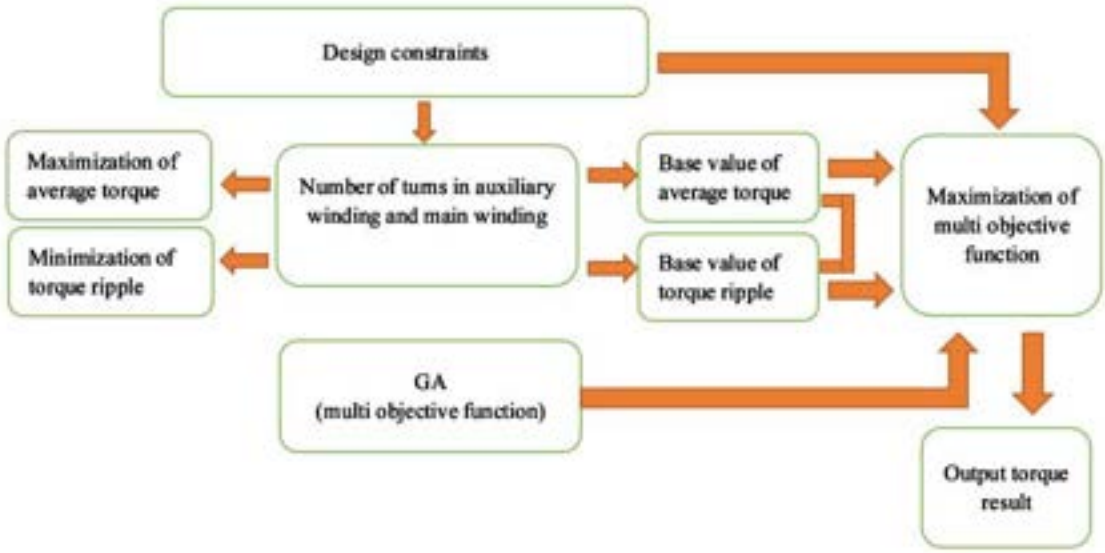

Figure 3.12: Block diagram of initial parameter optimization of selecting the number of turns using MOGA.

and genetics principles. Using GA, it is possible to find the optimal solution that maximizes the torque output and minimizes the torque ripple of the hybrid SRM.

The optimization process using GA involves several steps. First, an objective function is defined that represents the optimization problem. The objective function should be designed to maximize the torque output and minimize the torque ripple of the SRM. Next, the design variables are determined: the number of turns in the stator winding.

Using GA to optimize the number of turns can significantly improve the performance of the proposed HESRMs. By finding the optimal number of turns, it is possible to increase the magnetic flux, thereby increasing the motor's torque output and improving efficiency.

The optimization procedure to achieve the multi-objective functions of maximum average torque and the minimum degree of torque ripple is shown in the block diagram 3.12. The fundamental values of both torques are applied for that reason within the boundaries of the design. Ansys/Maxwell determines both windings' variable number of spins are iterated within the predetermined range.

The auxiliary and main winding poles are separated and designated for switching and the dc injection in this proposed hybrid SRM. Hence, choosing the number of turns for both windings is crucial. Following this, the MOGA technique employs several iterations of the number of turns in each pole to achieve maximum torque and minimal ripple. Following the GA's implementation observations, the auxiliary and main windings have chosen a fixed 20 turns per phase.

The number of turns in the main and auxiliary windings is chosen optimally using the MOGA method. The investigation determined a minimum ripple content

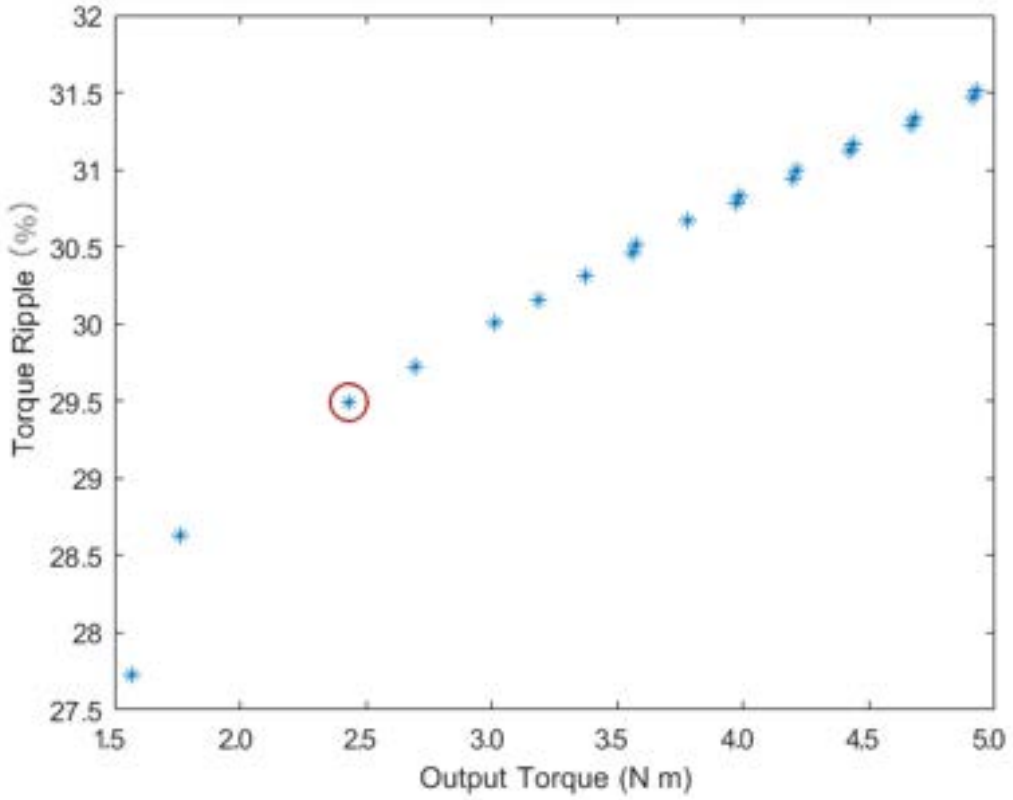

Figure 3.13: The Pareto results for selecting the number of turns in both windings.

of 29.5% and a maximum average torque of 2.5 N m, as shown in Figure 3.13. Hence, both windings have 20 turns per phase selected as the optimum number for obtaining the desired multi-objective constraints.

3.3.3 Step 3: DC Injection to the Auxiliary Poles

Due to the locking of the rotor, static dc cannot be used to provide the appropriate torque output; thus, pulsed dc is delivered to the split poles [116–118]. The auxiliary circuit is employed to switch half of the poles. The dc must be switched precisely to match the motor's speed like the other poles. Since the six isolated poles are coupled to a separate Maxwell circuit, there will be greater control over all aspects and increased redundancy. The variables such as input voltage, flux, and permeability are altered to produce better motor characteristics. The switching circuit controlled by the auxiliary poles is shown in Figure 3.14. The main and the auxiliary's excitation are given at the same interval with a similar pulse width.

The moving torque generated by the excitation of auxiliary windings at rated speed and torque is depicted in Figure 3.15. Compared to standard SRM switching topologies, the ripple value is comparatively decreased. The current drawn by the motor will grow as the load increases. Consequently, the average torque generated

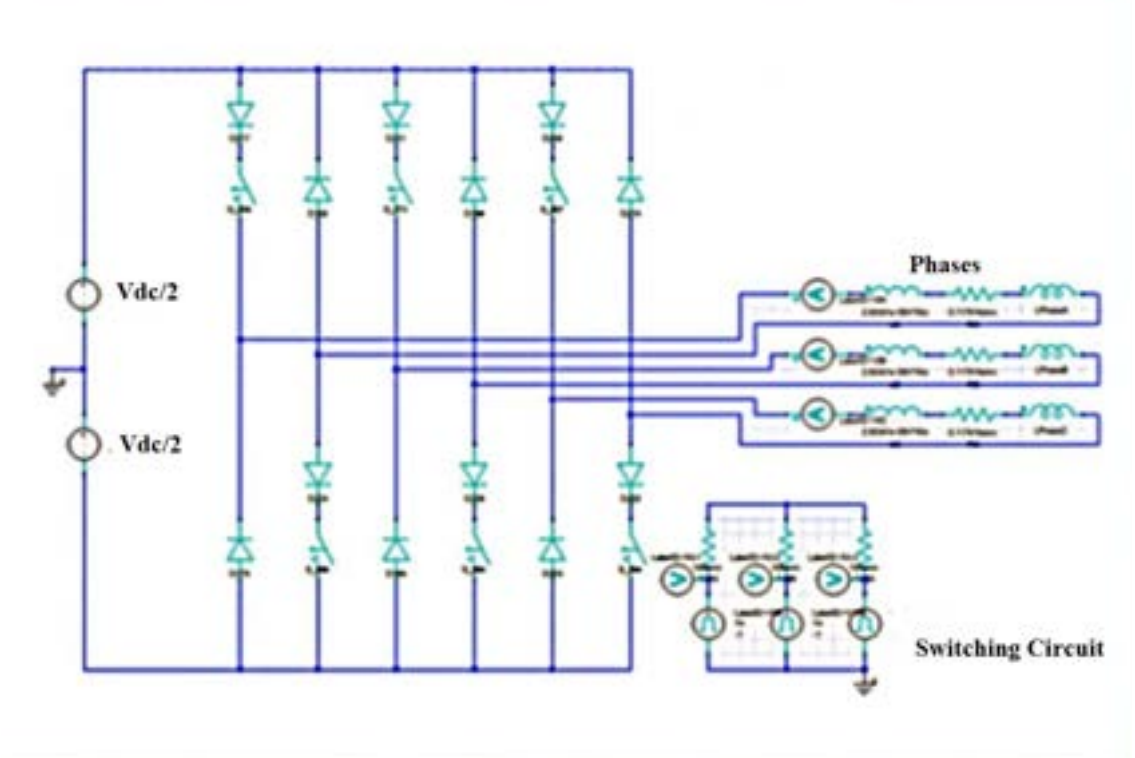

Figure 3.14: External circuit for an auxiliary winding excitation.

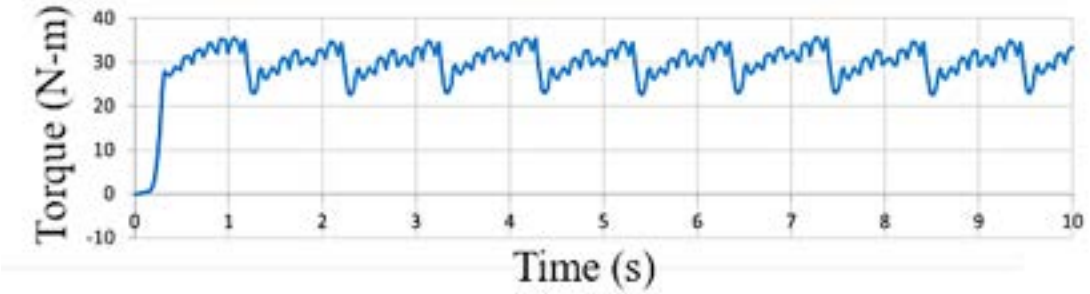

Figure 3.15: Moving torque with optimized value and modeled with separate excitation concerning time (s) and average torque (N-m).

will be substantial. Due to the increase in output torque with the given dc, the ripple content of the output will also be elevated, as depicted in Figure 3.16.

3.4 Objective 2: Design of Controller for Auxiliary Poles

3.4.1 DC Injection in the Auxiliary Winding

The conventional SRM employed in this research has a 12/8 three-phase topology with 12 stator poles and 8 rotor poles. Each phase consists of four poles that are structurally opposed and symmetrical to one another. Each phase is energized

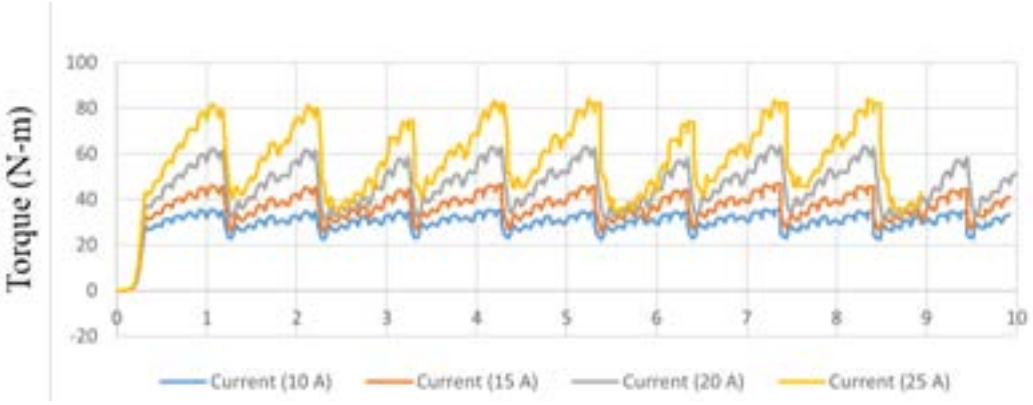

Figure 3.16: Moving torque output for various input currents to the auxiliary circuit.

sequentially to achieve the desired motor speed. Flux produced in the stator core and passing through the air gap and rotor flux paths allow the motor to rotate. As the input voltage rises, the flux densities will increase, and as a result, the motor's output torque will elevate as well. However, as the input current is increased further, the flux produced in the core will become saturated, preventing the machine from exceeding its rated parameters.

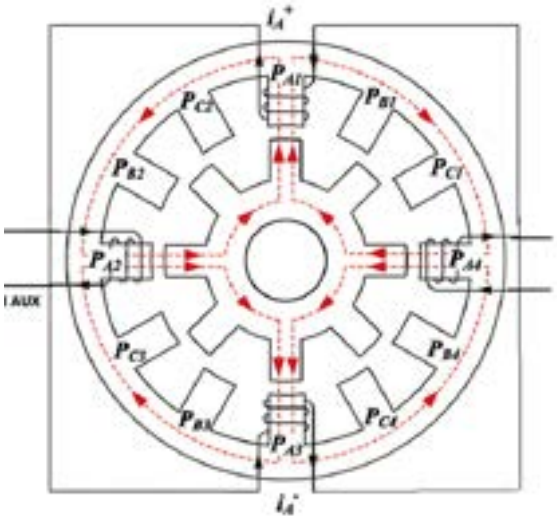

Figure 3.17: Flux path of HESRM without PMs excitation.

In hybrid excitation of switched reluctance motors, Figure 3.17 out of the 4 poles of each phase, 2 are isolated and separately excited. These auxiliary poles inject external dc as per the torque demand. This method provides better motor control and can derive the desired performance only at the necessary occasion. This method also eliminates the usage of permanent magnets inside the switched reluctance motors, as the auxiliary poles will replicate the same action of PMs.

To drive a motor, a series of voltage pulses are applied to each phase. Each phase is consequently activated, causing the motor to spin. As shown in Figure 3.18, the

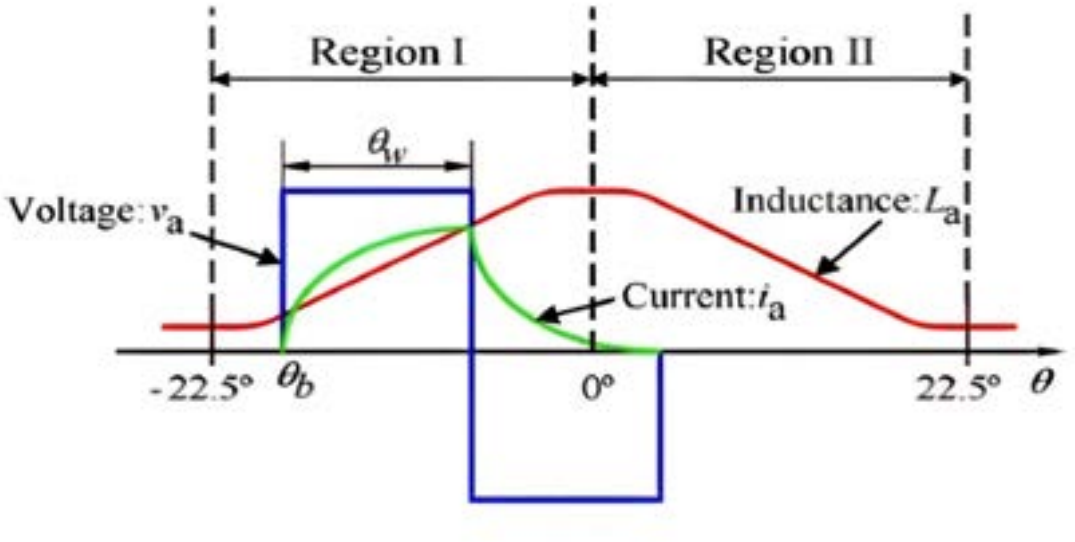

Figure 3.18: DC injection profile for the proposed HESRM.

current pulses must be applied to the energized winding of each phase at a precise rotor position. When any pair of rotor poles are perfectly aligned with the stator poles of the specified phase and the rotor is in the maximum stator inductance position, the phase is said to be aligned. The inductance profile of switched reluctance motors is trapezoidal, with a maximum value in the aligned position and a minimum value in the unaligned position. The idealized inductance profile of an SRM with three phases is a triangle, with one phase being emphasized. Electrically, the phases are shifted 45 degrees from one another.

3.4.2 Controller Design

3.4.2.1 Conventional SRM drive

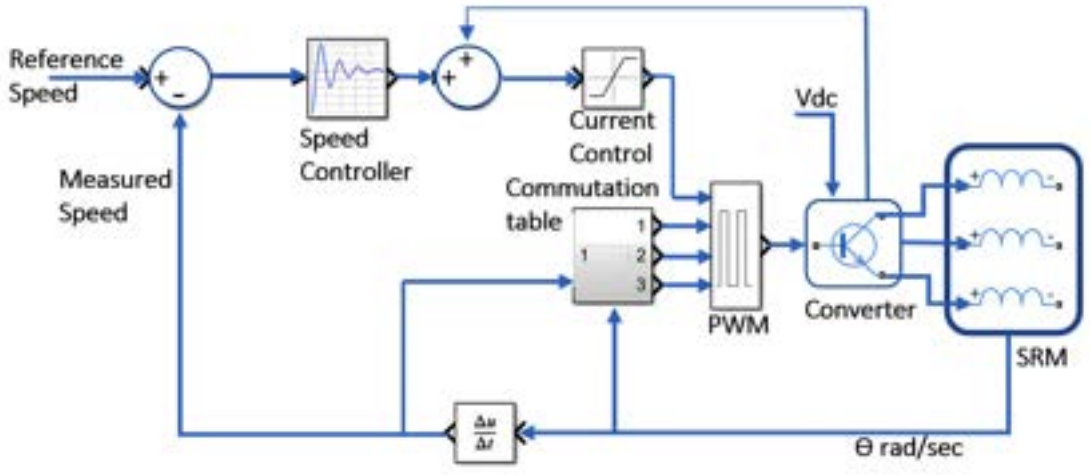

Figure 3.19: Block diagram of the Conventional SRM drive.

The primary conventional SRM drive concerning the switching circuit and the speed controller is shown in Figure 3.19. The closed-loop control of SRM is enabled and uses a proportional-integral (PI) controller as a speed reference. A PI controller directly controls the voltage applied to the phases of the motor. Hence, the speed controller calculates the phase voltage and processes the speed error (the difference between the expected and actual speed). The phase voltage is determined by a PWM duty cycle applied to the SRM inverter's dc-bus voltage. The speed of the plant motor is obtained from the speed encoder of the PMSM, which gives 2048 pulses in each rotation. The rotation angle is estimated from these pulses and converted to speed, which is provided as the input to the reference of the PI controller [119, 120]. The speed control used has external gain values Kp and ki values, which can be provided in real-time while the motor works; hence, the motor can be tuned after loading. The measured speed from the encoder is compared concerning generating the error, which is then provided to the PI controller.

3.4.2.2 Proposed HESRM Drive

In a conventional motor design, the main winding provides the flux; however, the proposed machine uses the main and auxiliary windings to provide added flux. Additionally, injecting more current into the auxiliary windings is possible, resulting in a substantial increase in air-gap flux density. This condition facilitates total control over the split poles and, consequently, the motor. Subsequently, the auxiliary poles' input voltage, current, and switching pattern can be effectively controlled [91, 121–123].

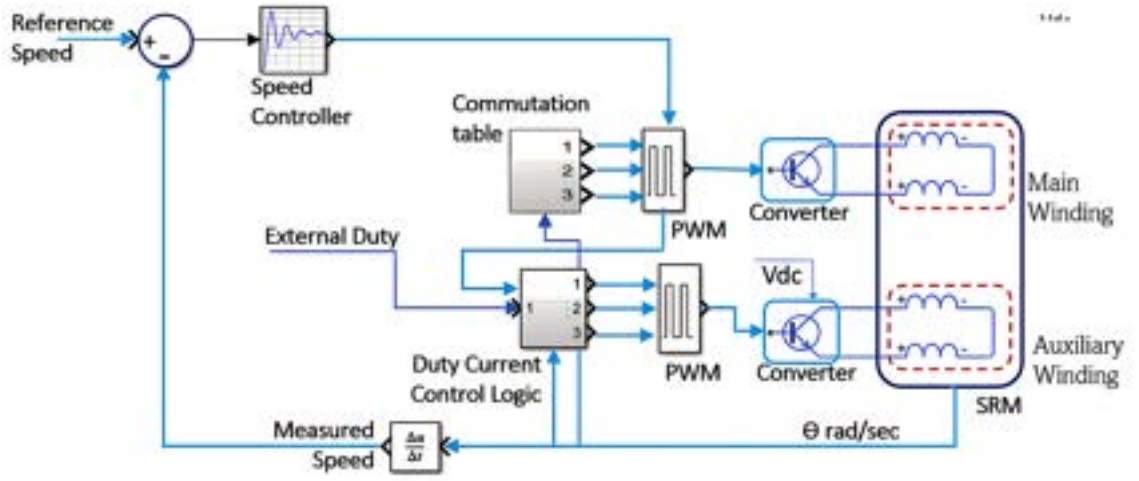

Figure 3.20: Proposed HESRM drive for main and auxiliary winding.

The 6 poles are separated from the 12 poles of the conventional SRM. These six poles have three phases: A, B, and C. Since the windings are concentric, it was simpler to reduce the number of poles from four to two without reducing the number

of turns. The primary 6 poles are controlled as usual, while the auxiliary six poles are used to inject additional dc for enhanced performance. This also provides the added benefit of improved motor control.

The motor parameters will be adjusted to obtain a smooth torque output with a maximum average and minimum torque ripple. These poles are injected with a fixed and variable dc, and the output is measured and analyzed. Since these poles have separate winding and switching circuits, the motor can be controlled efficiently.

The auxiliary poles are switched simultaneously with the main poles but through a buck converter topology. The voltage through these buck converters is controlled, thereby regulating current injection into the machine. PWMs for switching the main winding are provided through an asymmetric converter. The voltage through the auxiliary windings can be separately controlled simultaneously through the main winding switches, as shown in Figure 3.20.

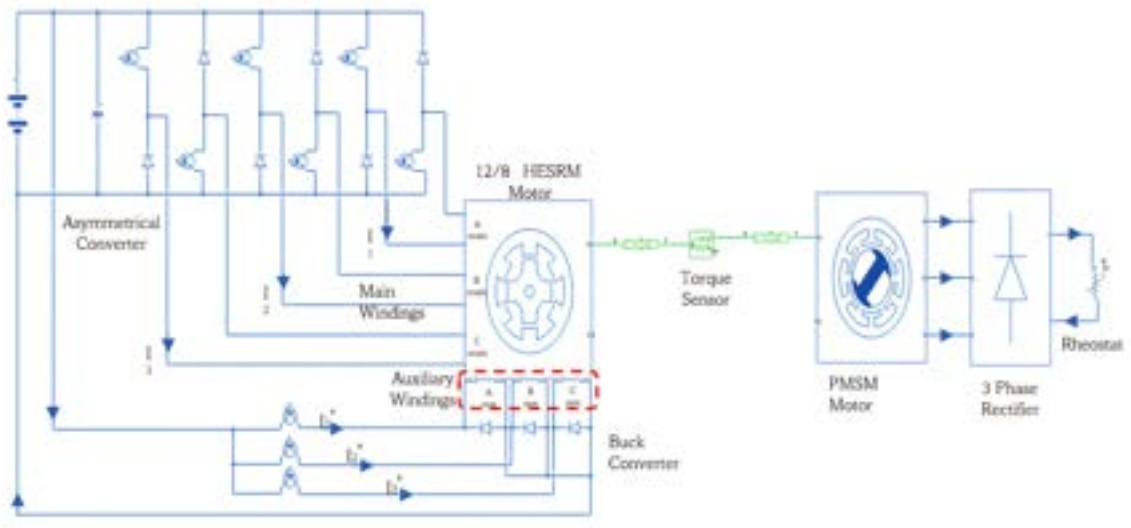

Figure 3.21: The proposed new switching pattern for proposed HESRM.

The auxiliary switching circuits shown in Figure 3.21 extend the circuit to switch the primary windings. To prevent the rotor from locking up during rotation, the MOSFETs driving the auxiliary poles must be fired simultaneously with those driving the main poles. To ensure this, the rising edges of the gate pulses that drive the main poles are analyzed, and an additional pulse train is generated during the ON time of this pulse. This pulse train is controlled with a particular duty so that the voltage and current flowing through the auxiliary poles can be regulated. As illustrated in Figure 3.22, the auxiliary circuit will only be turned on while the main circuit is switching.

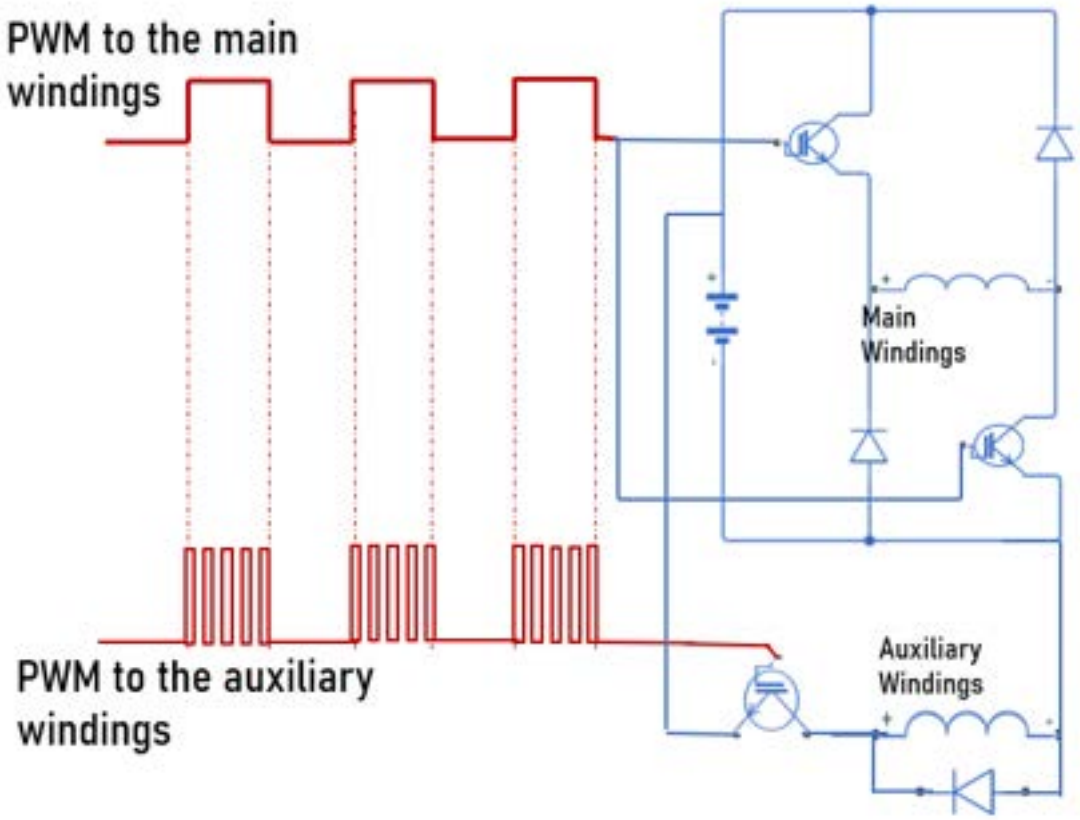

Figure 3.22: PWM excitation scheme for the dc-injected auxiliary windings.

3.5 Machine Topology 1

The machine topology of conventional SRM and HESRM without permanent magnets is shown in Figure 3.23. Both SRMs have twelve stator and eight rotor poles without any permanent magnets, but the windings of the poles per phase are assigned for different excitations [124–126]. These are named main winding and auxiliary winding excitation, respectively.

The stator of the HESRM is different from that of the conventional SRM; here, the stator poles are assigned to the main and auxiliary coils depending upon the excitation provided. Since there are twelve stator poles, six can be provided to both main and auxiliary windings, out of which four can be assigned to each phase. The number of poles for the main and auxiliary is kept constant to inject external flux to the poles simultaneously with the excitation of main windings. In a 12/8 SRM, separate dc excitation can increase the air gap's resultant flux due to the poles' symmetric nature. Figure 3.23 shows that the poles are separated as main and auxiliary by conserving electrical and mechanical symmetry. This geometry of twelve stators can effectively provide two separate windings for each phase.

Figure 3.24 demonstrates the magnetic field distribution of two SRMs. It can be observed that the field lines are the same for both SRMs. The HESRM flux is

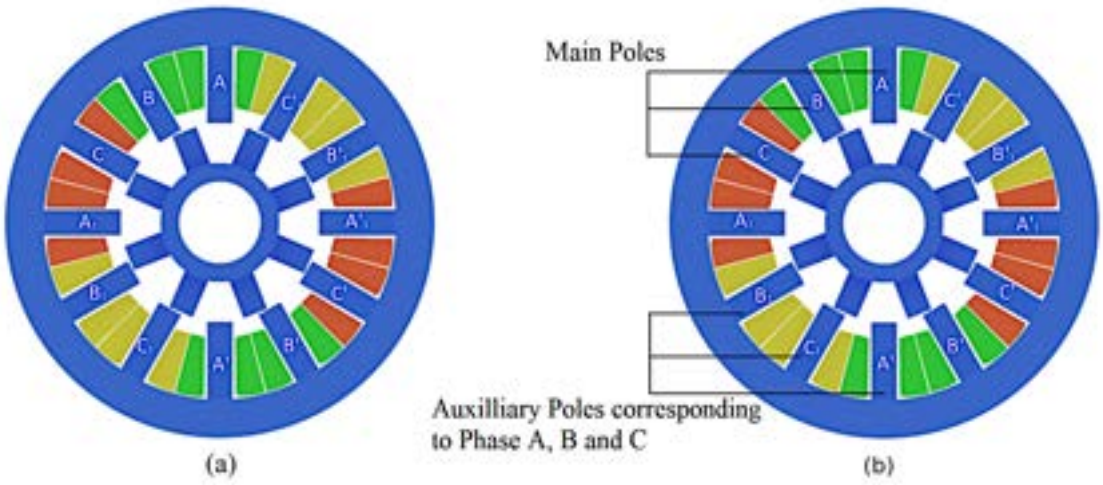

Figure 3.23: Machine topology of two SRMs with the same rating is shown as (a) a 12/8-pole conventional SRM and (b) a 12/8-pole hybrid excitation of SRM without PMs.

injected in the same path as the main winding flux.

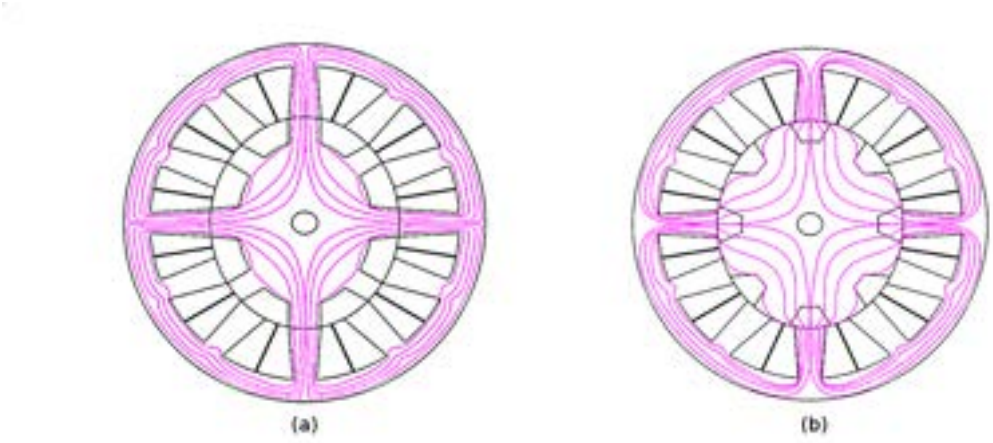

Figure 3.24: Magnetic flux path for the proposed SRM is shown as (a) Aligned poles and (b) Unaligned poles.

3.6 Mathematical Model of the HESRM

The proposed hybrid excitation method's equivalent magnetic circuit (MEC) model without permanent magnets is achieved by injecting dc according to the hypothesis illustrated. The torque equation is derived from the main and auxiliary windings [127–131].

When the HESRM is in excitation, total flux linkages created by dc-excited coils and phase-excited coils can be expressed as follows:

$$\psi_x = \psi_{i_x}(\theta, i_x) + \psi_{AC_x}(\theta, i_x) \tag{3.1}$$

where, ψ_x is the total flux linkage in the exciting phases, ψ_x (θ, i_x) is the flux linkage created by the field coils, $\psi_{AC_x}(\theta, i_x)$ is the flux due to dc field coils and θ is the rotor position.

The resulting flux from the exciting current can be indicated as the product of inductance and current.

Thus, the effective flux associated with the exciting phases can be written as:

$$\psi_x = L_{i_x}(i_x, \theta).i_x + \psi_{AC_x}(\theta, i_x) \tag{3.2}$$

where, $L_{i_x}(i_x, \theta)$. i_x is the inductance produced by the main phase current as a function of the exciting current and the rotor position.

The excited phase-x voltage equation can be expressed as:

$$v_x = r_{ph}.i_x + \frac{d\psi_x}{dt} \tag{3.3}$$

where, r_{ph} is the resistance of the phase; i_x is the exciting phase current; ψ_x is the phase linkage flux.

Substitute equation (3.2) in (3.3) we get,

$$v_x = r_{ph} i_x + L_{ix}(i_x, \theta)\frac{di_x}{dx} + i_x \frac{dL_{ix}(i_x, \theta)}{d\theta}\omega + \omega \frac{d\psi_{AC_x}(\theta, i_x)}{d\theta} \tag{3.4}$$

Phase voltage equation for 3 phase proposed HESRM can be expressed as:

$$\begin{bmatrix} v_A \\ v_B \\ v_C \end{bmatrix} = r_{ph} \begin{bmatrix} i_A \\ i_B \\ i_C \end{bmatrix} + \begin{bmatrix} L_{i_A} & 0 & 0 \\ 0 & L_{i_B} & 0 \\ 0 & 0 & L_{i_C} \end{bmatrix} \begin{bmatrix} \frac{di_A}{dt} \\ \frac{di_B}{dt} \\ \frac{di_C}{dt} \end{bmatrix} + \omega \begin{bmatrix} i_A & 0 & 0 \\ 0 & i_B & 0 \\ 0 & 0 & i_C \end{bmatrix} \begin{bmatrix} \frac{dL_{i_A}}{d\theta} \\ \frac{dL_{i_B}}{d\theta} \\ \frac{dL_{i_C}}{d\theta} \end{bmatrix} + \omega \begin{bmatrix} \frac{d\psi_{ACA}}{d\theta} \\ \frac{d\psi_{ACB}}{d\theta} \\ \frac{d\psi_{ACC}}{d\theta} \end{bmatrix} \tag{3.5}$$

The energy generated in the phase excited is obtained as:

$$W_x = W_{i_x}(\theta, i_x) + W_{AC_x}(\theta, i_x) \tag{3.6}$$

$W_{i_x}(\theta, i_x)$ can be represented as the co-energy produced by the exciting phase current. $W_{AC_x}(\theta, i_x)$ is the co-energy generated by the dc field coil.

Where T_x is the electromagnetic torque provided by one phase that can be obtained from the total energy of that phase.

$$T_x(\theta, i_x) = T_{rx}(\theta, i_x) + T_{AC_x}(\theta, i_x) \tag{3.7}$$

3.7 Magnetic Equivalent Circuit Model of the HESRM

In the proposed hybrid excitation of SRM, poles are isolated from each phase and provide additional control using drive circuits [132–137]. The separated pole windings are called auxiliary windings and are responsible for additional flux by indirectly injecting dc. To deliver this additional flux, the auxiliary windings must be controlled.

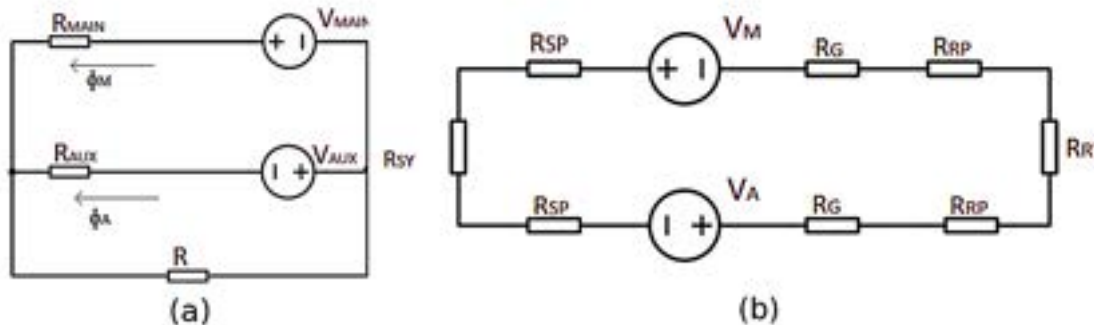

Figure 3.25: Magnetic equivalent circuit of the proposed HESRM (a) For different phases (b) Single MEC circuit.

The equivalent magnetic circuit shown in Figure 3.25 depicts the switching circuit patterns for the main and auxiliary windings. The equivalent circuit depicts the reluctance path produced by the exciting phases. The effective reluctance is the result of the main and auxiliary excited phases. The V_M and V_A are the magnetic potentials, and ϕ_M and ϕ_A denote the flux corresponding to the respective phases. Hence, the total reluctance produced is the result of both windings. The reluctance associated with each part of the motor is expressed in R. The total flux produced due to the sum of both fluxes will be much more vital to create substantial electromagnetic torque.

Table 3.6: Main dimensions and parameters of two SRMs

Dimensions	Conventional SRM	HESRM without PMs
Phase number	3	3
Stator and rotor poles	12/8	12/8
Stator pole assigned for excitation	12	6-6
Rated power (kW)	1.2	1.2
Rated speed (rpm)	2500	2500
The outer diameter of the stator (mm)	138	138
Outer diameter of rotor (mm)	81.50	81.50
Length of air-gap (mm)	0.5	0.5
Type of material	M15_26G	M15_26G

Table 3.6 illustrates the comparison between the conventional SRM and HESRM, where the parameters such as phase number, stator and rotor poles, rated power, speed, length of the air gap and type of material are the same. The excitation scheme provided for HESRM differs in separating poles as main and auxiliary. Initially, the motor is simulated with a high-rated motor (20 kW), and further, for testing the machine rated with (1.2kW), the initial results scaled down to the rated value.

3.8 Characteristics of the HESRM Using 2D FEA Analysis

This section presents the magnetic characteristics of the conventional SRM at aligned and unaligned positions. Both SRMs are given the same size, number of coils per pole, and similar types of windings to obtain better clarity and ease of comparison. The field lines where the stator and rotor iron have the shortest flux path are concentrated in the aligned position rather than the unaligned one.

3.8.1 Magnetic Characteristics of Two SRM

The cross-sectional areas of the two SRMs are the same due to the same rotor construction and geometric dimensions. Thus, SRMs, the stators, and rotor iron weights identical to the constructions have a 7.933 (kg) total net weight, and the stator and rotor core steel consumption (kg) are 7.05683 and 2.6735, respectively. Owing to the difference, only the excitation scheme provided the winding with different currents.

3.8.1.1 Field Line and Flux Distributions

The magnetic characteristics of the proposed SRM are similar to that of the conventional SRM. Here, the quantity of the flux lines will increase as more current is

injected into the auxiliary poles. As a result, the effective flux lines in the air gap increase, and the resultant electromagnetic torque increases. Figures 3.26 and 3.27 demonstrate the magnetic flux distribution and density of the conventional SRM and the proposed HESRM, respectively.

The excitation for the three-phase scheme for the conventional SRM with aligned and unaligned poles shows that the minimum flux density is 1.2–1.3 Tesla (T) for the unaligned pole and 1.7–1.8 T for aligned poles. The conventional SRM's range for maximum flux density is 0–1.9 T, and steel is the material used for the simulation.

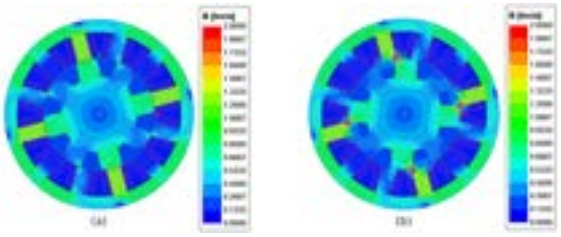

Figure 3.26: Magnetic flux distribution of conventional SRM: (a) Aligned poles (b) Unaligned poles.

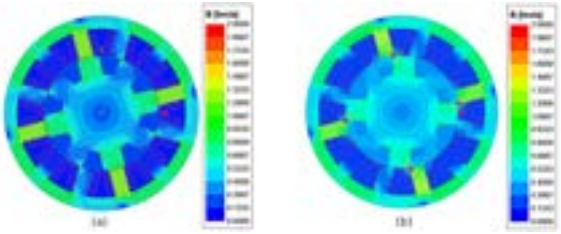

Figure 3.27: Magnetic flux distribution of the proposed HESRM: (a) Aligned poles (b) Unaligned poles.

3.8.1.2 Flux Density Distribution

Figure 3.28 shows the flux density characteristics of both SRMs' for the given excitation (5A) at aligned and unaligned positions. The maximum flux density at the aligned position is 0.55 T. At the unaligned position, it is 0.35 T. Because the auxiliary windings' unexcited pole is aligned with the excitation pole in the HESRM, it can reach 0.65 T in alignment with the same excitation current at 5 A. Auxiliary injection current helps to increase the magnetic flux density in an unaligned state in 0.38 T, comparing the magnetic flux distribution and flux intensity of the proposed HESRM, where both characteristics are identical.

Accordingly, there is only one difference in the intensity of flux carrying in the air gap due to different dc injections in the auxiliary poles. First, the excited state produces the main flux with the effect of the main winding, and the extra DC provided by the auxiliary excitation creates more electromagnetic torque.

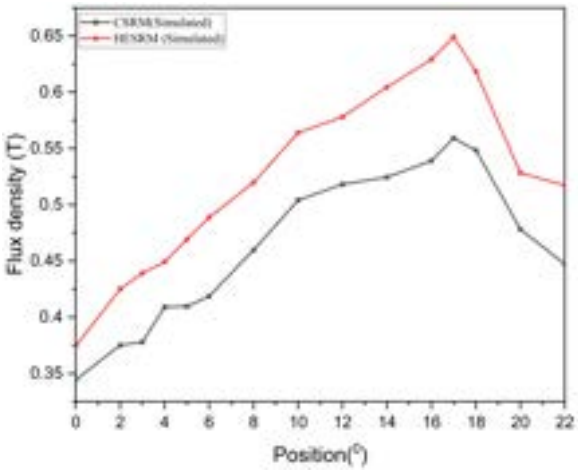

Figure 3.28: The characteristics of measured flux density of conventional SRM and the hybrid dc-excited SRM.

The principle of reluctance guides the strategic resource management of SRM. Therefore, the SRM generates the torque based on the magnetic reluctance of the motor. The magnetic circuit between the rotor and stator is very reluctant when not aligned. As the rotor tries to align with the powered stator poles at this point, the stator pole pairs are activated, reducing the magnetic reluctance. Reluctance torque is formed when the rotor can reach the minimal point of reluctance. It is necessary to precisely time the stator poles' excitation so that it only happens when the rotor attempts to align with the exciting pole. SRM may require positive feedback from encoders or Hall effect sensors to control the excitation of the stator based on a precise rotor position.

3.8.2 Steady-State Characteristics

The electromagnetic behavior of the proposed HESRM was analyzed through the FEM using commercial software ANSYS/Maxwell. MATLAB/Simulink carried out the motor drive simulation, and the co-simulation method held the interpretation. For this purpose, the feasibility of the proof of concept was verified with the help of software simulations by analyzing steady−state and dynamic behaviors.

3.8.2.1 Static Electromagnetic Torque

The static magnetic torque characteristics of two SRMs with phase excitations are shown in Figure 3.29. The conventional SRM static torque curves with the current of 15 A vary from 0 to 22.5 degrees, as shown in Figure 3.29a. Accordingly, the static torque for one-half of the excitation cycle of conventional SRM attains nonalignment to the aligned pole.

It can be seen that the torque varies from minimum to maximum and finally

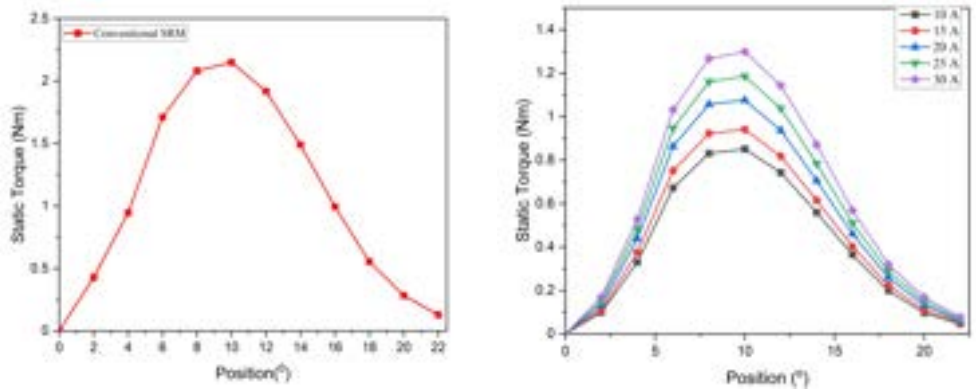

(a) (b)

Figure 3.29: Static torque characteristics: (a) Conventional SRM at rated current 15 A and (b) HESRM under various currents concerning the DC field injection.

reaches a minimum with the unaligned position. The maximum static torque that produces the phase excitation current of 15 A is 2.2 N−m. The comparison shows that the auxiliary excitation in which a different current is provided with the help of dc injection may attain different patterns of static currents. The auxiliary winding has a provision for carrying the maximum current to the rated value. Figure 3.29b shows that the static flux curve pattern increases the effect of varying according to the rises of dc in the auxiliary coils. Since the additional current is passed through in the auxiliary windings using special circuitry, the core's flux increases, resulting in higher torque and power density.

3.8.3 Dynamic Performance of Two SRM Drives in FEM

MATLAB/Simulink was used to study the performance of the motor drive system for two SRMs. The proposed HESRM drive system Simulink model has an asymmetric half-bridge converter, logic PWM, angle controller mechanical systems, DC sources, speed and current controllers, a separate auxiliary excitation with an extra switch, etc. The machine model is developed on the Ansys/Maxwell workbench. The dynamic performance of both machines was performed and compared under the same conditions.

3.8.3.1 Gate Pulse Characteristics of Two SRMs

Figure 3.30 shows the moving torque and current characteristics of two SRMs in which the gate pulses are given to the phases at the same turn ON and turn OFF times. In conventional SRM, the single PWM pulses sequentially provide the switching scheme for all phases. The hybrid excitation method provides identical gate pulses to the main and auxiliary windings separately. The torque characteristics of conventional SRM can be achieved with similar excitations in HESRM. Since the

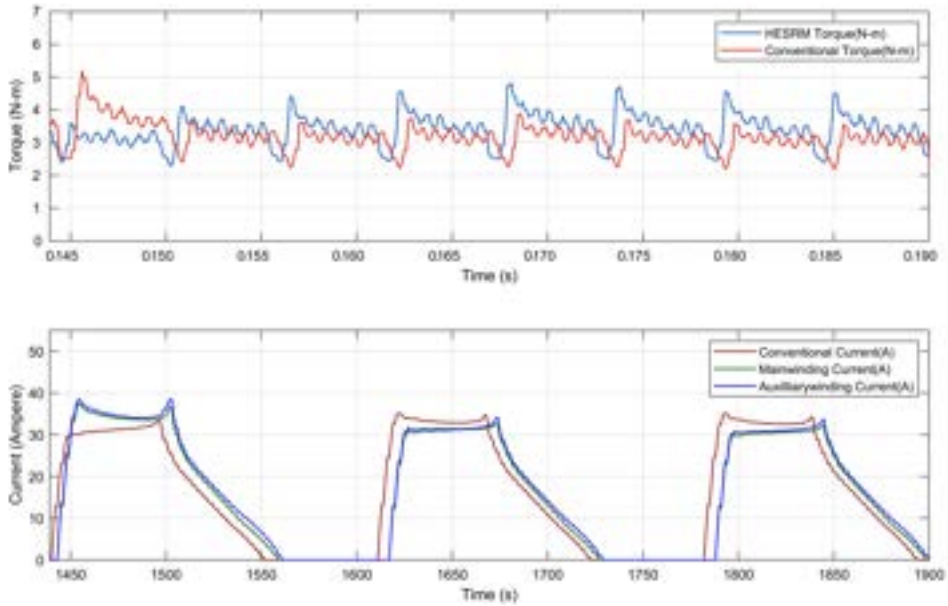

Figure 3.30: Comparison of characteristics of moving torque and current of two SRMs.

moving torque remains similar, the auxiliary current can be further increased to the rated value to achieve maximum performance.

3.8.3.2 Closed-Loop Current Control of Two SRMs

The closed-loop current control of the conventional SRM is established by obtaining current feedback from the windings and providing input to the current controller. The conventional and proposed HESRM showed similar results at various input currents with matching moving torque and slightly less ripple, as shown in Figure 3.31. The current from the windings can be sensed and used to provide additional flux through the auxiliary in this hybrid excitation method.

3.8.3.3 Variable-Speed Control Strategy for Two SRMs

The speed control of SRMs is established using a PI controller by measuring the actual speed and comparing it with the reference speed, which varies continuously from minimum to rated value. The proportional (k_p) and integral (k_i) values of the controller are tuned in such a way as to reach the set points as early as possible. The analysis of the two results shows similar characteristics at the same current rating and load. The additional torque needed for the motor can be identified and provided through these auxiliary windings to obtain better results. However, the HESRM method is derived to enhance the performance by separately injecting the dc with the help of auxiliary winding. Hence, these results elaborate on how to achieve the same performance through the different winding excitations separately.

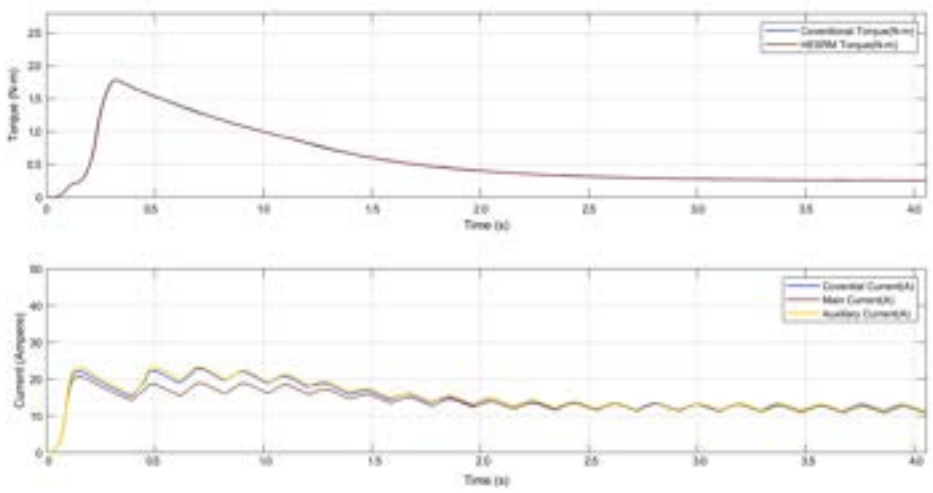

Figure 3.31: Comparison of closed-loop current control of conventional SRMs and HESRM.

However, the HESRM makes it possible only through different currents passing through the assigned winding. This method benefits by changing different currents through the controller to improve the average torque characteristics and reduce the torque ripple to the minimum level.

In a conventional SRM, the variable speed is related to the main current excitation and torque; in a HESRM, where there are two currents, the main current and an auxiliary current, the main current is responsible for both the excitations and the auxiliary current is responsible for the variable speed.

Figure 3.32 displays the torque and current characteristics of the traditional and hybrid SRM at variable speeds. The speed input is changed using ramps and steps to simulate how EVs operate in real-time. Steps of 1000 rpm are used to ramp up the speed from zero to 2500 rpm. The graphs show all three phases of the currents at various speeds. Since this motor is a three-phase switching machine, the irregularities in the phase currents are caused by the speed changes. The longer switching patterns indicate the motor transient behavior at the start of the operation.

3.9 Experimental Results

3.9.1 Rewinding and Remodelling

The conventional SRM has to be remodeled to the new topology for the proposed method, as shown in Figure 3.33. The conventional SRM has 6 leads at the output, each pair for one phase. For the proposed method, each winding has to be isolated for rewinding. Out of the 12 poles of the conventional SRM, half of the poles are separated. These 6 poles include 2 poles for each phase. The windings are concentric;

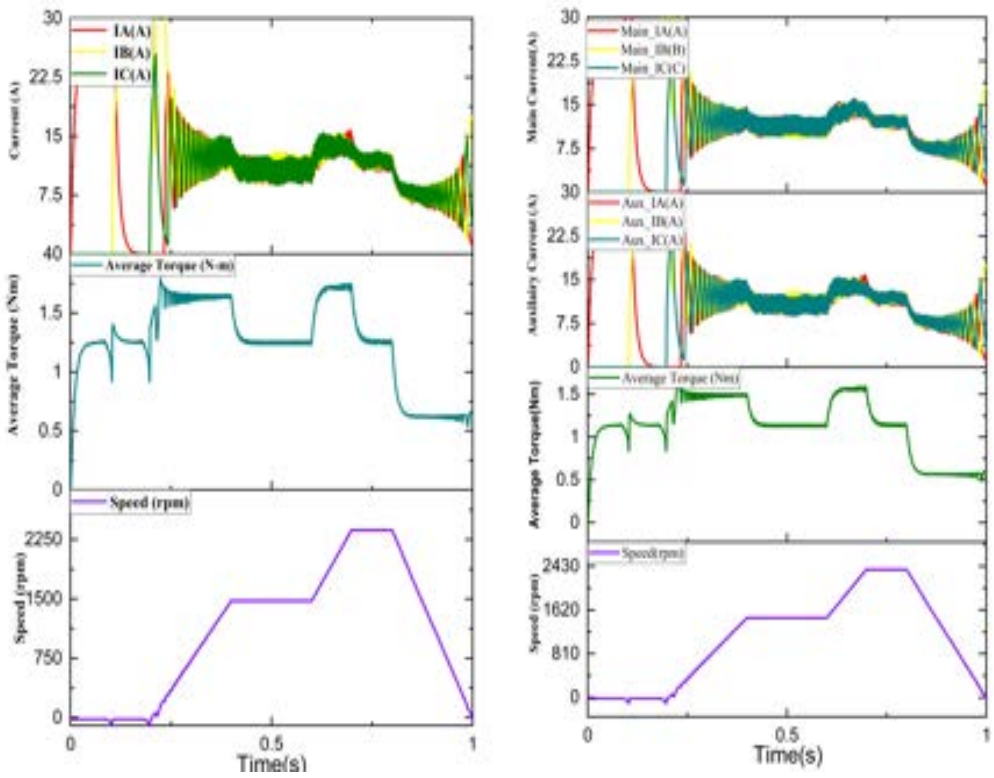

(a) (b)

Figure 3.32: Closed-loop variable-speed current control strategy: (a) conventional SRM and (b) HESRM; the curves are current (A), torque (N−m), and speed (rpm).

hence, splitting the windings from 4 poles to 2 without compromising the number of turns was easier. The main 6 poles are controlled as the conventional machine, whereas the 6 auxiliary poles are used to inject additional dc for extra performance. This also provides the added advantage of better control of the motor.

3.9.2 Motor Prototype

The torque characteristic of the SRM is the most critical performance parameter that must be measured. As shown in Figure 3.34, a back-to-back motor setup with a torque sensor coupled in between was constructed to analyze the characteristics. The motor used on the load side is a PMSM rated at 5000 revolutions per minute (rpm). This motor is tightly coupled with the motor of the plant. The nonlinearity of the Fluke torque sensor (model: TRD605) is +/−0.2%. This high-precision strain gauge sensor measures up to 250 N−m. The load-side PMSM contains an incremental speed encoder with a pulse per revolution (PPR) of 1024, which can be increased to 5000 by counting the rising and falling edges of the encoder pulses. The PMSM back EMF drives a three-phase rectifier to a resistive load. Changes to the resistance can be made to load the motor.

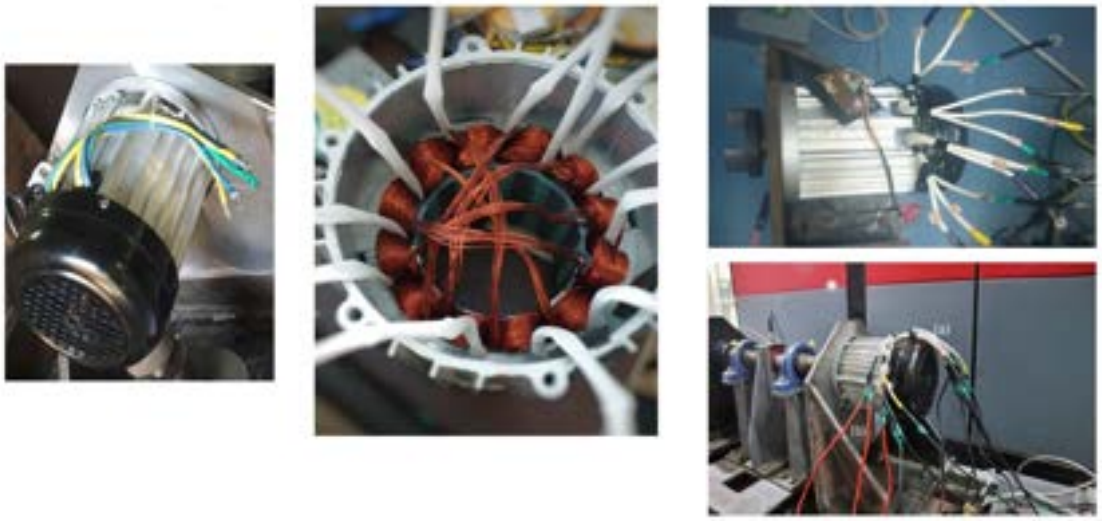

Figure 3.33: Photograph of rewinding the conventional SRM to HESRM (a) Main winding. (b) Auxiliary winding.

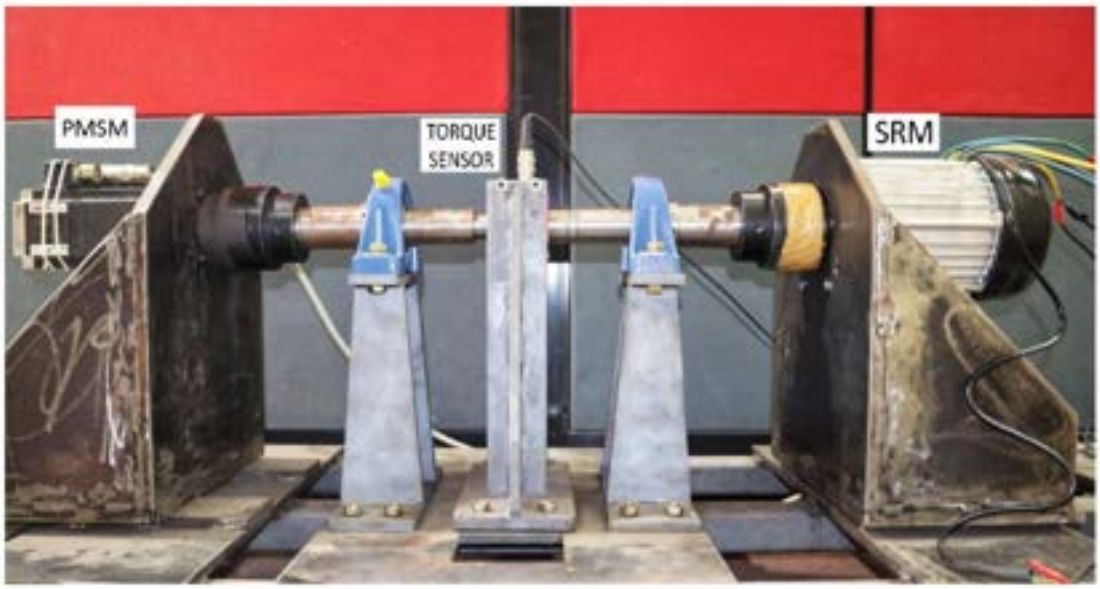

Figure 3.34: Test bench of SRM coupled with the electric loading

The setup for the controller circuit is shown in Figure 3.35. The asymmetrical switching circuits switch the windings as per the commutation signal provided. The waveact is a real-time controller which acts as a rapid control prototyping solution for power electronics applications. The system is Xillinx Zynq SoC based and is entirely user control function execution on FPGA fabric with high performance.

The waveact controller is a model-based design that works with MATLAB/Simulink HDL Coder and Xilinx System Generator (XSG). The main benefit is that binary and configuration files can be made with a single click.

It has the following features:

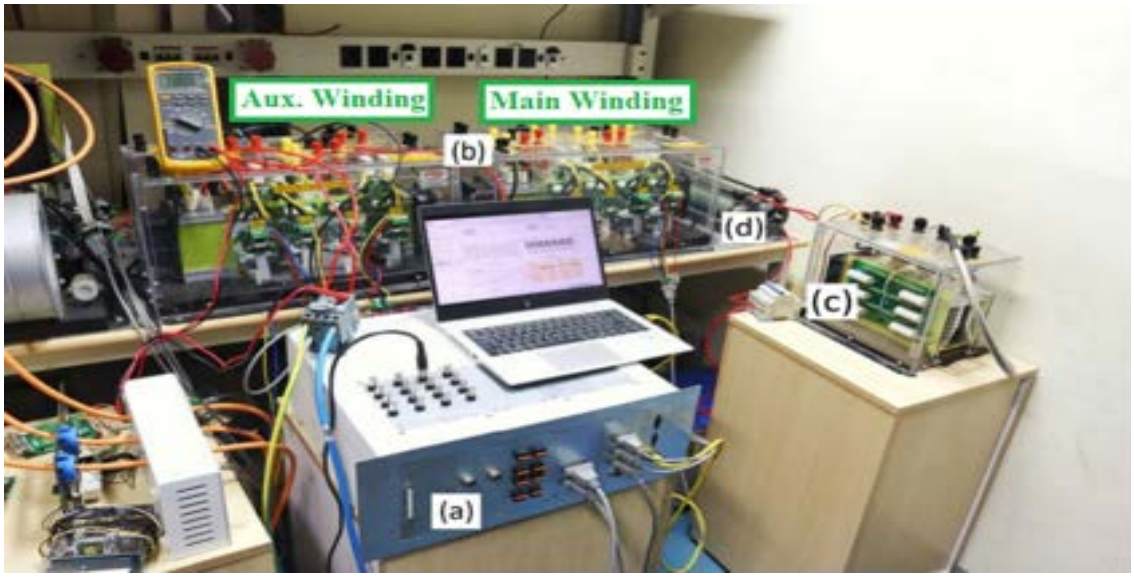

Figure 3.35: Controller circuit for exciting the main and auxiliary winding.

- Fast Step Time - 10/25/50 ns.
- Control Function Latency -in us.
- PWM Switching Frequency - up to 2 MHz, 5 ns resolution.
- High-Speed I/O's.
- 96/128 user programmable IO's.
- Embedded Voltage, Current Sensors, PWMs, Analog I/O, Digital I/O and more.
- Flexible slot-based IO architecture.

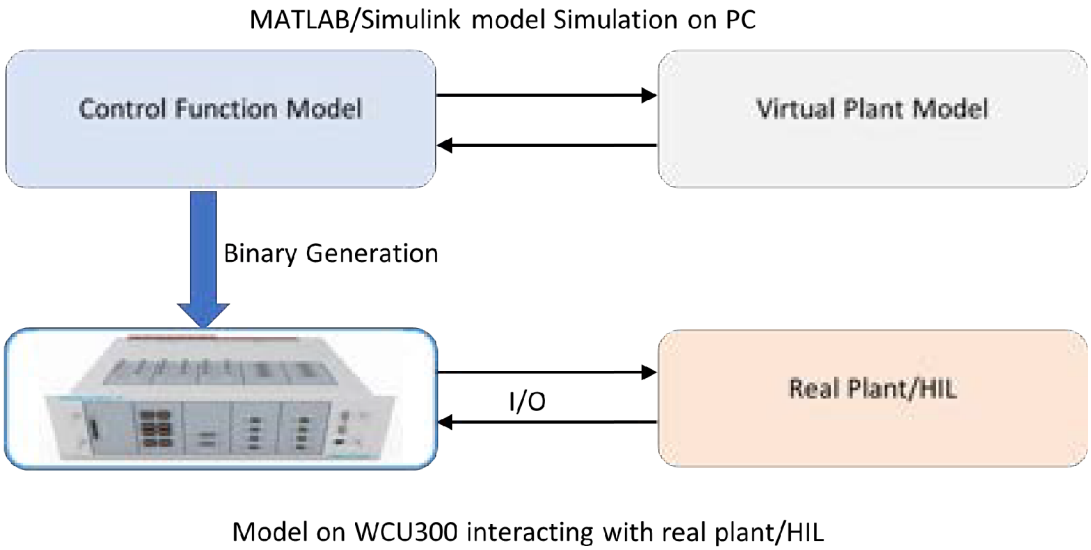

Figure 3.36: The real-time implementation of Waveact controller.

The execution diagram of the waveact controller and the model WU -300 interaction between the real-plant, Matlab/Simulink controller are shown in Figure 3.36. The model-based system is based on the following steps:

1. **Model** : MATLAB/Simulink HDL Coder and/or Xilinx System Generator(XSG) for Control Function modelling.
2. **Simulate**: Simulate the Control Function with the Plant Model and verify that model functionality is as expected.
3. **Build**: Single click Binary file generation for Control Function. No Manual coding (VHDL/Verilog/XDC) is required.
4. **Test**: Load generated Binary on WCU300 Controller with the help of WAVECT Suite and tested the model operation.

Figure 3.37: Testing platform for the proposed HESRM with hybrid excitation.

Figure 3.37 shows the testing platform for the proposed HESRM and the standard SRM. In this test, the machines are transformed only through the way the assigning winding is altered and how the windings are energized. For a conventional SRM, all the poles operate the switch and power the motor. After that, the proposed HESRM-allocated windings are excited in a way that is different from dc injection.

3.9.3 Dynamic Performance of HESRM without PMs

The dynamic performance of the conventional SRM and the proposed HESRM can be analyzed by enabling a closed-loop model. The experimental setup for both SRM drives is identical in all aspects and conditions. Conventional drive systems are

used for the analysis, while additional circuits provide excitation in the auxiliary. The motor has three hall sensors that are electrically separated by one twenty degrees. The three phases can be changed to run the motor using an asymmetric inverter stack. The control mechanism was enabled using Wavect, a universal rapid control prototyping platform for Motor Control Drives developed by Entuple Technologies, India. This FPGA-based controller implementation was developed to analyze real-time strategies that can be modeled, tested, and managed.

The current sensors in the wavect controller can obtain the instantaneous phase currents, and torque can be compared via an ADC channel. The primary advantage of this mechanism is the ability to compare current and torque simultaneously. Figure 3.37 depicts the rewinding structure with the testing platform. The waveform corresponds to the obtained moving torque and peak current when the motor is tested at various speeds and loaded to its peak current.

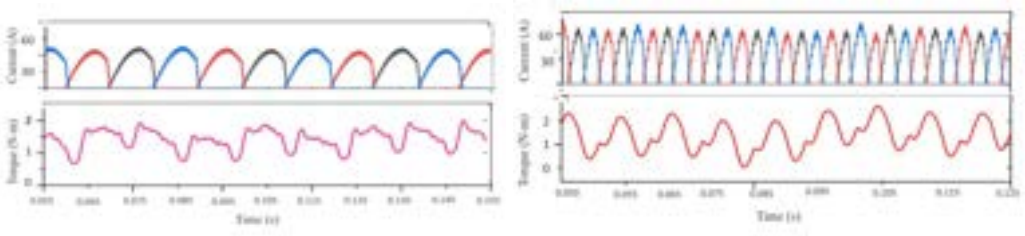

(a) (b)

Figure 3.38: Dynamic performance of conventional SRM with variable speed of (a) 1000 rpm and (b) 2500 rpm.

Figure 3.38 depicts the conventional SRM phase current and torque performance at 1000 and 2000 rpm. Figure 3.39 depicts the hybrid excitation method's auxiliary current and torque analysis. Different colors denote the three-phase current, and green indicates the auxiliary exciting current. In this method, the primary and secondary poles are excited simultaneously without injecting any currents; the performance matches the Ansys/Matlab software simulation results.

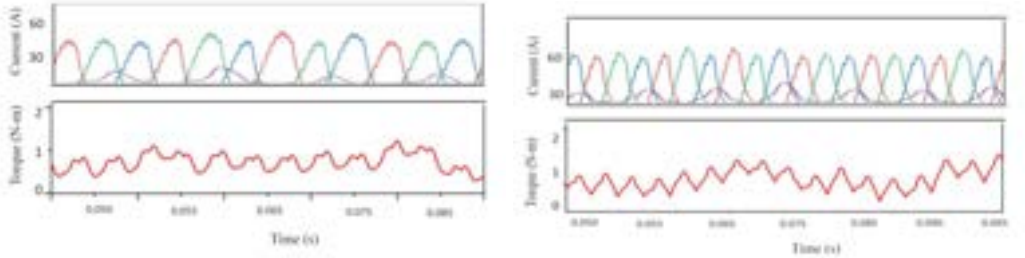

(a) (b)

Figure 3.39: Dynamic performance of proposed HESRM with variable speed of (a) 1000 rpm and (b) 2500 rpm.

The transient start-up response of the torque, phase current, and speed for two SRM drives with closed-loop control is tested and shown in Figure 3.40. The results under the same condition were evaluated with the dc-link voltage at 60 V and the load torque at 2 N−m, respectively. It was found that both SRMs similarly perform start-up, according to the switching scheme provided, and accelerate rapidly as per the commanded speed of 1000 rpm to rated 2500 rpm. They reach the time of 50 ms and 500 ms, respectively.

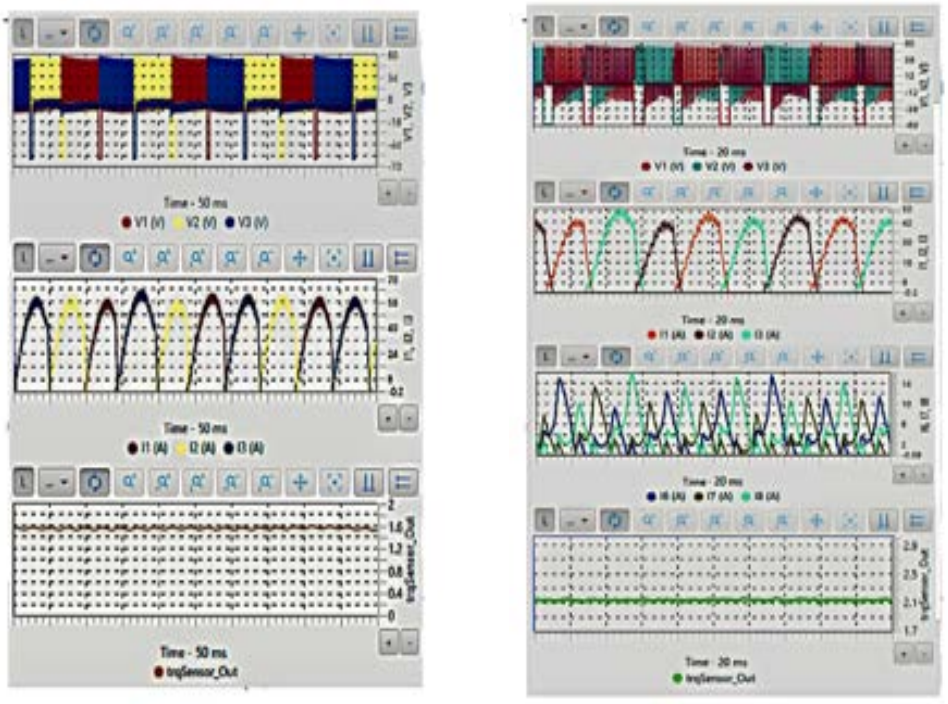

(a) (b)

Figure 3.40: Transient response of both SRMs at reference speed (a) Conventional SRM and (b) Proposed HESRM.

In other words, the speed changes from 500 rpm to 2500 rpm under closed-loop control and the gain parameter changes in a real-time manner to reach the commanded speed. The result shows the rotor speed tracks the command signal in all manner and achieves the substantial results obtained from the simulated one.

3.9.3.1 Auxiliary Current Injection Characteristics

The additional current injection for the variable speed characteristics is shown in Fig.3.41. For the speed from 500 rpm to 2500 rpm, there is an option to change the current from minimum to maximum value. Hence, there is a tendency to provide more flux. Thereby a chance to increase the electromagnetic torque.

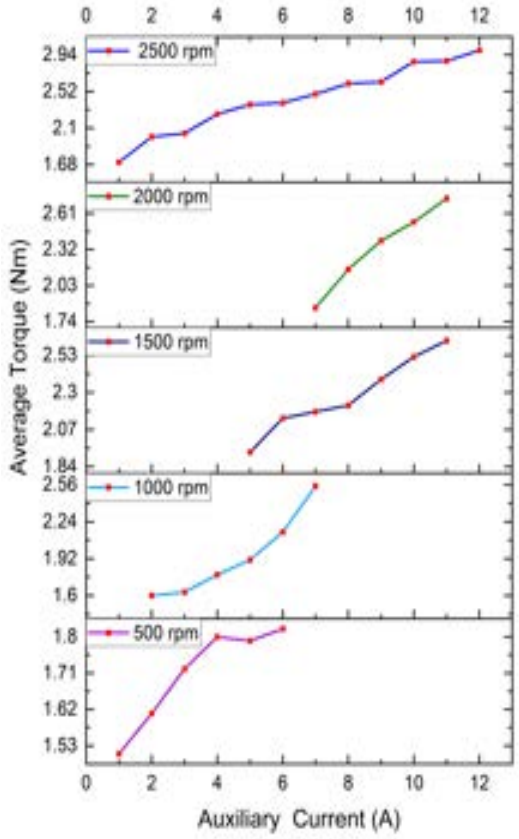

Figure 3.41: Characteristics of the auxiliary dc excitation for the proposed HESRM for different speeds.

3.10 Comparison of Hardware Solution with FEM Simulation Results

To validate the proof of concept with results from the software analysis and theoretical perdition, a 12/8 conventional SRM and a rewound SRM of the same size for the proposed method were prototyped and experimentally validated.

Figure 3.42 compares the measured and simulated average torque characteristics. The graphical analysis shows that the measured and simulated torque values are nearly identical. The average torque increased between 1000 and 2500 revolutions per minute.

In Figure 3.42a, at an initial speed of 1000 rpm, the average torque begins at 1.8 N−m. It increases exponentially as the effect of the auxiliary current varies. The variable-speed motors can adjust the auxiliary current from minimum to maximum to the rated value. Therefore, there is a tendency to provide more flux, thereby increasing the probability that the electromagnetic torque in the active region will increase.

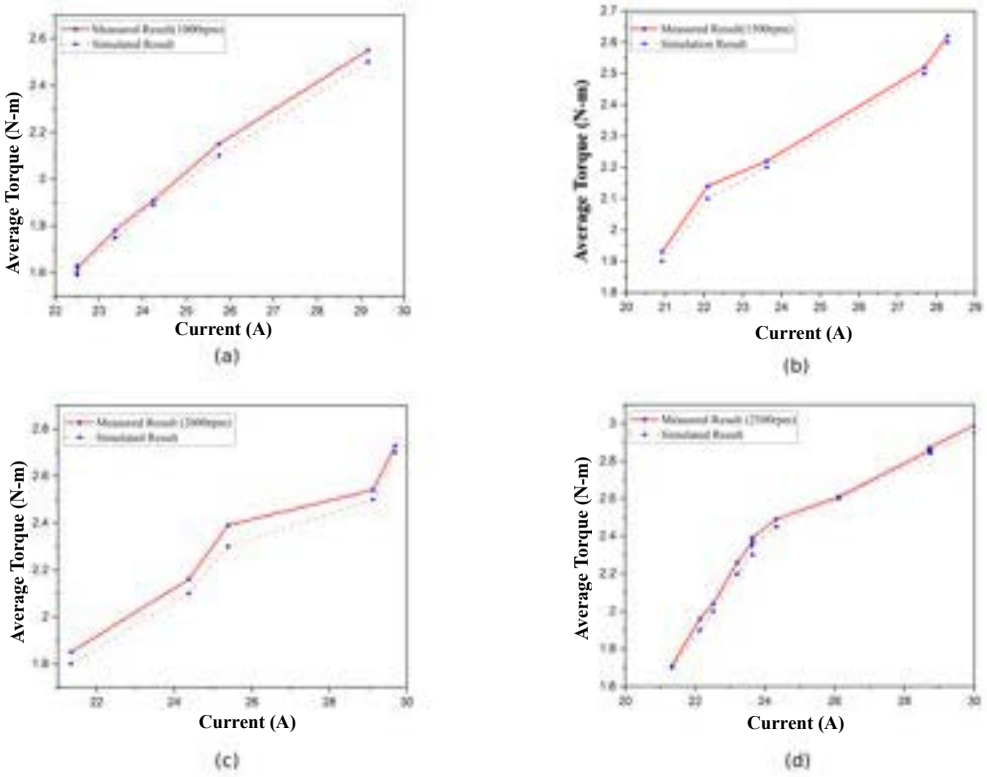

Figure 3.42: Average torque performance for variable speed of proposed HESRM: (a) 1000, (b) 1500, (b) 2000, and (d) 2500 rpm.

3.11 Comparison with Conventional SRM

Figure 3.43 compares the average torque between the conventional SRM and the proposed HESRM at various speeds. To demonstrate the benefit of this novel machine structure, the hybrid excitation without a permanent magnet is compared with two SRMs from the same platform. The average performances for the speed range vary from 1000 rpm to 2500 rpm, shown in different figures. At 1000 rpm, the torque is 2 N−m with the conventional current and excitation, while it reaches 2.5 N−m with the auxiliary. For this reason, there is a significant increase in torque performance, and the percentage of torque increase at all speeds is more significant than 20%. The pattern of torque response increase varies depending on speed and load.

3.12 Discussion

Figure 3.44a shows the plots of conventional and HESRM's average torque characteristics for various speeds. Both have a difference of 1 to 2 N−m at 500 rpm, and it gradually increases. The HESRM reaches almost 2.4 N−m at 1500 rpm, whereas the conventional one is only 2.1 N−m. The HESRM reaches a maximum torque of 2.6 N−m at 2500 rpm with a lead of almost 0.3 N−m.

The efficiencies for both SRMs were almost identical at the beginning of the

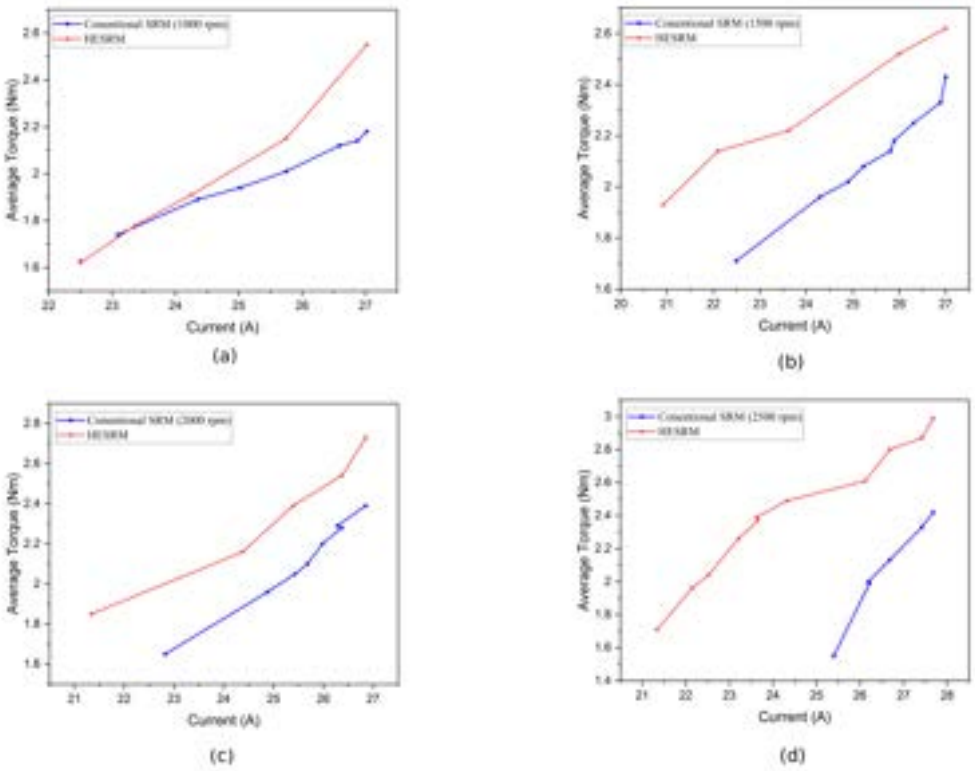

Figure 3.43: Comparison of average torque with variable speed for conventional SRM and proposed HESRM: (a) 1000, (b) 1500, (c) 2000, and (d) 2500 rpm.

test at 500 rpm. As speed increases, the efficiency of the HESRM makes clear leads compared with the conventional one. The speed reaches up to 1500 rpm, and the efficiencies of both motors follow a linear path with a difference of approximately 10%. At the rated speed of 2500 rpm, the efficiency of the motor differs to a maximum value of 80% and a minimum of 65%. The efficiency of the HESRM increased by 20%, as shown in Figure 3.44b.

The input power consumed by both motors is almost constant at 500 rpm, as seen in Figure 3.44c. As the speed increases, the input power consumed by the motors increases. The conventional SRM takes more power at all the respective rpm than the proposed one. At 1000 rpm, the conventional SRM draws almost 850 W, whereas the HESRM draws a minimum of 700 W. At maximum speed, the input power consumed has a difference of almost 50 W.

Torque ripple is one of the significant drawbacks of SRM, and hybrid excitation methods tend to provide higher possibilities. The proposed new HESRM without PM tends to exhibit less torque ripple than the conventional HESRM. In contrast, the conventional SRM exhibits a ripple of 3.72% at 2500 rpm, which decreases to 3.69% at 2000 rpm. Simultaneously, the proposed HESRM reduces torque ripple due to reduced pole switching, achieving 1.44% and 1.69% at 2500 and 2000 rpm, respectively.

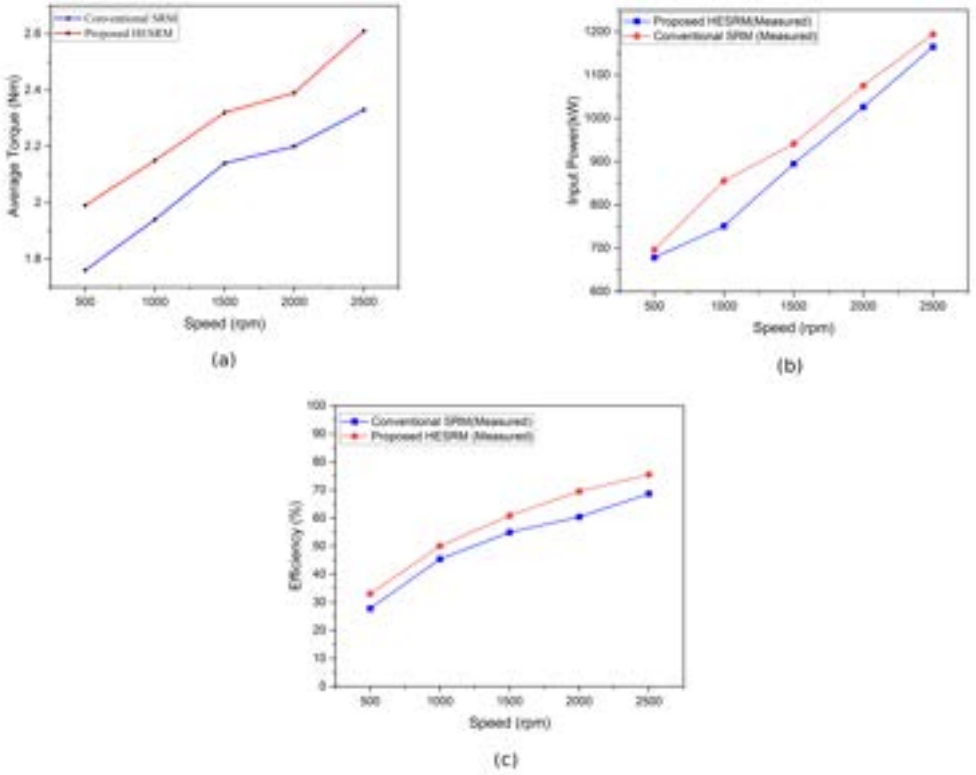

Figure 3.44: Comparison of conventional SRM with proposed HESRM: (a) Average torque, (b) Efficiency, and (c) Input power.

3.13 Inference: Topology I

When the average, static, and speed–torque characteristics of conventional and dc-injected hybrid SRMs are compared, it was found that HESRM significantly improved over conventional SRM. In addition, the properties and performance of the machines are improved without sacrificing their fundamental qualities. In addition to a high torque-per-ampere rating, it offers high efficiency, dependability, and redundancy. The standard SRM is outperformed by the proposed method, generating greater torque at significantly lower current levels. Furthermore, the proposed HESRM employs separate windings excitations, enhancing the controller's versatility.

The proposed topology may be a replacement for HESRM machines with PM insertion. Hence, this study demonstrates the enhanced performance of dual excitation, and the proposed system can be implemented in various applications, such as industrial and commercial. Moreover, improved average torque and smooth speed–torque characteristics have been accomplished, which can be an excellent solution for EVs. Finally, this new topology can achieve greater efficiency with torque ripple. This research's future objectives include designing and implementing advanced controllers to reduce torque ripples further.

3.14 Machine Topology II

This is another topology for switched reluctance motors to improve torque performance with the help of the hybrid excitation method. The torque developed is directly proportional to the flux produced in the air gap between the stator and rotor. When the flux intensity in this air gap increases, the torque output is directly improved. The flux path produced in the conventional SRM is large, which wastes a considerable amount of proper torque. This can be eliminated by creating a much smaller flux path, and the construction features are shown in Figure 3.45.

This can be achieved by choosing the poles accordingly to complete an entire path for the flux to flow. The main and auxiliary winding separated for the 1st prototyping can be arranged to create a short flux path. Alternate poles can be shorted together, building a short new path for the flux.

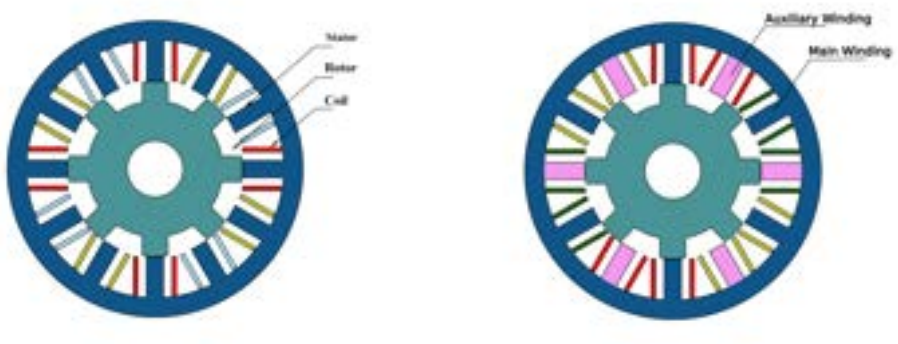

(a) (b)

Figure 3.45: Machine topology II of the new proposed HESRM with the same rating with 12/8-pole hybrid excitation of SRM without PMs (a) Conventional SRM (b) Proposed Topology II .

3.14.1 Software Analysis using FEM

The finite element analysis in the Ansys/Maxwell tool is used to find the software simulation for the proposed topology II. This analysis evaluated the performance of the hybrid excited SRM with PM excitation in the second topology of magnetic and static characteristics.

3.14.1.1 Magnetic Flux Distribution

This section shows the magnetic characteristics of conventional SRMs of aligned and unaligned positions. Both SRMs are given the same size, number of coils per pole and similar types of windings to obtain better clarity and ease of comparison. As

shown in Figure 3.46, the field lines of the stator and rotor iron have the shortest flux path and are very concentrated in the aligned position rather than the unaligned position.

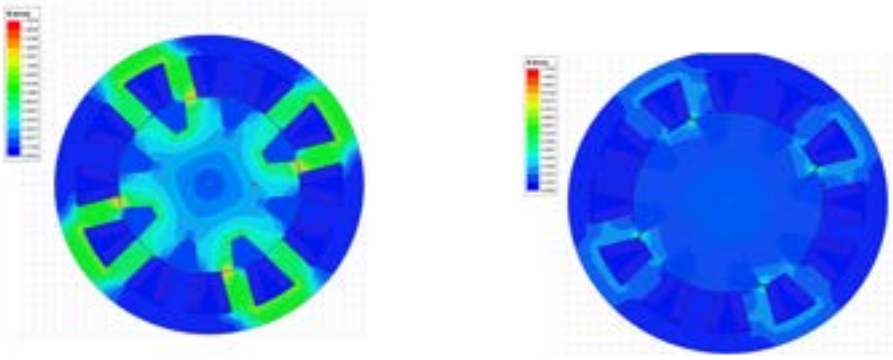

(a) (b)

Figure 3.46: Magnetic flux distribution for proposed HESRM: (a) Aligned position and (b) Unaligned position.

The magnetic characteristics of the proposed SRM are not similar to that of the conventional SRM; due to the auxiliary pole's excitation, the flux path is reduced. Here, the quantity of the flux lines will increase as more current is injected into the auxiliary poles. As a result, the effective flux lines in the air gap increase, and the resultant electromagnetic torque increases.

3.14.1.2 Static Electromagnetic Torque Analysis

The static torque of the conventional SRM is analyzed and plotted for different rotor positions. The static torque initially increases to a peak value and then decreases eventually. The separately dc-injected SRM shows the exact characteristics of the conventional SRM, but the peak rises as the input dc increases.

In the conventional SRM, the static torque is plotted by varying the position of the rotor from unaligned to aligned, as shown in Figure 3.47a, under standard conditions. Analyzing Figure 3.47b shows a substantial increase in static torque is experienced as the input dc is injected. It peaks from 80 N-m to 140 N−m due to increased dc from 10 A to 30 A, respectively.

3.14.2 Experimental Validations

3.14.2.1 Motor Prototype

The torque characteristic of the SRM is the critical parameter that needs to be measured. To produce these characteristics, a back-to-back motor setup is established with a torque sensor coupled in between. The motor used at the load side is a 1.5

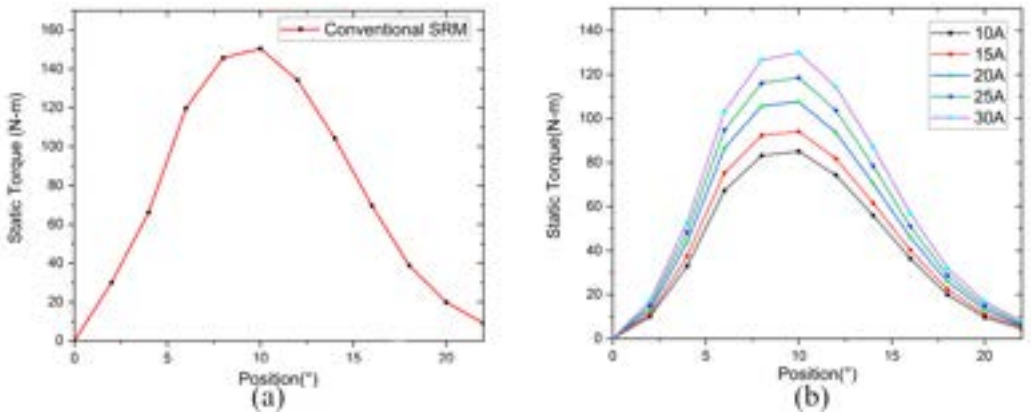

Figure 3.47: Static torque characteristics (a) Conventional SRM at rated current 15 A. (b) HESRM under various current excitation at the auxiliary coils.

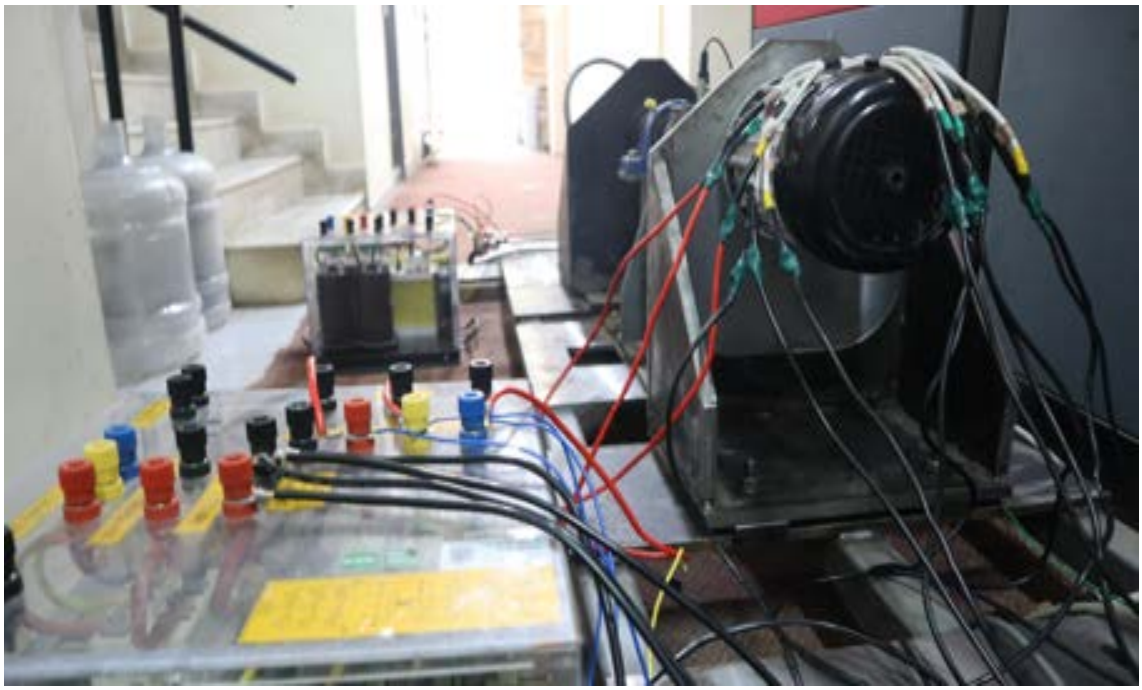

Figure 3.48: Testing platform for the proposed HESRM with separate excitation for auxiliary.

kW permanent magnet synchronous machine rated 5000 rpm. This motor is tightly coupled with the plant motor.

Figure 3.48 shows the testing platform for the proposed HESRM with separate excitation for an auxiliary winding. For assigning the auxiliary windings to different topologies, the windings are chosen to give to the specified excitation.

3.14.2.2 Dynamic Performance Analysis

3.14.2.2 .1 Moving Torque Characteristics The dynamic torque characteristics of conventional and HESRM are shown in Figure 3.49 and 3.50. The HESRM

produces much higher torque than conventional SRM, which is almost 1 to 1.5 newton−meter at rated rpm. In contrast, the torque ripple increased to 6%. The evident increase in average torque justifies the increase in torque ripple in HESRM, which can be further reduced using additional structural changes.

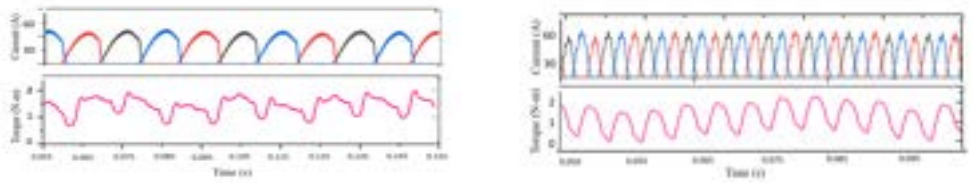

(a) (b)

Figure 3.49: Dynamic performance of conventional SRM variable speed (a) 1000 rpm (b) 2500 rpm.

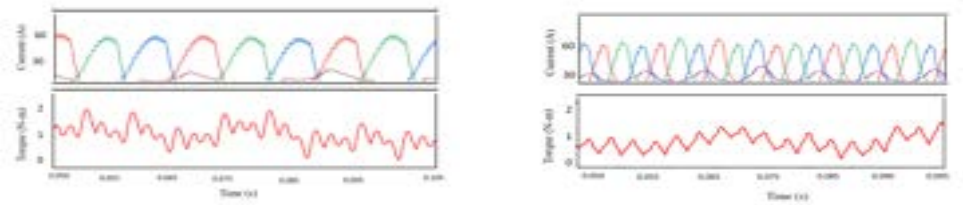

(a) (b)

Figure 3.50: Dynamic performance of proposed HESRM II variable speed (a) 1000 rpm (b) 2500 rpm.

3.14.2.2 .2 Auxiliary Current Injection Characteristics The additional current injection for the variable speed characteristics is shown in Figure 3.51. For the speed from 500 rpm to 2500 rpm, there is an option to change the current from minimum to maximum value. Hence, there is a tendency to provide more flux. Thereby chance to increase the electromagnetic torque.

3.15 Comparison of the Results of Software and the Hardware

The comparison between Ansys/Maxwell and hardware results of the conventional SRM at various speeds is shown in Figure 3.52. The results show similar characteristics compared to the slightly leading hardware results.

Comparing the hybrid excitation of SRM in topology II for different speeds with software results from Ansys/Maxwell and the experimental results for the average torque are almost identical. The results are analyzed for various speeds from 500

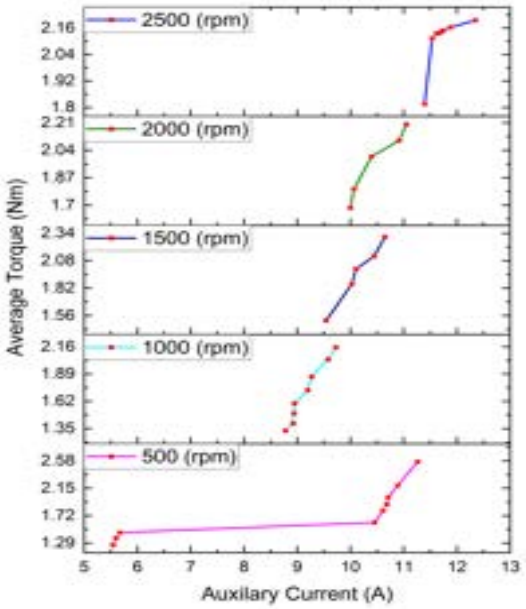

Figure 3.51: The auxiliary dc excitation characteristics of topology II HESRM for different speeds.

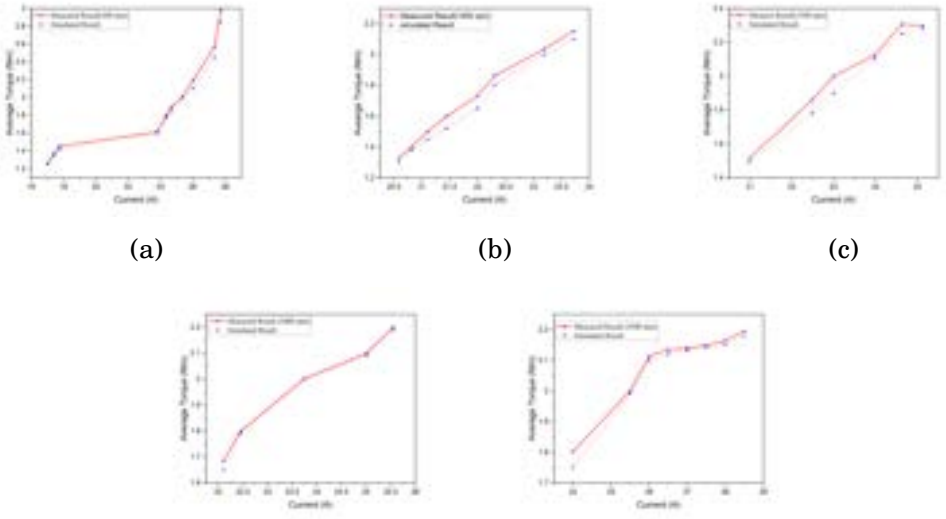

(a) (b) (c)

(d) (e)

Figure 3.52: Average torque performance for topology II HESRM: (a) 1000, (b) 1500, (c) 2000, and (d) 2500 rpm.

to 2500 rpm. The average torque concerning current at all ranges of speed shows a steady increase in the value as the current increases. For all the speed cases, within the rated current, the proposed motor attains maximum average torque that is more than the rated torque of the machine.

3.16 Comparison with Conventional SRM

The comparison between the hardware results of the conventional SRM and HESRM at various speeds is shown in Figure 3.53. While comparing the graphs from 500 rpm to 2500 rpm, the average torque is more for HESRM every instant. The average torque increases as the speed increases, peaking at a maximum of 2.99 N−m. Due to the injection of more current to the auxiliary, the range of torque production also expands.

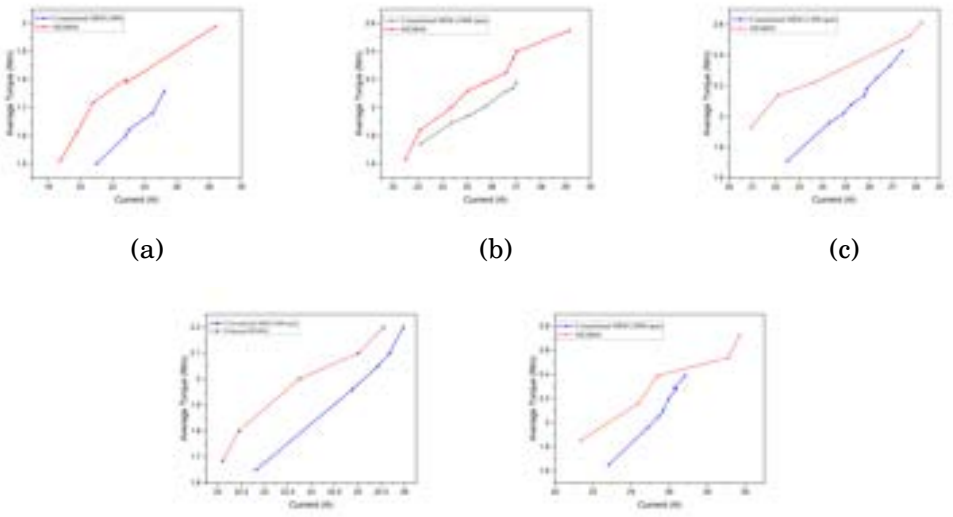

(a) (b) (c)

(d) (e)

Figure 3.53: Comparison of average torque of conventional SRM and proposed HESRM for different speeds: (a) 1000, (b) 1500, (c) 2000, and (d) 2500 rpm.

The average torque characteristics shown in Figure 3.53 is the comparison between conventional SRM and HESRM. Here, it is evident that the average torque has improved at all current ranges, starting from 0 A to 30 A. Both graphs start from zero, but HESRM shows evident lead as the current increases. At 15 A, the torque increases to a maximum of 1.5 N−m and saturates at 30 A. In Figure 3.53, the average torque of both the SRMs is compared concerning the speed, ranging from 500 to 2500 rpm. At lower speeds, the average torque of the HESRM shows 2 N−m compared to 1 N−m for the conventional. At higher speeds, the torque reduces for both machines with a 2.99 N−m lead at 2500 rpm.

3.17 Discussion

3.17.1 Speed- Torque Characteristics

Figure 3.54 plots the average torque characteristics of conventional and HESRM for various speeds. At 500 rpm, both have a difference of 1.8 N−m and decrease as it

gradually progresses. At 1500 rpm, the HESRM reaches almost 2.25 N−m, whereas the conventional is only 2.1 N−m. During 2500 rpm, the HESRM tops 2.45 N−m with a lead of almost 0.75 N−m.

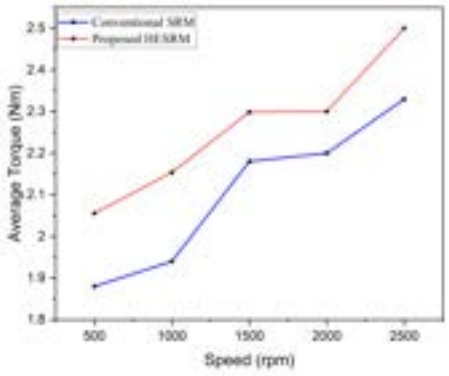

Figure 3.54: The comparison of average torque for conventional and proposed SRMs with variable speed.

3.17.2 Speed -Efficiency Characteristics

The efficiency plot of the conventional and proposed SRM is shown in Figure 3.55. Both motors' efficiencies are almost identical at the beginning of the test at 500 rpm. As speed increases, the efficiency of the HESRM makes clear leads compared to the conventional one. With the speed up to 1500 rpm, the efficiencies of both motors follow a linear path with a difference of approximately 10% to 15%. At the rated speed of 2500 rpm, the efficiency of the motor differs to a maximum value of 85 and a minimum of 62. The efficiency of the HESRM has increased by 42%.

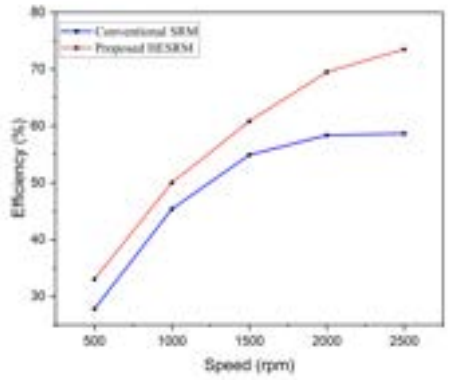

Figure 3.55: The efficiency comparison for conventional and proposed SRMs with variable speed.

3.17.3 Speed- Input Power Characteristics

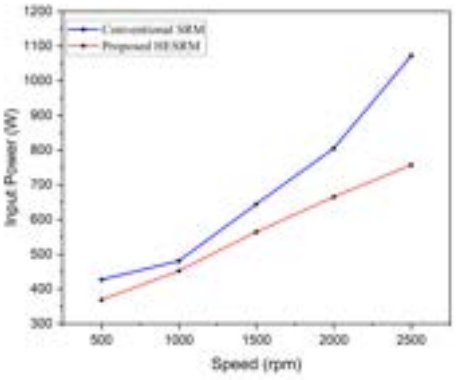

Figure 3.56: The comparison of input power for conventional and proposed SRMs with variable speed.

The input power comparison of conventional and proposed HESRM is shown in Figure 3.56. The input power consumed by both motors is almost constant at 500 rpm. As the speed increases, the input power consumed by the motors starts to increase. The conventional SRM takes more power at all the respective rpm than the proposed one. At 1000 rpm, the conventional SRM draws almost 450 W, whereas the HESRM draws a minimum of 300 W. At maximum speed, the input power consumed has a difference of almost 100 W.

3.18 Inference: Topology II

The new topology of HESRM enhances the performance in all aspects compared to conventional SRM and HESRM topology I. The controllable flux that can be generated in this proposed method is higher without using PMs or sacrificing the structural integrity of the SRM. Comparing the two HESRM topologies indicates that the HESRM II has better static and dynamic performance than the HESRM I, such as higher average torque, more extensive power and torque density. Additionally, the average torque value produced by the HESRM without PMs at the low, medium, and high-speed operations is more prominent than those of conventional SRM. Hence, it can be efficiently used in electric vehicle applications.

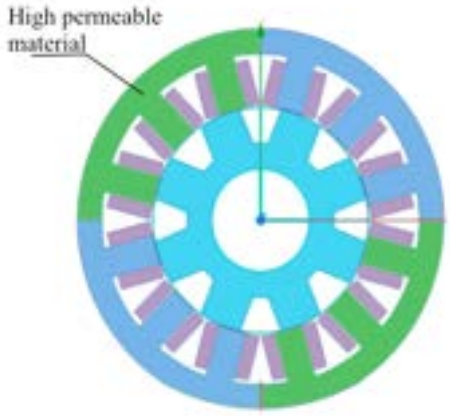

Figure 3.57: The isolated poles are changed to high permeable material in SHESRM.

3.19 Machine Topology III

3.19.1 Case (i): Segmenting the Auxiliary Core (SHESRM)

A high permeable material replaces the auxiliary poles and associated stator back iron as structured, as shown in Figure 3.57. This enhances the effective flux generated in the motor. When the stator is segmented and assigned with new materials with high permeability, the flux density becomes saturated through the back iron. This restricts flux from flowing through the air gap, decreasing the maximum average torque. To avoid this condition, the diameter of the stator back iron is increased to decrease the flux density and thereby enhance the total flux. This enhances the efficiency of the high permeability material to provide more flux, and the new back iron provides the path. Thus, using this method, the average flux can be further improved considerably with segmented HESRM (SHESRM).

3.19.1.1 Result and Discussion

3.19.1.1.1 Magnetic Field Distribution The magnetic field generated within the motor is responsible for the developed electromagnetic torque. Increasing the magnetic fields generated by the windings can increase the air gap flux. A material's flux density (B) is directly proportional to the applied magnetizing force (H). In other words, the flux density increases as the magnetizing force increases, and vice versa. The B-H curve can determine each material saturation limit for transporting flux. Therefore, in this method, the material in the stator is changed to a highly permeable material to transport more flux, increasing output torque. The magnetic flux path produced in this topology can be observed in Figure 3.58.

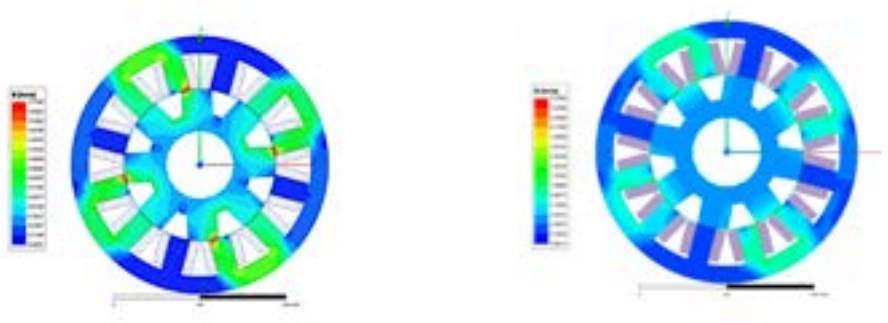

(a) (b)

Figure 3.58: Magnetic flux density of SHESRM when stator poles are (a) Aligned and (b) Unaligned.

3.19.1.1.2 Static and Average torque The average torque values of this method show a slow rise in its value from 8 to 10 N−m when the current increases from 10 to 40 Ampere, are shown in Figure 3.59a. The static torque of the machine with the

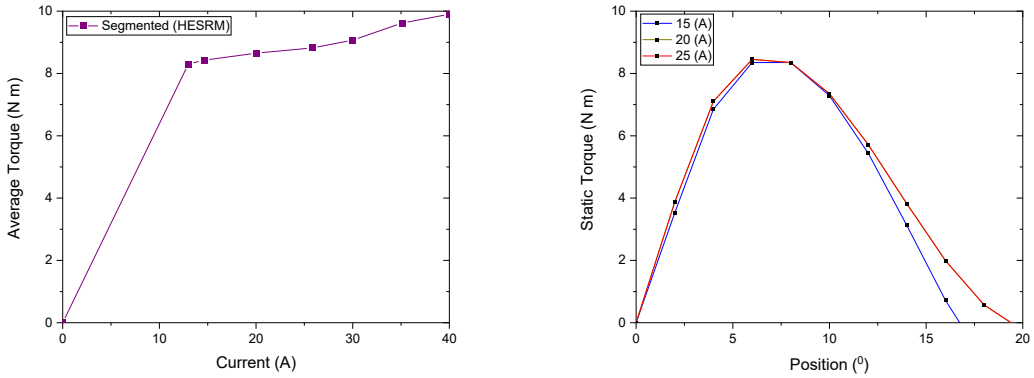

(a) (b)

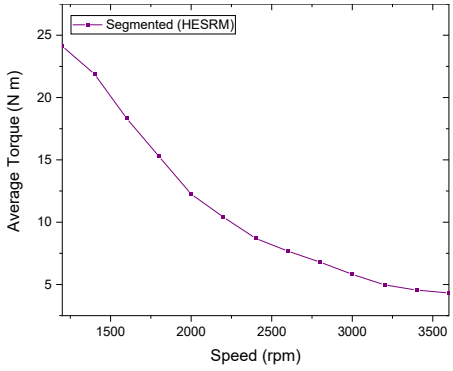

(c)

Figure 3.59: The results of segmented hybrid excited SRM (SHESRM) with non-PMs (a) Current versus average torque (b) Static torque versus position of the rotor and (c) Speed- Torque characteristics.

new high-permeable material follows the same as that of the conventional machine, which peaks up to 8 N−m of torque at all current ranges, illustrated in Figure 3.59b.

Figure 3.59c shows the torque output at a speed less than 1500 rpm is a maximum of 25 N−m, which declines to almost 5 N−m at a maximum speed of 3500 rpm.

3.19.1.2 Comparison with Conventional SRM Figure 3.60 compares this third topology and the conventional SRM. Figure 3.60a compares conventional, proposed, and segmented SRMs regarding current versus average torque. To reach a maximum of 5 N-m, the proposed method takes almost the same route. The proposed method will reach the maximum value quicker than the conventional method. This segmentation and the replacement of materials of auxiliary poles in the stator, particularly the auxiliary poles, increase flux production. This flux accounts for the electromagnetic torque produced by the motor. Consequently, the segmented machine's average torque increases significantly. It reaches a maximum of 9 N-m and reaches saturation after drawing about 20 A. This occurs because the iron core of the primary poles becomes saturated.

Upon analyzing the speed-torque characteristics of these topologies in Figure 3.60b, it is evident that the segmented SRM exhibits significantly superior torque about speed, producing a maximum of 50 N-m of torque during startup, which drops to approximately 10 N-m at top speed. The torque produced by the other methods varies from approximately 20 to 5 N-m across the entire speed range, which is much lower than the segmented SRM.

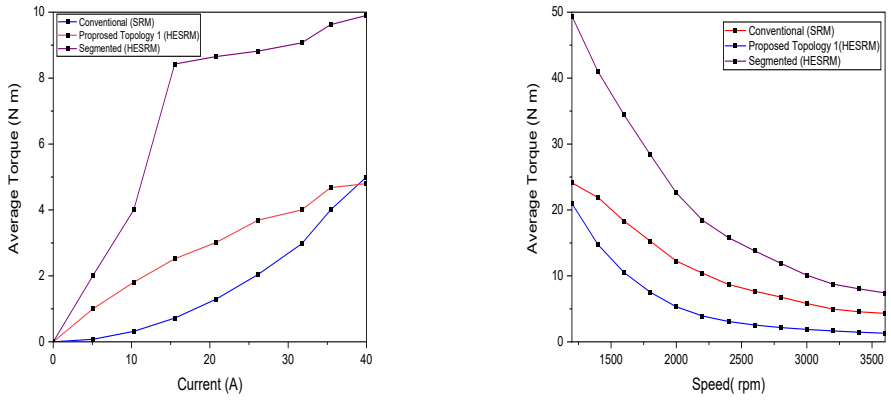

(a) (b)

Figure 3.60: Comparison of average torque for the three topologies (a) Current-Torque characteristics (b) Speed-Torque characteristics .

3.19.2 Case (ii) By Changing Stator Outer Diameter

The assigning of highly permeable materials will result in high flux density. Since the stator back iron is still less permeable, these new flux lines will be saturated. To provide more paths for the flux to travel, the stator outer diameter (OD) is adjusted, as shown in Figure 3.61. There are two cases for changing the diameter of the stator core. Case (i) Segmenting the auxiliary pole and varying the outer diameter. Case (ii) Varying the outer diameter and segmenting the auxiliary core.

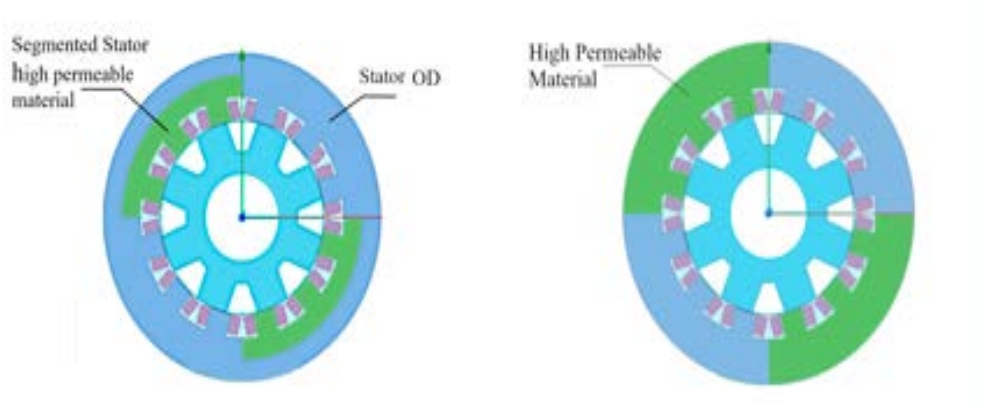

(a) (b)

Figure 3.61: Segmenting the auxiliary core for changing the stator outer diameter (a) Case (i) and (Case (ii)).

As discussed during the development of SHESRM, the stator iron's low permeability resulted in the saturation of the flux. Consequently, it is essential to provide sufficient space for the flux to flow. In the first method, as shown in Figure 4.48 a, the stator's segmented portion is maintained while the diameter increases. As the area increases, more flux can flow, boosting upward torque. This method is superior because the torque can be increased with less expensive, high-permeability material than conventional steel.

The second method also improves the flux flowing through the stator. In contrast to the previous method, the stator's outer diameter is expanded, and the auxiliary poles are segmented. Because of the higher incorporation of highly permeable material, the output characteristics of this method are comparatively higher. This method is considerably more expensive than its predecessor.

3.19.2.1 Result and Discussion

3.19.2.1.1 Magnetic Flux Density and Intensity The magnetic flux density analysis produced in the stator of case (i) can be observed in Figure 3.62. The development and flow of flux and field lines indicate the flux direction. By analyzing the magnetic flux density depicted in this case (ii) in Figure 3.63, it is evident that

the flux paths utilize the entire stator core, beginning at the auxiliary poles and spreading throughout the iron. The field lines indicate the flux's path within the stator iron.

Based on the software analysis of both cases, it is observed that case (ii) generates a more significant amount of electromagnetic torque. The output will continue to improve with increasing impregnation of highly permeable material into the stator. Despite these qualities, the machine will be considerably more expensive to manufacture.

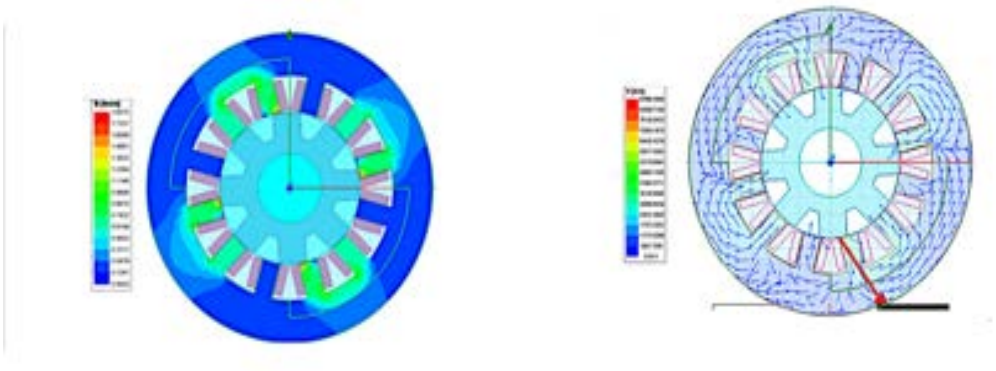

(a) (b)

Figure 3.62: Segmenting the auxiliary core for changing the stator outer diameter, case(i): (a) Magnetic flux density and (b) Magnetic field lines.

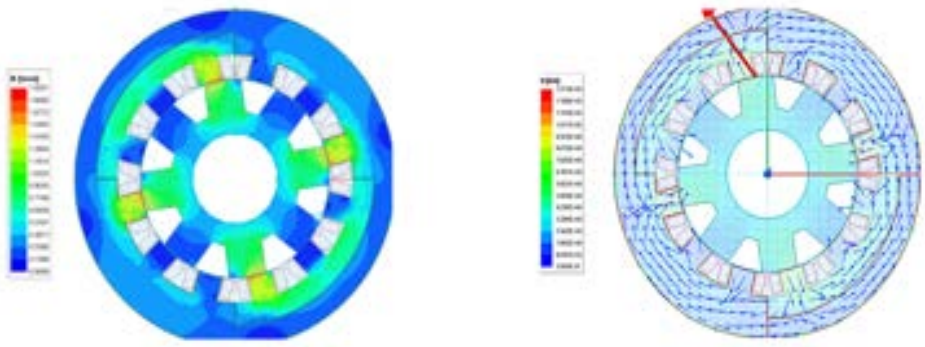

(a) (b)

Figure 3.63: Segmenting the auxiliary core for changing the stator outer diameter, case(ii): (a) Magnetic flux density and (b) Magnetic field lines.

3.19.2.1.2 Average Torque Figure 3.64a illustrates the average torque characteristics concerning the current. These characteristics rise to a maximum value of 4.5 N-m when the current is 30 A. As the amount of current the machine draws increases, there is a gradual linear increase in the torque.

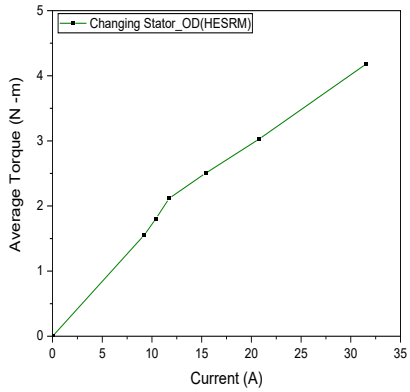

(a)

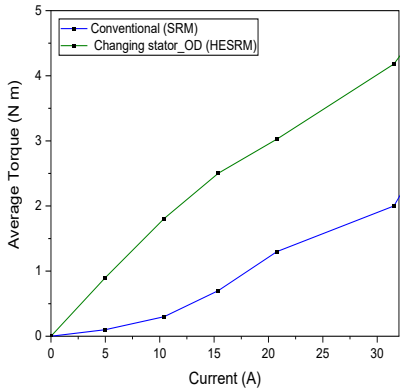

(b)

Figure 3.64: Average torque characteristics of changing stator OD and the results compared with conventional SRM (a) Torque-current characteristics of both cases (b) Comparison of average torque.

When the machine operates in its rated condition and draws 15 amperes of current, the conventional SRM produces almost 1 N-m of torque, whereas the new method produces up to 2.5 N-m. This is shown in Figure 3.64b, which compares the average torque produced by changing the stator outer diameter and conventional SRM. Both machines exhibit a noticeable gap of 2 N-m when loaded to their maximum capacity.

3.19.3 Case (iii) Adding Active Poles

The switched reluctance motor employed in this study is a 12/8 motor having 12 stator poles and 8 rotor poles. According to the methodology, half of these poles are separated and isolated so that each phase receives an equal amount of poles. In this instance, each phase consists of four poles, of which two are designated auxiliary poles. As a result of the limitation of the auxiliary poles to two per phase, the current injected through them will be constrained.

For motors with a more significant number of poles, such as 24/16 or 36/24, more primary poles can be used as auxiliary poles, as structured in Figure 3.65, allowing for the injection of more current. The motor's performance may be enhanced despite the structural challenges involved in its production. Since the width of the auxiliary poles is relatively less, the torque ripple is also significantly reduced.

3.19.3.1 Result and Discussion

Examining the torque current characteristics of various machines with increased stator poles indicates that increasing the number of poles will improve the motor's torque output, as shown in Figure 3.66. The 46/32 SRM produces the most torque,

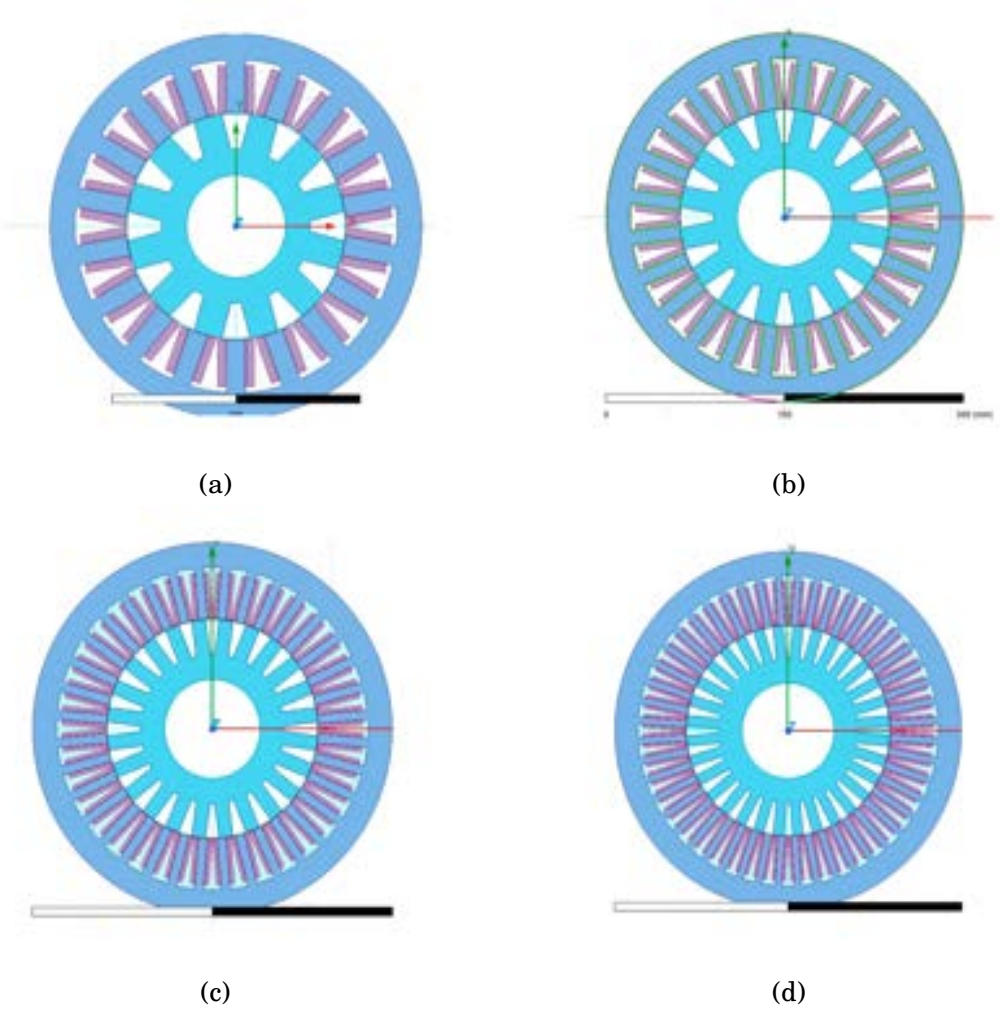

(a) (b)

(c) (d)

Figure 3.65: Adding stator and rotor poles for improving active poles to 25% to 75% : (a) 18/12 (b) 24/16 (c) 36/24 (d) 46/32 poles .

while the 12/8 SRM produces the least, with the variation in output ranging from 5 to 35 N-m. The uniformity of the model's attributes indicates that the machine's performance will remain the same despite the increase in torque output.

3.20 Inference: Topology III

Increasing the outer diameter of the stator can lead to an increase in the amount of magnetic flux produced by the windings, which can increase the motor's torque output. Moreover, this method reduces the cogging torque of the motor, which is the pulsating torque that can occur due to the interaction between the rotor and stator poles. The permeability of the stator material is an essential factor that affects the performance of the SRM. A higher permeability material can increase the field windings' magnetic flux, leading to higher torque output. In conclusion, these modifications can reduce the losses that occur in the motor, improve the motor's

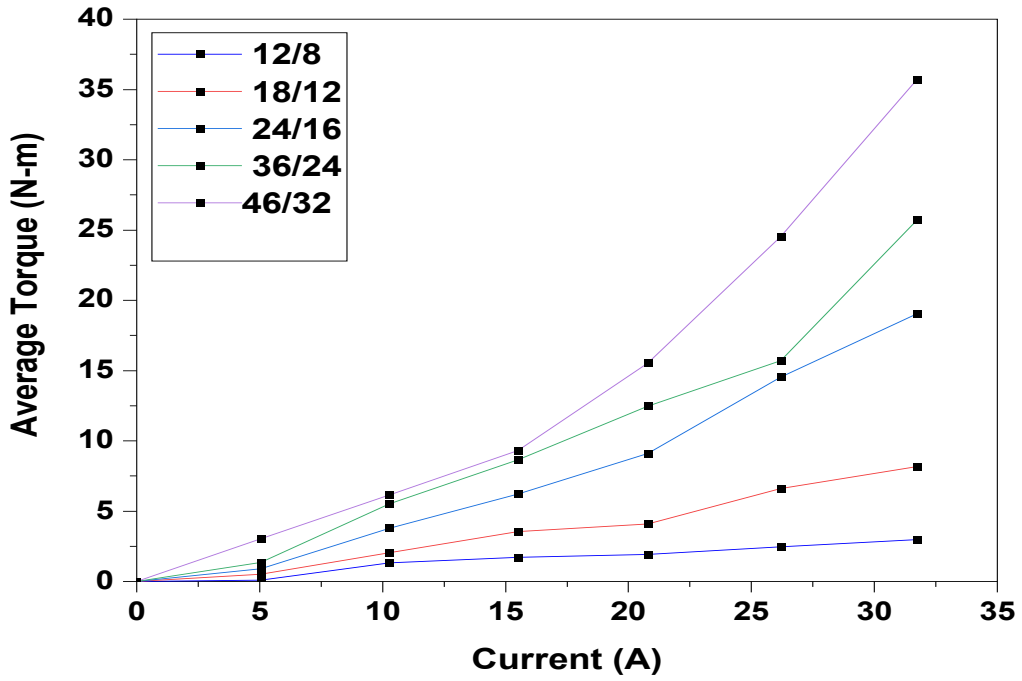

Figure 3.66: Comparison of average torque of SRMs added active poles.

efficiency, and boost the machine's torque performance in the SHESRMs.

Increasing the number of poles can increase the rotor-stator pole pairs, generating higher torque output. Thus, adding poles can result in a smoother motor operation with higher active poles. The percentage of active and auxiliary poles in the proposed HESRMs are the same. Furthermore, this topology strengthens the torque profile by adding the main poles. The poles are only added to the active poles, and there are always two auxiliary poles for each phase. When the percentage of active poles increases, the average torque rises while the torque ripple declines.

3.21 Comparison of Different Topologies

Table 3.7 Compares conventional SRM and average torque, efficiency, and input power of different proposed topologies. The SRM produces an average of 3.08 N-m of torque at 2500 rpm; therefore, it's evident that its performance improves as the speed increases. Topology II provides the added benefit of alternating poles, which creates the shortest flux path. Consequently, the torque output will be more significant than topology I. Due to this, the efficiency likewise goes way up when utilizing the second method. The current drawn by the motor directly correlates with the motor's efficiency. Topology II consumes less current in all speed ranges than the standard topology, which consumes the most power. As previously indicated, the formation of the shortest flux path in the second topology by the excitation of alternate poles, torque ripple, will increase. To achieve better outcomes, the ripple content must be

Table 3.7: Comparison of average torque with conventional SRM and topology I and II of HESRM.

Sl.No	Speed (rpm)		Average Torque (N m)	Percentage of Increase (%)	Efficiency (%)	Percentage of Increase (%)	Input Power (kW)	Percentage of Decrease (%)
1	500	Conventional SRM	1.88		28.37		543.67	
2		Topology 1	1.99	**5.85%**	29.47	**27.27%**	480.03	**11.70%**
3		Topology 2	2.13	**13.29%**	38.09	**34.26%**	430.25	**20.86%**
4	1000	Conventional SRM	2.18		40.38		662.86	
5		Topology 1	2.55	**16.97%**	47.67	**18.05%**	557.65	**15.87%**
6		Topology 2	2.65	**21.55%**	51.28	**26.99%**	465.89	**29.71%**
7	1500	Conventional SRM	2.43		56.25		722.93	
8		Topology 1	2.62	**7.81%**	61.4	**9.15%**	702.73	**2.79%**
9		Topology 2	2.86	**17.69%**	66.85	**18.84%**	603.88	**16.46%**
10	2000	Conventional SRM	2.39		59.25		858.3	
11		Topology 1	2.73	**14.22%**	67.92	**14.63%**	832.16	**3.04%**
12		Topology 2	2.97	**24.26%**	72.27	**21.97%**	708.02	**17.50%**
13	2500	Conventional SRM	2.42		58.68		1167.02	
14		Topology 1	2.99	**23.55%**	77.57	**32.19%**	1089.34	**6.65%**
15		Topology 2	3.08	**27.27%**	85.32	**45.39%**	976.82	**16.29%**

significantly reduced.

3.22 Comparison with Existing Methods

Figure 3.67 compares the average torque and efficiency of the HESRM with conventional, hybrid, and segmented SRM methods, both with and without permanent magnets. Compared to the other methods, the hybrid excited SRM does not require permanent magnets to deliver the highest possible average torque while maintaining the highest possible efficiency. By utilizing this technique, it is possible to achieve values of up to 3 N-m and an efficiency of more than 80%. The HESRM uses permanent magnets and has an efficiency of 70 percent and torque of 2.25 N-m. The remaining methods are not as effective and only produce minimal torque at the output.

In conclusion, HESRMs have a greater torque output than conventional SRMs due to the additional excitation, which increases the motor's power density and speed range by generating additional magnetic flux. The HESRM can achieve higher efficiencies in all speed ranges due to its lower input power consumption.

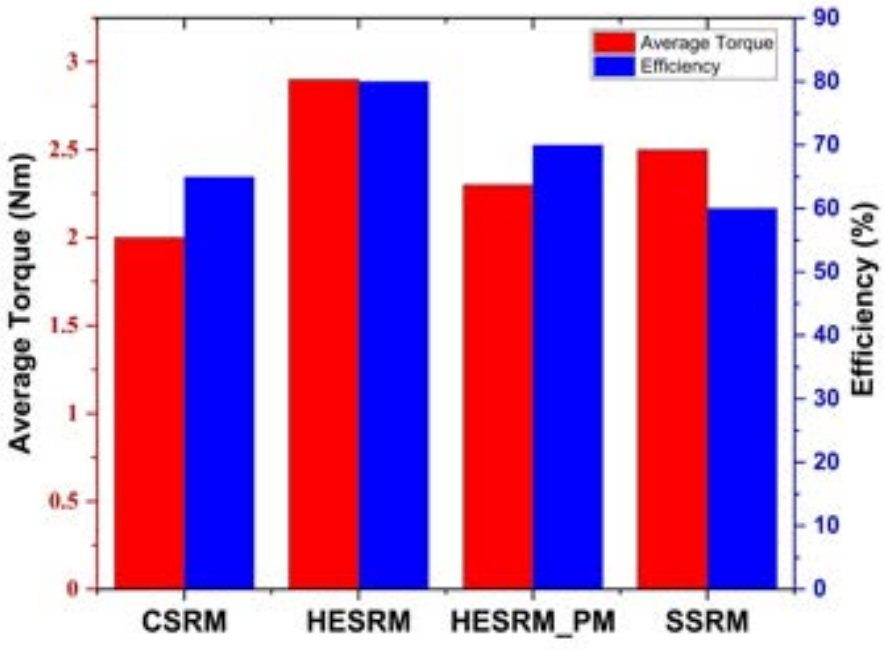

Figure 3.67: Comparison of average torque with existing methods.

3.23 Conclusions

In conclusion, the research on the new hybrid excitation of switched reluctance motors without permanent magnets demonstrated its potential as a high-performance and cost-effective solution for various applications. The new SRM design was found to have improved average torque output compared to conventional SRMs due to the absence of permanent magnets. The isolation of poles and dc injection of current to the auxiliary windings aided the creation of more flux, producing more output torque.

The second topology increases the output torque further due to introducing the shortest flux path in the motor. However, the high level of torque ripple was also observed in the new SRM design, which can negatively impact the performance and reliability of the motor. This issue is addressed in the following chapters by enabling different topologies to suppress the ripple produced.

CHAPTER 4

TORQUE RIPPLE REDUCTION IN HESRMS

This chapter describes the hybrid excitation topology for a switched reluctance motor that improves torque performance and reduces torque ripple for electric vehicle applications. The described topologies, however, provide high average torque with ripple. For this purpose, introduce the methodology to minimize the torque ripple by advancing the switching phase current on and off time with the help of the torque ripple minimization method. For instance, analyze both topologies in software and validate the results using the hardware implementation. The findings demonstrate that the new HESRM without permanent magnet excitation topology can produce more electromagnetic torque with minimal ripple. The torque ripple minimization of conventional SRM is detailed in 4.16a, and the different topology ripple minimizations are explained in 4.5 and 4.5, respectively.

4.1 Objective 3: Torque Ripple Reduction in HESRMs

4.1.1 Principle of Operation

The block diagram shown in Figure 4.1 for the proposed HESRM illustrates the dual excitation principle for the main and auxiliary winding. As per the switching scheme, the commutation table is generated for the PWM signal to switch the phase of the motor [138]. The main windings controller is purposed to give the motor the proper switching direction. At the same time, the auxiliary circuit is designed for the injection of dc as per the torque requirement. Thus, the more current injection in the auxiliary windings has generated more flux; hence, the total sum of electromagnetic

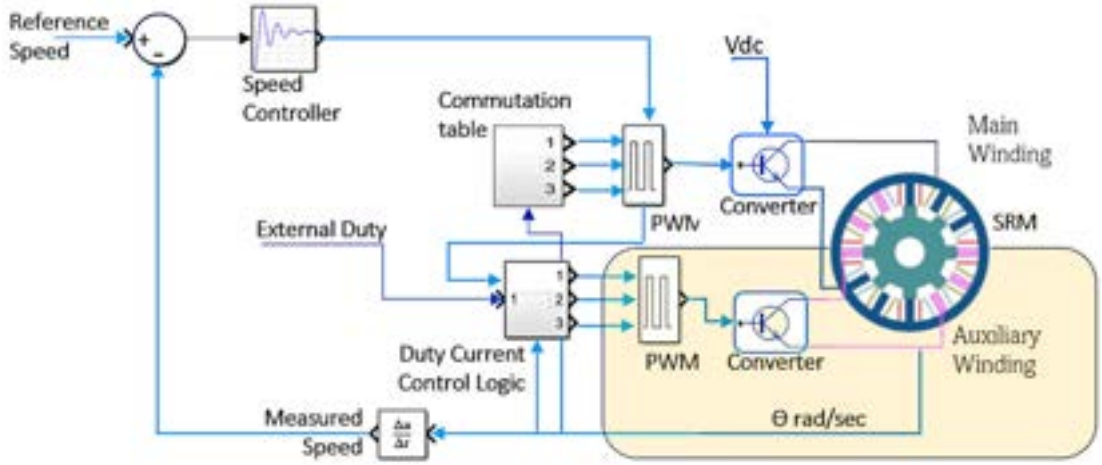

Figure 4.1: Block diagram for the proposed HESRM without PMs excitation.

flux produced by the two windings exhibits more electromagnetic torque.

The block diagram in Figure 4.2 explains that the torque ripple minimization method executes in the proposed HESRM. In this approach, the phase advancing method is incorporated with the new topology of HESRM. This is achieved by reducing the time between the on, and off-phase excitation of each switching [84]. For this purpose, the rotor rotation angle (θ) changes the Turn-on and Turn-off time to deduct the switching delay time. It is given to the controller to accomplish the regular operation. Due to this, the torque ripple minimization occurred during a wide speed range with maximum torque capability [139–142].

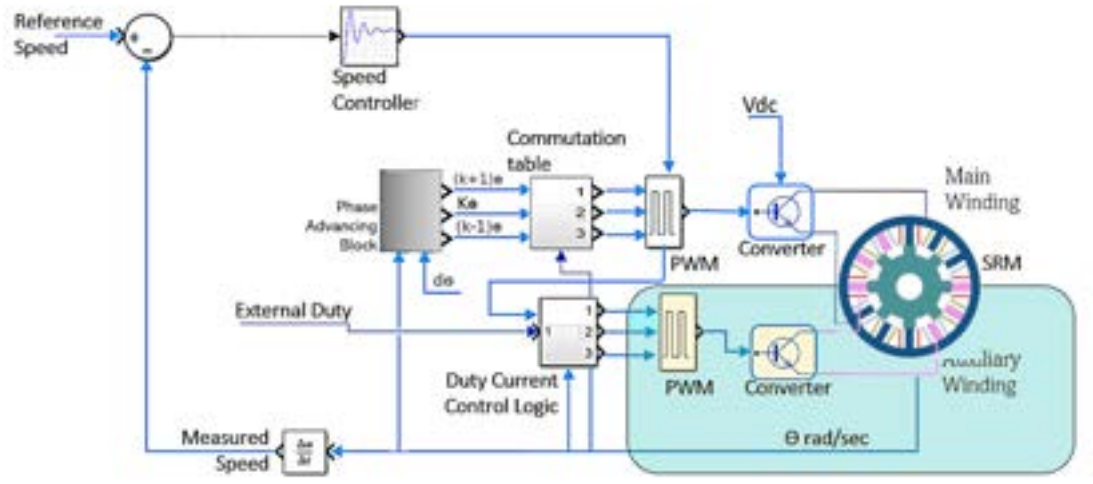

Figure 4.2: Block diagram for torque ripple minimization in proposed HESRM without PMs.

The optimum Turn-on angle is selected to manage the excitation angle such that

the phase current at the preceding phase's Turn-off time should meet the incoming phase's maximum current (θ_k). The ripple minimization excitation scheme will be switched as A-AB-B-BC-C-CA in the proposed HESRM. Figure 4.3 [85, 143, 144] shows the graphical representation of the torque ripple minimization for the phases.

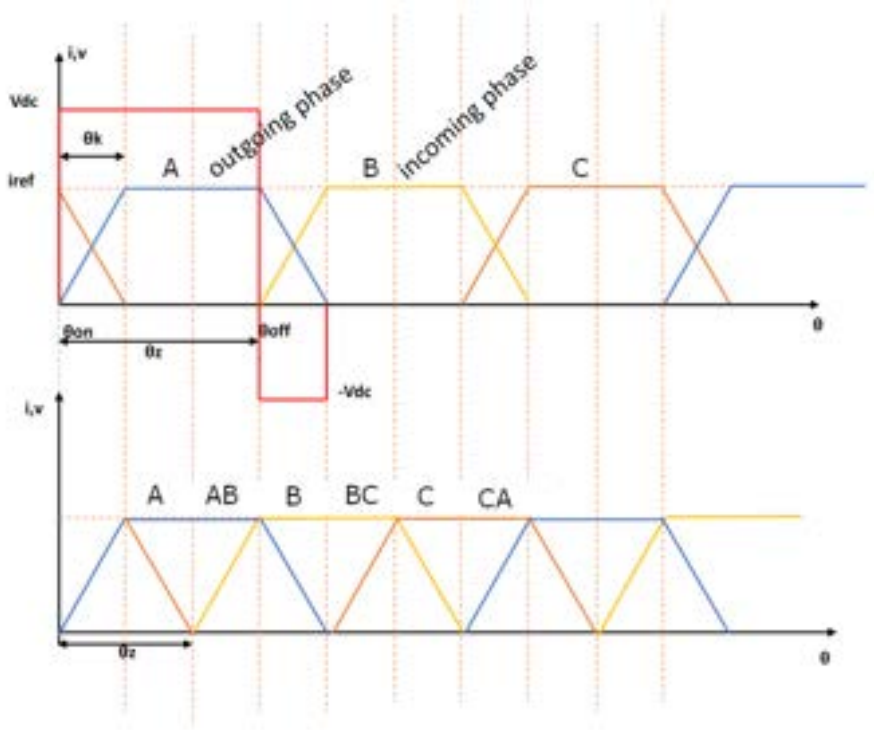

Figure 4.3: The graphical representation of torque ripple minimization.

4.2 Torque Ripple Minimization in Conventional SRM

4.2.1 Principle of Operation

Figure 4.4 is a block diagram showing the phase advance method's performance in the conventional SRM. To reduce torque ripple, the switching phase is relocated forward by changing the angles of when the motor turns on and off [145]. As such, the outgoing phase is turned off when the incoming phase current reaches its rated reference current value. The delta angle changes the angle needed to Turn off the phase current. After the phase advances, the commutation angle is transmitted to the driver circuit to spin the motor [146, 147].

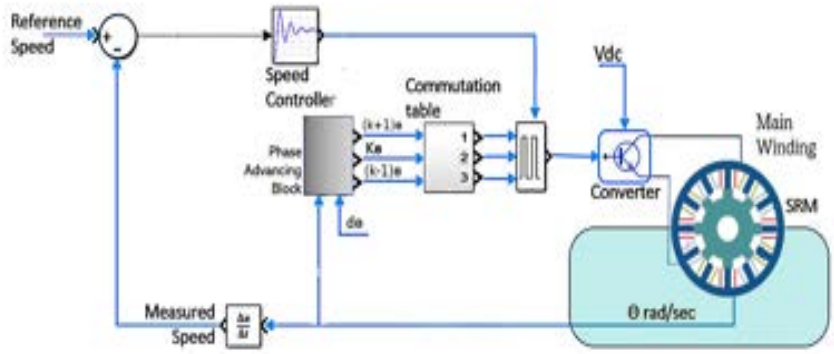

Figure 4.4: The block diagram of torque ripple minimization in conventional SRM.

4.2.2 Transient Response

The current, voltage, and speed are measured using the torque ripple minimization strategy on the dynamic analysis of conventional SRM. Figure 4.5 is a dashboard that shows the measured value of the reference speed, or theta, about the current waveform. In this direction, the delta angle will change to a great extent to reduce the ripple. The switching scheme providers admit a maximum change of (+ or -) 5% delta angle. Based on the real-time analysis, the value of the delta is changed to achieve the highest level of accuracy. As a result, the torque reduction is higher than with other techniques.

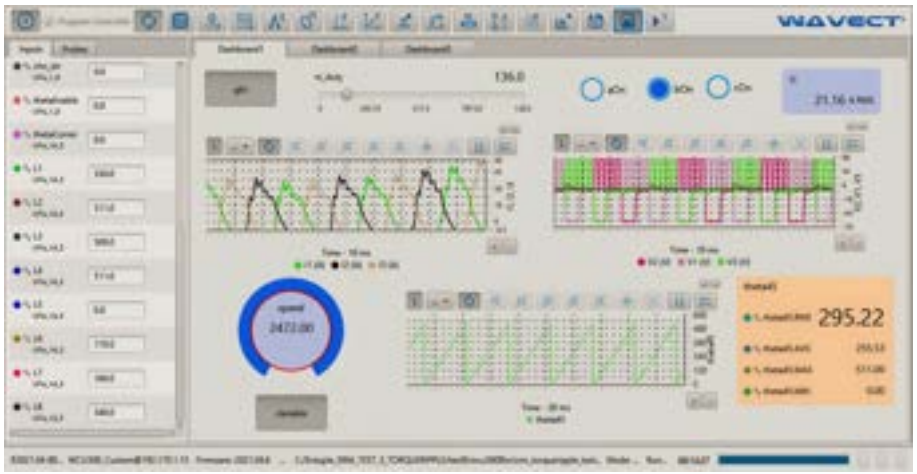

Figure 4.5: The switching of phase advance method for torque ripple minimization in conventional SRM.

With the help of moving torque characteristics, the performance of the torque ripple was analyzed, and the average, maximum, and minimum rms values of the

torque were shown in Figure 4.6. Hence, the torque ripple can be estimated as a percentage based on the formula.

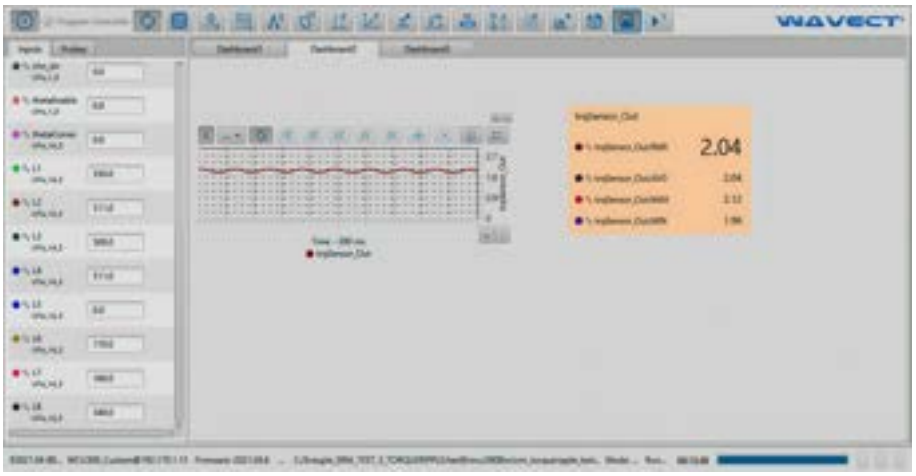

Figure 4.6: Performance of torque ripple characteristics in conventional SRM.

4.3 Comparison of Torque Ripple in CSRM

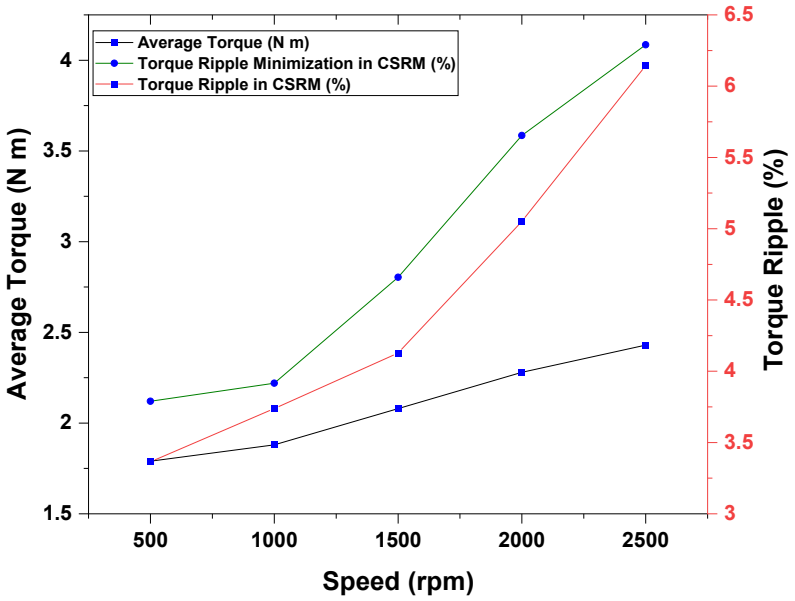

Figure 4.7: Torque ripple comparison of the conventional SRM.

Figure 4.7 compares the torque ripple in the conventional SRM. The result of the torque ripple comparison in the conventional SRM shows that the ripple percentage gets higher as the speed increases. After examining the mean torque and speed, the analysis found the torque ripple in each interval. The graph shows that the ripple

Table 4.1: Comparison of torque ripple in CSRM.

Sl.No	Speed (rpm)	Torque Ripple(%)	Torque Ripple Minimization (%)	Percentage of Decrease (%)
1	500	6.41	2.92	**54.36%**
2	1000	6.11	2.89	**52.66%**
3	1500	5.53	2.79	**49.48%**
4	2000	4.84	2.73	**43.63%**
5	2500	4.11	2.29	**43.18%**

gets more prominent as the speed increases and that the average torque reaches its rated value when the speed is at its rated value. With phased advancing and a fixed average torque, the torque ripple was kept to a minimum over the speed range. Hence, the phase-advancing techniques were used in all speed ranges, and the ripple was cut by more than 40%.

In Table 4.1, the torque ripple of the conventional SRM is compared in all the speed ranges up to the rated speed of 2500 rpm. At 2500 rpm, its most torque ripple can be reduced by 54%; at that speed, the slightest ripple can be reduced by 43%. The table shows that the conventional SRM can reach the highest range of ripples corresponding to the torque reduction in the percentage of specified speed. The evaluation of the results shows that the phase advance method can achieve a maximum torque ripple reduction of at least 40% in all speed ranges.

4.4 Inference-CSRM

Before placing the technique for reducing torque ripple into the proposed method, a real-time analysis was done in the conventional SRM to determine the amount of ripple that could be reduced. To accomplish this, evaluate the torque ripple about all the speed ranges and tilt the delta angle so that all the outgoing Turn-off and incoming Turn-on angles match the reference current value. Hence, the analysis results suggested that the phase advance method is the most effective means of minimizing ripples to a great extent.

4.5 Torque Ripple Minimization in Topology I

4.5.1 Structural Analysis

The structure of the proposed HESRM machine and the conventional SRM is shown in Figure 4.8. The machine topologies of the ratings are 12/8 poles, 1.2 kW, 2 N-m,

and 2500 rpm, and the main specifications are detailed in Table 4.2. It can be seen that both SRMs have the same stator and rotor pole configuration, which features four poles per phase without any PM in the machine core.

(a) (b)

Figure 4.8: The structural diagram of 12/8, three-phase conventional SRM and proposed HESRM (a) Conventional SRM and (b) Proposed SRM.

4.5.2 Motor Topology

Table 4.2: Specification of the two SRMs.

Dimensions	Conventional SRM	HESRM
Number of phases	3	3
Number of stator poles	12	6-6 (12)
Number of rotor poles	8	8
Diameter (mm)	300	300
Rated Power	1.2kW	1.2kW
Stack length (mm)	70	70
Core	M15_26G	M15_26G

In the conventional SRM, the three-phase switching circuit, the motor consists of 12 stator poles and 6 rotor poles. Hence, each phase has 4 concentrically connected poles for contributing flux in the active region [148, 149]. For newly designed HESRM with non-PM, the windings are assigned for the different excitations, namely the main winding and the auxiliary windings. Therefore, half of the total active poles are equally separated, electrically and mechanically, and allocated as the switching provided to the main winding. The rest of the poles were given to the auxiliary poles, which use separate injecting of the dc with the help of an independent controller. For this purpose, both windings have a carrying capacity of different currents for

each switching phase. As a result of the symmetric nature of the pole alignment of the proposed HESRM, the flux path is similar to that of conventional; the only difference is the intensity of the flux carried in the active region. Subsequently, using two separate windings for each phase influences more electromagnetic torque than the conventional.

4.5.3 Magnetic Flux Line Distribution

Concerning the phase current, Figure 4.9 shows the magnetic flux pattern for the conventional HESRM with 12/8 poles and the suggested HESRM with 12/8 poles with phase A excited in the unaligned and aligned positions, respectively. The magnetic flux distribution paths of the proposed HESRM excitation method and conventional SRMs are identical in the unaligned and aligned positions. This is because the auxiliary pole winding topology is set up to send flux in the same direction as the main pole winding. The fact that the main and auxiliary windings are set up symmetrically affects the shortest flux path for the new method proposed to make the most electromagnetic torque.

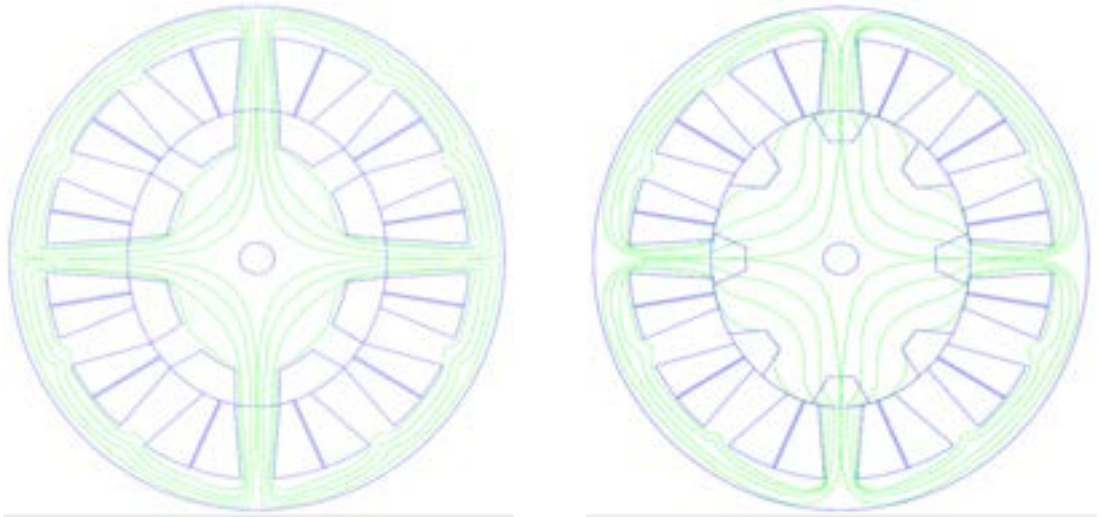

(a) (b)

Figure 4.9: The magnetic flux distribution characteristics of both SRMs in aligned and unaligned pole conditions (a) Aligned pole (b) Unaligned pole .

4.6 MEC Model and Torque Equation

The magnetic equivalent circuit (MEC) depicted in Figure 4.10 illustrates the switching circuit patterns for the main and auxiliary windings. The equivalent circuit shows the reluctance path produced simultaneously by the various exciting phase switches based on the dual excitation scheme [150, 151]. The effective reluctance

path from both winding phases creates the shortest flux path associated with the reluctance R [152]. Consequently, the total reluctance produced results from both windings, representing each core part of the motor. The total flux produced by the windings will be significantly more critical for generating substantial electromagnetic torque [153]. Therefore, the total torque production in the proposed HESRM is the sum of torque owing to the main and auxiliary winding.

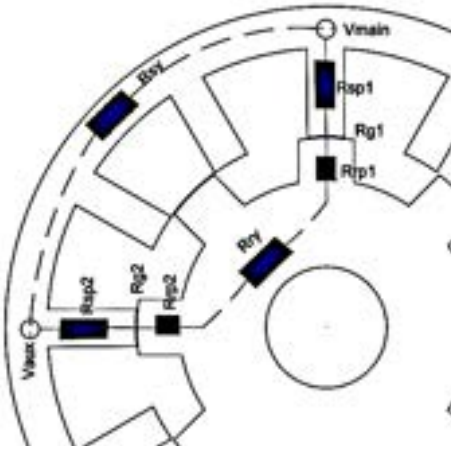

Figure 4.10: Magnetic equivalent circuit model for the cross-sectional view of pole pair of proposed 12/8 HESRM without permanent magnet excitation.

$$T_x(\theta, i_x) = T_{MC_x}(\theta, i_M) + T_{AC_x}(\theta, i_A) \tag{4.1}$$

T_x is the electromagnetic torque provided by one phase that can be obtained from the total energy of that phase. $T_{MC_x}(\theta, i_M)$ is the torque to the main winding excitation, and the $T_{AC_x}(\theta, i_A)$ is the torque due to the auxiliary.

4.7 Result and Discussion

4.7.1 Software Analysis Using 2D-FEM

This section presents software analysis in the Ansys/Maxwell 2D-FEM results of the magnetic characteristics and the static electromagnetic performance of the proposed HESRM compared with the conventional SRM concerning the aligned pole and the unaligned position. Thus, the SRMs' construction, total net weight, and steel consumption are identical.

4.7.1.1 Magnetic Flux Density Distribution

The magnetic flux density pattern of two SRMs constructed using the same material is shown in Figure 4.11. The aligned pole experiences maximum flux density, and

the unaligned pole experiences the lowest flux density when one phase of the conventional SRM is excited at 15 A. Due to the same stator and rotor pole, a similar circumstance occurred in the intended HESRM with the same aligned and unaligned angle. The auxiliary winding in the proposed machine can carry extra current up to the rated amount, resulting in a varied flux density carried in the core. As a result, the hybrid excitation increases the auxiliary winding's capacity to carry additional current, significantly influencing the generation of electromagnetic torque.

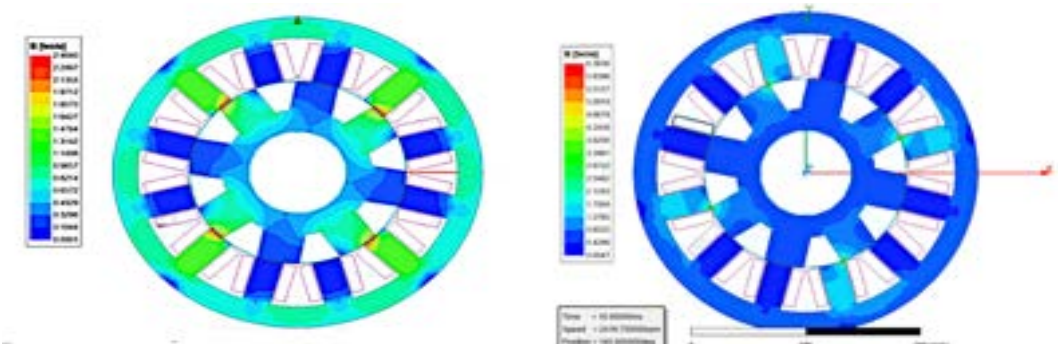

(a) (b)

Figure 4.11: The magnetic flux density characteristics of the proposed HESRM for aligned and unaligned positions (a) Aligned (b) Unaligned.

4.7.1.2 Magnetic Flux Linkage

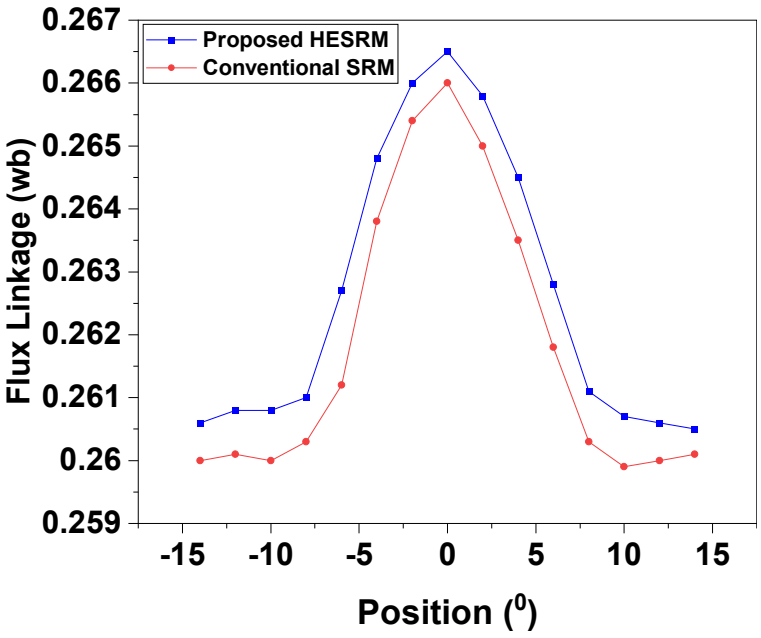

Figure 4.12: The magnetic flux linkage characteristics of both SRMs.

The rotor position dependence of the flux linkage properties of the conventional and the proposed 12/8 SRMs is shown in Figure 4.12. In general, the area enclosed between the aligned and the unaligned curves gives the co-energy for fixed MMF, which is the torque corresponding to a single energy stroke.

In Figure 4.12, the proposed HESRM achieves more prominent flux linkage in all the rotor positions concerning the aligned and unaligned positions. With the same position, the conventional SRM generates a feasible flux compared to the proposed one. The new method portrays the same characteristics as the conventional SRM but with an extended amplitude with a maximum of 0.27 Weber. In other words, the proposed HESRM generates more torque at the same rotor position due to the doubly excited current injection in the auxiliary windings.

4.7.1.3 Static Electromagnetic Torque

Torque analyzed during individual rotor position is measured using software analysis. The static electromagnetic characteristics of two SRMs with phase excitation are shown in Figure 4.13a. In the conventional SRM, a current of 15 A excites each phase from aligned to unaligned. In the proposed HESRM, 15 A is only given to the auxiliary winding and the main winding acting as a switching function. The static electromagnetic torque is shown to vary concerning the angle to reach its most excellent torque of 1.5 N-m at the aligned position. The static electromagnetic torque in Figure 4.13b changes according to the various excitations produced by the auxiliary winding in the new topology. The suggested machine exhibits various electromagnetic patterns depending on the current injection rate, which ranges from a minimum current of zero to a maximum current of 30 A. As the direct auxiliary gradually changes, the static flux pattern increases.

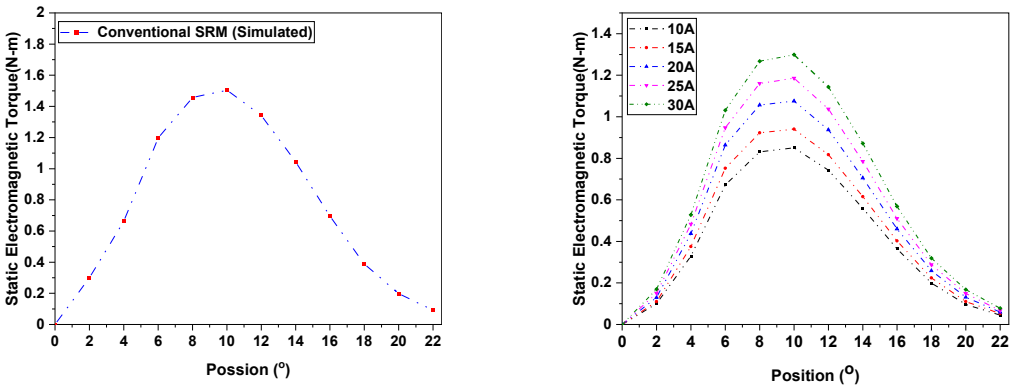

(a) (b)

Figure 4.13: The static electromagnetic torque characteristics of both SRMs with phase excitations (a) Conventional SRM and (b) Proposed HESRM.

4.7.2 Dynamic Performance using SRM Drive

The dynamic performance of the proposed HESRM and the conventional SRM are simulated and tested simultaneously. In the simulation, the designed control circuit for the auxiliary and the main winding will be the same for the experiment. Furthermore, the control strategies are the same for both motors; instead of one winding excitation, the proposed scheme provides auxiliary excitation with the help of a secondary controller.

4.7.2.1 Moving Torque Characteristics

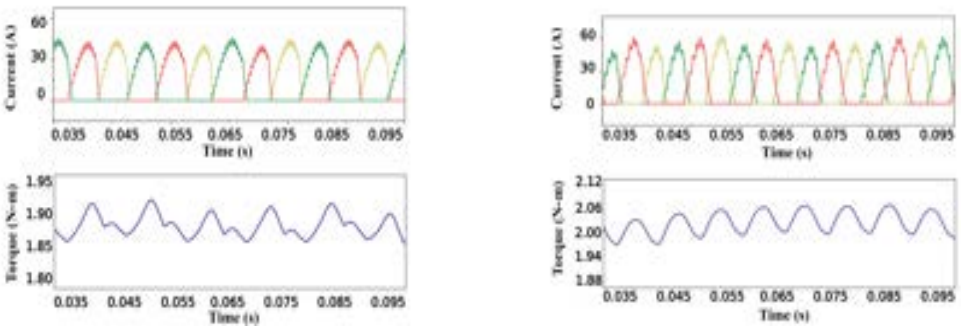

(a) (b)

Figure 4.14: Experimental results of phase current and the moving torque characteristics of the conventional SRM at variable speed (a) 1500 rpm and (b) 2000 rpm.

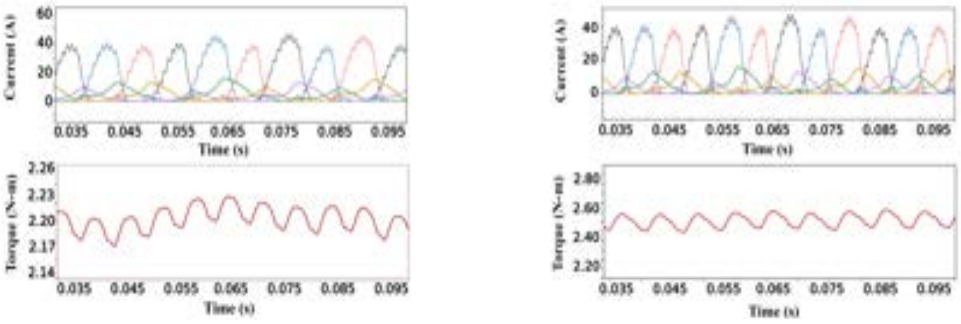

(a) (b)

Figure 4.15: Experimental results of phase current and the moving torque characteristics of the proposed HESRM without PM at variable speed (a) 1500 rpm and (b) 2000 rpm.

Simulated measurements are made of the motor's torque change at a given speed and varying load. The moving torque characteristics compared with the corresponding phase currents are shown in Figure 4.14 and Figure 4.15. Both motors are operated at rated load conditions with variable speed range from 500 rpm to 2500 rpm. At each speed, by changing the load up to the required rated current, the

conventional SRM and the proposed HESRM generate torques. In Figure 4.14a and Figure 4.14b, at 1500 rpm, the conventional SRM produces an average torque of 2.4 N-m and 2.6 N-m at 2000 rpm. Consequently, the proposed HESRM methods enhance the torque to 2.6 N-m at 1500 rpm and 3 N-m at 2000 rpm, respectively, as shown in Figure 4.15a and Figure 4.15b. The simulated Conventional SRM shows stable operation due to the dynamic behavior of switching the poles. In HESRM, the switching happens in 2 poles simultaneously; hence, it shows a stable operation for a short time interval.

4.7.2.2 Torque Ripple Characteristics

From the average torque characteristics, it is clear that the motor lacks a smooth torque profile. The maximum and minimum torque produced by the conventional SRM and the proposed HESRM varies, and the difference in these values creates torque ripple. High torque ripple diminishes the advantages of the newly designed high torque capability motors; hence, reducing ripple is mandatory for the specified applications.

The torque ripple can be calculated as,

$$T_{ripple} = (T_{max} - T_{min})/T_{avg} \times 100\% \tag{4.2}$$

Where T_{ripple} is the torque ripple, and T_{max}, T_{min}, and T_{avg} are the maximum, minimum and average torque, respectively.

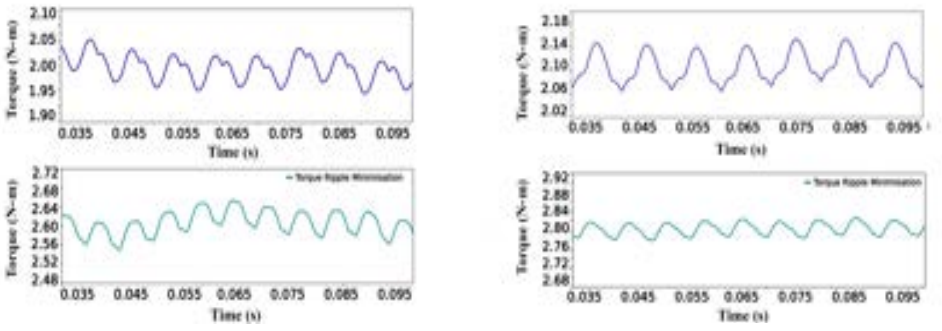

(a) (b)

Figure 4.16: Experimental results of implementing torque ripple minimization in 12/8 conventional SRM and the proposed HESRM without PM (a) Conventional SRM and (b) Proposed HESRM.

The comparison of the output torque ripple characteristics with and without enabling phase advancing is shown in Figure 4.16. The bottom graph shows the results of phase advancement, and the top graph shows the content of ripples in the torque waveforms of conventional and hybrid SRM. The SRM is a three-phased excited motor employed in this experiment, and the A, B, and C phases are all

stimulated at the respective time intervals,Äîthe resulting current and voltage adjustment cause a ripple in the output torque. The ripples can be decreased by shortening the time between switching. However, if the switching is too close together, the current will exceed itself by superimposing on itself. Phase advancing is a method in which the preceding phase is activated quickly to minimize the ripple. A control mechanism that prevents the current from overshooting alters the limit of this shift from the outside.

4.8 Experimental Validation

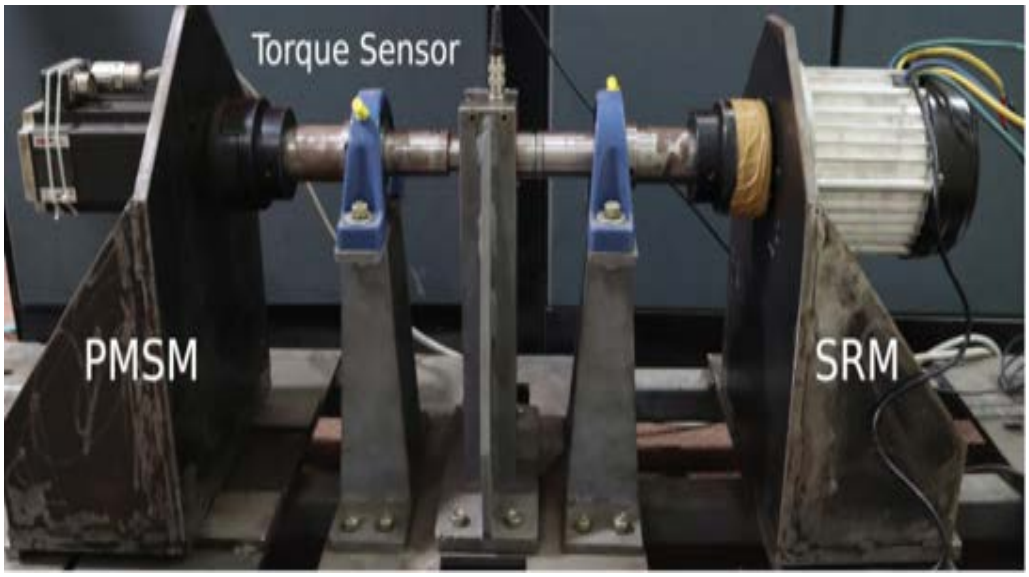

Figure 4.17: Back-to-back set up for experimentation for the SRMs.

A 12/8 SRM prototype is designed, made, and tested to check the proposed HESRM's concept proof. A permanent magnet synchronous motor is electrically connected back-to-back on the load side. A torque sensor is connected to the motor's center to acquire instantaneous data. A Waveact Controller with FPGA architecture is used for real-time control prototyping. Using inverters and the PWMs generated by this controller, the SRM is switched. As shown in Figure 4.17, the SRM was loaded with the back-emf generated by the PMSM using rheostats.

The experimental setup for executing the controller is shown in Figure 4.18. The suggested HESRM topology is followed while rewinding the stator terminals. Secondary excitation executes and implements dual excitation without a permanent magnet. Because of this excitation, the secondary controller can carry different currents to produce more torque. Consequently, the experimental setup consists of two inverter stacks and an FPGA-based wavect controller.

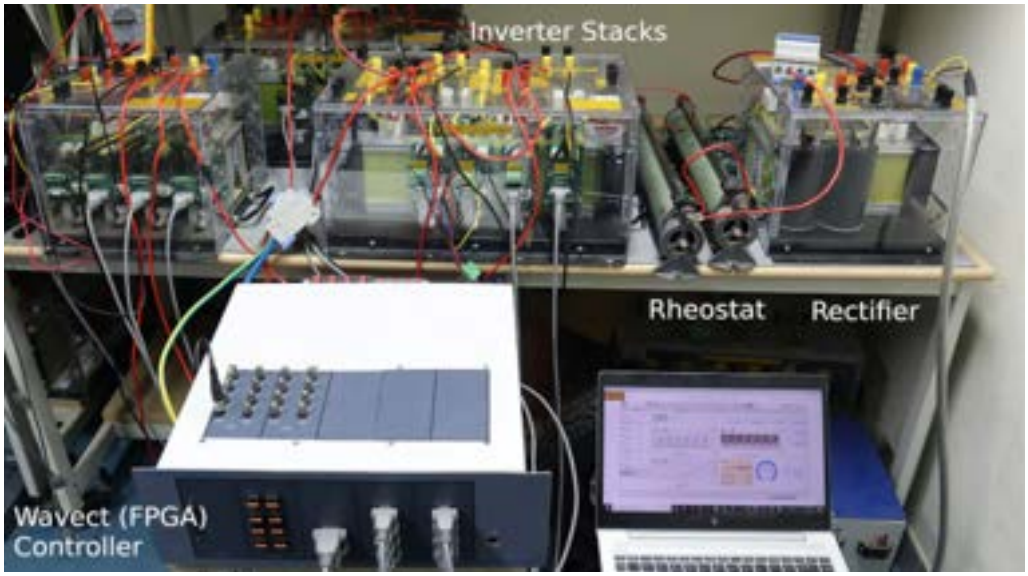

Figure 4.18: Experimental platform for the proposed HESRM.

4.8.1 Transient Response of Two SRM's Drive

According to the same parameters, 60 V for the dc-link voltage and 2 N-m for the load torque, the results are shown in Figure 4.19. The torque, phase current and speed responses of two SRM drives with closed-loop control were examined.

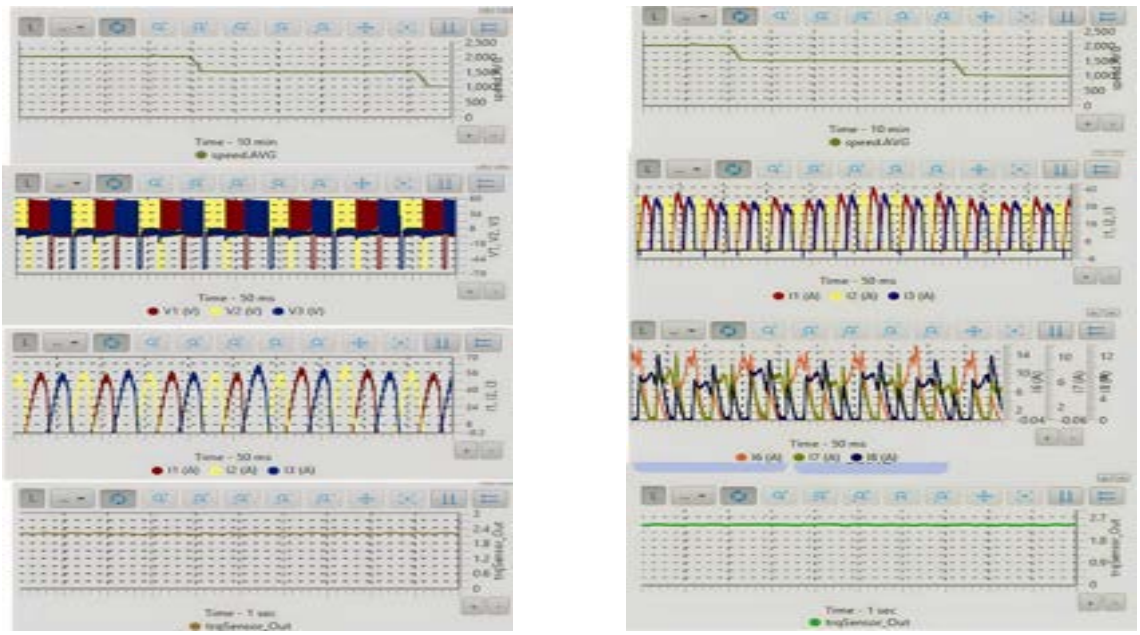

(a) Conventional SRM (b) Proposed HESRM

Figure 4.19: Time-varying excitation characteristics of two SRMs (a) Conventional SRM and (b) Proposed HESRM.

It has been found that both SRMs use the same switching strategy and move quickly from the recommended speed of 1500 rpm to the rated speed of 2500 rpm during the start condition. In other words, under closed-loop control, as the speed

changes from 500 to 2500 rpm, the gain parameter changes in real time to keep the speed where it should be. The result shows that the speed of the rotor follows the command signal in every possible way and gets the same significant results as the simulation.

The time-varying excitation properties of a conventional SRM, including speed, voltage, phase current, and requisite torque, are shown in Figure 4.19a. The intended transient characteristics are stimulated with two separate currents in Figure 4.19b; the graph represents the main winding phase current and the auxiliary dc injection.

4.8.2 Experimental Validation of Torque Ripple

The simulation results of the proposed system and the torque measurements were taken with the help of hardware implementation. The experimental results of the Wavect controller, which displays the torque measurement, are shown in Figure 4.20. This window creates the result after enabling excitation switching; it includes torque sensor output concerning the time, the angle of rotor position theta, speed, input power, output power, and efficiency. Furthermore, the results are in rms and cover the average, maximum, and minimum values. The results were executed with a rated current of 1500 rpm and a maximum and minimum torque of 2.59 N-m and 2.50 N-m, respectively. And with an average torque of 2 N-m, the constant torque ripple is 3.54%.

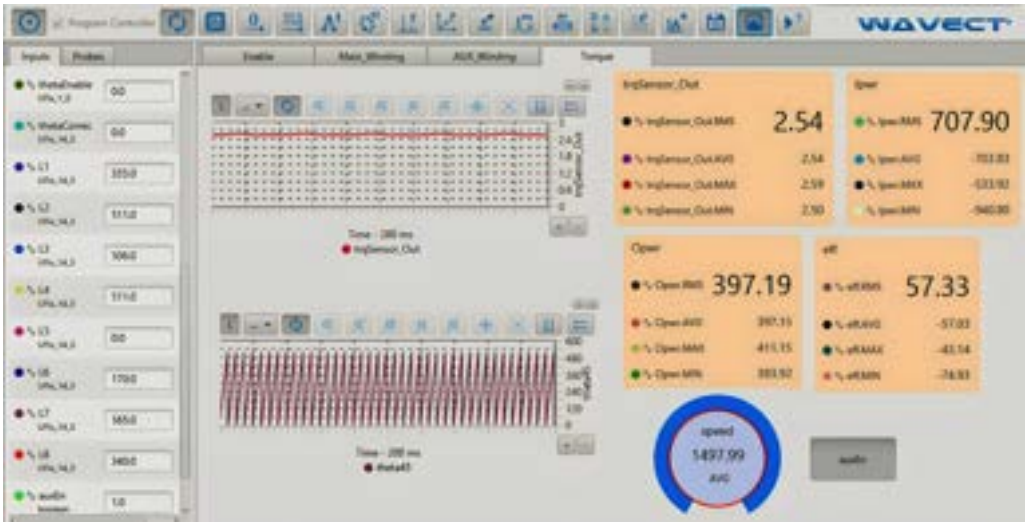

Figure 4.20: Experimental results of Wavect controller outcomes with torque measurement.

4.9 Comparison of Performance using Hardware and Software Solutions

The comparison of software analysis with the hardware-measured values is graphically represented and compared with conventional SRM and the proposed HESRM. The average torque with respect to the current and the speed are evaluated for two analysis measurements in both SRMs.In both analysis methods, the results are similar.

4.9.1 Average Torque Characteristics

Based on simulations and experimental data about speed and torque characteristics, Figure 4.21 compares the average torque of the proposed and conventional machines. The torque produced by the proposed machine at each current excitation is leading because of the increased flux in the air gap. The suggested machine achieves 1.6 N-m at 15 A, compared to 1.2 N-m at peak current for the existing machine.

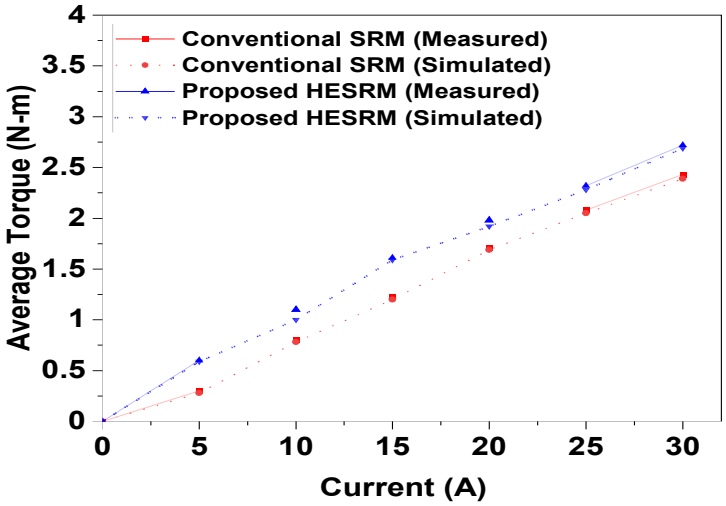

Figure 4.21: Comparison between measured average torque and those predicted using 2-D finite elements of conventional SRM and the proposed hybrid dc excited SRM.

4.9.2 Speed Torque Characteristics

The speed-torque characteristics provide information on how the motor torque varies when the speed of the motor changes. The speed-torque characteristics of both SRMs are shown in Figure 4.22. Speed and torque have an anti-proportional relationship. However, in contrast to conventional machines, which always have a nearly 1 N-m higher, the HESRM has a peak torque of 2.6 N-m at the rated current of the base

speed. At 2000 rpm, the proposed HESRM's output torque may vary by up to 2.5 N-m; conventional reaches 2 N-m. The results of the experiment closely reflect the characteristics of the simulation.

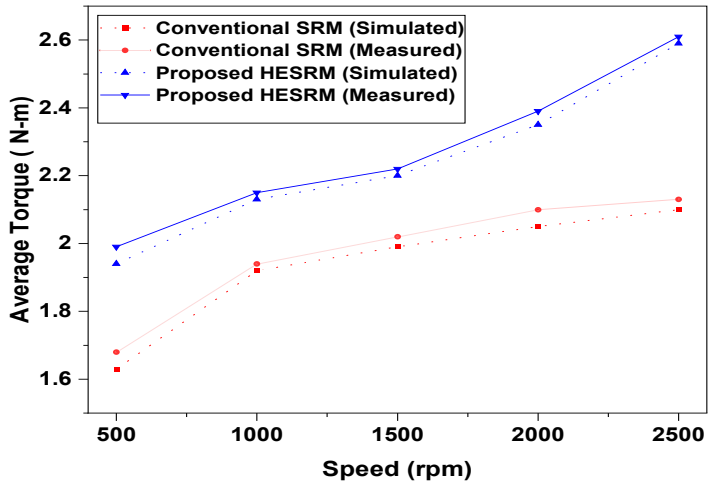

Figure 4.22: Comparison of speed-torque characteristics of two SRMs between measured quantity and those predicted using 2-D finite elements.

4.10 Comparison with Conventional SRM

4.10.1 Torque Ripple

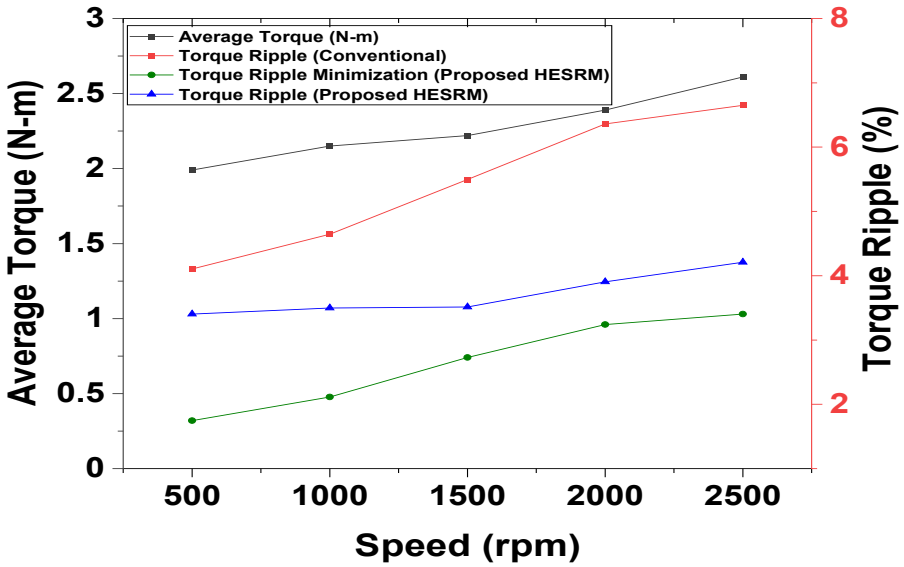

Figure 4.23: Torque ripple comparison of the conventional and proposed SRMs.

The torque ripple of the proposed HESRM is compared with conventional SRM, and ideally, it should be lower than the conventional SRM. The suggested HESRM

method's performance analyses are compared with traditional SRM. Figure 4.23 compares the torque ripple responses over the variable speed range and displays the average torque produced by the newly developed machines. The conventional SRM torque ripple increases from 500 to 2500 rpm. In addition, the recommended HESRM achieves a lower torque ripple than the conventional SRM in each speed range. Consequently, torque ripple reduction using phase advance reduces the amount of ripple by 58% compared to conventional SRM and by 33% compared to the proposed method.

4.10.2 Efficiency

In addition, it should be noted that efficiency is an additional essential factor to discuss and analyze. The effectiveness is then compared to that of conventional SRM. In Figure 4.24, it is observed that the proposed HESRM has a higher efficiency in all speed ranges than the conventional SRM. At 2500 rpm, the proposed machine is 21 percent more efficient than the conventional one. Consequently, the torque ripple minimization topologies exhibit a greater efficiency of 10 percent across all speed ranges.

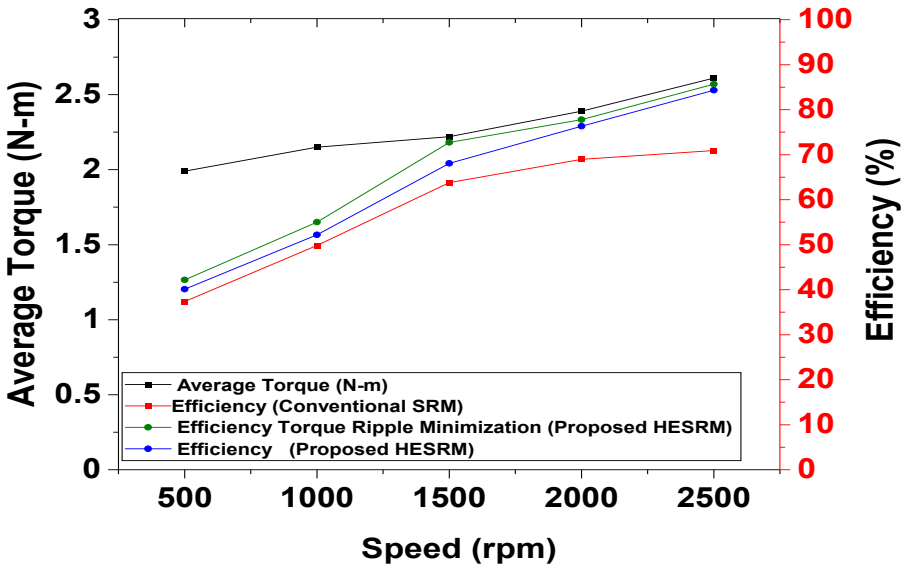

Figure 4.24: Efficiency comparison of the conventional and proposed SRMs.

4.10.3 Input Power

The amount of power the motor needs to start functioning is known as input power, and the proposed solution should ideally use less power than the conventional SRM. Both motors use roughly the same input power at 500 revolutions per minute, as shown in Figure 4.25. The motors' input power consumption begins to rise as the

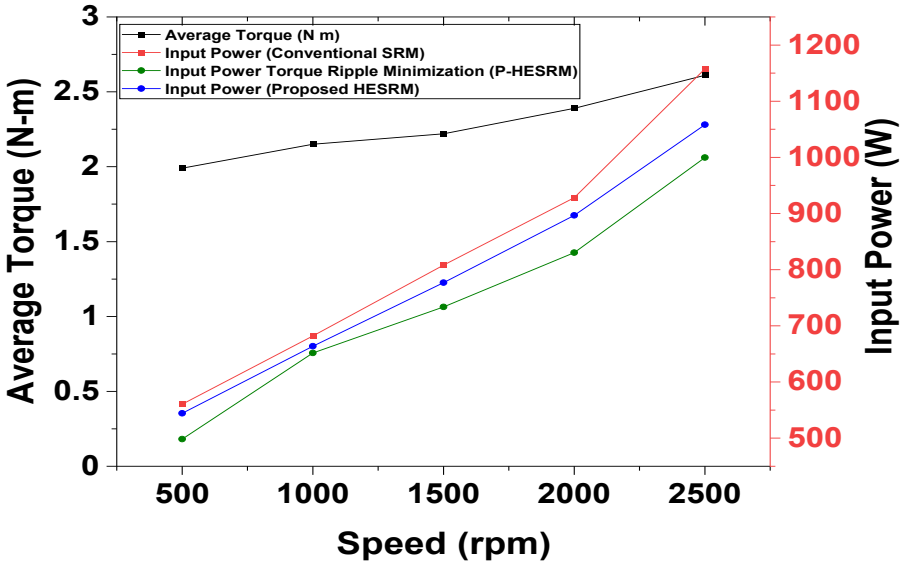

Figure 4.25: Input power comparison of the conventional and proposed SRMs.

speed rises. Compared to the suggested SRM, the traditional SRM draws greater power at each rpm. The HESRM draws a minimum of 650 W, whereas the traditional SRM draws over 700 W at 1000 rpm. The input power used by the suggested approach decreases by 8.69% at maximum speed. Similar to the other two, the phase advance approach in the suggested method shows a lower input power of 13%.

4.11 Comparison of Torque Ripple Minimization in Topology I

Table 4.3: Comparison of torque ripple minimization in topology I.

Sl.No	**Speed (rpm)**	**Torque-Ripple(%)**	**Torque-Ripple Minimization (%)**	**Percentage of Decrease (%)**
1	500	6.35	3.35	**47.20%**
2	1000	4.65	1.96	**57.84%**
3	1500	4.18	1.53	**63.51%**
4	2000	3.55	1.26	**64.67%**
5	2500	1.79	1.00	**44.06%**

Table 4.3 compares the percentage of torque ripple reduction in the first topology of the proposed hybrid excitation method in which the speed ranges varied from minimum to the rated value of 2500 rpm. Thus, after implementing the torque ripple reduction criteria to the proposed scheme sequentially, it tends to reduce the ripple factor by more than 40% in all the speed ranges. The maximum reduction percentage

occurred in the speed range of 2000 rpm at a value of 64%. Meanwhile, 44% is the nominal reduction percentage value for the speed of 2500 rpm.

4.12 Inference-Torque Ripple Minimization in Topology I

A novel 12/8 hybrid excitation SRM was proposed for EV applications with high torque and less ripple SRM. The structure and operating principle were shown graphically. The experimental analysis is compared to the conventional SRM for the identical application to verify the validity. The comparison result demonstrates that the proposed HESRM generates greater average torque than the conventional SRM. In addition, because of its switching characteristics, it tends to generate torque ripple. However, the performance of the phase advance method implemented in the proposed method is superior to previous results. Table 4.3 comparing the results proves that the proposed minimization technique reduces the torque ripple 40-50% of the proposed topology. In addition, it reduced torque ripple to produce a smooth high-value torque profile in all speed ranges. Due to the dual winding controller, this proposed method has the advantages of feasible control, improved redundancy, and high efficiency. Consequently, this HESRM methodology is ideally suited for electric vehicle applications.

4.13 Torque Ripple Minimization in Topology II

Torque ripple minimization results in a smoother output torque waveform and enhanced performance, including reduced vibration and noise, enhanced efficiency, and increased power density [154, 155]. Minimizing torque ripple improves motor control, which can be advantageous in applications requiring precise control, such as servo motors and precision positioning systems. Minimizing torque ripple can also improve energy efficiency by reducing ripple-related power losses [65, 156].

The second topology introduced a short flux path by energizing the alternate poles of the motor, as described previously. This will result in the production of enhanced flux intensity, thereby increasing the electromagnetic torque. As a result of the simultaneous excitation of adjacent poles, the rotation of the motor will not be as smooth as the first topology, resulting in significantly more torque ripple.

4.13.1 Principle of Operation

The torque ripple produced in the second topology is considerably higher than the conventional and the output of the first topology. In this torque method, minimization

is done by utilizing the phase advancing of the phases [157, 158].

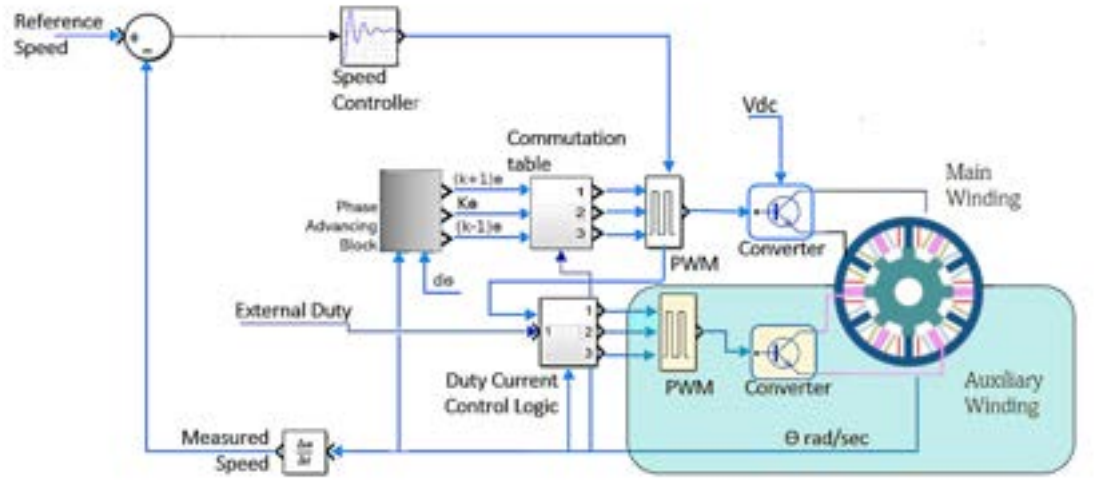

Figure 4.26: Block diagram for torque ripple minimization in proposed HESRM for topology II without PMs.

The phase advancing in switched reluctance motor control refers to the technique of controlling the phase current waveform in a way that advances the timing of the current waveform relative to the position of the rotor. The goal of phase advancing is to produce a positive torque contribution from the motor and to minimize torque ripple [159].

In the proposed topologies, the torque is produced by the interaction between the rotor and the stator magnetic fields. The torque waveform produced by the motor is directly related to the phase current waveform, and optimizing the phase current waveform can result in improved performance, reliability, and energy efficiency.

Phase advancing works by controlling the phase current waveform so that the current is applied to the phase winding before the rotor reaches the position corresponding to that phase. This generates a magnetic field ahead of the rotor, producing a positive torque contribution [160, 161].

The position of the rotor is obtained by analyzing the angle obtained from the motor as shown in the block diagram in Figure 4.26. This angle is supplied to the phase advancing control block, which precisely times the switching of the phases. An external duty is provided to control the advancing of the pulse with protection to avoid overlapping current signals. The advanced angle will be utilized further to generate the PWMs to switch the motor [162–164].

4.14 Dynamic Characteristics -Topology II

The current and torque waveform of switched reluctance motors are vital factors that determine the performance of these motors. The current waveform is directly related to the torque production and speed control of SRMs, while the torque waveform provides insight into the efficiency and reliability of the motor.

The current waveform in SRMs is controlled by the switching pattern of the stator phases, and the current waveform is applied to the windings. The current waveform can significantly impact the torque production, speed control, and efficiency of SRMs.The torque waveform in SRMs is influenced by the magnetic reluctance of the rotor and the current waveform applied to the stator windings. The torque waveform can be used to evaluate the efficiency and reliability of the motor and detect any faults that may occur during operation. For example, a smooth and stable torque waveform indicates good efficiency and reliability, while a distorted or irregular waveform may indicate a problem with the motor.

4.14.1 Moving Torque Characteristics

By analyzing the torque ripple characteristics of the output torque obtained from the SRM, compared with the conventional SRM, the torque ripple is comparatively high even though the average torque is high. The conventional method generates an average torque from 2.2 to 2.5 N-m from rated to a maximum speed of 2000 rpm. The ripple measured ranges from 2.7 to 4% are shown in Figure 4.27.

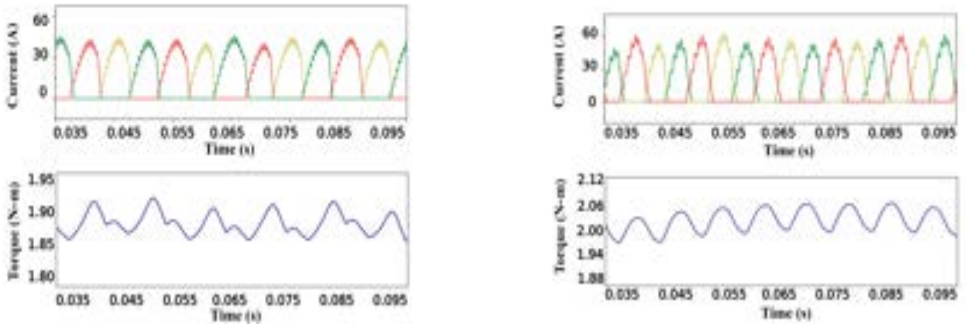

(a) (b)

Figure 4.27: Experimental results of phase current and the moving torque characteristics of the conventional SRM at variable speed (a) 1500 rpm and (b) 2000 rpm.

Figure 4.28 clearly shows the output waveform of the second topology of the proposed SRM for various speeds. The results show a high torque ripple from 3.6 to 8% compared to the conventional method. This is evident from the irregular torque waveform when the current levels change.

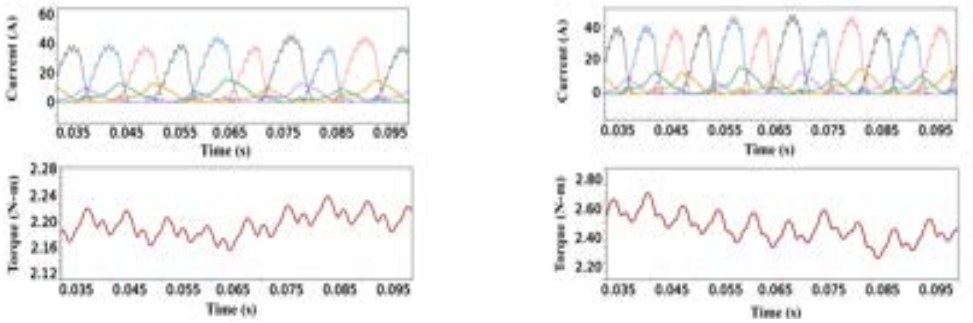

(a) (b)

Figure 4.28: Experimental results of phase current and the moving torque characteristics of the proposed HESRM without PM at variable speed (a) 1500 rpm and (b) 2000 rpm.

4.14.2 Torque Ripple Characteristics

The phase advancing techniques enable the control logic of the torque ripple minimization technique to show outstanding results compared to both the conventional and proposed HESRM, which are shown in Figure 4.29. At 1500 rpm, the ripple is reduced from 3.6 to 3%; at 2000 rpm, the ripple content reduces from 8 to 1.4%.

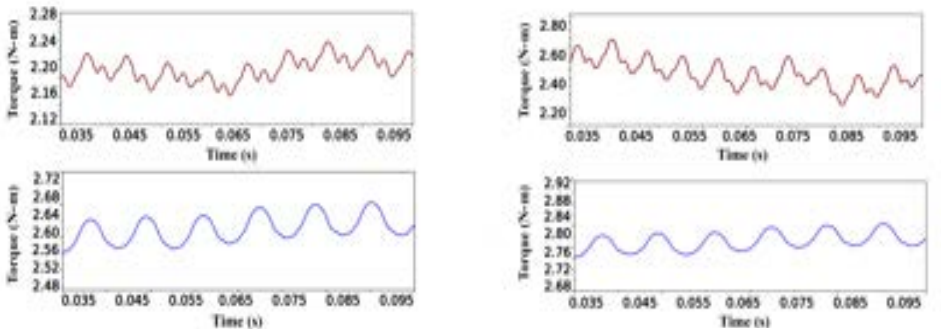

(a) (b)

Figure 4.29: Experimental results of an implementation of torque ripple minimization in 12/8 conventional SRM and the proposed HESRM without PM (a) Conventional SRM and (b) Proposed HESRM.

4.15 Comparison of Performance using Hardware and Software Solutions

4.15.1 Average torque characteristics

Comparison between measured average torque and those predicted using 2-D finite elements of conventional SRM and the proposed hybrid dc excited SRM is depicted in Figure 4.30. The conventional and the proposed SRM show similar characteristics

when measuring from zero to 30 amperes of current. The proposed HESRM produces more torque due to the ultra-small flux path inside the motor. At maximum current, the HESRM outputs a maximum of 3 N-m while the conventional only delivers up to 2.4 N-m. These results are almost matching with the simulation results obtained.

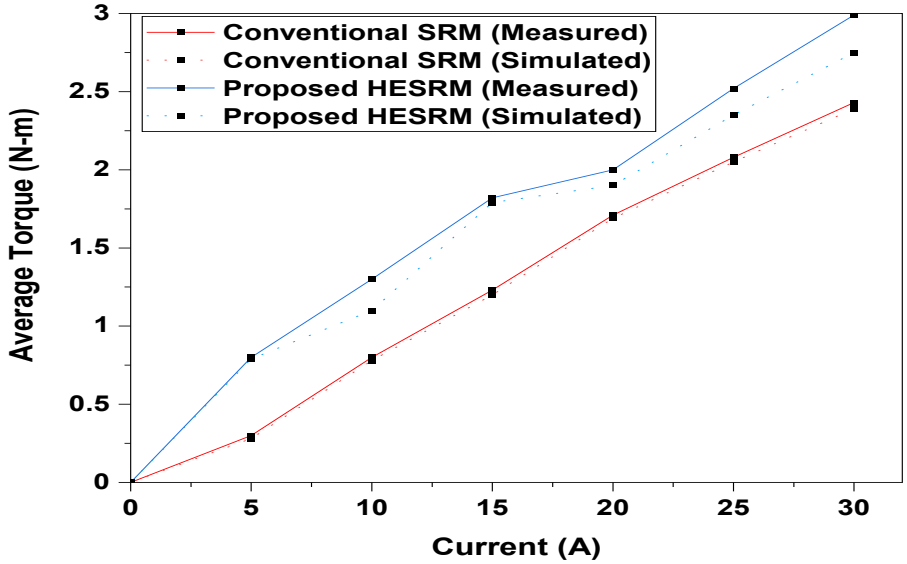

Figure 4.30: Comparison between measured average torque and those predicted using 2-D finite elements of conventional SRM and the proposed hybrid dc excited SRM.

4.15.2 Speed Torque Characteristics

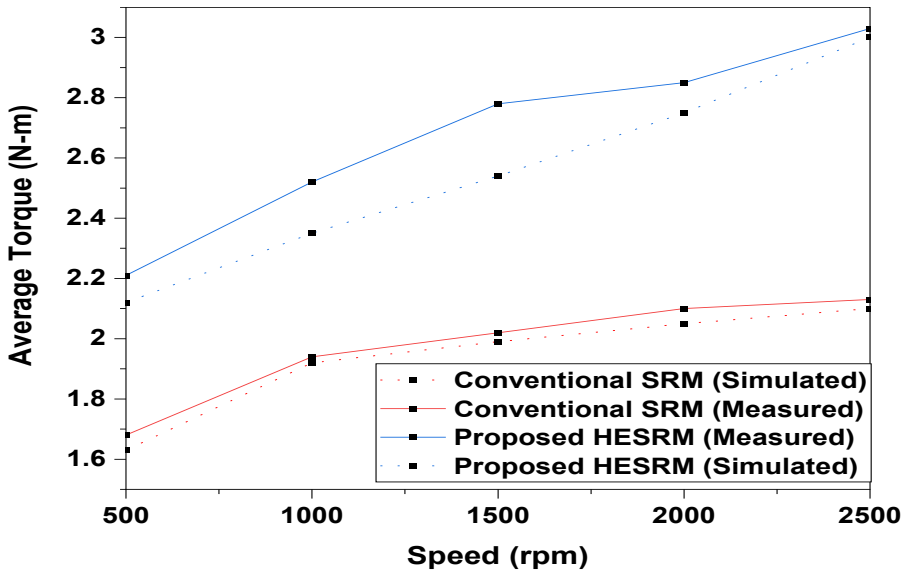

Figure 4.31: Comparison of speed-torque characteristics of two SRMs between measured quantity and those predicted using 2-D finite elements.

Figure 4.31 presents a head-to-head comparison of the speed-torque characteristics of two SRMs, with the measured quantities on the left and the predicted values

on the right using 2-D finite elements. The average torque produced at various speeds from 500 to 2500 rpm is analyzed and compared with the conventional SRM. The conventional SRM produces a torque of 1.6 N-m at low speeds, and the HESRM produces 2.2 N-m. They do not show much difference at maximum speed, which only goes to 2 N-m, and the HESRM output up to 3 N-m.

4.16 Experimental Validation

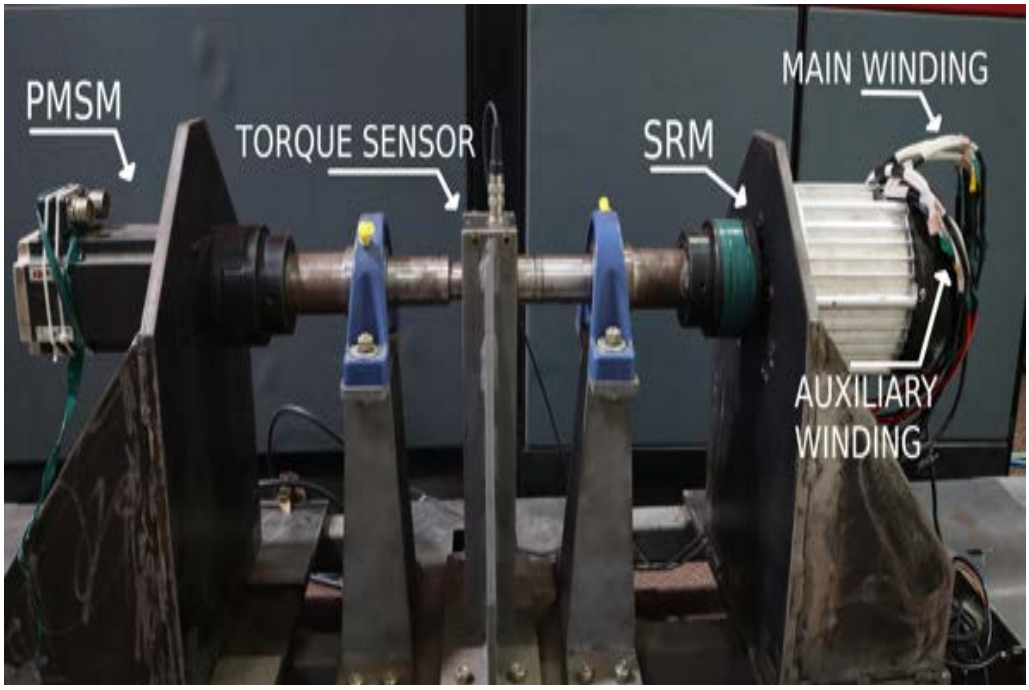

Figure 4.32: Back-to-back set up for torque ripple minimization experimentation.

A back-to-back motor setup uses two electric motors to share a standard shaft and operate in opposite directions. In this back-to-back setup with a permanent magnet synchronous motor and the switched reluctance motor, the two motors are connected in series and operate as a single unit. Various tests can be performed to evaluate the performance of the back-to-back setup under different loads and operating conditions. The smoothness of the torque waveform produced by the back-to-back setup can be analyzed to measure the ripple content produced in the motor, as shown in Figure 4.32.

The windings of the conventional SRM are unsuitable for switching the second topology; hence, it is altered as alternate poles are switched simultaneously. The poles corresponding to R, Y and B are altered as R, R', Y, Y' and B, B's, where R and R' are the main and auxiliary poles, respectively. Since the SRM has concentric windings, the poles could be isolated easily without cutting the winding in half. The winding is given separate excitation as shown in Figure 4.33.

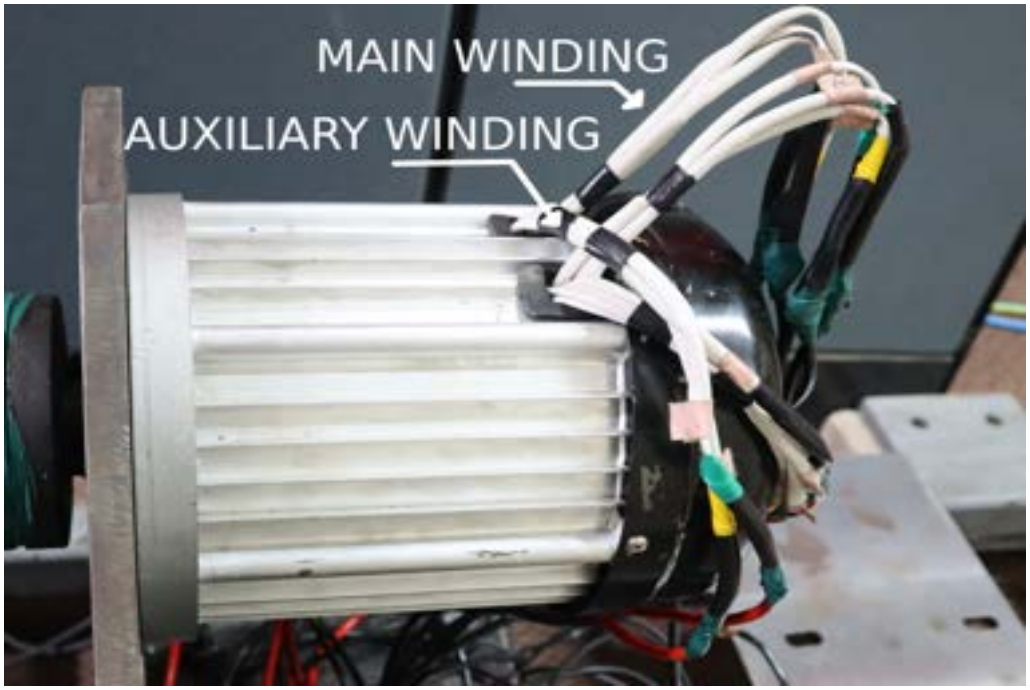

Figure 4.33: Assigning the main and auxiliary winding for DC excitation.

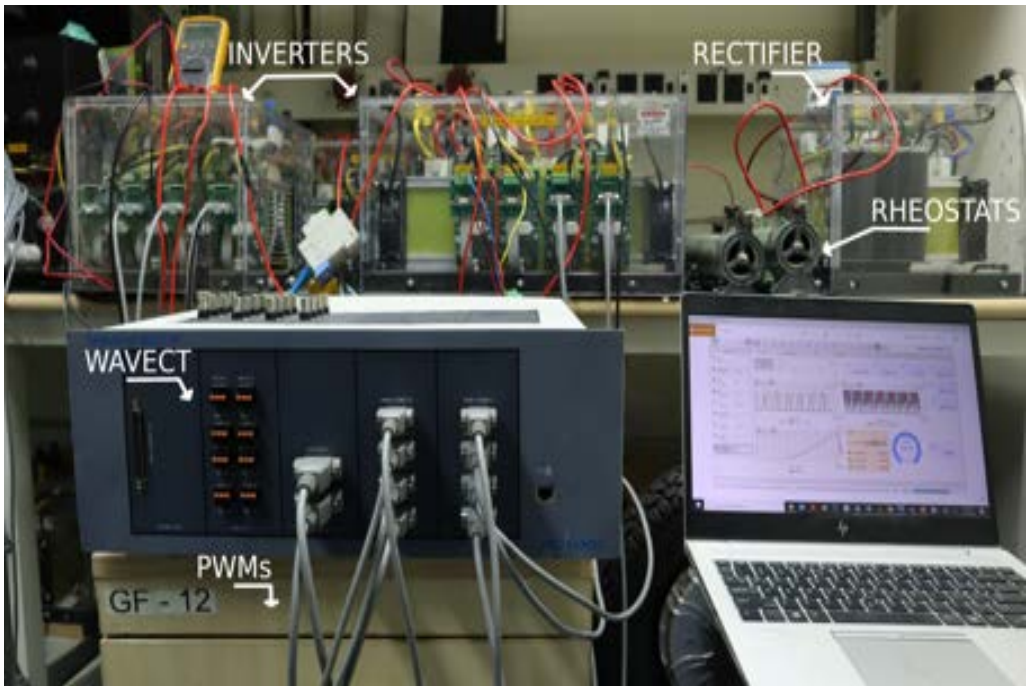

Figure 4.34: Controller circuit for the proposed torque minimization topology.

The controller set-up for the testing of the SRM is shown in Figure 4.34. The PWM signals are generated and provided to the SEMIKRON inverters to switch the phases. The output of the load motor is connected to a rectifier and then to a loaded setup using rheostats.

4.16.1 Transient Response of Two SRM's Drive

The transient response of the second topology with torque ripple minimization is shown in Figure 4.35. It has two windows, one for the main winding excitation and the other for the auxiliary field. The waveforms of the voltage source, phase current for the main, auxiliary winding, speed measurement meter, and rms values are measured.

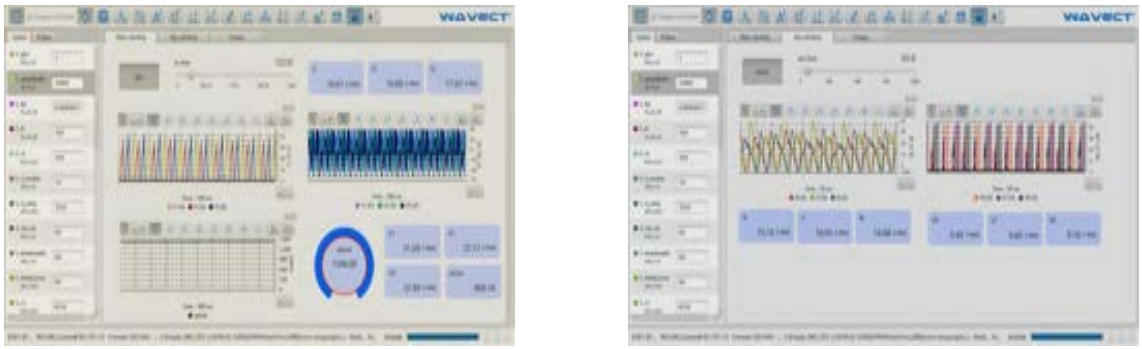

(a) (b)

Figure 4.35: Time-varying excitation characteristics of two SRMs (a) Main winding excitation (b)Auxiliary winding excitation.

4.16.2 Experimental Validation of Torque Ripple

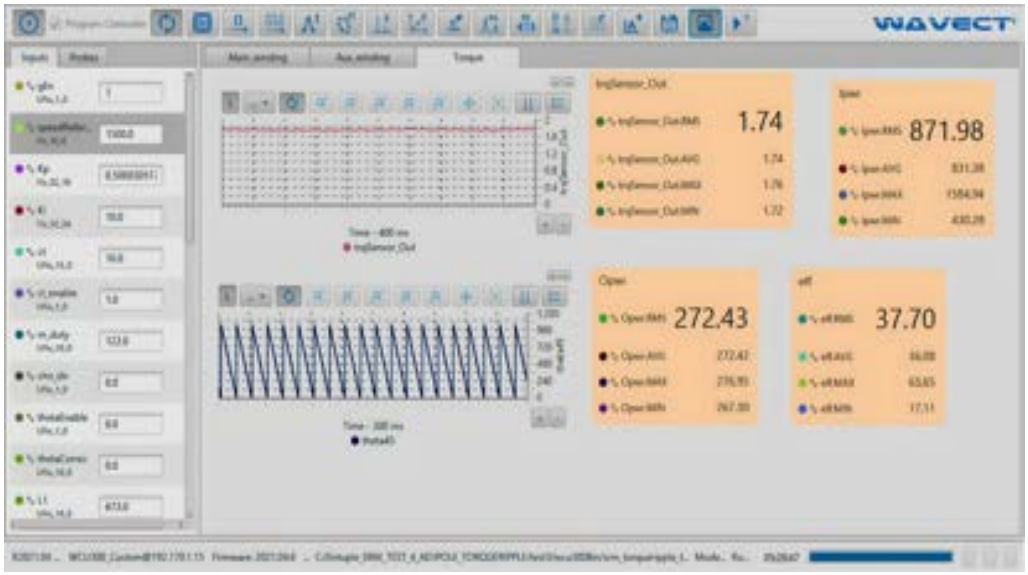

Figure 4.36: Experimental results of Wavect controller outcomes with torque measurement.

The experimental validation of the proposed torque ripple topology is shown in Figure 4.36, in which the average, maximum, and minimum torque values are executed and plotted in the panel. Moreover, the rms values of each iteration are

elaborated in the measurement box. The rms value of torque ripple characteristics is implemented and verified accurately.

4.17 Comparison of Proposed HESRM with Conventional SRM

4.17.1 Torque Ripple

The torque ripple characteristics of the SRMs' output torque compared with other proposed SRMs in all speed ranges. Even though the average torque is high, the torque ripple is relatively high compared to conventional SRM. The conventional method produces an average torque between 2.2 and 2.5N-m at a maximum speed of 2000 rpm. The measured ripple ranges from 2.7% to 4%.

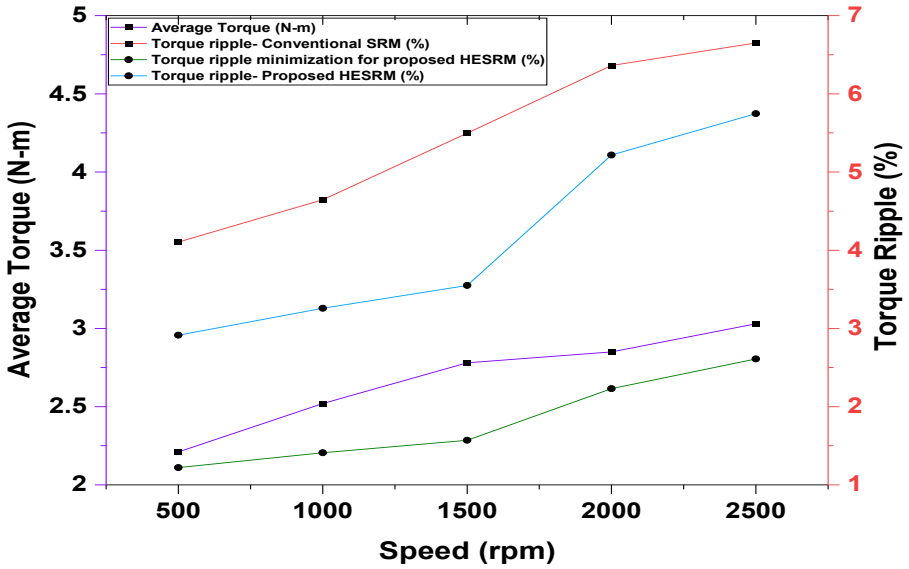

Figure 4.37: Torque ripple comparison of the conventional and proposed SRMs.

As shown in Figure 4.37, the output waveform of the second topology of the proposed SRM at different speeds. Compared to the conventional method, the results reveal a high torque ripple of 3.6% to 8%. This is evident from the fluctuating torque waveform when the current levels change.

In comparison to both the conventional and proposed HESRM, the phase-advancing techniques enabled by the control logic of the torque ripple minimization technique produce outstanding results. At 1500 rpm, the ripple decreases from 3.6% to 3%; at 2000 rpm, it decreases from 8% to 1.4%.

4.17.2 Efficiency

When comparing a conventional SRM with a torque ripple minimized HESRM, the machine typically exhibits higher efficiency due to the reduced energy loss associated with the minimized torque ripple. However, the actual improvement in efficiency will depend on various factors, such as the design of the motor, the operating conditions, and the control strategies used to regulate the motor operation. The efficiency reaches 90%

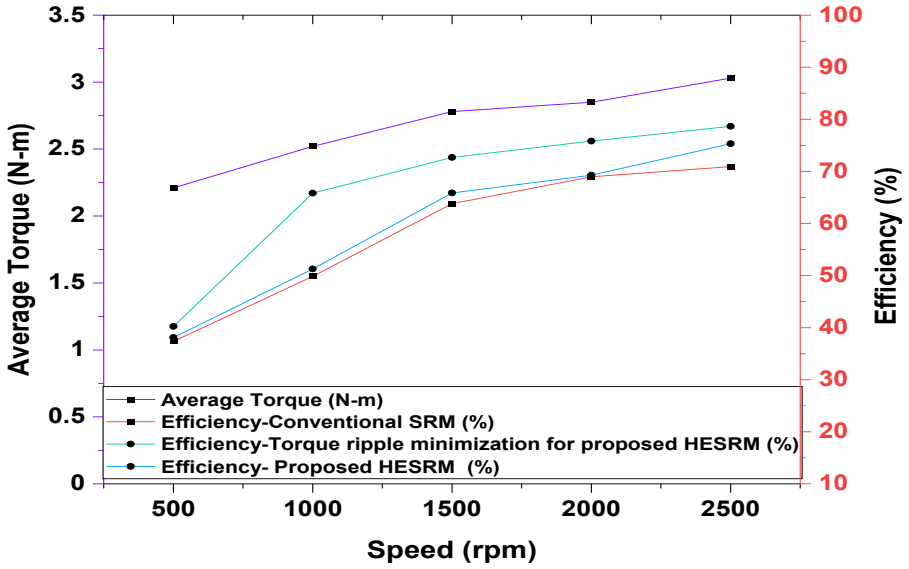

Figure 4.38: Efficiency comparison of the conventional and proposed SRMs.

4.17.3 Input Power

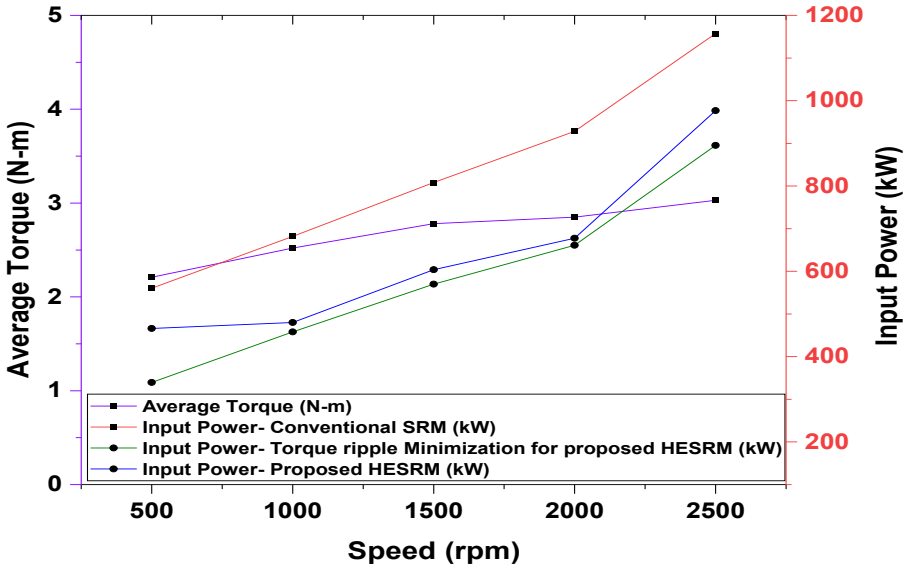

Figure 4.39: Input power comparison of the conventional and proposed SRMs.

Figure 4.39 compares input power (kW) with topology II and the torque ripple minimization results. The input power intake while using the torque ripple minimization technique would be lesser than others. The conventional SRM needed more power when compared with the two SRMs. Furthermore, comparisons with variable speed and average torque with torque ripple are made.

4.18 Comparison of Torque Ripple Minimization in Topology II

Table 4.4 shows the extent to which the second topology of the proposed hybrid excitation method without a permanent magnet excitation cuts down on torque ripple, in which the speed ranged from the lowest value to the maximum, which would have been rated at 2500 rpm. Hence, after adding the criteria for reducing torque ripple to the proposed scheme, the ripple factor decreases by more than 30% in all speed ranges. The speed range of 1500 rpm seemed to be where the most significant reduction happened, with a value of 46%. The nominal reduction percentage for 2500 rpm is 15%. The torque ripple minimized technique achieved an added advantage of high torque with a ripple minimum and consumed less input power than the conventional SRM for all the speed ranges.

Table 4.4: Comparison of torque ripple in topology II

Sl.No	**Speed (rpm)**	**Torque Ripple(%)**	**Torque Ripple Minimization (%)**	**Percentage of Decrease (%)**
1	500	14.58	9	**38.27%**
2	1000	12.25	8.79	**28.24%**
3	1500	10.75	5.74	**46.60%**
4	2000	5.21	3.28	**37.04%**
5	2500	2.71	2.29	**15.49%**

4.19 Inference-Topology II

In Table 4.5, the torque ripple results of conventional topology I and topology II are compared to the output results with minimized ripple. The percentage of output ripple reduction for various speeds indicates that a significant reduction can be achieved at lower speeds, with a maximum of 64% and a minimum of 15%. The second topology develops more torque but produces more ripple than the other methods but can be controlled using advanced control strategies.

Table 4.5: Comparison of torque ripple for different topologies.

Sl.No	Speed (rpm)		Conventional SRM	Percentage of Decrease (%)	Topology 1	Pecentage of Decrease (%)	Topology 2	Percentage of Decrease (%)
1	500	Torque Ripple (%)	6.41		6.35		14.58	
2		Torque Ripple Minimization (%)	2.92	**54.36%**	3.35	**47.20%**	9.00	**38.27%**
3	1000	Torque Ripple (%)	6.11		4.65		12.25	
4		Torque Ripple Minimization (%)	2.89	**52.66%**	1.96	**57.84%**	8.79	**28.24%**
5	1500	Torque Ripple (%)	5.53		4.18		10.75	
6		Torque Ripple Minimization (%)	2.79	**49.48%**	1.53	**63.51%**	5.74	**46.60%**
7	2000	Torque Ripple (%)	4.84		3.55		5.21	
8		Torque Ripple Minimization (%)	2.73	**43.63%**	1.26	**64.67%**	3.28	**37.04%**
9	2500	Torque Ripple (%)	4.11		1.79		2.71	
10		Torque Ripple Minimization (%)	2.29	**43.18%**	1.00	**44.06%**	2.29	**15.49%**

In summary, phase advancing is a technique used to minimize torque ripple in SRMs by adjusting the timing of the stator current pulses to align the magnetic field with the position of the rotor poles. This technique can improve the performance and efficiency of SRMs, reducing unwanted vibrations and noise and improving the overall operation of the motor. This technique enhances the ripple content and preserves the motor's torque output. By enabling this phase, advancing the second topology can be made further efficient by reducing the ripple, which was a significant disadvantage. The improved stability of the torque output allowed for more consistent and reliable performance of the motor, which is reflected in the results of the efficiency and power density tests.

4.20 Conclusions

Switching reluctance motors are suited for various industrial applications because of their high torque density, efficiency, and dependability. However, one of the primary challenges of SRMs is the existence of torque ripple, which may result in vibration, noise, and decreased efficiency.

Reducing torque ripple may result in the smoother running of the motor, leading to enhanced performance with decreased vibration, noise, and efficiency. Moreover, it may result in less mechanical stress on the motor's components, such as the rotor and stator, contributing to a longer motor life and more excellent dependability. Furthermore, less mechanical stress on the motor's components means less wear and tear, resulting in fewer maintenance requirements and downtime.

Torque ripple may also generate electromagnetic interference and noise, which can cause issues with sensitive electronic equipment. Reducing torque ripple may decrease interference and enhance the motor's electromagnetic compatibility. Reducing torque ripple may result in a more consistent output torque, which can enhance

the power quality of the motor by lowering harmonics and enhancing the overall power factor.

Enabling this phase method, advancing the ripple produced in the conventional and HESRM can be significantly reduced. This makes the machine much more suitable for EV application for a better and smoother operation.

In conclusion, decreasing torque ripple in SRMs may enhance performance, life, maintenance, electromagnetic interference, and power quality.

CHAPTER 5

SYSTEM-LEVEL OPTIMIZATION

5.1 Introduction

This section elaborates on the prerequisites for system-level optimization and the method for achieving the optimum value of high average torque with minimum torque ripple. This research consists of many phases of optimization. Chapter 2 depicts the optimization of machine parameters in the initial stage before starting the FEM analysis to determine the optimal design value for achieving the objective. After evaluating and assessing the observational evidence, the proposal has been proven. The hybrid excitation approach, without the necessity of permanent magnet excitation, has achieved the maximum average torque with the lowest torque ripple.

Nonetheless, this strategy seeks to achieve optimal output values by parameter optimization. In light of this, the system-level method using a multi-objective genetic algorithm yields the most precise parameters for the whole system. The system-level strategy encompasses the complete application, including the motor, controller, and EV parameters.

5.2 Objective 4: System-level Optimization in HESRM

Several system-level considerations must be made when optimizing machine and controller parameters for electric vehicle loads. Optimizing machine parameters while constructing economical and high-performance electric vehicles is essential [165, 166]. These are many crucial machine characteristics that may be optimized for electric vehicle applications:

- Electric vehicles need tuned motors for maximum efficiency, power density, and torque output. The vehicle's capacity and speed should determine the size and type of the motor and acceleration needs [167].

- Converter Parameters: The converter circuit switches the phase to drive the motor. The design of the converter may have a measurable impact on the vehicle's efficiency, power production, and thermal performance.

- The control algorithms used in the machines and controllers of electric vehicles are vital to the vehicle's overall performance and efficiency. These algorithms may be optimized to enhance the vehicle's acceleration, braking, and overall driving experience.

An optimization technique for the parameters of machines and controllers for electric vehicle loads necessitates a comprehensive strategy considering several system-level approaches towards the machine and controller parameters [166–170]. By concentrating on efficiency, power density, and control algorithms, electric vehicles with more outstanding performance, range, and dependability may be designed that incorporate motor, controller, and EV as parameters.

5.3 Optimization Algorithms

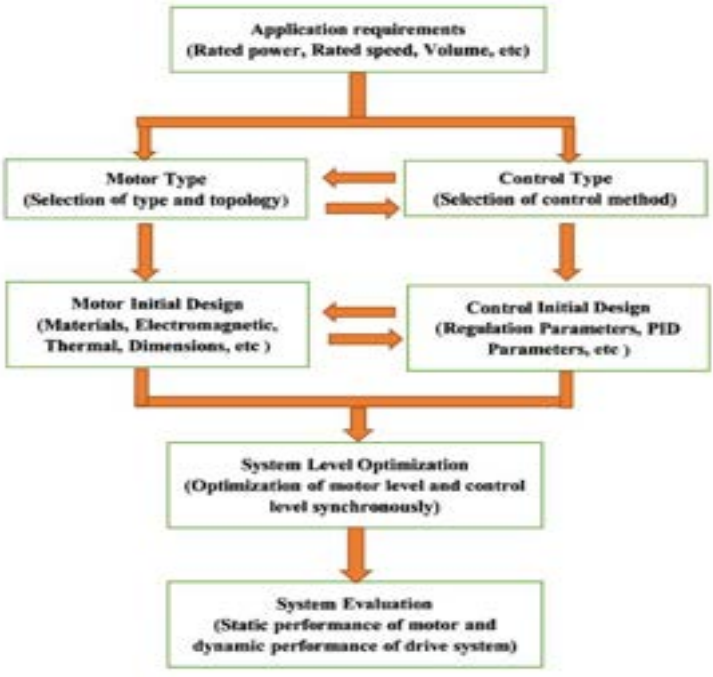

Figure 5.1: Flow chart of the system-level optimization.

Figure 5.1 shows the flowchart for system-level optimization. Assign the application requirements, such as the rated power, speed, size, etc. For this reason, the simulated load parameters from Table 5.2 have all been set to constant values. The motor and controller drive system characterization for the variable speed ranges was evaluated using these fundamental parameters. The motor and the control parameters from the system are separated and optimized individually to create the most optimal solution to meet the two objectives of the final goals. The optimized motor and controller levels are examined synchronously to determine the maximum torque capability within the defined design restrictions. For instance, Ansys/Simplorer can be applied to simulate the performance analysis of the motor drive system.

There are different levels of optimization algorithms to find out the optimum values of parameters for the system. Each algorithm has a different set of solutions for a problem. These all are detailed in the following sections,

5.3.1 Random Surface Methodology

Response surface methodology is a statistical and mathematical optimization approach for processes and systems. RSM entails performing experiments to gather data, constructing a mathematical model that specifies the link between input factors and output response, and using the model to determine the optimal input circumstances that will yield the intended output response [171–174].

RSM is often used in industrial and technical contexts to optimize processes, enhance product quality, and minimize costs. The technique employs statistical instruments such as regression analysis, analysis of variance (ANOVA), and experimental design (DOE).

The essential stages of RSM are:

1. Designing a set of experiments: The first phase of RSM is to create a series of experiments that will enable the gathering of data on the input variables and output response. The experimental design should ensure that the gathered data spans the whole range of input variables [175].

2. Collecting data: The second stage is conducting experiments and collecting input variables and output reaction data. Collecting precise and trustworthy data to verify the model's accuracy is crucial [176].

3. Building a mathematical model: The third phase is constructing a mathematical model that specifies the link between the input variables and the output response. The model may be linear or nonlinear and based on several approaches, including regression analysis or ANOVA.

4. Evaluating the model: The fourth stage analyses the model to verify that it appropriately reflects the link between the input variables and the output response. Statistical approaches such as hypothesis testing, goodness-of-fit tests, and cross-validation may be used.

5. Optimizing the process: The last stage in optimizing the process is using the model to determine the optimal input circumstances to yield the intended output response. Optimization methods such as response surface optimization or Monte Carlo simulation may accomplish this.

RSM is an effective strategy for improving a process or system by constructing a mathematical model representing the link between input factors and output response [177]. In various industrial and technical applications, RSM may assist in decreasing costs, enhancing product quality, and boosting productivity.

5.3.2 Computer-Based Optimal Design

A computer algorithm is used to develop an optimum design for a given issue as a component of the computer-generated optimal design procedure. Typically, the method entails defining the goals of the design and the restrictions that must be met, followed by using an optimization algorithm to confirm the design that best satisfies these requirements [178].

Several optimization methods, such as genetic algorithms, simulated annealing, and particle swarm optimization, may be utilized for computer-generated optimum design [179]. These algorithms repeatedly search the space of potential designs and assess them based on their fitness or goal function.

Several applications exist for computer-generated optimum design, including engineering, product design, and architecture. It may be used, for instance, to design efficient and cost-effective structures, components, and systems or to improve the form and functioning of a building or area [180].

A benefit of the computer-generated optimum design is that it often identifies solutions that would be difficult or impossible to obtain using conventional design techniques [181]. However, it demands a thorough comprehension of the issue and the design goals and proficiency in the selection and use of the optimization technique.

Genetic algorithm approaches have recently been developed to generate these optimal computer-generated designs.

5.3.3 Genetic Algorithm Approach

Genetic algorithms are optimization method that draws inspiration from natural selection and evolution processes. They are often used when conventional optimization

approaches are inefficient or unfeasible to handle complex issues [182].

The fundamental concept behind genetic algorithms is to generate a population of viable solutions and develop and enhance it through natural selection and genetic operators such as mutation and crossover. Each possible answer is represented as a string of genes, and its fitness is determined depending on how effectively it addresses the issue at hand [183, 184].

The genetic algorithm then employs the principles of natural selection to breed the most practical solutions from the population and remove the less advantageous ones. In the expectation that the optimal solution would ultimately emerge, this procedure is repeated across numerous generations.

In addition to engineering design, scheduling, financial modeling, and game-playing, genetic algorithms have been effectively used for various optimization issues [185]. Nevertheless, they may be computationally intensive and need fine-tuning factors like population size, mutation rate, and selection criteria to produce desirable outcomes.

A basic genetic algorithm consists of the following six steps [186–188]:

- Initialization: It is assembling a starting population of possible answers. The problem's complexity often defines the population size, and each solution is frequently represented as a string of genes.

- Evaluation: After creating the initial population, each solution is assessed according to its fitness or objective function. This entails evaluating the effectiveness of each approach in resolving the issue at hand.

- Selection: The fittest solutions within the population are found through a selection method once the fitness of each solution has been established. This often entails discarding weaker answers and choosing ones with a better fitness score.

- Crossover: The next stage combines components from the fittest solutions to generate new ones. Crossover is choosing two or more parent solutions and fusing their Genetic code to produce an entirely new child solution.

- Mutation: Crossover and mutation involve introducing new genetic material into the population. This entails randomly changing one or more population solutions' genes.

- Termination: The algorithm's timing must be decided in the last step. This may depend on completing several generations or discovering a workable solution. The method now returns the best answer discovered throughout the optimization procedure.

In RSM, GA is often used to improve the input parameters of a mathematical model that depicts the system response. Mathematical models often use regression equations to link the system response to the input variables. The optimization process aims to find the collection of input variables that optimizes the system's response.

The benefit of GA in RSM is that it can more quickly and accurately find the ideal input variables than conventional optimization approaches. Getting excellent results, however, takes rigorous parameter optimization and a thorough grasp of the present problem.

5.3.4 Multi-Objective Genetic Algorithm Method

Multiple-objective issues may be solved using the multi-objective genetic algorithm, an optimization approach. MOGA is built on the concepts of genetic and evolutionary algorithms. Instead of focusing on a single purpose, it seeks to identify solutions that best balance many objectives [189]. A population of possible solutions is developed and assessed in a standard MOGA, depending on how much they fulfill certain objective functions and how they fit the objective, gauging a solution's quality concerning each aim. The solutions are developed across generations using genetic operators like mutation, crossover, and selection [190].

The evaluation and the rate of solutions that maximize several goals is one of the main issues in MOGA. MOGA commonly employs a Pareto dominance strategy to accomplish this [181, 191]. If a solution is superior in at least one goal and as good as the other in all objectives, it can dominate the other solution. Pareto optimum solutions are those that are not dominated by any other solutions.

The real benefit of MOGA is that it may provide various compromise solutions between opposing goals in the form of trade-off solutions. This may be helpful in various real-world scenarios where many goals need to be maximized, including resource allocation, financial planning, and engineering design [192, 193].

MOGA does, however, have significant drawbacks. Finding the ideal balance between exploring and using the solution space is one of the significant issues [194–196]. Moreover, MOGA may be computationally demanding, especially when tackling broad or intricate problem areas. However, MOGA is still a solid and popular optimization method for multi-objective problems.

The flow chart shows in Figure 5.2 that the approach for the MOGA optimization technique's algorithm works to help the study achieve its two objectives. Both goals are directly dependent on and influenced by various machines and controller factors. Fix the baseline values of average torque and ripple factor, which are thought to be optimized to maximum average torque and minimal ripple for the design restrictions,

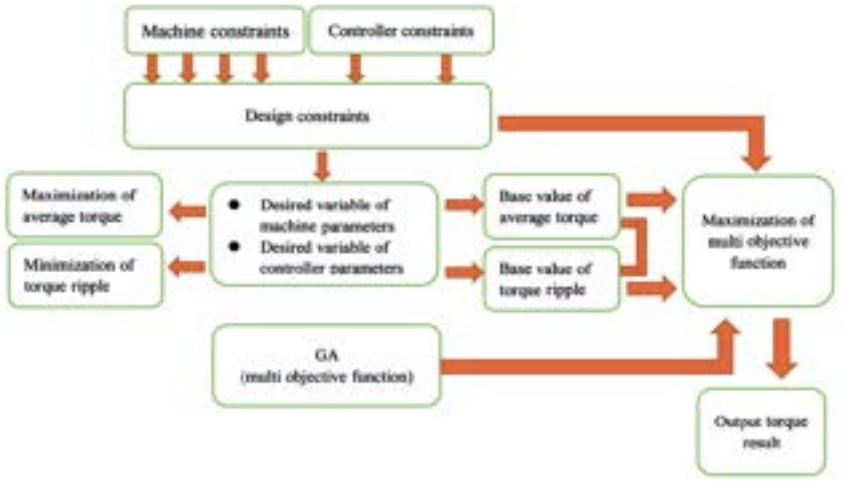

Figure 5.2: Flow chart for the multi-objective genetic algorithm optimization technique.

including the overall system that fits the demands of the EV application. Using consistent EV load characteristics, the machine and controller parameters were individually assessed and optimized from the overall systems.

5.4 Optimization of Parameters in HESRMs

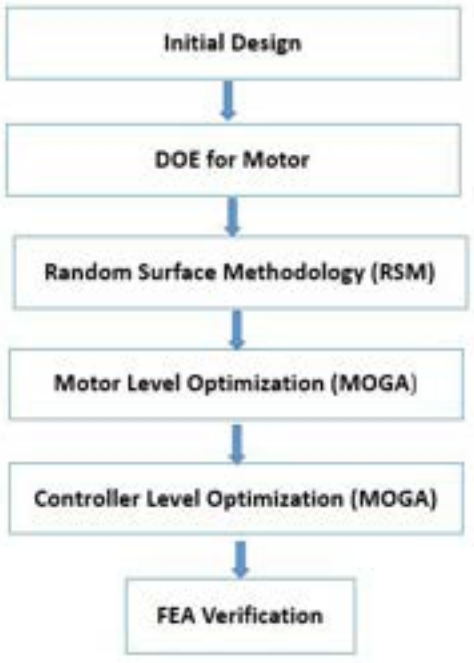

Figure 5.3: Flow chart of the optimization technique employed in this research.

Optimization is a powerful resource that may help determine the designed system's precise value to increase efficiency, improve decision-making, raise accuracy, and speed up calculation [197, 198]. The optimization tools identify novel approaches to issues that might result in innovations.

Table 5.1: Initial parametric value.

Description	Unit	Value
STATOR CORE DATA		
Number of Stator Poles		12
Outer Diameter of Stator	mm	138
Inner Diameter of Stator	mm	82
Yoke Thickness	mm	9
Pole Embrace		0.5
Length of Stator Core	mm	70
Stacking Factor of Stator Core		0.95
STATOR COIL DATA		
Slot Insulation Thickness	mm	0.3
End Length Adjustment	mm	28
Number of Turns per Pole		216
Wire Diameter	mm	0.541
Wire Wrap Thickness	mm	0
ROTOR CORE DATA		
Number of Rotor Poles		8
Length of Air Gap	mm	0.25
Inner Diameter of Rotor	mm	26
Yoke Thickness	mm	18.25
Pole Embrace		0.4
Length of Rotor Core	mm	70

The main dimensions of the stator core, stator coil, and rotor core data, as well as the initial parameters developed for the machine before optimization, are described in Table 5.1. The stator and rotor cores are used in the machine parameters at the initial optimization stage.

This research utilizes two distinct categories to optimize the newly established motor. Figure 5.3 depicts the flow chart for the various optimization phases in this analysis. Before the study, the fundamental categories focus on optimizing the initial base values that reflect the machine design parameters. The factors that affect the average torque and the torque ripple are considered while choosing the parameters. The random initialization of the design machine parameters is assigned to find the optimum value of the proposed motor using the MOGA algorithm with the

FEM approach. Chapter 3 explains in detail the results obtained from the initial optimization analysis.

The second step of optimization, the whole system, focuses on the EV load requirement to accomplish the specified multi-objective functions, for both machine and controller parameters are varied. This study uses a combined finite element analysis of the machine drive system and EV applications. They are split into the first and second optimization levels, where the first concern depends on the machine parameters. It is coupled to the controller and load, directly affecting the torque factors. Second-level design considerations governing the controller parameter are directed to the torque factor that optimization is carried out, which carries out the criteria corresponding to the goals to perform at their highest accurate level.

5.5 System Model

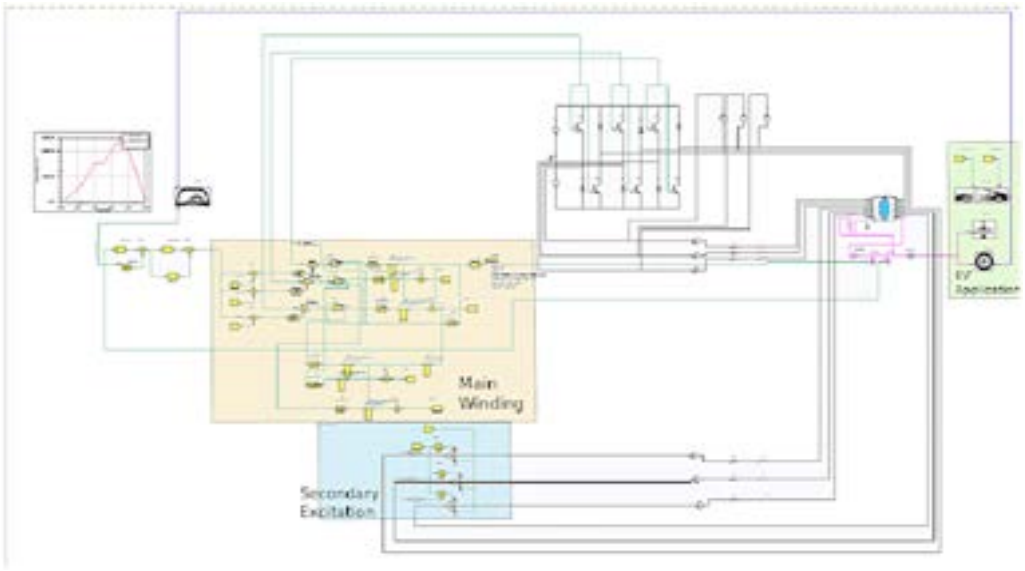

Figure 5.4: System modeling, including main and secondary excitation and vehicle level simulation.

Designing and developing an EV model for real-time system analysis is difficult. Therefore, in the analysis for identifying the operating condition of the EV model, the designed prototyped 1.2 kW standard SRM connecting with a half-car model and executed. The parameters used for the EV design are illustrated in Table 5.2.

For simulation and analysis purposes, the prototyped proposed HESRM research has characteristics similar to EV motors, such as size, weight, and construction. The traction characteristics are to be identified with the help of a system-level approach. The machine operated with 2500 rpm and a rated power of 1.2 N-m are combined to the gear body of 1: 10 to attain the vehicle torque.

The systems are analyzed in the ANSYS/Simplorer platform to set up the models and parameters of the EV motor drive. The optimal data can be used to refine the design and adjust the motor more accurately to simulate the behavior of the actual EV motor.

The results obtained from the vehicle-level simulation by considering gradient, aero-dynamics, tire radius, and numerous other vehicle-level parameters show the performance of proposed machines from the software analysis. Hence, the concept is validated and suitable for vehicle-level applications.

The recommended motor's execution to satisfy the EV requirements is examined by the system model using the platform of Ansys/Simplorer software shown in Figure 5.4. The motor is implemented under the suggested design elements, including the controller to drive the EV load. The main and auxiliary winding controllers are separated and allocated to model the system for the dc injection for high torque performance in the designated EVs. As seen in Table 5.2, the EV load parameters remain constant, and the reference speed for the vehicle is used to drive it. The suggested machine enables the motor to operate with the main windings and uses a variable-speed drive to move the load vehicle. The auxiliary windings controller is connected to the system when the load demands greater torque while maintaining speed.

5.5.1 Torque-Speed Characteristics

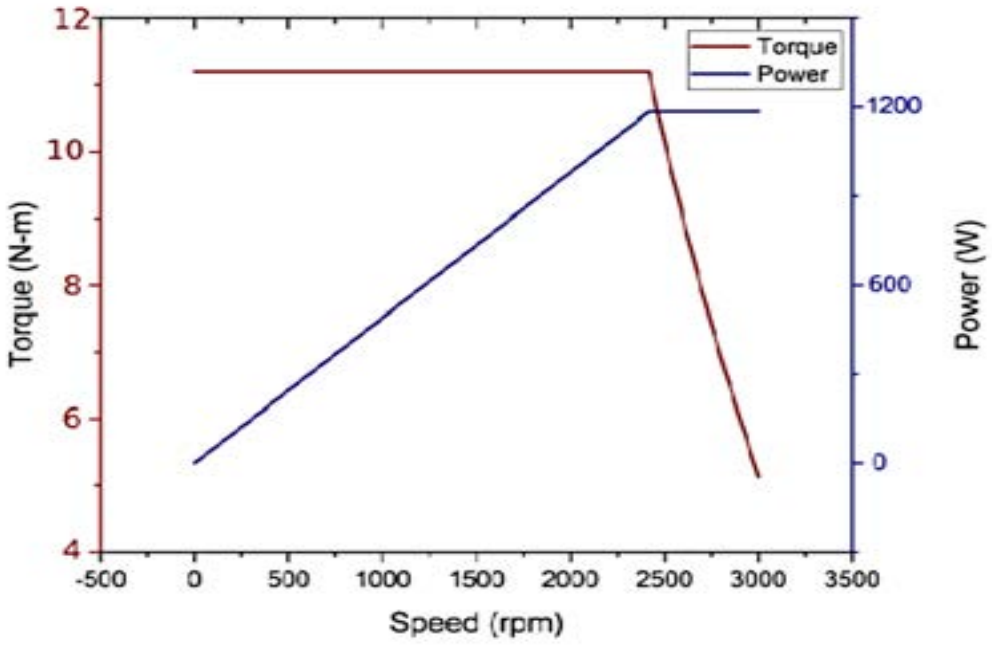

Figure 5.5: Torque-speed characteristics response from the system model analysis.

Table 5.2: Electric vehicle data for system-model simulation.

Vehicle Data	
vehicle type	**Half Car Model**
rider mass	80 kg
vehicle mass	237 kg
CG height	254 mm
drag coefficient	1.2
front axle	1520 mm
rear axle	1400 mm
front area	1.33 m^2
Tire Parameters	
tire-b	10
tire-c	1.9
tire-d	1
tire-e	0.97
tire diameter	18 inch
tire inertia	1e-3 kg*m^2
roll_resistance	0.005

Figure 5.5 displays the observations from the motor characteristics derived from system modeling. The torque-speed characteristics of the suggested machine describe the performance of the EV load. It reaches a maximum average torque of 12 N-m in the constant torque region before dropping when speed is increased. The maximum torque extent for the given design consideration with the rated power is determined by examining the system model.

5.6 Multi-Objective GA Optimization in HESRM

The objectives of first-level optimization for the analysis consider the outer diameter and York thickness, although these two factors are directly associated with torque production. The average torque was associated with the flux path's core effect [199, 200]. Hence, torque and torque ripple can be influenced by the stator and rotor embracing parameters [184, 201]. The second level is also presumed to be the control parameter, which contains the buck converter's gain factor and the PWM signal's

pulse width. For these reasons, MOGA considers these five factors to achieve the highest average torque with the minimal possible torque ripple [197, 202–204].

The mathematical representation of the multi-objective function is

$$Min/Max[f_1(x), f_2(x).....f_n(x)] \tag{5.1}$$

Where $f_i(x)$= i^{th} objective function to be optimized.

n= number of objectives.

$$x(min) \leq (x) \leq x(max) \tag{5.2}$$

The multi-objective function considerations' values vary from initial to final. The values derived from the FEM in Ansys/Maxwell are assessed throughout this approach. Machine and controller restrictions are used to their fullest, the most accurate extent to identify the most acceptable values to fulfill the multi-objective criteria [205–207].

The desired variables for optimizing the motor variables are:

1. Desired Machine Variables (First Level)

1. Outer Diameter of Stator (Dy)
2. Stator Embrace (SPe)
3. Rotor Embrace (RPe)
4. Stator Yoke thickness (Yt)

The desired variables for optimizing the control variables are:

2. Desired Control Variables (Second Level)

1. Pulse Width of PWM (Pw)
2. Buck Gain Factor (AG)

The range of machine constraints values:

- 128 ≤ Dy ≤ 148
- 0.2 ≤ SPe ≤ 0.5
- 0.2 ≤ RPe ≤ 0.5

- $7 \leq \text{Yt} \leq 11$

The range of controller constraints values:

- $12 \leq \text{Pw} \leq 16$
- $0.25 \leq \text{AG} \leq 1$

The maximum average torque obtained within the defined machine design restrictions determined by the system model method is 12 N m. Moreover, the lowest ripple that could be measured after the first round of optimization is 29.5%. Thus, the fixed range of multi-objective functions' maximum and lowest values is as follows:

The first objective is maximizing the average torque in Eqn.5.3.

$$\sum_{i=0}^{n} f(max) \leq T_{avg} \leq 12Nm \tag{5.3}$$

The second objective is minimizing the torque ripple in Eqn.5.4.

$$\sum_{i=0}^{n} f(min) \leq T_{ripple} \leq 29.5\% \tag{5.4}$$

5.6.1 Pareto Result

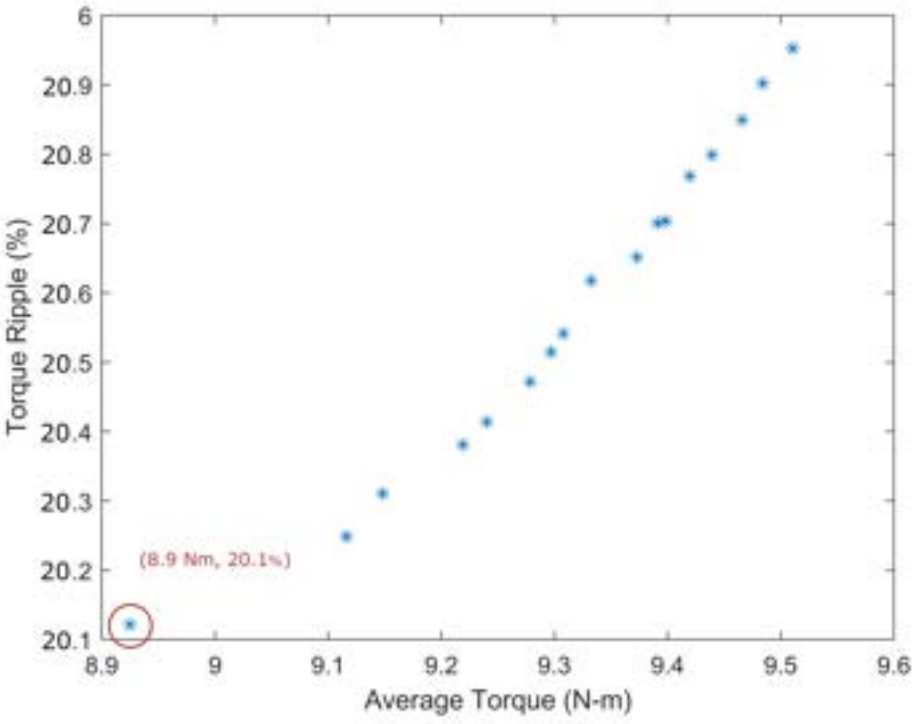

Figure 5.6: Results of first-level optimization for machine parameters.

Figures 5.6 and 5.7 represent the results from the two optimization stage levels. In the first stage, the machine analysis desired variables were optimized, and conclusions were drawn from the findings. The lowest torque ripple begins at 20.1%, and the average torque also rises as the ripple grows. Consequently, the machine-level optimization's best value from the Pareto findings is the minimum torque ripple of 20.1% and high average torque of 8.9 N-m, shown in Figure 5.6.

Consequently, the second-level strategy is based on the controller-level optimization of two desired variables. The outcomes satisfy maximum average torque requirements with the lowest ripples, as shown in Figure 5.7; the values are 10.8 N-m and 15%

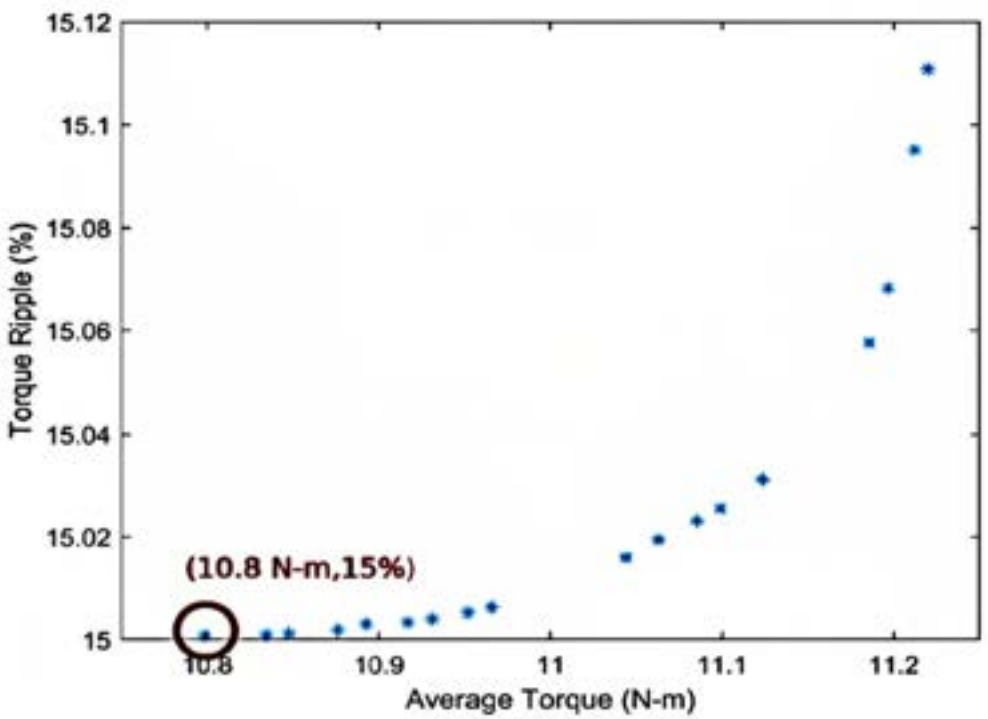

Figure 5.7: Results of second-level optimization for controller parameters.

The rank of chromosome values from lower to higher by goal function and the designated desirable machine parameter variables for the optimization outcomes are shown in Tables 5.3 and 5.4. The four desired variables and the optimization outcomes for achieving the multi-objective goal are shown in Table 5.3. Iterations between 1 and 18 are performed from the analysis to fill the final objectives. The initial set of variables is confirmed for the appropriate machine parameters. The machine variables are V1, V2, V3, and V4; the multi-function goals are F1 and F2. Nevertheless, the yoke thickness and stator outer diameter are standardized at 11.0696 mm and 147.9166 mm, respectively. Moreover, the stator and rotor's embrace factors are 0.485 and 0.4996, respectively, taken from the first second of iterations.

The second level optimization for the controller constants and the set of Pareto

Table 5.3: Iteration results of first-level machine variables

Sl.No	V1	V2	V3	V4	F1	F2
1	147.92	0.485	0.4996	11.07	8.925	20.122
2	147.91	0.4331	0.4997	11.073	9.116	20.249
3	147.95	0.4825	0.4996	11.068	9.148	20.131
4	147.93	0.4598	0.4996	11.08	9.21	20.381
5	147.96	0.4995	0.4982	11.064	9.24	20.414
6	147.94	0.4994	0.4991	11.058	9.278	20.472
7	147.93	0.4538	0.4996	11.052	9.297	20.514
8	147.93	0.4468	0.4997	11.061	9.308	20.541
9	147.91	0.4399	0.4997	11.07	9.332	20.618
10	147.93	0.4973	0.4991	11.073	9.373	20.652
11	147.91	0.4189	0.4997	10.963	9.391	20.7
12	147.96	0.4995	0.4982	11.064	9.398	20.704
13	147.92	0.426	0.4997	10.969	9.42	20.768
14	147.92	0.4739	0.4995	11.079	9.45	20.82
15	147.93	0.4904	0.4995	11.062	9.512	20.94
16	147.95	0.4959	0.4994	11.062	9.565	20.97
17	147.93	0.4594	0.4996	11.064	9.572	20.98
18	147.91	0.467	0.4997	10.97	9.589	20.99

outcomes variables are thus summarised in Table 5.4. Consequently, using the first set of variables, the dual objectives of minimal torque ripple and best average torque are accomplished while adhering to the limitations. The outcomes are shown in Table 5.4- the two control variables V1 and V2 with the multi-function F1 and F2. Finally, the buck gain variable is assigned to its ideal value of 1, and the PWM pulse width of 16 is decided. The first set of iterations is chosen for the minimum ripple data set.

5.7 Result and Discussion

5.7.1 Analysis of Moving Torque

The moving torque characterized after the initial, first-level, and second-level optimization is shown in Figure 5.8. The average torque first approaches a maximum of 2 N-m, then 8.9 N-m during machine controller tuning, and ultimately 10.9 N-m after applying controller settings. According to the sequence of first- and second-level optimization, torque ripple achieves a comparable reduction route after the first stage of 29.5%

Table 5.4: Iteration result of second-level controller variables

Sl.No	V1	V2	F1	F2
1	1	16	10.8	15
2	1	16	10.83	15
3	1	16	10.85	15
4	1	16	10.88	15
5	1	16	10.89	15
6	1	16	10.92	15
7	1	16	10.97	15.01
8	1	16	11.04	15.02
9	1	16	11.06	15.02
10	1	16	11.09	15.02
11	1	16	11.1	15.03
12	1	16	11.12	15.03
13	1	16	11.19	15.06
14	1	16	11.2	15.07
15	1	16	11.21	15.1
16	1	16	11.22	15.11

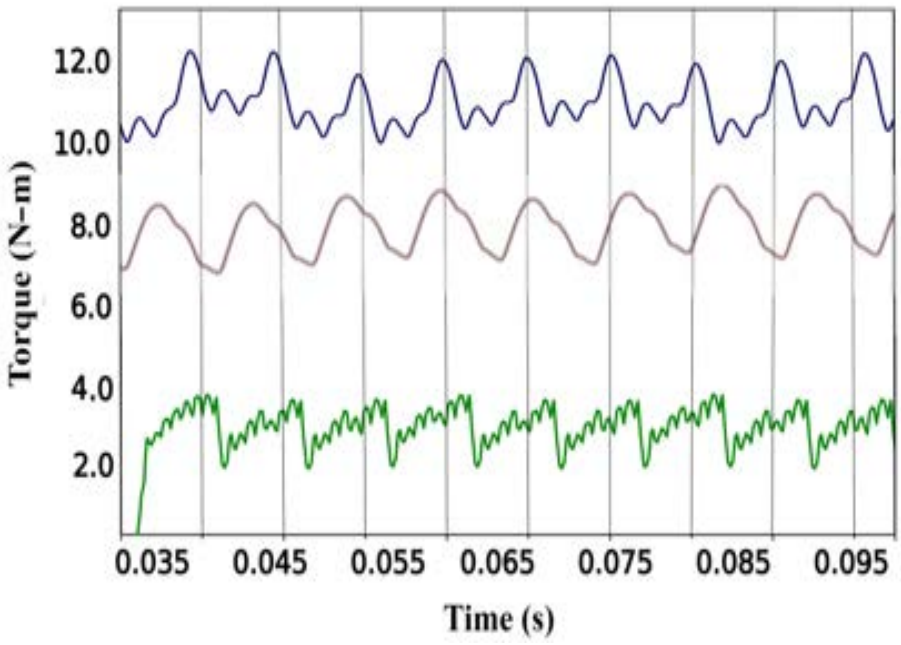

Figure 5.8: Moving torque characteristics before and after optimization.

5.7.2 Result of Parameters Optimized

Table 5.5 provides information on the starting and optimum values for the parameters of the machine and the controller variables. Although the fundamental value for the outside diameter is 138 mm, it increases to 147.91 mm for the optimal values. Similarly, the stator yoke thickness was set between 7 and 11.06 millimeters to increase torque with the slightest ripple. The stator and rotor of the embrace factor shift from their original values of 0.4 to 0.485 and 0.499, respectively. Before and after optimization, the PWM signal's pulse width changes to 15 and 16. The buck converter gain values shift from 0.5 to 1 a consecutively.

Table 5.5: Parameter optimized initial and final values.

Symbol	**Unit**	**Initial Value**	**Optimized**
Outer Diameter of Stator (Dy)	mm	138	147.91
Stator Embrace (SPe)		0.4	0.485
Rotor Embrace (RPe)		0.4	0.499
Stator Yoke thickness (Yt)	mm	7	11.06
Pulse Width of PWM (Pw)		15	16
Buck Gain Factor (AG)		0.5	1

5.7.3 Results of Objectives Before and After Optimization

The evaluated data for the desired machine and controller parameters to satisfy the multi-objective functions F1 and F2 is shown in Table 5.6. Before optimization, the machine's base value had an average torque of 2 N-m and a ripple percentage of 32%

Table 5.6: Evaluation table before and after optimization.

	Desired machine variables				Desired controller variables			
	(Dy)	**(SPe)**	**(RPe)**	**(Yt)**	**(Pw)**	**(AG)**	**F1**	**F2**
Before optimization	138	0.4	0.4	9	15	0.25	2	32%
Initial Optimization	138	0.4	0.4	9	15	0.25	2.5	29.50%
After first level optimization	147.9	0.48	0.49	11	15	0.25	8.9	20.1%
After second level optimization	147.9	0.48	0.49	11	16	1	10.9	15%

5.8 Conclusions

This chapter focused on the system-level optimization techniques for finding the optimum value of parameters to attain the multiple objectives of high average torque with minimum torque ripple. A comprehensive analysis of the motor and the controller are held separately to attain the multi-objective goals. Simultaneously, the result of the synchronized optimum parameters added the performance and load

EV with the help of the system model. From the analysis of performance obtained from the EV model, the proposed system can enhance performance and extend the average torque to the maximum for the designed constraints. Initially, the base motor has a rate of 1.2 kW and attains a maximum torque of 2 N-m. After different optimization stages and executing the proposed strategy in the new HESRM for the specified rate, the maximum torque attains 12 N-m. A specific design developed for the new HESRM results indicates that it fits the application of EVs.

CHAPTER 6

CONCLUSIONS AND RECOMMENDATION FOR FUTURE WORKS

Switched reluctance motors are widely used in different applications because of their constraint features. Whereas, in the field of an electric vehicle, the application incorporates special electrical machines that demand the required performance. For this reason, the SRM is in a leading role that provides the required torque performance, which the existing topology cannot produce without compromising its structural integrity. Existing machines include permanent magnets to provide controllable flux for better performance. In present conditions, placing permanent magnets inside automobile motors is unprecedented. It is inevitable to foresee the future of electronic commutated (EC) motors rectifying these problems. The proposed topology conserves the unique behavior of EC machines, reducing the weight and space required.

A selected number of the poles is separated and independently excited with a different electronic circuit. The total active stator poles of the classic machines to the whole power part are divided into two; 75% of the power is generated with the active poles provided by the main winding. The remaining power from the auxiliary poles with an independent current control algorithm delivers more current for achieving the high torque/power characteristics per the customer's needs. The auxiliary and active poles' external electronic circuits work with the same control and switching frequency, eliminating the separate control circuits.

The proof of concept can be proved with the help of Ansys/Maxwell software analysis with the 20 kW and 1.2 kW rated machines. The results show the torque performance upgraded by 40% within the rated current values. For the new designs, various currents can drive the machines for various applications. In the same phase,

coupled with different current values, the controlled algorithm profiles the current so that the system utilizes the maximum positive inductance region to enhance the flux capability of the machine. The new phase-based current controlled algorithm reduces the usage of rare earth materials and gives customized performance for the specified applications. Correspondingly, it may cause a high degree of redundancy and reduce the risk of failure. Also, these results proved the overload capabilities and the high bandwidth for operating the machine control.

The experimental machine results have proven 40% torque improvement under similar conditions of the motor with the machine rated 1.2 kW, improving the torque per ampere for the utilization of the auxiliary poles. Hence, the primary windings can work in the speed control while the auxiliary windings can work in the current control. The energy efficiency to match the sustainability goals reached 20% higher than the conventional machines. It attained a flat efficiency curve in a wide range of speed and torque loads, which will be a break throughout all applications, particularly in an electric vehicle, where the operational range of the vehicle is the primary source of concern.

The fault-tolerant, maintenance-free, and long life SRM drive has advantages over other ac and dc drives. It overcomes their disadvantages, namely brush maintenance in dc drives, permanent magnet in BLDC motors, and single-phase ac drives. Moreover, the SRM drive can overcome the dependency on magnets from China, with 97% of the world's magnet production in China, the significant raw material for permanent magnet BLDC motors and permanent magnet synchronous machines. There is a substantial potential that Chinese magnet supplies may be cut off and prevent the usage of materials, causing a severe disruption in the permanent magnet motor manufacturing industry.

The dynamic performance of the conventional SRM and the proposed HESRM can be analyzed by enabling a closed-loop model. The experimental setup for the two SRM drives is identical in all aspects and conditions. The conventional drive systems used for the analysis are the traditional methods, and in the auxiliary, excitation is given with the help of additional circuits.

- At the initial stage, the software simulation achieved impressive results. The machine modeling and structural analysis using FEM give the profile of the proposed system's electromagnetic static and average torque responses. Injecting the dc instead of uncontrollable flux may improve the static torque, and the average torque depends on the variable current inputs.

- At low speeds, the HESRM has 1.8 N-m vs. 1 N-m for the conventional. Higher speeds diminish both machines' torque by 2.9 N-m at 2500rpm, and the average

torque peaks at 3.1 N m as speed increases. Due to additional current in the auxiliary, the torque range expands.

- Both motors' efficiencies are almost identical at the beginning of the test at 500 rpm. As speed increases, the efficiency of the HESRM makes clear leads compared to the conventional one. The efficiency of the HESRM has increased by 36%.

- Both motors' power is almost always 500 rpm. The power needed to run the motors increases as the speed increases. The traditional SRM takes more power at all rpm than the proposed one. At 1000 rpm, the standard SRM uses almost 600W of power, while the HESRM uses at least 300 W. At top speed, input power varies by almost 50 W.

6.1 Conclusions

The research proved that the SRM attained a flat efficiency curve in a wide range of speed and torque loads, which will be a breakthrough criterion for electric vehicles. Moreover, the in-dependency on magnets will force the economy to rely less on other nations for the raw materials for motor manufacturing.

Comparing the findings obtained from the conventional and dc-injected hybrid SRMs reveals that significant improvements have been made to the average, static, and speed-torque characteristics. In addition, the properties and the machines' performance are enhanced without losing fundamental qualities. It offers the benefits of high efficiency, high reliability, and redundancy in addition to a high torque per ampere rating. The standard SRM is outperformed by the suggested technique, which generates higher torque at much reduced current levels. In addition, the suggested HESRM uses separate excitation for the winding, allowing the controller greater versatility.

The proposed topology could be the solution for substituting the PM-inserted and the conventional reluctance machines for high torque applications. Indeed, this study illustrates the enhanced performance; thus, the proposed system can be employed in various applications, including electric vehicles. Furthermore, better average and smooth speed torque characteristics have been achieved, which can be an excellent solution for EVs. Finally, this new topology can gain better efficiency with less torque ripple. The future aim of this research is to design and implement advanced optimized controllers for further reducing the torque ripples.

1. From the different topologies, the second topology can produce maximum torque, and there is an increase of 27%, efficiency of 43%, and decrease in the

power input of 29%.

2. The permanent magnet excitation achieves the torque performance only by 20%.

3. The torque ripple reduction attained in the two topologies is 64% and 46%, respectively.

4. In the system-level optimization approach for the machine, parameters reach the average torque of 8.9% with the help of optimum control parameters to attain the torque of 10.9%.

6.2 Impacts of the Thesis

The benefits are that this new model has no permanent magnets, is cost-effective, has less maintenance, is energy-efficient, and is designed to be more compact. It is an excellent torque-speed response for electric vehicle applications, especially high-speed range. The concurred method of excitation helps to stay on the road for a long time, and it may overcome the main challenge of the electric vehicle. The added benefits also enhance domestic appliances' and general machinery's performance and efficiency.

The proposed methods have numerous perks, including better motor control due to the combined action of the two controllers. The proposed method delivers more torque at lower current levels than conventional SRM. Auxiliary windings can be used to inject dc and hence reach the maximum capability of the machine. More flexibility and redundancy: two separate controllers switch the motor. This machine exhibits significantly increased flux in its stator yoke compared to conventional machines. This proposed machine exhibits the highest torque and, hence, the most significant output power capability.

- Greater motor control results from the two controllers working together.
- More torque per ampere: Compared to conventional SRMs, the suggested approach produces higher torque at lower current levels.
- Redundancy: When two controllers operate the motor, one may operate the machine if the other controller malfunctions.
- The motor's high efficiency, which is essential for electric vehicle applications, may be attained with the suggested HESRMs.
- Intelligent control algorithm: The suggested EV motor uses an auxiliary dc to improve torque performance. The independent controllers swap the primary winding to drive the rotor between different positions.

- Reliability: The SRMs' key characteristics were more reliable than other motors. Moreover, the recommended HESRM achieves higher dependability than others.
- The main windings of the proposed HESRMs may be used for speed control, while the auxiliary windings can be used for current management.
- Compared to typical machines, the device has a larger torque capacity because more current may be supplied via the auxiliary to operate the motor at speeds much higher than the rated values.
- Because of its higher average torque and, thus, greater output power capacity, the suggested machine has the greatest torque in all speed ranges.
- Due to the distinct motor and dc injection controllers, the proposed HESRMs are more flexible than the traditional SRMs.
- The auxiliary windings' ability to be utilized to individually inject dc and, therefore, maximize the machine's potential within the limitations of the design is what accounts for the torque enhancement.

6.3 Recommendation for Future Works

These are the relevant areas to be considered for further improving these topologies to a real-time prototype.

Future work will be conducted on the following aspects:

(i) **A sophisticated controller for the separate windings**

1. Modern power electronics converters have a very bright future. Power electronics systems may perform better, be more efficient, and be more reliable when using modern power electronics converters, such as multi-level converters, soft-switching converters, and high-frequency converters. The implementation of the advanced power electronics independent controller for both windings will become a significant advance in the future.

2. The capability of modern power electronics converters to handle larger power levels is another benefit. This is crucial in applications like electric cars and renewable energy systems, with a rising need for high-power systems. Modern power electronics converters, which provide more dependable and efficient power conversion, may aid in meeting this need.

3. Modern power electronics converters may be coupled with other technologies, including energy storage systems and smart grid technologies, to improve their performance further. For instance, modern power electronics converters and energy storage systems may be combined to provide grid stability and peak-shaving capabilities.

4. Advanced power electronics converters have a very bright future. It may anticipate seeing them used more often in various applications, from electric cars and renewable energy systems to industrial and commercial machinery. Nevertheless, adopting these technologies will call for dedication to innovation, cross-industry cooperation, and continuing progress in research and development.

(ii) **Optimization of topologies for the various parameters**

Machine topology optimization applies computer techniques to create machine parts' best topology or arrangement, depending on predetermined criteria, including performance, efficiency, weight, and cost. To find the design that performs the best, the method often entails creating many design iterations and assessing each one in light of the given requirements.

Machine topology optimization may make use of several important factors, including:

1. Performance: A performance metric might be a machine's top speed, torque output, power density, or other performance indicators. Based on these considerations, machines may be designed using the topology optimization method to perform at peak levels.

2. Efficiency: With its potential to significantly affect energy usage and operational costs, efficiency is crucial in many machine design applications. The topology optimization method may be used to build machines that function as efficiently as possible, reducing energy usage and enhancing overall performance.

3. Weight: Machine topology optimization may create as light as feasible components while still fulfilling performance and other design specifications in applications where weight is crucial, such as aerospace or automotive design.

4. Cost: Another crucial aspect of machine design is cost. Topology optimization may create efficient machines to build and satisfy performance and other design criteria.

A designer will often use computer-aided design (CAD) software to generate a virtual model of the machine that can be examined using computational fluid dynamics (CFD), finite element analysis, or other simulation tools to do machine topology optimization. Each design iteration is often created with a new topology or configuration as part of the topology optimization process, and each iteration is then evaluated according to the predetermined criteria.

The best machine topology design is chosen based on a study of each iteration's outcomes. Machine topology optimization is a valuable tool for designers and engineers in various applications because it may improve machine performance, efficiency, weight, and cost considerably.

(iii) **Use of cutting-edge materials**

As technology develops, the use of sophisticated materials in machinery is growing in popularity. Advanced materials provide several advantages over conventional materials, including higher strength, decreased weight, and enhanced resistance to wear and corrosion. Examples of these advanced materials include composites, ceramics, and high-strength alloys. These materials enhance various devices' performance, dependability, and longevity, from industrial machinery to consumer goods.

The strength-to-weight ratio of modern materials is one of their main advantages. For instance, conventional metals like steel or aluminum are substantially heavier than composites while retaining high levels of strength and rigidity. They are thus perfect for usage in systems like airplanes, automobiles, and wind energy systems where weight reduction is crucial. Adopting innovative materials may make machines lighter and more effective, resulting in lower energy use and better performance.

Advanced materials are renowned for their resilience to wear and corrosion and longevity. For instance, ceramic components are perfect for cutting tools, bearings, and other high-wear components because they are solid and wear-resistant. Further enhancing materials' resistance to wear and corrosion is possible via sophisticated coatings and surface treatments, which results in more dependable machines that last longer.

The durability of modern materials in high temperatures and harsh conditions is another advantage. For instance, high-strength alloys and composites may be used in high-temperature applications like gas turbines and engines. In contrast, high-temperature and high-pressure applications like heat exchangers and valves can use ceramics.

Due to their various advantages, modern materials are increasingly being used

in machinery. These materials are perfect for various applications in many sectors because they provide higher performance, decreased weight, increased durability, and increased resistance to wear and corrosion. To anticipate advances in sophisticated materials and their use in machinery as technology develops.

(iv) **Further experimental confirmation of the various topologies is needed**

Further experimental testing of different topologies is required to verify the outcomes of topology optimization. Experimental testing is required to verify the actual performance of the optimized designs, even if computational approaches might provide valuable insights into the performance of various topologies.

The effectiveness of various machine topologies may be evaluated experimentally using a range of measures, including efficiency, power production, durability, and other crucial performance elements. Individual components or whole machines may be tested experimentally using various techniques, including dynamo-meter, temperature, and fatigue.

One advantage of experimental testing is that it may provide insightful input that can be used to improve and enhance the machine's design. For instance, the design may be changed to increase performance if experimental testing identifies a flaw or performance problem in a particular component or topology.

Experiments may also be utilized to verify the precision of computer simulations used for topology optimization. Designers and engineers can confirm the quality of their simulation models and make any required improvements by comparing the outcomes of computational simulations to actual experimental data.

Generally, actual testing is required to confirm the effectiveness of various topologies in practical applications, even if computational approaches are valuable tools for machine topology optimization. Designers and engineers may create optimal machine designs that satisfy the particular performance criteria of their intended use by combining computational modeling and experimental testing.

APPENDIX A

APPENDIX

A.1 Calculation of Torque Equation in SRM

A.1.1 By Electromagnetically Energy Conversion in a Solenoid

The torque production in the switched reluctance motor is explained using the elementary principle of electromechanical energy conversion in a solenoid,

Let N be the number of turns of a solenoid with an excited current of I, and the produced flux is taken as ϕ; then, the electrical input energy is given by the equation.

$$W_e = \int eidt = \int idt\frac{dN\phi}{dt} = \int Nid\phi = \int Fd\phi \tag{A.1}$$

Where e stands for induced emf, and F stands for the mmf. The explained w_e input electrical energy, W_e, is equal to the sum of energy stored in the coil,W_f, and energy converted into mechanical work, W_m. It is written as:

$$W_e = W_f + W_m \tag{A.2}$$

Figure A.1 below shows solenoids and their Flux versus MMF characteristics. When no mechanical work is done, as in the case of the armature starting from position x_1, the stored field energy equals the input electrical energy given by Eq.A.1. This corresponds to area OBEO in Figure A.1. The complement of the field energy, termed co-energy, is given by area OBAO in Figure and mathematically expressed as $\int \phi dF$. Similarly, for the position x_2 of the armature, the field energy corresponds

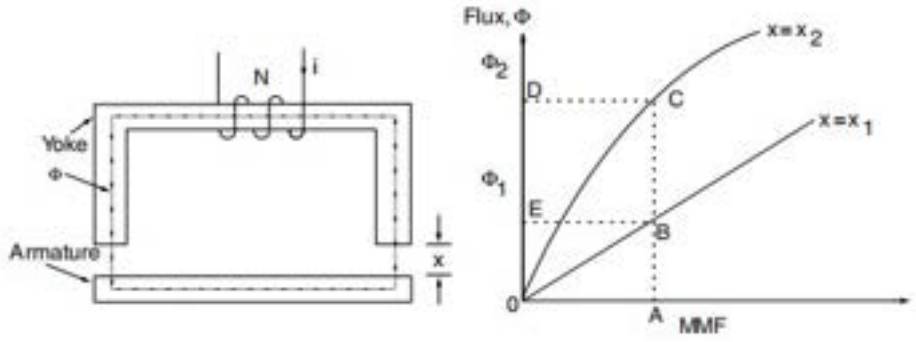

Figure A.1: Solenoid and Flux versus MMF characteristics.

to area OCDO and the co-energy is given by area OCAO. For incremental changes, Eq.A.2 is written as:

$$\delta W_e = \delta W_f + \delta W_m \tag{A.3}$$

For a constant excitation of F_1 given by the operating point A in Figure A.1, the various energies are derived as:

$$\delta W_e = \int_{\Phi_1}^{\phi_2} F_1 d\phi = F_1(\phi_1 - \phi_2) = area(BCDEB) \tag{A.4}$$

$$\delta W_e = \delta W_{f\,|x=x_2} - \delta W_{m\,|x=x_1} = area(OCDO) - area(OBEO) \tag{A.5}$$

Using Eqs. A.3 to A.5, the total mechanical energy is derived as:

$$\delta W_m = \delta W_e - \delta W_f = area(OBCO) \tag{A.6}$$

And that is the area between the two curves for a given magneto-motive force. In the case of a rotating machine, the total mechanical energy in terms of the electromagnetic torque and change in rotor position is written as:

$$\delta W_m = T_e \delta\Theta \tag{A.7}$$

where T_e is the electromagnetic torque and $\delta\theta$ is the incremental rotor angle. Hence, the electromagnetic torque is given by,

$$T_e = \frac{\delta w_m}{\delta\theta} \tag{A.8}$$

For the case of constant excitation (i.e., when the MMF is constant), the incremental mechanical work done is equal to the rate of change of co-energy, which is nothing but the complement of the field energy. Hence, the incremental mechanical work done is written as:

$$\delta W_m = \delta W'_f \tag{A.9}$$

$$W'_f = \int \phi F d = \int \phi d(Ni) = \int (N\phi) di = \int \lambda(\theta, i) di = \int L(\theta, i) i di \tag{A.10}$$

Here, the rotor position and current functions are θ and λ. When the rotor position varies from θ_2 to θ_1, the co-energy also changes, and then the torque equation can give the co-energy represented as a function of rotor position and current.

$$T_e = \frac{\delta w_m}{\delta \theta} = \frac{\delta w'_f}{\delta \theta} = \frac{\delta w'_f(i, \theta)}{\delta \theta} |_(i = constant) \tag{A.11}$$

If the inductance is linearly varying with the rotor position for a given current, then the torque becomes

$$T_e = \frac{dL(\theta, i)}{d\theta} . \frac{i^2}{2} \tag{A.12}$$

where,

$$\frac{dL(\theta, i)}{d\theta} = \frac{L(\theta_2, i) - L(\theta_1, i)}{\theta_2 - \theta_1} |_(i = constant) \tag{A.13}$$

The differential inductance can be considered the torque constant expressed in $N - m/A^2$. At this juncture, it is essential to emphasize that this is not a constant and varies continuously.

A.1.2 By Equivalent Circuit

For finding the torque equation neglecting the mutual inductance between the phases from the equivalent circuit. The applied voltage is equal to the sum of the resistive voltage drop and the rate of the flux linkages and is given as:

$$V = R_s i + \frac{d\lambda(\theta . i)}{dt} \tag{A.14}$$

where, R_s is the resistance per phase, and λ is the flux linkage per phase given by:

$$\lambda = L(\theta, i) i \tag{A.15}$$

Where L is the inductance dependent on the rotor position and phase current.

The Phase voltage equation is given by:

$$V = R_s i + \frac{dL(\theta, i) i}{dt} = R_s i + L(\theta, i) \frac{di}{dt} + i \frac{d\theta}{dt} . \frac{dL(\theta, i)}{d\theta} = R_s i + L(\theta, i) \frac{di}{dt} + \frac{dL(\theta, i)}{d\theta} \omega_m i \tag{A.16}$$

The three terms on the right-hand side represent the resistive voltage drop, inductive voltage drop, and induced emf, respectively. The induced emf is given by:

$$e = \frac{dL(\theta,i)}{d\theta}\omega_m i = K_b \omega_m i \tag{A.17}$$

Here K_b may be construed as an emf constant and is given by,

$$K_b = \frac{dL(\theta,i)}{d\theta} \tag{A.18}$$

From the voltage and the induced emf equation, the equivalent circuit for one phase of the SRM is derived and shown in Figure A.2. While adding the flux linkages in the voltage equation and multiplying with the current, then the input power expression becomes:

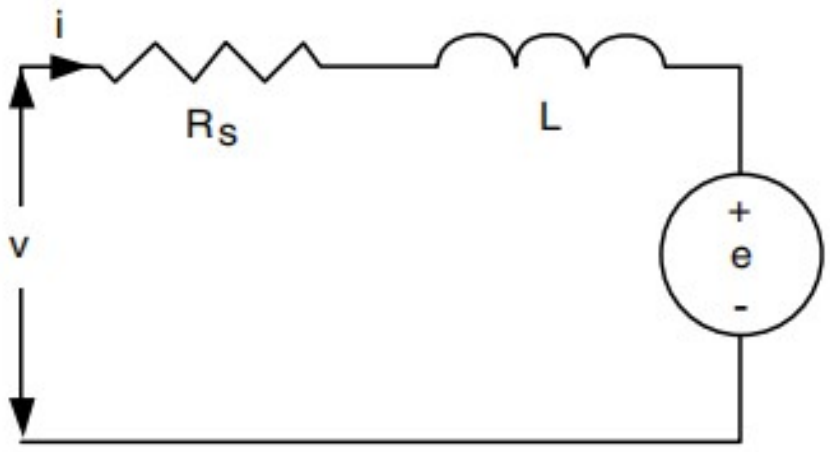

Figure A.2: Equivalent circuit of the SRM.

$$p_i = vi = R_s i^2 + i^2 \frac{dL(\theta,i)}{dt} + L(\theta,i) i \frac{di}{dt} \tag{A.19}$$

The term is physically uninterruptible that can be cast in terms of known variables as in the following:

$$\frac{d}{dt}(\frac{1}{2}(L,\theta)i^2) = L(\theta,i) i \frac{di}{dt} + \frac{1}{2} i^2 \frac{dL(\theta,i)}{dt} \tag{A.20}$$

Substituting the above into Eq. A.19 gives:

$$p_i = vi = R_s i^2 + \frac{d}{dt}(\frac{1}{2}(L,\theta)i^2) + \frac{1}{2} i^2 \frac{dL(\theta,i)}{dt} \tag{A.21}$$

Substituting for the time in terms of the rotor position and speed, with

$$t = \frac{\theta}{\omega_m} \tag{A.22}$$

Then the air-gap power becomes,

$$p_a = \frac{1}{2} i^2 \frac{dL(\theta, i)}{dt} = \frac{1}{2} i^2 \frac{dL(\theta, i)}{d\theta} . \frac{d\theta}{dt} = \frac{1}{2} i^2 \frac{dL(\theta, i)}{d\theta} \omega_m \tag{A.23}$$

The air gap power is the product of the electromagnetic torque and rotor speed expressed by,

$$p_a = \omega_m T_e \tag{A.24}$$

By equating Eqs. A.22 and A.23, the torque obtained is,

$$T_e = \frac{1}{2} i^2 \frac{dL(\theta, i)}{d\theta} \tag{A.25}$$

The equivalent circuit and equations for evaluating electromagnetic torque, air gap power, and input power to the SRM both for dynamic and steady-state operations.

BIBLIOGRAPHY

[1] C. G. Bataille, "Physical and policy pathways to net-zero emissions industry," *Wiley Interdisciplinary Reviews: Climate Change*, vol. 11, no. 2, p. e633, 2020.

[2] J. Rogelj, O. Geden, A. Cowie, and A. Reisinger, "Three ways to improve net-zero emissions targets," *Nature*, vol. 591, no. 7850, pp. 365–368, 2021.

[3] K. Akimoto, "Assessment of road transportation measures for global net-zero emissions considering comprehensive energy systems," *IATSS Research*, 2023.

[4] M. Nieto, "Whatever it takes to reach net zero emissions around 2050 and limit global warming to 1.5 c: the cases of united states, china, european union and japan," *BAFFI CAREFIN Centre Research Paper*, no. 2022-170, 2022.

[5] D. S. Renné, "Progress, opportunities and challenges of achieving net-zero emissions and 100% renewables," *Solar Compass*, p. 100007, 2022.

[6] G. K. Ayetor, "Towards net zero electric vehicle emissions in africa," *Current Sustainable/Renewable Energy Reports*, pp. 1–7, 2022.

[7] A. Nunes, L. Woodley, and P. Rossetti, "Re-thinking procurement incentives for electric vehicles to achieve net-zero emissions," *Nature Sustainability*, vol. 5, no. 6, pp. 527–532, 2022.

[8] T.-C. Kuo, Y.-S. Shen, N. Sriwattana, and R.-H. Yeh, "Toward net-zero: The barrier analysis of electric vehicle adoption and transition using anp and dematel," *Processes*, vol. 10, no. 11, p. 2334, 2022.

[9] H. Treasury, "Net zero review: Interim report," 2020.

[10] G. Zhao and J. Baker, "Effects on environmental impacts of introducing electric vehicle batteries as storage-a case study of the united kingdom," *Energy Strategy Reviews*, vol. 40, p. 100819, 2022.

[11] K. G. Logan, J. D. Nelson, C. Brand, and A. Hastings, “Phasing in electric vehicles: Does policy focusing on operating emission achieve net zero emissions reduction objectives?” *Transportation Research Part A: Policy and Practice*, vol. 152, pp. 100–114, 2021.

[12] V. Heinisch, L. Göransson, R. Erlandsson, H. Hodel, F. Johnsson, and M. Odenberger, “Smart electric vehicle charging strategies for sectoral coupling in a city energy system,” *Applied Energy*, vol. 288, p. 116640, 2021.

[13] M. Chaudry, L. Jayasuriya, S. Blainey, M. Lovric, J. W. Hall, T. Russell, N. Jenkins, and J. Wu, “The implications of ambitious decarbonisation of heat and road transport for britain,Äôs net zero carbon energy systems,” *Applied Energy*, vol. 305, p. 117905, 2022.

[14] S. Majumder, K. De, and P. Kumar, “Zero emission transportation system,” in *2016 IEEE International Conference on Power Electronics, Drives and Energy Systems (PEDES)*. IEEE, 2016, pp. 1–6.

[15] F. Czerwinski, “Critical minerals for zero-emission transportation,” *Materials*, vol. 15, no. 16, p. 5539, 2022.

[16] S. R. Jape and A. Thosar, “Comparison of electric motors for electric vehicle application,” *international Journal of Research in Engineering and Technology*, vol. 6, no. 09, pp. 12–17, 2017.

[17] Z. Cao, A. Mahmoudi, S. Kahourzade, and W. L. Soong, “An overview of electric motors for electric vehicles,” in *2021 31st Australasian Universities Power Engineering Conference (AUPEC)*. IEEE, 2021, pp. 1–6.

[18] P. Bhatt, H. Mehar, and M. Sahajwani, “Electrical motors for electric vehicle–a comparative study,” *Proceedings of Recent Advances in Interdisciplinary Trends in Engineering & Applications (RAITEA)*, 2019.

[19] H. El Hadraoui, M. Zegrari, A. Chebak, O. Laayati, and N. Guennouni, “A multi-criteria analysis and trends of electric motors for electric vehicles,” *World Electric Vehicle Journal*, vol. 13, no. 4, p. 65, 2022.

[20] S. Madichetty, S. Mishra, and M. Basu, “New trends in electric motors and selection for electric vehicle propulsion systems,” *IET Electrical Systems in Transportation*, vol. 11, no. 3, pp. 186–199, 2021.

[21] E. Alaca, N. F. O. Serteller, and G. Komurgoz, “Comparison of permanent magnet electric motors used in electric vehicles,” in *2022 IEEE 20th International Power Electronics and Motion Control Conference (PEMC)*. IEEE, 2022, pp. 107–112.

[22] N. F. OYMAN SERTELLER, "Comparison of permanent magnet electric motors used in electric vehicles," 2022.

[23] S. Hamidizadeh, *Study of magnetic properties and demagnetization models of permanent magnets for electric vehicles application*. McGill University (Canada), 2016.

[24] C. P. Cho and R. H. Johnston, "Electric motors in vehicle applications," in *Proceedings of the IEEE International Vehicle Electronics Conference (IVEC'99)(Cat. No. 99EX257)*. IEEE, 1999, pp. 193–198.

[25] T. Finken, M. Hombitzer, and K. Hameyer, "Study and comparison of several permanent-magnet excited rotor types regarding their applicability in electric vehicles," in *2010 Emobility-Electrical Power Train*. IEEE, 2010, pp. 1–7.

[26] X. Xu, X. Qiao, N. Zhang, J. Feng, and X. Wang, "Review of intelligent fault diagnosis for permanent magnet synchronous motors in electric vehicles," *Advances in Mechanical Engineering*, vol. 12, no. 7, p. 1687814020944323, 2020.

[27] M. Toren, "Comparatıve analysis of the magnet effects on the permanent magnet bldc motor performance used in electric vehicles," *Electrical Engineering*, vol. 104, no. 5, pp. 3411–3423, 2022.

[28] B. Lv, L. Shi, L. Li, K. Liu, and J. Jing, "Performance analysis of asymmetrical less-rare-earth permanent magnet motor for electric vehicle," *IET Electrical Systems in Transportation*, vol. 12, no. 1, pp. 36–48, 2022.

[29] Y. Lan, Y. Benomar, K. Deepak, A. Aksoz, M. E. Baghdadi, E. Bostanci, and O. Hegazy, "Switched reluctance motors and drive systems for electric vehicle powertrains: State of the art analysis and future trends," *Energies*, vol. 14, no. 8, p. 2079, 2021.

[30] R. B. Inderka, M. Menne, and R. W. De Doncker, "Control of switched reluctance drives for electric vehicle applications," *IEEE Transactions on Industrial Electronics*, vol. 49, no. 1, pp. 48–53, 2002.

[31] K. M. Rahman, B. Fahimi, G. Suresh, A. V. Rajarathnam, and M. Ehsani, "Advantages of switched reluctance motor applications to ev and hev: design and control issues," *IEEE transactions on industry applications*, vol. 36, no. 1, pp. 111–121, 2000.

[32] C. Gan, J. Wu, Q. Sun, W. Kong, H. Li, and Y. Hu, "A review on machine topologies and control techniques for low-noise switched reluctance motors in electric vehicle applications," *IEEE Access*, vol. 6, pp. 31 430–31 443, 2018.

[33] Z. Wang, T. W. Ching, S. Huang, H. Wang, and T. Xu, "Challenges faced by electric vehicle motors and their solutions," *IEEE Access*, vol. 9, pp. 5228–5249, 2020.

[34] M. S. Kumar and S. T. Revankar, "Development scheme and key technology of an electric vehicle: An overview," *Renewable and Sustainable Energy Reviews*, vol. 70, pp. 1266–1285, 2017.

[35] J. De Santiago, H. Bernhoff, B. Ekergård, S. Eriksson, S. Ferhatovic, R. Waters, and M. Leijon, "Electrical motor drivelines in commercial all-electric vehicles: A review," *IEEE Transactions on vehicular technology*, vol. 61, no. 2, pp. 475–484, 2011.

[36] A. E. Aliasand and F. Josh, "Selection of motor foran electric vehicle: A review," *Materials Today: Proceedings*, vol. 24, pp. 1804–1815, 2020.

[37] M. Agrawal and M. S. Rajapatel, "Global perspective on electric vehicle 2020," *International Journal of Engineering Research & Technology*, vol. 9, no. 1, pp. 8–11, 2020.

[38] K. M. Rahman and M. Ehsani, "Performance analysis of electric motor drives for electric and hybrid electric vehicle applications," in *Power Electronics in Transportation*. IEEE, 1996, pp. 49–56.

[39] X. Xue, K. W. E. Cheng, and N. Cheung, "Selection of electric motor drives for electric vehicles," in *2008 Australasian Universities power engineering conference*. IEEE, 2008, pp. 1–6.

[40] M. Yildirim, M. Polat, and H. Kürüm, "A survey on comparison of electric motor types and drives used for electric vehicles," in *2014 16th International Power Electronics and Motion Control Conference and Exposition*. IEEE, 2014, pp. 218–223.

[41] A. A. S. Bukhari, W. Cao, T. Yuan, and K. A. Samo, "International journal of engineering sciences & research technology design and comparative investigation of a 12/8 and a 6/4 switched reluctance machines for electric vehicles."

[42] N. Hashemnia and B. Asaei, "Comparative study of using different electric motors in the electric vehicles," in *2008 18th International Conference on Electrical Machines*. IEEE, 2008, pp. 1–5.

[43] C. Chan, "Present status and future trends of electric vehicles," in *1993 2nd International Conference on Advances in Power System Control, Operation and Management, APSCOM-93.* IET, 1993, pp. 456–469.

[44] A. Bălţăţanu and L. M. Florea, "Comparison of electric motors used for electric vehicles propulsion," in *Proceeding of International Conference of Scientific Paper AFASES*, 2013.

[45] J. F. Gieras and N. Bianchi, "Electric motors for light traction," *EPE journal*, vol. 14, no. 1, pp. 12–23, 2004.

[46] T. A. Zarma, A. A. Galadima, and M. A. Aminu, "Review of motors for electrical vehicles," *Journal of Scientific Research and Reports*, vol. 24, no. 6, pp. 1–6, 2019.

[47] M. Hernandez, M. Messagie, O. Hegazy, L. Marengo, O. Winter, and J. Van Mierlo, "Environmental impact of traction electric motors for electric vehicles applications," *The International Journal of Life Cycle Assessment*, vol. 22, pp. 54–65, 2017.

[48] X. Sun, Z. Li, X. Wang, and C. Li, "Technology development of electric vehicles: A review," *Energies*, vol. 13, no. 1, p. 90, 2019.

[49] S. J. Rind, Y. Ren, Y. Hu, J. Wang, and L. Jiang, "Configurations and control of traction motors for electric vehicles: A review," *Chinese Journal of Electrical Engineering*, vol. 3, no. 3, pp. 1–17, 2017.

[50] M. Kebriaei, A. H. Niasar, and B. Asaei, "Hybrid electric vehicles: An overview," in *2015 International Conference on Connected Vehicles and Expo (ICCVE)*. IEEE, 2015, pp. 299–305.

[51] A. Thattil, S. Vachhani, D. Raval, P. Patel, and P. Sharma, "Comparative study of using different electric motors for ev," *International Research Journal of Engineering and Technology (IRJET)*, vol. 6, no. 4, pp. 4601–4604, 2019.

[52] Z. Zhu, W. Chu, and Y. Guan, "Quantitative comparison of electromagnetic performance of electrical machines for hevs/evs," *CES Transactions on Electrical Machines and Systems*, vol. 1, no. 1, pp. 37–47, 2017.

[53] M. Zeraoulia, M. E. H. Benbouzid, and D. Diallo, "Electric motor drive selection issues for hev propulsion systems: A comparative study," *IEEE Transactions on Vehicular technology*, vol. 55, no. 6, pp. 1756–1764, 2006.

[54] M. Wardach, R. Palka, P. Paplicki, P. Prajzendanc, and T. Zarebski, "Modern hybrid excited electric machines," *Energies*, vol. 13, no. 22, p. 5910, 2020.

[55] A. A. Abd Elhafez, M. A. Aldalbehia, N. F. Aldalbehia, F. R. Alotaibi, N. A. Alotaibia, and R. S. Alotaibi, "Comparative study for machine candidates for high speed traction applications," *International Journal of Electrical Engineering*, vol. 10, no. 1, pp. 71–84, 2017.

[56] D. Baidya, S. Dhopte, and M. Bhattacharjee, "Sensing system assisted novel pid controller for efficient speed control of dc motors in electric vehicles," *IEEE Sensors Letters*, 2023.

[57] N. Akhtar and V. Patil, "Electric vehicle technology: Trends and challenges," *Smart Technologies for Energy, Environment and Sustainable Development, Vol 2: Select Proceedings of ICSTEESD 2020*, pp. 621–637, 2022.

[58] V. Gulhane, M. Tarambale, and Y. Nerkar, "A scope for the research and development activities on electric vehicle technology in pune city," in *2006 IEEE Conference on Electric and Hybrid Vehicles*. IEEE, 2006, pp. 1–8.

[59] G. Boztas, M. Yildirim, and O. Aydogmus, "Design and analysis of multiphase bldc motors for electric vehicles," *Engineering, Technology & Applied Science Research*, vol. 8, no. 2, pp. 2646–2650, 2018.

[60] R. Pindoriya, B. Rajpurohit, R. Kumar, and K. Srivastava, "Comparative analysis of permanent magnet motors and switched reluctance motors capabilities for electric and hybrid electric vehicles," in *2018 IEEMA Engineer Infinite Conference (eTechNxT)*. IEEE, 2018, pp. 1–5.

[61] A. Sheela, M. Suresh, V. G. Shankar, H. Panchal, V. Priya, M. Atshaya, K. K. Sadasivuni, and S. Dharaskar, "Fea based analysis and design of pmsm for electric vehicle applications using magnet software," *International Journal of Ambient Energy*, vol. 43, no. 1, pp. 2742–2747, 2022.

[62] X. Liu, M. Li, and M. Xu, "Kriging assisted on-line torque calculation for brushless dc motors used in electric vehicles," *International Journal of Automotive Technology*, vol. 17, pp. 153–164, 2016.

[63] A. M. Lulhe and T. N. Date, "A technology review paper for drives used in electrical vehicle (ev) & hybrid electrical vehicles (hev)," in *2015 international*

conference on control, instrumentation, communication and computational technologies (ICCICCT). IEEE, 2015, pp. 632–636.

[64] A. Anekunu, S. Chowdhury, and S. Chowdhury, "A review of research and development on switched reluctance motor for electric vehicles," in *2013 IEEE Power & Energy Society General Meeting*. IEEE, 2013, pp. 1–5.

[65] J. G. West, "Dc, induction, reluctance and pm motors for electric vehicles," *Power Engineering Journal*, vol. 8, no. 2, pp. 77–88, 1994.

[66] K. Vijayakumar, R. Karthikeyan, S. Paramasivam, R. Arumugam, and K. Srinivas, "Switched reluctance motor modeling, design, simulation, and analysis: a comprehensive review," *IEEE Transactions on Magnetics*, vol. 44, no. 12, pp. 4605–4617, 2008.

[67] M. Ehsani, K. M. Rahman, and H. A. Toliyat, "Propulsion system design of electric and hybrid vehicles," *IEEE Transactions on industrial electronics*, vol. 44, no. 1, pp. 19–27, 1997.

[68] Y. Yang, A. Walton, R. Sheridan, K. Güth, R. Gauß, O. Gutfleisch, M. Buchert, B.-M. Steenari, T. Van Gerven, P. T. Jones *et al.*, "Ree recovery from end-of-life ndfeb permanent magnet scrap: a critical review," *Journal of Sustainable Metallurgy*, vol. 3, pp. 122–149, 2017.

[69] J.-W. Ahn and G. F. Lukman, "Switched reluctance motor: Research trends and overview," *CES Transactions on Electrical Machines and Systems*, vol. 2, no. 4, pp. 339–347, 2018.

[70] P. Andrada, M. Torrent, B. Blanqué, and J. Perat, "Switched reluctance drives for electric vehicle applications," *RE & PQJ*, vol. 1, no. 1, pp. 311–317, 2003.

[71] S. W. Moore, K. M. Rahman, and M. Ehsani, "Effect on vehicle performance of extending the constant power region of electric drive motors," *SAE transactions*, pp. 2187–2191, 1999.

[72] A. Lange, W.-R. Canders, F. Laube, and H. Mosebach, "Comparison of different drive systems for a 75 kw electrical vehicle drive," in *ICEM 2000: international conference on electrical machines (Espoo, 28-30 August 2000)*, 2000, pp. 1308–1312.

[73] O. Bitsche, J. Friedrich, and K. NOREIKAT, "Electric drives for hybrid, fuel cell and battery powered vehicles," in *International conference on electrical machines*, 2000, pp. 1317–1321.

[74] A. Rajapakshe, U. K. Madawala, and D. Muthumani, "A model for a fly-wheel driven by a grid connected switch reluctance machine," in *2008 IEEE International Conference on Sustainable Energy Technologies*. IEEE, 2008, pp. 1025–1030.

[75] N. Zabihi and R. Gouws, "A review on switched reluctance machines for electric vehicles," in *2016 IEEE 25th International Symposium on Industrial Electronics (ISIE)*. IEEE, 2016, pp. 799–804.

[76] J. Lindsay, R. Arumugam, and R. Krishnan, "Finite-element analysis characterisation of a switched reluctance motor with multitooth per stator pole," in *IEE Proceedings B (Electric Power Applications)*, vol. 133, no. 6. IET, 1986, pp. 347–353.

[77] J. Corda and J. Stephenson, "Analytical estimation of the minimum and maximum inductances of a double salient motor," in *International Conference on Stepping Motors and Systems*. The Department of Electrical and Electronic Engineering, University of Leeds, 1979, pp. 50–59.

[78] T. S. Donahoe and A. R. Nelson, "Electrically operated linear motor with integrated flexure spring and circuit for use in reciprocating compressor," Oct. 10 2000, uS Patent 6,129,527.

[79] T. J. E. Miller, *Switched reluctance motors and their control*. Magna physics publishing and clarendon press, 1993.

[80] R. Krishnan, *Switched reluctance motor drives: modeling, simulation, analysis, design, and applications*. CRC press, 2017.

[81] A. Labak and N. C. Kar, "Designing and prototyping a novel five-phase pancake-shaped axial-flux srm for electric vehicle application through dynamic fea incorporating flux-tube modeling," *IEEE Transactions on Industry Applications*, vol. 49, no. 3, pp. 1276–1288, 2013.

[82] C. Lee, R. Krishnan, and N. S. Lobo, "Novel two-phase switched reluctance machine using common-pole e-core structure: concept, analysis, and experimental verification," *IEEE transactions on industry applications*, vol. 45, no. 2, pp. 703–711, 2009.

[83] J. D. Widmer and B. C. Mecrow, "Optimized segmental rotor switched reluctance machines with a greater number of rotor segments than stator slots," *IEEE Transactions on Industry Applications*, vol. 49, no. 4, pp. 1491–1498, 2013.

[84] W. Ding, G. Liu, and P. Li, "A hybrid control strategy of hybrid-excitation switched reluctance motor for torque ripple reduction and constant power extension," *IEEE Transactions on Industrial Electronics*, vol. 67, no. 1, pp. 38–48, 2019.

[85] M. A. Kabir and I. Husain, "Design of mutually coupled switched reluctance motors (mcsrms) for extended speed applications using 3-phase standard inverters," *IEEE Transactions on Energy Conversion*, vol. 31, no. 2, pp. 436–445, 2015.

[86] T. Higuchi, Y. Nakao, and T. Abe, "Characteristics of a novel segment type srm with 2-step slide rotor," in *2009 International Conference on Electrical Machines and Systems*. IEEE, 2009, pp. 1–4.

[87] Z. Xu, J. Liu, M.-J. Kim, D.-H. Lee, and J.-W. Ahn, "Characteristics analysis and comparison of conventional and segmental rotor type 12/8 switched reluctance motors," *IEEE Transactions on Industry Applications*, vol. 55, no. 3, pp. 3129–3137, 2018.

[88] B. Mecrow, E. El-Kharashi, J. Finch, and A. Jack, "Segmental rotor switched reluctance motors with single-tooth windings," *IEE Proceedings-Electric Power Applications*, vol. 150, no. 5, pp. 591–599, 2003.

[89] J. Oyama, T. Higuchi, T. Abe, and K. Tanaka, "The fundamental characteristics of novel switched reluctance motor with segment core embedded in aluminum rotor block," in *2005 International Conference on Electrical Machines and Systems*, vol. 1. IEEE, 2005, pp. 515–519.

[90] T. Higuchi, K. Suenaga, and T. Abe, "Torque ripple reduction of novel segment type switched reluctance motor by increasing phase number," in *2009 International Conference on Electrical Machines and Systems*. IEEE, 2009, pp. 1–4.

[91] X. Chen, Z. Deng, X. Wang, J. Peng, and X. Li, "New designs of switched reluctance motors with segmental rotors," 2010.

[92] Z. Xu, K.-I. Jeong, D.-H. Lee, and J.-W. Ahn, "Preliminary performance evaluation of a novel 12/8 segmental rotor type srm," in *2016 19th International Conference on Electrical Machines and Systems (ICEMS)*. IEEE, 2016, pp. 1–5.

[93] R. Vandana, N. Vattikuti, and B. Fernandes, "A novel high power density segmented switched reluctance machine," in *2008 IEEE Industry Applications Society Annual Meeting*. IEEE, 2008, pp. 1–7.

[94] Z. Xu and J.-W. Ahn, "A novel 6/5 segmental rotor type switched reluctance motor: Concept, design and analysis," in *2013 International Conference on Electrical Machines and Systems (ICEMS)*. IEEE, 2013, pp. 582–585.

[95] J. D. Widmer, R. Martin, and B. C. Mecrow, "Optimization of an 80-kw segmental rotor switched reluctance machine for automotive traction," *IEEE Transactions on Industry Applications*, vol. 51, no. 4, pp. 2990–2999, 2015.

[96] W. Ding, Y. Hu, and L. Wu, "Investigation and experimental test of fault-tolerant operation of a mutually coupled dual three-phase srm drive under faulty conditions," *IEEE Transactions on Power Electronics*, vol. 30, no. 12, pp. 6857–6872, 2015.

[97] W. Ding, Z. Yin, L. Liu, J. Lou, Y. Hu, and Y. Liu, "Magnetic circuit model and finite-element analysis of a modular switched reluctance machine with e-core stators and multi-layer common rotors," *IET Electric Power Applications*, vol. 8, no. 8, pp. 296–309, 2014.

[98] K. Nakamura and O. Ichinokura, "Super-multipolar permanent magnet reluctance generator designed for small-scale wind-turbine generation," *IEEE Transactions on Magnetics*, vol. 48, no. 11, pp. 3311–3314, 2012.

[99] W. Ding, S. Yang, Y. Hu, S. Li, T. Wang, and Z. Yin, "Design consideration and evaluation of a 12/8 high-torque modular-stator hybrid excitation switched reluctance machine for ev applications," *IEEE Transactions on industrial electronics*, vol. 64, no. 12, pp. 9221–9232, 2017.

[100] E. Sunan, F. Kucuk, H. Goto, H.-J. Guo, and O. Ichinokura, "Three-phase full-bridge converter controlled permanent magnet reluctance generator for small-scale wind energy conversion systems," in *2014 IEEE PES Asia-Pacific Power and Energy Engineering Conference (APPEEC)*. IEEE, 2014, pp. 1–9.

[101] M. Abd Elmutalab, A. Elrayyah, T. Husain, and Y. Sozer, "Extending the speed range of a switched reluctance motor using a fast demagnetizing technique," *IEEE Transactions on Industry Applications*, vol. 54, no. 4, pp. 3294–3304, 2018.

[102] K. Lu, U. Jakobsen, and P. O. Rasmussen, "Single-phase hybrid switched reluctance motor for low-power low-cost applications," *IEEE transactions on magnetics*, vol. 47, no. 10, pp. 3288–3291, 2011.

[103] N. Ding, K. Prasad, and T. T. Lie, "The electric vehicle: a review," *International Journal of Electric and Hybrid Vehicles*, vol. 9, no. 1, pp. 49–66, 2017.

[104] Y. Hasegawa, K. Nakamura, and O. Ichinokura, "A novel switched reluctance motor with the auxiliary windings and permanent magnets," *IEEE transactions on magnetics*, vol. 48, no. 11, pp. 3855–3858, 2012.

[105] W. Ding, H. Fu, and Y. Hu, "Characteristics assessment and comparative study of a segmented-stator permanent-magnet hybrid-excitation srm drive with high-torque capability," *IEEE Transactions on Power Electronics*, vol. 33, no. 1, pp. 482–500, 2017.

[106] W. Ding, Y. Hu, H. Fu, and Q. Chen, "Evaluation of a segmented-stator hybrid excitation switched reluctance machine with permanent magnets for electric vehicles," in *2016 Eleventh International Conference on Ecological Vehicles and Renewable Energies (EVER)*. IEEE, 2016, pp. 1–8.

[107] C. Zhihui, S. Yaping, and Y. Yangguang, "Static characteristics of a novel hybrid excitation doubly salient machine," in *2005 International Conference on Electrical Machines and Systems*, vol. 1. IEEE, 2005, pp. 718–721.

[108] E. Sulaiman, T. Kosaka, and N. Matsui, "High power density design of 6-slot–8-pole hybrid excitation flux switching machine for hybrid electric vehicles," *IEEE Transactions on Magnetics*, vol. 47, no. 10, pp. 4453–4456, 2011.

[109] S. Jia, R. Qu, J. Li, D. Li, and W. Kong, "A stator-pm consequent-pole vernier machine with hybrid excitation and dc-biased sinusoidal current," *IEEE transactions on magnetics*, vol. 53, no. 6, pp. 1–4, 2017.

[110] R. Y. Tang *et al.*, "Modern permanent magnet machines: theory and design," *Beijing: Mechanism Industry*, pp. 1–4, 1997.

[111] G. Velmurugan, S. Bozhko, and T. Yang, "A review of torque ripple minimization techniques in switched reluctance machine," in *2018 IEEE International Conference on Electrical Systems for Aircraft, Railway, Ship Propulsion and Road Vehicles & International Transportation Electrification Conference (ESARS-ITEC)*. IEEE, 2018, pp. 1–6.

[112] J.-W. Ahn, S.-J. Park, and D.-H. Lee, "Hybrid excitation of srm for reduction of vibration and acoustic noise," *IEEE Transactions on Industrial Electronics*, vol. 51, no. 2, pp. 374–380, 2004.

[113] K. Lu, P. O. Rasmussen, S. J. Watkins, and F. Blaabjerg, "A new low-cost hybrid switched reluctance motor for adjustable-speed pump applications," *IEEE Transactions on Industry Applications*, vol. 47, no. 1, pp. 314–321, 2010.

[114] D. Wang, Z. Feng, H. Zheng, and X. Wang, "Comparative analysis of different topologies of linear switched reluctance motor with segmented secondary for vertical actuation systems," *IEEE Transactions on Energy Conversion*, vol. 36, no. 4, pp. 2634–2645, 2021.

[115] V. Petrus, A. Pop, C. Martis, J. Gyselinck, and V. Iancu, "Design and comparison of different switched reluctance machine topologies for electric vehicle propulsion," in *The XIX International Conference on Electrical Machines-ICEM 2010*. IEEE, 2010, pp. 1–6.

[116] E. Elwakil and M. Darwish, "Critical review of converter topologies for switched reluctance motor drives," 2007.

[117] O. Ellabban and H. Abu-Rub, "Switched reluctance motor converter topologies: A review," in *2014 IEEE international conference on industrial technology (ICIT)*. IEEE, 2014, pp. 840–846.

[118] V. V. Hadke and M. P. Thakre, "Integrated multilevel converter topology for speed control of srm drive in plug in-hybrid electric vehicle," in *2019 3rd International Conference on Trends in Electronics and Informatics (ICOEI)*. IEEE, 2019, pp. 1013–1018.

[119] M. Deepak, G. Janaki, and C. Bharatiraja, "Power electronic converter topologies for switched reluctance motor towards torque ripple analysis," *Materials Today: Proceedings*, vol. 52, pp. 1657–1665, 2022.

[120] S. Vukosavic and V. R. Stefanovic, "Srm inverter topologies: A comparative evaluation," *IEEE Transactions on industry applications*, vol. 27, no. 6, pp. 1034–1047, 1991.

[121] H. Plesko, J. Biela, J. Luomi, and J. W. Kolar, "Novel concepts for integrating the electric drive and auxiliary dc–dc converter for hybrid vehicles," *IEEE transactions on power electronics*, vol. 23, no. 6, pp. 3025–3034, 2008.

[122] M. A. Khan, A. Ahmed, I. Husain, Y. Sozer, and M. Badawy, "Performance analysis of bidirectional dc–dc converters for electric vehicles," *IEEE transactions on industry applications*, vol. 51, no. 4, pp. 3442–3452, 2015.

[123] E. Van Dijk, J. Spruijt, D. M. O'sullivan, and J. B. Klaassens, "Pwm-switch modeling of dc-dc converters," *IEEE Transactions on Power electronics*, vol. 10, no. 6, pp. 659–665, 1995.

[124] V. Abhijith, M. Hossain, G. Lei, and A. Premlal, "Performance improvement of switched reluctance motor using hybrid excitation method without permanent magnets," in *2021 24th International Conference on Electrical Machines and Systems (ICEMS)*. IEEE, 2021, pp. 74–78.

[125] V. Abhijith, M. Hossain, G. Lei, and P. A. Sreelekha, "A hybrid excited switched reluctance motor for torque enhancement without permanent magnet behavior in electric vehicle applications."

[126] V. Abhijith, M. Hossain, G. Lei, P. A. Sreelekha, T. P. Monichan, and S. V. Rao, "Hybrid switched reluctance motors for electric vehicle applications with high torque capability without permanent magnet," *Energies*, vol. 15, no. 21, p. 7931, 2022.

[127] H. Vasquez and J. K. Parker, "A new simplified mathematical model for a switched reluctance motor in a variable speed pumping application," *Mechatronics*, vol. 14, no. 9, pp. 1055–1068, 2004.

[128] A. Nirgude, M. Murali, N. Chaithanya, S. Kulkarni, V. Bhole, and S. R. Patel, "Nonlinear mathematical modeling and simulation of switched reluctance motor," in *2016 IEEE International Conference on Power Electronics, Drives and Energy Systems (PEDES)*. IEEE, 2016, pp. 1–6.

[129] V. Tkachuk and M. Klytta, "Switched reluctance motor and its mathematical model," in *2007 Compatibility in Power Electronics*. IEEE, 2007, pp. 1–5.

[130] M. Chaple and S. B. Bodkhe, "The simulation and mathematical modeling of switched reluctance motor based on phase winding inductance," in *2017 International Conference on Energy, Communication, Data Analytics and Soft Computing (ICECDS)*. IEEE, 2017, pp. 3048–3052.

[131] K. Deguchi, S. Sumita, and Y. Enomoto, "Analytical method applying a mathematical model for axial-gap-switched reluctance motor," *Electrical Engineering in Japan*, vol. 196, no. 3, pp. 30–38, 2016.

[132] M. Ayaz and A. B. Yildiz, "An equivalent circuit model for switched reluctance motor," in *MELECON 2006-2006 IEEE Mediterranean Electrotechnical Conference*. IEEE, 2006, pp. 1182–1185.

[133] W. Sun, Q. Li, L. Sun, L. Zhu, and L. Li, "Electromagnetic analysis on novel rotor-segmented axial-field srm based on dynamic magnetic equivalent circuit," *IEEE Transactions on Magnetics*, vol. 55, no. 6, pp. 1–5, 2019.

[134] D. Lin, P. Zhou, S. Stanton, and Z. Cendes, "An analytical circuit model of switched reluctance motors," *IEEE Transactions on Magnetics*, vol. 45, no. 12, pp. 5368–5375, 2009.

[135] V. Valdivia, R. Todd, F. J. Bryan, A. Barrado, A. Lázaro, and A. J. Forsyth, "Behavioral modeling of a switched reluctance generator for aircraft power systems," *IEEE Transactions on Industrial Electronics*, vol. 61, no. 6, pp. 2690–2699, 2013.

[136] F. P. Cebolla, A. Martinez, B. Martin, E. Laloya, C. Montano, S. Méndez, and J. Vicuña, "Experimental equivalent circuit parameters identification of a switched reluctance motor," in *2009 35th Annual Conference of IEEE Industrial Electronics*. IEEE, 2009, pp. 1140–1145.

[137] N. Grebennikov, T. Talakhadze, and A. Kashuba, "Equivalent magnetic circuit for switched reluctance motor with strong mutual coupling between phases," in *2019 26th international workshop on electric drives: improvement in efficiency of electric drives (IWED)*. IEEE, 2019, pp. 1–5.

[138] M. Dowlatshahi, S. M. S. Nejad, and J.-W. Ahn, "Torque ripple minimization of switched reluctance motor using modified torque sharing function," in *2013 21st Iranian conference on electrical engineering (ICEE)*. IEEE, 2013, pp. 1–6.

[139] J. Widmer, B. Mecrow, C. Spargo, R. Martin, and T. Celik, "Use of a 3 phase full bridge converter to drive a 6 phase switched reluctance machine," in *6th IET international conference on power electronics, machines and drives (PEMD 2012)*. IET, 2012, pp. 1–6.

[140] T. Husain, A. Elrayyah, Y. Sozer, and I. Husain, "Unified control for switched reluctance motors for wide speed operation," *IEEE Transactions on Industrial Electronics*, vol. 66, no. 5, pp. 3401–3411, 2018.

[141] A. Vagati, M. Pastorelli, G. Francheschini, and S. C. Petrache, "Design of low-torque-ripple synchronous reluctance motors," *IEEE Transactions on industry applications*, vol. 34, no. 4, pp. 758–765, 1998.

[142] R. S. Wallace and D. G. Taylor, "A balanced commutator for switched reluctance motors to reduce torque ripple," *IEEE Transactions on Power Electronics*, vol. 7, no. 4, pp. 617–626, 1992.

[143] H.-J. Hu, G.-Z. Cao, S.-D. Huang, C. Wu, and Y.-P. Peng, "Drive circuit-based torque-ripple suppression method for single-phase bldc fan motors to re-

duce acoustic noise," *IET Electric Power Applications*, vol. 13, no. 7, pp. 881–888, 2019.

[144] W. A. Salah, D. Ishak, and K. J. Hammadi, "Minimization of torque ripples in bldc motors due to phase commutation-a review," *Przeglad Elektrotechniczny*, vol. 87, no. 1, pp. 182–188, 2011.

[145] I. Husain and M. Ehsani, "Torque ripple minimization in switched reluctance motor drives by pwm current control," *IEEE transactions on power electronics*, vol. 11, no. 1, pp. 83–88, 1996.

[146] K. Zhang, G. Li, Z. Zhu, and G. Jewell, "Investigation on contribution of inductance harmonics to torque production in multiphase doubly salient synchronous reluctance machines," *IEEE Transactions on Magnetics*, vol. 55, no. 4, pp. 1–10, 2019.

[147] T. Husain, A. Elrayyah, Y. Sozer, and I. Husain, "Adaptive flux weakening control of switched reluctance machines in rotating reference frame," in *2013 IEEE Energy Conversion Congress and Exposition*. IEEE, 2013, pp. 912–919.

[148] I. Husain, "Minimization of torque ripple in srm drives," *IEEE transactions on Industrial Electronics*, vol. 49, no. 1, pp. 28–39, 2002.

[149] H. Kotb, A. H. Yakout, M. A. Attia, R. A. Turky, and K. M. AboRas, "Speed control and torque ripple minimization of srm using local unimodal sampling and spotted hyena algorithms based cascaded pid controller," *Ain Shams Engineering Journal*, vol. 13, no. 4, p. 101719, 2022.

[150] M. J. Navardi, B. Babaghorbani, and A. Ketabi, "Efficiency improvement and torque ripple minimization of switched reluctance motor using fem and seeker optimization algorithm," *Energy Conversion and Management*, vol. 78, pp. 237–244, 2014.

[151] S. Kurian and G. Nisha, "Torque ripple minimization of srm using torque sharing function and hysteresis current controller," in *2015 International Conference on Control Communication & Computing India (ICCC)*. IEEE, 2015, pp. 149–154.

[152] C. Labiod, K. Srairi, B. Mahdad, and M. Benbouzid, "A novel control technique for torque ripple minimization in switched reluctance motor through destructive interference," *Electrical Engineering*, vol. 100, pp. 481–490, 2018.

[153] A. Chithrabhanu and K. Vasudevan, "Online compensation for torque ripple reduction in srm drives," in *2017 IEEE Transportation Electrification Conference (ITEC-India)*. IEEE, 2017, pp. 1–6.

[154] A. Shahabi, A. Rashidi, and S. Saghaian-Nejad, "Torque ripple reduction of srm drives below the base speed using commutation angles control," in *2013 21st Iranian Conference on Electrical Engineering (ICEE)*. IEEE, 2013, pp. 1–6.

[155] S. J. Evangeline and S. S. Kumar, "Torque ripple minimization of switched reluctance drives-a survey," in *5th IET International Conference on Power Electronics, Machines and Drives (PEMD 2010)*. IET, 2010, pp. 1–6.

[156] D. Mohanraj, J. Gopalakrishnan, B. Chokkalingam, and L. Mihet-Popa, "Critical aspects of electric motor drive controllers and mitigation of torque ripple-review," *IEEE Access*, 2022.

[157] M. S. Islam and J. Husain, "Torque-ripple minimization with indirect position and speed sensing for switched reluctance motors," *IEEE Transactions on Industrial Electronics*, vol. 47, no. 5, pp. 1126–1133, 2000.

[158] R. Abdel-Fadil, F. Al-Amyal, and L. Számel, "Torque ripples minimization strategies of switched reluctance motor-a review," in *2019 International IEEE Conference and Workshop in Óbuda on Electrical and Power Engineering (CANDO-EPE)*. IEEE, 2019, pp. 41–46.

[159] A. Krasovsky, S. Vasyukov, and E. Vostorgina, "Obtaining the mtpa mode in the three-phase traction srm with a flat topped shape of phase current," in *2021 International Conference on Industrial Engineering, Applications and Manufacturing (ICIEAM)*. IEEE, 2021, pp. 378–383.

[160] K. Zhang, G. Li, Z. Zhu, and G. Jewell, "Torque performance improvement of doubly salient synchronous reluctance machines by current harmonic injection," in *2019 IEEE International Electric Machines & Drives Conference (IEMDC)*. IEEE, 2019, pp. 1222–1227.

[161] B. C. Mecrow, E. A. El-Kharashi, J. W. Finch, and A. G. Jack, "Preliminary performance evaluation of switched reluctance motors with segmental rotors," *IEEE Transactions on Energy Conversion*, vol. 19, no. 4, pp. 679–686, 2004.

[162] W. Fei, P. C. K. Luk, J. X. Shen, B. Xia, and Y. Wang, "Permanent-magnet flux-switching integrated starter generator with different rotor configurations

for cogging torque and torque ripple mitigations," *IEEE Transactions on Industry Applications*, vol. 47, no. 3, pp. 1247–1256, 2011.

[163] M. Ehsani, I. Husain, and A. B. Kulkarni, "Elimination of discrete position sensor and current sensor in switched reluctance motor drives," *IEEE Transactions on Industry Applications*, vol. 28, no. 1, pp. 128–135, 1992.

[164] M. Aryanezhad, "85a novel designing approach to dual rotor switched reluctance motor based electric vehicles," in *2015 30th International Power System Conference (PSC)*. IEEE, 2015, pp. 54–59.

[165] G. Lei, J. Zhu, Y. Guo, C. Liu, and B. Ma, "A review of design optimization methods for electrical machines," *Energies*, vol. 10, no. 12, p. 1962, 2017.

[166] G. Lei, T. Wang, Y. Guo, J. Zhu, and S. Wang, "System-level design optimization methods for electrical drive systems: Deterministic approach," *IEEE Transactions on Industrial Electronics*, vol. 61, no. 12, pp. 6591–6602, 2014.

[167] K. Diao, X. Sun, G. Lei, Y. Guo, and J. Zhu, "Multiobjective system level optimization method for switched reluctance motor drive systems using finite-element model," *IEEE Transactions on Industrial Electronics*, vol. 67, no. 12, pp. 10 055–10 064, 2020.

[168] G. Lei, T. Wang, J. Zhu, Y. Guo, and S. Wang, "System-level design optimization method for electrical drive systems‚Äîrobust approach," *IEEE Transactions on Industrial Electronics*, vol. 62, no. 8, pp. 4702–4713, 2015.

[169] G. Lei, Y. Guo, J. Zhu, T. Wang, X. Chen, and K. Shao, "System level six sigma robust optimization of a drive system with pm transverse flux machine," *IEEE Transactions on Magnetics*, vol. 48, no. 2, pp. 923–926, 2012.

[170] G. Lei, C. Liu, J. Zhu, and Y. Guo, "Techniques for multilevel design optimization of permanent magnet motors," *IEEE Transactions on Energy Conversion*, vol. 30, no. 4, pp. 1574–1584, 2015.

[171] Y.-K. Kim, J.-P. Hong, and J. Hur, "Torque characteristic analysis considering the manufacturing tolerance for electric machine by stochastic response surface method," *IEEE Transactions on Industry Applications*, vol. 39, no. 3, pp. 713–719, 2003.

[172] A. Cavagnino, G. Bramerdorfer, and J. A. Tapia, "Optimization of electric machine designs-part ii," *IEEE Transactions on Industrial Electronics*, vol. 65, no. 2, pp. 1700–1703, 2017.

[173] W. Jiang, T. Jahns, T. Lipo, W. Taylor, and Y. Suzuki, "Machine design optimization based on finite element analysis in a high-throughput computing environment," in *2012 IEEE Energy Conversion Congress and Exposition (ECCE)*. IEEE, 2012, pp. 869–876.

[174] L. Chen, J. Wang, P. Lazari, and X. Chen, "Optimizations of a permanent magnet machine targeting different driving cycles for electric vehicles," in *2013 International Electric Machines & Drives Conference*. IEEE, 2013, pp. 855–862.

[175] Y.-K. Kim, S.-h. Rhyu, and I.-S. Jung, "Robust design based on the response surface method for bldc motor," in *2010 International Conference on Electrical Machines and Systems*. IEEE, 2010, pp. 1159–1162.

[176] A. D. Karaoglan, D. G. Ocaktan, A. Oral, and D. Perin, "Design optimization of magnetic flux distribution for pmg by using response surface methodology," *IEEE Transactions on Magnetics*, vol. 56, no. 6, pp. 1–9, 2020.

[177] P. Stewart, P. J. Fleming, and S. A. MacKenzie, "On the response surface methodology and designed experiments for computationally intensive distributed aerospace simulations," in *Proceedings of the Winter Simulation Conference*, vol. 1. IEEE, 2002, pp. 476–482.

[178] S. Skaar and R. Nilssen, "Genetic optimization of electric machines, a state of the art study," 2004.

[179] S.-W. Jung, J.-S. Ro, and H.-K. Jung, "A hybrid algorithm using shape and topology optimization for the design of electric machines," *IEEE Transactions on Magnetics*, vol. 54, no. 3, pp. 1–4, 2017.

[180] T. Sato, K. Watanabe, and H. Igarashi, "Multimaterial topology optimization of electric machines based on normalized gaussian network," *IEEE transactions on magnetics*, vol. 51, no. 3, pp. 1–4, 2015.

[181] S. Silber, W. Koppelstätter, G. Weidenholzer, G. Segon, and G. Bramerdorfer, "Reducing development time of electric machines with symspace," in *2018 8th international electric drives production conference (EDPC)*. IEEE, 2018, pp. 1–5.

[182] C. Chang, W. Fu, and F. Wen, "Load frequency control using genetic-algorithm based fuzzy gain scheduling of pi controllers," *Electric Machines and power systems*, vol. 26, no. 1, pp. 39–52, 1998.

[183] D.-H. Cho, J.-K. Kim, H.-K. Jung, and C.-G. Lee, "Optimal design of permanent-magnet motor using autotuning niching genetic algorithm," *IEEE Transactions on Magnetics*, vol. 39, no. 3, pp. 1265–1268, 2003.

[184] J. W. Jiang, B. Bilgin, B. Howey, and A. Emadi, "Design optimization of switched reluctance machine using genetic algorithm," in *2015 IEEE International Electric Machines & Drives Conference (IEMDC)*. IEEE, 2015, pp. 1671–1677.

[185] C.-H. Yoo, "A new multi-modal optimization approach and its application to the design of electric machines," *IEEE Transactions on Magnetics*, vol. 54, no. 3, pp. 1–4, 2017.

[186] M. Dabrowski and A. Rudenski, "Application of evolutionary algorithms for optimisation of electric machines," in *6th International Conference on Computational Electromagnetics*. VDE, 2006, pp. 1–2.

[187] Y. Duan, R. Harley, and T. Habetler, "Comparison of particle swarm optimization and genetic algorithm in the design of permanent magnet motors," in *2009 IEEE 6th international power electronics and motion control conference*. IEEE, 2009, pp. 822–825.

[188] N. Rostami, M. R. Feyzi, J. Pyrhonen, A. Parviainen, and V. Behjat, "Genetic algorithm approach for improved design of a variable speed axial-flux permanent-magnet synchronous generator," *IEEE Transactions on Magnetics*, vol. 48, no. 12, pp. 4860–4865, 2012.

[189] D.-K. Lim, D.-K. Woo, H.-K. Yeo, S.-Y. Jung, J.-S. Ro, and H.-K. Jung, "A novel surrogate-assisted multi-objective optimization algorithm for an electromagnetic machine design," *IEEE Transactions on Magnetics*, vol. 51, no. 3, pp. 1–4, 2015.

[190] S. Arslan, O. Gurdal, and S. Akkaya Oy, "Design and optimization of tubular linear permanent-magnet generator with performance improvement using response surface methodology and multi-objective genetic algorithm," *Scientia Iranica*, vol. 27, no. 6, pp. 3053–3065, 2020.

[191] G. Y. Sizov, D. M. Ionel, and N. A. Demerdash, "Multi-objective optimization of pm ac machines using computationally efficient-fea and differential evolution," in *2011 IEEE International Electric Machines & Drives Conference (IEMDC)*. IEEE, 2011, pp. 1528–1533.

[192] A. Mansouri, N. Smairi, and H. Trabelsi, "Multi-objective optimization of an in-wheel electric vehicle motor," *International Journal of Applied Electromagnetics and Mechanics*, vol. 50, no. 3, pp. 449–465, 2016.

[193] S. Doi, H. Sasaki, and H. Igarashi, "Multi-objective topology optimization of rotating machines using deep learning," *IEEE transactions on magnetics*, vol. 55, no. 6, pp. 1–5, 2019.

[194] J. Gao, L. Dai, and W. Zhang, "Improved genetic optimization algorithm with subdomain model for multi-objective optimal design of spmsm," *CEs transactions on electrical machines and systems*, vol. 2, no. 1, pp. 160–165, 2018.

[195] S. Stipetic, W. Miebach, and D. Zarko, "Optimization in design of electric machines: Methodology and workflow," in *2015 Intl Aegean Conference on Electrical Machines & Power Electronics (ACEMP), 2015 Intl Conference on Optimization of Electrical & Electronic Equipment (OPTIM) & 2015 Intl Symposium on Advanced Electromechanical Motion Systems (ELECTROMOTION)*. IEEE, 2015, pp. 441–448.

[196] Y.-m. You, "Multi-objective optimal design of permanent magnet synchronous motor for electric vehicle based on deep learning," *Applied Sciences*, vol. 10, no. 2, p. 482, 2020.

[197] S. Smaka, S. Konjicija, S. Masic, and M. Cosovic, "Multi-objective design optimization of 8/14 switched reluctance motor," in *2013 International electric machines & drives conference*. IEEE, 2013, pp. 468–475.

[198] T. D. Strous, X. Wang, H. Polinder, and J. B. Ferreira, "Finite element based multi-objective optimization of a brushless doubly-fed induction machine," in *2015 IEEE International Electric Machines & Drives Conference (IEMDC)*. IEEE, 2015, pp. 1689–1694.

[199] M. Balaji and V. Kamaraj, "Evolutionary computation based multi-objective pole shape optimization of switched reluctance machine," *International Journal of Electrical Power & Energy Systems*, vol. 43, no. 1, pp. 63–69, 2012.

[200] W. Yan, H. Chen, X. Liu, X. Ma, Z. Lv, X. Wang, R. Palka, L. Chen, and K. Wang, "Design and multi-objective optimisation of switched reluctance machine with iron loss," *IET Electric Power Applications*, vol. 13, no. 4, pp. 435–444, 2019.

[201] M. Afifi, H. Rezk, M. Ibrahim, and M. El-Nemr, "Multi-objective optimization of switched reluctance machine design using jaya algorithm (mo-jaya)," *Mathematics*, vol. 9, no. 10, p. 1107, 2021.

[202] A. Zahid and B. Bilgin, "Determining the control objectives of a switched reluctance machine for performance improvement in generating mode," *IEEE Open Journal of Industry Applications*, 2023.

[203] R. REBBAH, B. H. R. EL-HANA, B. AMAR, and R. FARES, "Multi-objective optimization design of 8/6 switched reluctance motor using ga and pso algorithms," *Journal of Electrical Engineering*, vol. 15, no. 4, pp. 8–8, 2015.

[204] S. Zhang, S. Li, R. G. Harley, and T. G. Habetler, "An efficient multi-objective bayesian optimization approach for the automated analytical design of switched reluctance machines," in *2018 IEEE Energy Conversion Congress and Exposition (ECCE)*. IEEE, 2018, pp. 4290–4295.

[205] J. Branke, T. Kaußler, and H. Schmeck, "Guidance in evolutionary multi-objective optimization," *Advances in engineering software*, vol. 32, no. 6, pp. 499–507, 2001.

[206] C. A. Coello Coello and A. D. Christiansen, "Moses: A multiobjective optimization tool for engineering design," *Engineering Optimization*, vol. 31, no. 3, pp. 337–368, 1999.

[207] R. T. Marler and J. S. Arora, "Function-transformation methods for multi-objective optimization," *Engineering Optimization*, vol. 37, no. 6, pp. 551–570, 2005.